
Electronic Thesis and Dissertation Repository

1-22-2013 12:00 AM

Engineering nanocomposites for antimicrobial application

Binyu Yu

The University of Western Ontario

Supervisor

Jun Yang

The University of Western Ontario

Graduate Program in Biomedical Engineering

A thesis submitted in partial fulfillment of the requirements for the degree in Doctor of Philosophy

© Binyu Yu 2013

Follow this and additional works at: <https://ir.lib.uwo.ca/etd>



Part of the [Biomaterials Commons](#), and the [Other Biomedical Engineering and Bioengineering Commons](#)

Recommended Citation

Yu, Binyu, "Engineering nanocomposites for antimicrobial application" (2013). *Electronic Thesis and Dissertation Repository*. 1083.

<https://ir.lib.uwo.ca/etd/1083>

This Dissertation/Thesis is brought to you for free and open access by Scholarship@Western. It has been accepted for inclusion in Electronic Thesis and Dissertation Repository by an authorized administrator of Scholarship@Western. For more information, please contact wlsadmin@uwo.ca.

Engineering nanocomposites for anti-biofouling application

(Spine title: Engineering nanocomposites for anti-biofouling application)

(Thesis format: Integrated Article)

by

Binyu **Yu**

Biomedical Engineering Graduate Program

Faculty of Engineering

A thesis submitted in partial fulfillment
of the requirements for the degree of
Doctor of Philosophy

The School of Graduate and Postdoctoral Studies
The University of Western Ontario
London, Ontario, Canada

© Binyu Yu 2013

CERTIFICATE OF EXAMINATION

Supervisor

Examiners

Dr. Jun Yang

Dr. Jesse Zhu

Supervisory Committee

Dr. Paul Charpentier

Dr. Leo Lau

Dr. Xueliang A Sun

Dr. Jin Zhang

Dr. Jesse Greener

The thesis by

Binyu Yu

entitled:

Engineering nanocomposite for antimicrobial application

is accepted in partial fulfillment of the
requirements for the degree of
Doctor of Philosophy

Date

Chair of the Thesis Examination Board

Abstract

In this thesis, active and passive antimicrobial methods have been applied to fabricate antifouling surfaces. In the first study, we reported the synthesis and characterization of neat TiO_2 and Ag-TiO_2 composite nanofilms prepared on silicon wafer by sol-gel method. The synthesized Ag-TiO_2 thin films showed enhanced bactericidal activities compared to the neat TiO_2 nanofilm both in the dark and under UV illumination. The advantage of Ag-TiO_2 nanocomposites is to expand the nanomaterial's antibacterial function to a broader range of working conditions. In the second study, we reported the synthesis, characterization and environmental application of nitrogen doped TiO_2 photocatalyst in the form of powder and film. TiO_2 photocatalysts were synthesized by hydrolysis of titanium tetra-isopropoxide in the presence of urea as nitrogen source. The visible light induced photocatalytic inactivation of bacteria (*Escherichia coli*) with the obtained nano-powders and nano-films was tested.

In the following study, we reported the successful formation of a titanium dioxide (TiO_2) layer on butyl rubber (BR) substrate, cotton sheet and silicon wafer surfaces by using modified liquid phase deposition (LPD) method at mild environmental conditions. Various synthetic conditions were studied to control the morphology and nanostructures of the deposited TiO_2 coatings. Superoleophobic TiO_2 coatings were prepared after surface fluorination. The formed TiO_2 coatings showed excellent antibacterial adhesion ability.

Superoleophobic surfaces, which are thought to limit bacterial contamination, were fabricated by an easy spray method. The surface of any polymers can be made superoleophobic using the following simple three-step process: (1) the spraying of polymer-nanoparticle mixtures; (2) cross-linking the coating to the substrate; and (3) chemical modification of the outer surface by perfluorosilane. Superoleophobicity is achieved by the combination of re-entrant and convex morphology of multiscale agglomerates produced by nano-particles embedded in polymer matrix and surface fluorination. Preparation parameters were optimized. Surface characterizations were extensively studied on the surface morphology, roughness and chemical compositions of the composite coatings with different nanofillers loading. The superoleophobic coatings presented excellent resistance to non-

specific protein adsorption and show antibacterial adhesion. It is a promising material for biomedical and industrial applications.

Keywords: Titanium oxide, nitrogen doped, butyl rubber, liquid phase deposition superoleophobic, non-fouling, biofilm, protein adsorption, bacterial adhesion.

Co-Authorship Statement

This doctoral thesis has been carefully prepared according to the regulations for an integrated-article format thesis stipulated by the Faculty of Graduate and Postdoctoral Studies at the University of Western Ontario, and has been co-authored as follows:

CHAPTER 2: SYNTHESIS OF SILVER-TIO₂ COMPOSITE NANO-THIN FILM FOR ANTIMICROBIAL APPLICATION

All the preparation for experimental testing and set-up was undertaken by B. Yu under the supervision of Dr. J. Yang. All the experiments were conducted by B. Yu under the supervision of Dr. J. Yang. Drafts of Chapter 2 were prepared by B. Yu and reviewed by Dr. J. Yang. A paper co-authored by B. Yu, W.M.Lau and J. Yang has been published on Nanotechnology.

CHAPTER 3: PREPARATION AND CHARACTERIZATION OF NITROGEN-TIO₂ PHOTOCATALYST WITH HIGH CRYSTALLINITY AND ENHANCED PHOTOINACTIVATION

All the preparation for experimental testing and set-up was undertaken by B. Yu under the supervision of Dr. J. Yang. All the experiments were conducted by B. Yu under the supervision of Dr. J. Yang. Drafts of Chapter 3 were prepared by B. Yu and reviewed by Dr. J. Yang. A paper co-authored by B. Yu, and J. Yang is to be submitted.

CHAPTER 4: CHARACTERIZATION AND ANTIBACTERIAL ADHESION PERFORMANCE OF TIO₂ COATING PREPARED BY LIQUID PHASE DEPOSITION METHOD

All the preparation for experimental testing and set-up was undertaken by B. Yu under the supervision of Dr. J. Yang. All the experiments were conducted by B. Yu under the

supervision of Dr. J. Yang. Drafts of Chapter 4 were prepared by B. Yu and reviewed by Dr. J. Yang. A paper co-authored by B. Yu, and J. Yang is to be submitted.

CHAPTER 5: A NOVEL METHOD FOR ENGINEERING SUPEROLEOPHOBIC AND CONDUCTIVE DUAL-FUNCTIONAL COATINGS ON FLEXIBLE AND STRETCHABLE SUBSTRATES

All the experiments were conducted by B. Yu under the supervision of Dr. J. Yang. An invention report was submitted to World Discoveries. Drafts of Chapter 5 were prepared by B. Yu and reviewed by Dr. J. Yang. A paper co-authored by B. Yu, and J. Yang is to be submitted.

CHAPTER 6: SUPEROLEOPHOBIC SURFACES AND THE RESISTANCE TO PROTEIN ADSORPTION AND BACTERIAL ADHESION

All the preparation for experimental testing and set-up was undertaken by B. Yu under the supervision of Dr. J. Yang. All the experiments were conducted by B. Yu under the supervision of Dr. J. Yang. Drafts of Chapter 6 were prepared by B. Yu and reviewed by Dr. J. Yang. A paper co-authored by B. Yu, and J. Yang is to be submitted.

ACKNOWLEDGMENTS

First I would like to thank my research supervisor, Prof. Jun Yang, for his guidance, support and discussions throughout my PhD research work. I also thank Prof. Jun Yang for providing me the opportunity to work with industry partners, including Ross-tech Inc. and LANXESS. I would also like to thank my committee members, Prof. Leo Lau and Prof. Jin Zhang, for your time and constructive suggestion for this thesis.

Furthermore, I would like to thank all my colleagues, to these who help me and challenge me during my PhD study. My sincere thanks also go to Dr. Richard Gardiner, Karen Nygard and Nicole Bechard from Biotron, Kimberley R. Law from Department of Earth Science for your discussions and helpful technical support during this research work. I also acknowledge technicians and scientists in Surface Science Western, including Mr. Ross Davidson, Ms. Mary Jane Walzak, Mr. Brad Kobe, Dr. Mark Biesinger, Dr. Heng-Yong Nie and Ms. Heather Bloomfield, for the help and assistance in sample measurement. My thanks also go to my other friends in and outside of Western for the generous help and encouragement during my PhD study.

Finally, I would like to dedicate this thesis to my family. I deeply thank my parents for the years of understanding and supporting. And to my dear husband Jie, who always inspire me, encourage me and turn my life to a different and positive way and made me to become more than I was. Thanks for your endless love.

Table of Contents

CERTIFICATE OF EXAMINATION	ii
Abstract.....	iii
Co-Authorship Statement	v
ACKNOWLEDGMENTS	vii
Table of Contents	viii
List of Tables	xiii
List of Figures	xiv
Chapter 1	1
1 General introduction	1
1.1 Problems of biofouling in the environment and biomedical field.....	1
1.2 Principle of Biofouling.....	3
1.2.1 Protein adsorption	3
1.2.2 Bacterial adhesion.....	6
1.3 Strategies to prepare antifouling surface	10
1.3.1 Active antifouling coatings	10
1.3.2 Passive antifouling coatings.....	16
1.4 Scope of the thesis.....	25
1.5 Literature citations	27
Chapter 2.....	41
2 Synthesis of Ag-TiO ₂ composite nano-thin film for antimicrobial application	41
2.1 Introduction	41
2.2 Materials and methods.....	43
2.2.1 Materials	43
2.2.2 Preparation of silicon wafer supported TiO ₂ and Ag-TiO ₂ films.....	44

2.2.3	Materials characterization	45
2.2.4	Measurements of photoinduced super-hydrophilicity	45
2.2.5	Antibacterial activity evaluation	46
2.3	Results and discussion	47
2.3.1	Characterization of the TiO ₂ and Ag-TiO ₂ films.....	47
2.3.2	Hydrophilicity.....	55
2.3.3	Antibacterial activity evaluation.....	56
2.4	Conclusions	60
2.5	References.....	61
Chapter 3	65
3	Preparation and characterization of Nitrogen doped TiO ₂ photocatalst with high crystallinity and enhanced photoinactivation.....	65
3.1	Introduction	65
3.2	Materials and methods.....	67
3.2.1	Chemicals and materials.....	67
3.2.2	Preparation of materials	67
3.2.3	Characterization methods.....	68
3.2.4	Photocatalytic activity measurement.....	69
3.3	Results and discussion	70
3.3.1	Characterization of N-TiO ₂	70
3.3.2	Photocatalytic degradation of Methyl blue under visible light	77
3.3.3	Antibacterial activity evaluation.....	80
3.4	Conclusions	82
3.5	References.....	83
Chapter 4	88
4.	Characterization and antibacterial adhesion performance of TiO ₂ coatings prepared by liquid phase deposition	88

4.1 Introduction	88
4.2. Methodology	89
4.2.1 Chemicals and materials.....	89
4.2.2 Preparation of seeds.....	90
4.2.3 Preparation of TiO ₂ coating	90
4.2.4 Surface characterization	91
4.2.5 Tape test.....	91
4.2.6 Bacterial adhesion test.....	91
4.3 Results and Discussion	92
4.3.1 Reaction mechanism of LPD-derived TiO ₂ coating	92
4.3.2 Characterization of LPD-derived TiO ₂ coating on different substrates	93
4.3.3 Morphology control by addition of seeds.....	98
4.3.4 Effect of the amount of additives	99
4.3.5 Effect of the surface property of additives.....	101
4.3.6 Customized the LPD-derived TiO ₂ coating in the presence of seed	102
4.3.7 Surface wettability	104
4.3.8 Bacterial adhesion activity of the LPD-derived TiO ₂ coating.....	106
4.4 Conclusions	107
4.5 References.....	108
Chapter 5.....	112
5 A novel method for engineering superoleophobic and conductive dual- functional coatings on flexible and stretchable substrates	112
5.1 Introduction	112
5.2 Experimental Section	114
5.2.1 Materials	114

5.2.2 Preparation of Ultraviolet (UV) cross-linked coatings on butyl rubber surface	115
5.2.3 Wettability Test	116
5.2.4 Tensile Testing	116
5.2.5 Surface Characterization	116
5.2.6 Conductivity Measurements	117
5.3 Results and Discussion	117
5.3.1 Superoleophobic results for UV cross-linked coatings.....	117
5.3.2 Adhesion of the UV Cross-linked Coatings.....	124
5.3.3 Effect of cross-linking method on contact angle.....	126
5.3.4 Effect of Strain on Contact Angle	127
5.3.5 Electrical Conductivity of the UV cured coatings.....	128
5.4 Conclusions	129
5.5 References.....	130
Chapter 6.....	132
6 Superoleophobic surfaces and the resistance to protein adsorption and bacterial adhesion	132
6.1 Introduction	132
6.2 Materials and methods.....	134
6.2.1 Materials	134
6.2.2 General procedure for silane-coated glass/silicon wafer surface...	135
6.2.3 Preparation of PIP-CB-TiO ₂ coatings on PET	135
6.3 Surface contact angle measurement and surface characterization	136
6.3.1 Contact angle measurements	136
6.3.2 XPS, SEM and EDX measurements.....	136
6.3.3 Atomic force microscope (AFM) characterization	136
6.4 Protein solution preparation and single protein adsorption studies.....	137

6.5 Antifouling experiment	138
6.5.1 Static growth	138
6.5.2 Dynamic growth	138
6.6 Results and Discussion	139
6.6.1 X-ray photoelectron spectroscopy	139
6.6.2 Surface morphology of various coatings	144
6.6.3 Single protein adsorption on various surfaces	153
6.6.4 Bacterial adhesion on various surfaces	158
6.7 Conclusions	162
6.8 References	162
Chapter 7	166
Curriculum Vitae	169

List of Tables

Table 2-1: Composition of Ag-TiO ₂ composite films according to EDX analysis	53
Table 2-2: Surface roughness of the resultant films with different silver content.....	55
Table 2-3: The antibacterial test result of the composite films with different silver content against E. coli.....	57
Table 5-1: Concentration of solutions/dispersions for UV cured spray coatings.	118
Table 5-2: Apparent contact angle of UV cross-linked spray coatings.	122
Table 6-1: XPS elemental analysis. Atomic percent concentration (at.%) of the elements taken on fluorinated polymer-nanoparticle composite surface and reference PEO and PFTS modified silicon wafer surface.	140
Table 6-2: Apparent contact angle for hexadecane of various coatings.	151

List of Figures

Figure 1-1: Schematic view of simplification of protein model, with hydrophobic, neutral hydrophilic, negatively and positively charged domains (sides). The adsorption occurred on the domains that can interact with a surface having comparable properties. Reproduced from Reference [14].....	4
Figure 1-2: Scheme of biofilm development. Reproduced from Reference [43].	7
Figure 1-3: Scheme of the biofilm development. Details of the step 2 in the bacterial adhesion process. Reproduced from Reference[43].	8
Figure 1-4: Schematic photoexcitation on TiO ₂ after UV excitation. Reproduced from Reference [96].....	12
Figure 1-5: The photodegradation of bacteria. Reproduced from Reference [105].	14
Figure 1-6: The chemical structures of polymers for antifouling coating.	19
Figure 1-7: Three different wetting models. (1) Young's model, (2) Wenzel model and (3) Cassie-Baxter model.	23
Figure 2-1: Wide-angle x-ray scattering patterns of the result films with different Ag contents: sample SG0-SG4 is labeled as (a)-(e) in sequence.....	47
Figure 2-2: XPS spectra of TiO ₂ (a) and Ag-TiO ₂ (b) composite films of SG4.....	48
Figure 2-3: High-resolution XPS spectra of Ag 3d _{5/2} in Ag-TiO ₂ composite film SG4. (a) before UV exposure and (b) after 0.6 mW cm ⁻² UV exposure for 1 h.	49
Figure 2-4: Scanning electron micrographs of the (a) the neat TiO ₂ film surface of SG0, (b) SG1, (c) SG2, (d) SG3 and (e) SG4 Ag-TiO ₂ composite film surfaces. (a)-2, (b)-2, (c)-2, (d)-2 and (e)-2 are enlarged images of (a), (b), (c), (d) and (e) respectively. (f) The thickness of the films is about 370 nm as determined by the cross-section image.....	52

Figure 2-5: AFM top view images (left) and AFM angle view images(right) of the composite films: (a) SG0, (b) SG2, (c) SG3, (d) SG4.....	54
Figure 2-6: Zone of inhibition test results. Comparison of the composite Ag-TiO ₂ film and the neat TiO ₂ film for E.coli with agar plating.	57
Figure 2-7: Killing ratio of E.coli in the liquid film on Ag-TiO ₂ composite film and neat TiO ₂ film under 1h UV light illumination (0.6mW cm ⁻²) and in the dark for 1h. For the blank silicon wafer, the killing ratio is 18±5% under the same UV-irradiation.....	58
Figure 3-1: XRD patterns of the doped and undoped TiO ₂ nanoparticles prepared at different pH with $r = 100$, (a) pH = 1, without urea, (b) pH = 1, with urea, (c) pH = 3, without urea, (d) pH = 3, with urea. A represents anatase phase and B represents brookite phase. All the powder samples have been annealed at 400 °C for 4 h.....	71
Figure 3-2: XRD patterns of TiO ₂ powder samples prepared with molar ratio of water to TTIP at 10 and pH = 3 in the presence of various content of urea, (a) NT4, (b) NT3, (c) NT2, (d) NT1 and (e) NT0.....	72
Figure 3-3: TEM image of typical TiO ₂ powder (sample NT3).	73
Figure 3-4: (a) The XPS spectra of N-TiO ₂ (NT3). (b) Ti 2p of N-TiO ₂ XPS region; (c) N 1s of N-TiO ₂ XPS region.....	74
Figure 3-5: N ₂ adsorption-desorption isotherm of (a) homemade pure TiO ₂ , (b) N-doped TiO ₂ (NT3) and (c) P25.	75
Figure 3-6: UV-visible diffuse reflectance spectra of the N-TiO ₂ with various content of urea in the precursor solution as well as the undoped TiO ₂ samples. (a) NT1, (b) NT2, (c) NT3 and (d) NT4. The insets on the right side show the pictures of (i) undoped and (ii) N-TiO ₂ sample (NT3).	76
Figure 3-7: Comparison of percentage degradation of methylene blue aqueous solution by Degussa P25, N-TiO ₂ (NT1, NT2, and NT3) under the visible light irradiation and in the dark condition.	78

Figure 3-8: (i) adsorption followed by photocatalytic degradation of MB over various photocatalysts under visible light ($\lambda > 400$ nm) irradiation. (a) no catalyst (b) Degussa P25 (c) N-TiO ₂ powders (NT3). (ii) the UV visible spectroscopic changes of the MB solution over the N-TiO ₂ sample (NT3).	79
Figure 3-9: Schematic illustrations of the photodisinfection test.	80
Figure 3-10: Emission spectrum of (a) halogen lamp and (b) 13 W fluorescent lamp used in the visible light photo disinfection measurement, (1) without filter, (2) with 400 nm cut off filter.....	80
Figure 3-11: Killing ratio of <i>E.coli</i> (10^5 CFU mL ⁻¹) in the presence of N-doped TiO ₂ nano material and pure TiO ₂ nano material after exposure to the halogen lamp and fluorescent lamp source. (a) Illumination was carried out under halogen lamp at a light density of 3×10^4 lux for 1 h with nanoparticles (b) Illumination was carried out under halogen lamp at a light density of 3×10^4 lux for 15 min with nanothin film (c) Illumination was carried out under fluorescent lamp at a light density of 5000 lux for 18 h with nanothin film. Bacterial solution alone under various light illumination was chosen as control. Bars indicate average value from three independent experiment data. ($\bullet p < 0.05$)	81
Figure 4-1: SEM images of TiO ₂ coated on various substrates with different magnification. (a) LPD-derived TiO ₂ coating on UV/Ozone treated butyl rubber; (a)-2 zoom in picture in the white square area of (a); (b) LPD-derived TiO ₂ coating on pristine cotton sheet; (b)-2 zoom in picture in the white square area of (b); (c) LPD-derived TiO ₂ coating on prianha solution treated silicon wafer; (c)-2 zoom in picture in the white square area of (c); (a)-4 EDX result corresponding to (a)-2, carbon comes from the butyl rubber substrate, and fluorine comes from the LPD solution, Pt comes from the deposited conductive Pt layer.....	95
Figure 4-2: Optical microscopy of TiO ₂ coated on butyl rubber substrates after tape test. (a) LPD-derived TiO ₂ coating on UV/Ozone treated butyl rubber, (b) after tape test once, (c) after tape test twice. The circle area showed the changes after tape test.....	96
Figure 4-3: The XRD patterns of (a)TiO ₂ coating on butyl rubber surface and (b) TiO ₂ powders collected from precipitates from LPD method.	97

Figure 4-4: AFM images of 3D morphology and height images of the TiO ₂ coating on a butyl rubber surface deposited by the LPD method.....	97
Figure 4-5: SEM micrographs of the silicon wafer surface immersed in 0.05 M (NH ₄) ₂ TiF ₆ and 0.15 M H ₃ BO ₃ solution with seed of 0.3 μg mL ⁻¹ at 50 °C after (a) 6 h and (b) 12 h.	99
Figure 4-6: SEM micrographs of the silicon wafer substrates immersed in 0.05 M (NH ₄) ₂ TiF ₆ and 0.15 M H ₃ BO ₃ solution at 50 °C for 12 h with or without various concentration of seed (a) without seed, (b) with seed 0.15 μg mL ⁻¹ , (c) with seed 0.4 μg mL ⁻¹ , (d) with seed 3 μg mL ⁻¹	100
Figure 4-7: SEM micrographs of the silicon wafer surface immersed in 0.05 M (NH ₄) ₂ TiF ₆ and 0.15 M H ₃ BO ₃ solution at 50 °C for 12 h with (a) PEI modified seed at 2 μg mL ⁻¹ (b) PAA modified seed at 2 μg mL ⁻¹	102
Figure 4-8: Typical SEM micrographs of sphere-like TiO ₂ crystallites on the silicon wafer surface.....	103
Figure 4-9: Typical SEM micrograph of TiO ₂ crystallites formed clusters in sedimentation.....	103
Figure 4-10: SEM micrographs of the fluorinated silicon wafer surface with coating which immersed in 0.05 M (NH ₄) ₂ TiF ₆ and 0.15 M H ₃ BO ₃ solution at 50 °C for 6 h with seed at 1μg mL ⁻¹ . Optical image of the hexadecane contact angle is inserted in the top-right corner of the SEM images. (a)-(d) The top view of the surface coating with different magnification. (e) The cross-section view of the TiO ₂ particles formed cluster structure. EDX result showed the chemical composition of the cluster.	104
Figure 4-11: Representative SEM micrographs of the silicon wafer substrates with LPD-derived TiO ₂ coating after 6 h incubation in E. coli suspensions: (a) pristine LPD-derived TiO ₂ coating deposited for 6 h without seed, (b) fluorinated pristine LPD-derived TiO ₂ coating deposited for 6 h without seed, (c) LPD-derived TiO ₂ coating deposited for 12 h with seed, (d) fluorinated LPD-derived TiO ₂ coating with hierarchical structure.....	106

Figure 5-1: Schematic illustration of the spray apparatus. The spray distance (L) is 15 cm and the pressure P is 60 psi under room temperature (T=25 °C) and a range of relative humidity (RH: 40-50%).....	116
Figure 5-2: Representative SEM images at various magnifications showing the surface morphology of the UV cross-linked coatings with a solute concentration of 12.5 mg mL ⁻¹ . The solute concentrations are: (a) 50/50 wt% PIP/CB, (b) 45/55 wt% PIP/CB, (c) 40/60 wt% PIP/CB, and (d) 34/66 wt% PIP/CB. The insets are contact angle images of hexadecane (left) and methanol (right).....	119
Figure 5-3: SEM images of the UV cross-linked superoleophobic coating (P45C55) in cross-section at different magnification increasing from left to right. The cross-section was produced by freeze-fracturing.....	120
Figure 5-4: High resolution C (1s) spectrum of a spray coating containing 66% CB. Note the evidence of the -OH functionality on the surface.	121
Figure 5-5: SEM images of UV cured coatings sprayed on 6×6 cm ² butyl rubber substrate (P40C60, 40/60 wt% PIP/CB blends, 12.5 mg mL ⁻¹) using different suspension volumes: (a) 50 mL, (b) 25 mL and (c) 15 mL. Optical images of the hexadecane contact angles are given as inserts in the top-right corner of the corresponding surface.	123
Figure 5-6: Different magnification SEM images showing the coating morphology before and after tape test. Sample P40 C60 (40/60 wt% PIP/CB blends, 12.5 mg mL ⁻¹) was sprayed on 6×6cm ² butyl rubber substrate using 25 mL of suspensions. (a) UV cured and before tape test; (b) UV cured and after tape test; (c) not UV cured and before tape test and (d) not UV cured and after tape test. Optical image of the hexadecane contact angles are inserted in the top-right corner of the SEM images.....	125
Figure 5-7: SEM morphology of coatings (P50 C50, 50/50 wt% PIP/CB blends, 12.5 mg mL ⁻¹) with different crosslinking methods. (a) HHIC treatment for 2 min treatment (b) UV cured 20 min. Optical image of the hexadecane contact angles are inserted in the right corner of the corresponding SEM images.	126

Figure 5-8: Contact angles of Hexadecane as a function of strain for coatings deposited on butyl rubber substrate. The contact angle measurements were averaged for each data point.	128
Figure 5-9: Resistivity of composite coatings on butyl rubber substrate with different CB percentage (12.5 mg mL^{-1}).	129
Figure 6-1: XPS survey spectra performed on PEO modified silicon wafer surface in the binding energy range of 0-1100 eV with a pass energy of 80 eV.	142
Figure 6-2: XPS high-resolution C 1s spectrum of PEO control ($(\text{EtO})_3\text{Si}-(\text{CH}_2)_3-(\text{OCH}_2\text{CH}_2)_{6-9}-\text{OCH}_3$ grafted silicon wafer). The observed C 1s peak was fitted with two Gaussian peaks at binding energies of 284.99 eV (C-C/C-H), 286.78 eV (C-O).	142
Figure 6-3: XPS survey spectra performed on PFTS modified silicon wafer surface in the binding energy range of 0-1100 eV with a pass energy of 80 eV.	143
Figure 6-4: XPS high-resolution C 1s spectrum of PFTS grafted silicon wafer (PFTS control). The observed C 1s peak was fitted with five Gaussian peaks at binding energies of 285.00 eV (C-C/C-H), 286.50 eV (C-O/C-O-C), 288.0 eV (CF _x), 290.29 eV (CF ₂) and 292.76 (CF ₃).	143
Figure 6-5: Plan view for polyisoprene-nanofiller composite coating on PET surface of 33.3 wt% of polyisoprene with different nanofiller loading: (a) CB 6.7 wt%, titanium dioxide 60.3 wt%; (b) CB 13.4 wt%, titanium dioxide 53.6 wt%; (c) CB 33.4 wt%, titanium dioxide 33.3 wt%. Optical image of the hexadecane contact angles are inserted in the top-right corner of the corresponding surface.	147
Figure 6-6: Plan view for polyisoprene-nanofiller composite coating on PET surface (a) polyisoprene 40 wt%, CB 30 wt%, titanium dioxide 30 wt%; (b) polyisoprene 50 wt%, CB 25 wt%, titanium dioxide 25 wt%. Optical image of the hexadecane contact angles are inserted in the top-right corner of the corresponding surface.	148

Figure 6-7: (a) Plan view for Polyisoprene-TiO ₂ composite coating (polyisoprene 33 wt%, titanium dioxide 67 wt%) on PET surface. (b) the zoom-in image of the area as highlighted by the black circle in (a).....	149
Figure 6-8: Details of a superoleophobic surface coating on PET surface with composition of polyisoprene 40 wt%, CB 30 wt% and titanium dioxide 30 wt% and EDX element mapping.	150
Figure 6-9: 2D and 3D AFM topographical images of (a) composite film with the composition of PIP 40 wt%, CB 30 wt%, titanium dioxide 30 wt%, R _q =500±46 nm.(b) composite film with the composition of PIP 50 wt%, CB 25 wt%, titanium dioxide 25 wt%, R _q =375±47 nm. RMS roughness (R _q) of the composite coating surface, defined as the standard deviation of the elevation, z values. The average RMS roughness value was determined for responding surface from three different locations.....	152
Figure 6-10: Representative fluorescence microscopy graphs of samples immersed in 0.1 mol L ⁻¹ BSA PBS solution surface for 3 h. (a) PCT (PIP 40 wt%, CB 30 wt%, titanium dioxide 30 wt%), (b) FPCT (superoleophobic coatings with the composition of PIP 40 wt%, CB 30 wt%, titanium dioxide 30 wt%).....	154
Figure 6-11: Relative BSA (0.1 mg mL ⁻¹) adsorption on various surfaces for 3 h. FPCT stands for superoleophobic coatings with the composition of PIP 40 wt%, CB 30 wt%, titanium dioxide 30wt%. Fluorinated silicon wafer and PEO silane modified silicon wafer was used as reference.....	154
Figure 6-12: Representative fluorescence microscopy graphs of samples immersed in 1 mg L ⁻¹ BSA PBS solution surface for 3 h. (a) PCT (PIP 40 wt%, CB 30 wt%, titanium dioxide 30 wt%), (b) FPCT (superoleophobic coatings with the composition of PIP 40 wt%, CB 30 wt%, titanium dioxide 30 wt%).....	155
Figure 6-13: Representative fluorescence microscopy graphs of samples immersed in 0.1 mg L ⁻¹ fibrinogen PBS solution surface for 3 h. (a) PCT (PIP 40 wt%, CB 30 wt%, titanium dioxide 30 wt%), (b) FPCT (superoleophobic coatings with the composition of PIP 40 wt%, CB 30 wt%, titanium dioxide 30 wt%).....	155

Figure 6-14: Relative fibrinogen (0.1mg mL^{-1}) adsorption on various surfaces for 3 h. FPCT stands for superoleophobic coatings with the composition of PIP 40 wt%, CB 30 wt%, titanium dioxide 30 wt%. Fluorinated silicon wafer and PEO silane modified silicon wafer was used as reference..... 156

Figure 6-15: SEM images after various coatings immersed in E.coli suspensions (10^8 CFU mL^{-1}) for 24 h at different magnification: (a) pristine PET substrate, (b) FPCT composite coating on PET substrate, (c) pristine PCT composite coating on PET substrate. 159

Figure 6-16: SEM images of various coatings after dynamic growth using a parallel-plate flow chamber with E coli 10^8 CFU mL^{-1} for 24 h (shear rate 3.6 s^{-1}). (a) pristine PET substrate, (b) FPCT composite coating on PET substrate, (c) pristine PCT composite coatings on PET substrate. 160

Figure 6-17: Representative fluorescence microscopy images of attached E.coli cells from a suspension with 10^8 CFU mL^{-1} for 24 h dynamic growth. Bacterial cells were stained with LIVE/DEAD BacLight. Live cells fluoresce green. (a) Pristine PET substrate imaged at $20\times$ (b) FPCT superoleophobic coating imaged at $63\times$, (c) Pristine PCT composite coating imaged at $20\times$ 161

Chapter 1

1 General introduction

1.1 Problems of biofouling in the environment and biomedical field

Microorganisms are found everywhere in our daily life and most are harmless. However, humans and animals can be infected by microorganisms, such as bacteria, yeast, spores, and viruses, which may come from contaminated food and other sources. Common surfaces such as doorknobs, key boards and cell phones being constantly touched by hands, and ceramic tile in public washrooms are all compatible places for bacteria to grow and spread. Door handles and ceramic tiles themselves normally do not have antibacterial activity and microorganisms easily breed on their surfaces, resulting in biofilm formation and bacterial spread. These areas can serve as reservoirs of microbes for the transfer of infections. Public places, such as schools and hospitals, are risk areas for infection when children and patients may be vulnerable due to a weakened immune system. Disinfection is crucial to prevent infectious diseases.

Controlling bacterial adhesion and protein adsorption is crucial to the safe function of biosensors, therapeutic and diagnostic devices, and implant materials where the long-term exposure to physiologic fluids is required. In physiologic fluids, biofouling produced by protein and cell accumulation on vascular stents and cardiovascular implants, can result in thrombus and vascular occlusion [1, 2]. The nonspecific adsorption of proteins on biosensors decreases signal quality and reduces the efficacy of biomedical devices [3, 4]. Protein adsorption on surfaces provides the condition for bacterial colonization and subsequent biofilm formation. Bacterial colonization on surgical tools, catheters and contact lenses, impairs the function of such devices and the surface microbial infestation can cause serious infections [5]. There are considerable interests in the development of antimicrobial materials and surfaces to suppress bacterial growth and to reduce the risk for infestation.

Staphylococcus bacteria are known as a major cause of both hospital-acquired and community-based infections [6]. Coagulase-negative staphylococci (CoNS) that secrete bacterial slime (a polysaccharide) and form a biofilm firmly adhering on surfaces, are by far the most common cause of bacteremia related to indwelling devices [7]. Particularly, the bacteria *Escherichia coli* (*E.coli*) have been recognized as a significant cause of catheter infections [8]. Since the first report about drug resistance in *Staphylococci aureus* (*S.aureus*) in early 1960s [9], the increasing rate of drug resistance among *S.aureus* and CoNS species has been reported. In addition, *S.aureus* and CoNS, particularly those strains acquired in hospital, have become resistant to multiple antimicrobial agents [6].

Disinfectants to kill microbes are widely used in hospitals and other health care settings for a variety of topical and hard-surface applications. They are non-selective towards microorganisms in a broader spectrum of biocide ability, compared to antibiotics which are essential to prevent nosocomial infection. A variety of active chemical agents including alcohols, iodine, chlorine and triclosan have been used for a long time in disinfection. However, the use of chemical disinfectants is accompanied by the risk of allergic reactions and toxicity to humans. The traditional surface cleaning procedures might not be sufficient to remove formed biofilms and kill attached bacteria [10]. Due to the outbreak of infectious diseases caused by different pathogenic bacteria and the emergence of more-resistant microorganism owing to widespread use of antibiotics, more rigorous hygienic standards in public areas and hospitals are being promoted [11]. There is an urgent need to develop alternative efficient and sustainable antibacterial strategies, which are non-toxic and green (i.e. environmentally compatible and biodegradable).

In this thesis, we focused on the antimicrobial adhesion and anti-protein adsorption surfaces, which are able to reduce microbial contamination of the inanimate environment to prevent infectious diseases. First of all, microbial adhesion and protein adsorption mechanisms and processes will be introduced. Current strategies and recent reports to prepare surfaces with bactericidal ability, antifouling ability and resistance to microbial adhesion will be further discussed.

1.2 Principle of Biofouling

1.2.1 Protein adsorption

Biofouling is a dynamic process, in the form of protein, and bacterial attachment on a solid surface. When biomedical materials contact biological fluids such as blood, serum proteins regulate the process of bacterial adhesion [12], and protein adsorption is the first stage. A material surface that resists the adsorption of protein is normally a good candidate to resist bacterial adhesion [13]. Generally, proteins include serum proteins, enzymes, antibodies and foreign antigens. They are complex biopolymers composed of amino acids as monomeric units which have highly ordered structures. The approaching of protein molecules to the interface is driven by diffusion processes, which is dependent on the bulk concentration and the appropriate diffusion coefficient [14]. Protein adsorption spontaneously occurs if Gibbs free energy of the system decreases, $\Delta_{\text{ads}}G = \Delta_{\text{ads}}H - T\Delta_{\text{ads}}S < 0$, where G, H, S and T are the Gibbs free energy, enthalpy, entropy and the absolute temperature, respectively. Δ_{ads} represents the change of the thermodynamic function. Partial or complete conformational changes lead to an increase in conformational entropy, providing the driving force for protein adsorption. In contrast to small rigid molecules that can simply attach to or detach from an interface with certain adsorption and desorption probabilities, the irreversible adsorption of proteins is generally observed, owing to complex composition and structure of protein [15]. Protein at interfaces affects a wide variety of phenomena, including mammalian cell growth, reactions to implanted biomaterials, the formation of organized layers of protein and growth of bacteria [16]. Often protein adsorption onto a surface is energetically favorable to reduce the interfacial energy.

The environment of the solution in which the protein adsorption experiments are conducted, including pH, ionic strength, temperature and buffer composition, have significant effects on adsorption behaviour. Under mimicked physiological conditions, the environmental parameters of the solution are fixed. Furthermore, various proteins with remarkably diverse characteristics like size, structural stability and composition, have different behaviours on solid surfaces. For small and rigid proteins such as lysozyme, β -Lactoglobulin demonstrate little tendency for structural change upon surface

adsorption [17-19]. For high-abundance plasma proteins such as albumin, transferrin and immunoglobulin, the conformational reorientations occur in the course of surface adsorption [20]. The class of proteins with high molecular weight shows a strong affinity to hydrophobic surfaces with significant conformational reorientation owing to the large content of lipids or glycans in the structure [21]. Fig 1-1 illustrates the possible collision of protein to surface. The affinity of protein to any surface is determined by its independent acting domains.

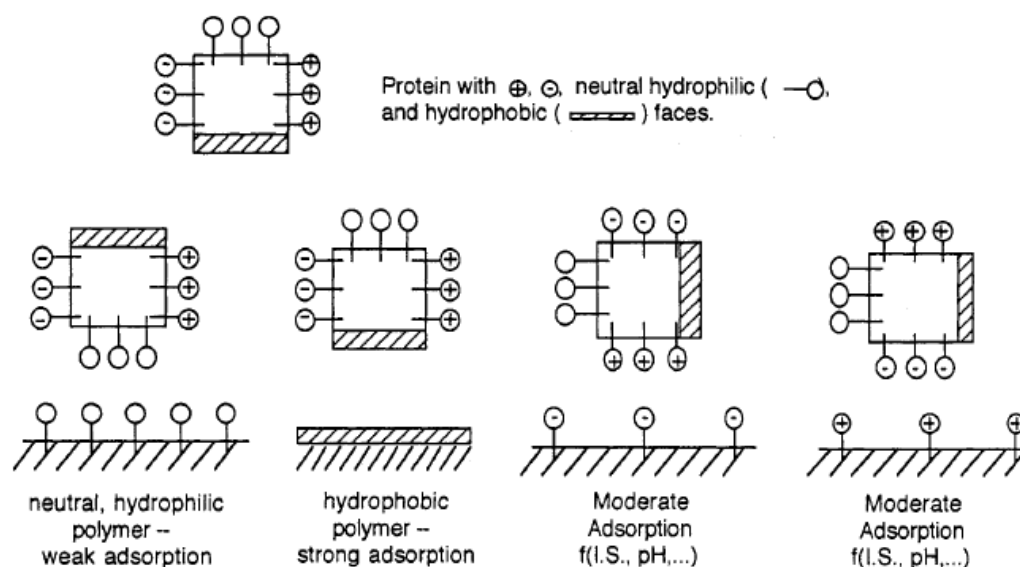


Figure 1-1: Schematic view of simplification of protein model, with hydrophobic, neutral hydrophilic, negatively and positively charged domains (sides). The adsorption occurred on the domains that can interact with a surface having comparable properties. Reproduced from Reference [14].

Other than the influence of the intrinsic properties of protein on the protein-surface interaction, the surface properties also play an important role, including surface morphology, surface energy, polarity and charge [22]. A series of experiments on materials with the potential applications on implant materials, biosensor surfaces and filter membranes have been performed to investigate protein adsorption behaviour on solid flat surfaces, especially self-assembled monolayers with various chemical

properties [23-29]. In most case, protein adsorption increases on hydrophobic substrates and decreases on hydrophilic substrates. As indicated in Fig 1.1, the non-polar surfaces destabilize proteins and facilitate conformational reorientations due to the strong hydrophobic interactions [25]. In general, proteins tend to adhere more strongly to nonpolar surfaces than to polar ones, to high surface tension rather than to low surface tension surfaces and to charged rather than to uncharged surfaces [20].

The kinetics of protein adsorption is complicated, including factors such as surface diffusion, aggregation and conformational changes, which are sensitive to surface properties. For example, many investigations studied the effect of surface morphology on protein adsorption both experimentally and theoretically [30-33]. The overall effect of nano-topographic factors, including roughness, curvature and geometry, on protein adsorption is still not clear according to the recent reports. Cai et al. [34] studied the protein adsorption of titanium films with different topographies ($2 \text{ nm} < R_{\text{rms}} < 21 \text{ nm}$) produced by electron beam deposition. The protein adsorption results (with albumin and fibrinogen) indicated that nano-scale roughness had little effect. Han et al. [35] also reported that there was no obvious correlation between roughness ($5 \text{ nm} < R_{\text{ave}} < 60 \text{ nm}$) and the amount of adsorbed protein (in the case of lysozyme). However, Rechendorff et al. [36] showed that the saturation amount of fibrinogen increased by about 70% with only 20% increase of surface area which was attributed to the nano-rough surface morphology. Dolatshahi et al. [37] also found similar results that the fibrinogen adsorption was influenced by surface roughness. Greater fibrinogen uptakes compared to more smoothly shaped surface features have been observed. The nano-rough surface morphology, in particular the sharp sidewalls of whisker-like surface protrusions, might force individual fibrinogen molecules to adsorb in a more upright position, thus, forming more closely packed protein layers leading to increased affinity [37]. The different results might be attributed to the methods applied to measure protein adsorption, the kind of protein and the roughness scale of the substrates. In our judgement, the inconsistent results require further investigation particularly the effect of surface roughness on protein adsorption behaviour, before general conclusions can be drawn.

Surface curvature as a measure of topography also influences protein-surface interaction. Lundqvist et al. [38] analyzed the adsorption of human carbonic anhydrase, a globular protein of comparable size to albumin, to the surface of silica nanoparticles with various diameters (6 to 15 nm) and found that particles with a larger diameter caused more perturbations of the protein secondary structure owing to larger particle–protein interaction surfaces. The same effect has also been reported from studies of the adsorption of egg lysozyme on silica nanoparticles of varying size (4, 20 and 100 nm) [39]. The author also reported that more α -helix structure of protein was lost on large silica nanoparticles. It is suggested that the decreased curvature of larger nanoparticles produced a shorter distance from the silica surface to the protein molecule and caused stronger interaction (Columbic and hydrophobic interaction). In contrast to small globular proteins, bigger conformational changes of fibrinogen on smaller nanoparticles (radius less than 30 nm) have been observed [40]. More studies are needed involving a broader range of proteins and different surfaces to explore the effect of curvature on protein adsorption.

Current literatures suggested that the surface morphology and nano-scale roughness have influence on protein adsorption to the surface on the amount of adsorption, conformation change. More experimental results are needed in order to draw general conclusions.

1.2.2 Bacterial adhesion

Bacteria are prokaryotic cells with size range from under 1 μm to 10 μm . Their semi-rigid walls are composed of phospholipids responsible for maintaining the three-dimensional shape of bacteria. Gram-positive bacteria have thick cell walls consisting of many layers of peptidoglycan and teichoic acids, whereas Gram-negative bacteria have a relatively thinner cell wall but more complex structures, containing a few layers of peptidoglycan, polysaccharides, proteins and lipids [41]. Bacterial survival depends on membrane lipid homeostasis and bacteria have the ability to adjust lipid compositions to acclimatize to different environments [42].

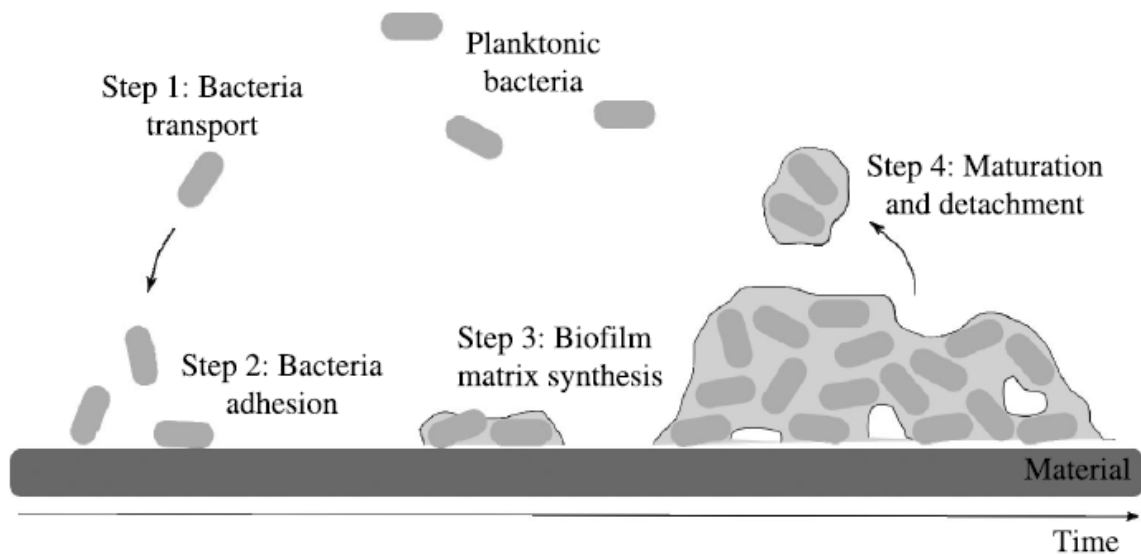


Figure 1-2: Scheme of biofilm development. Reproduced from Reference [43].

Bacterial adhesion to a surface and consequent biofilm development can be described as a four-phase process as schematised in Fig 1-2, including 1) the transport of the bacterium to the surface, 2) the initial surface interaction with a reversible physical phase and the attachment by specific interactions, a time-dependent and irreversible adhesion, 3) proliferation, formation of micro-colonies and synthesis of biofilm matrix and 4) maturation and detachment events [44, 45]. Other than the simple passive assembly of cells at the surface, the biofilms are structurally and dynamically complex biological systems consisting of an active aggregate of cells immersed in a matrix of extra-cellular polymeric substances (EPS). Biofilms trap nutrients from the environment and provide shelter for bacterial growth [46, 47]. In the final mature stage, biofilms release microorganisms back to the environment. As biofilms are particularly durable and persistent, the preventing of their initial formation to limit the detrimental impact is more effective than remediation [10]. Therefore, it is very important to control the initial attachment of bacteria to solid surfaces. Herein, we focus on the bacterial adhesion in the initial physical phase and bacteria substratum surface interactions.

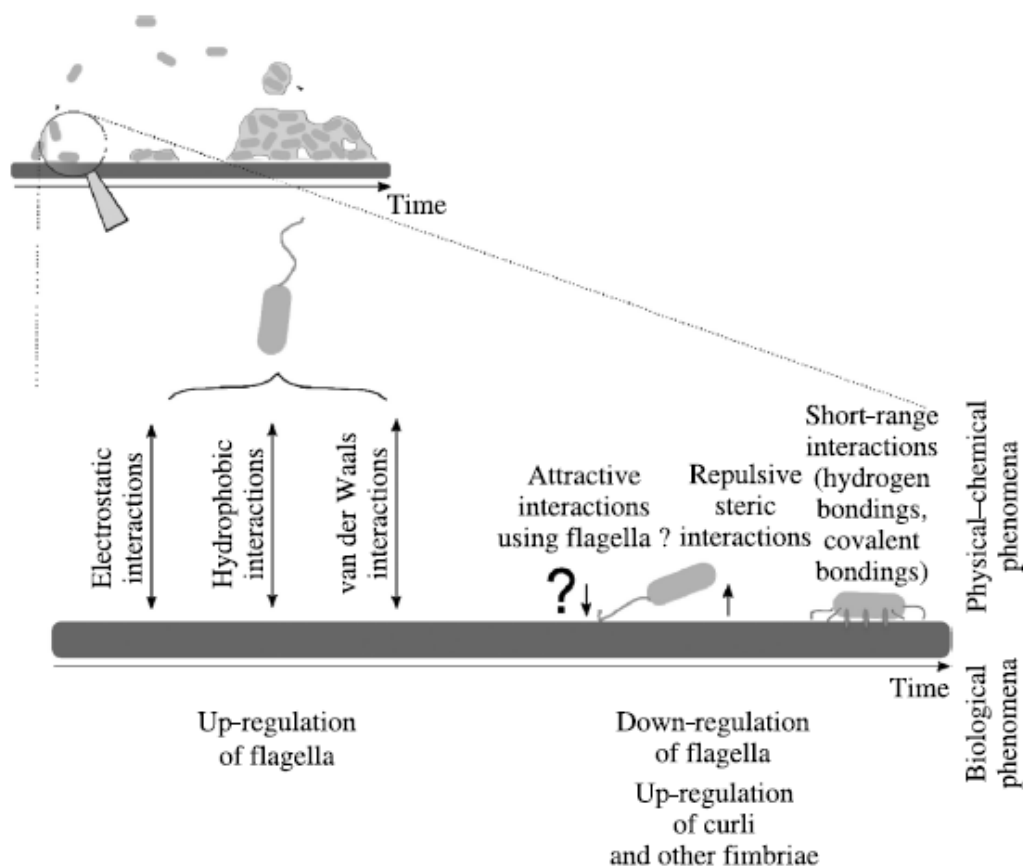


Figure 1-3: Scheme of the biofilm development. Details of the step 2 in the bacterial adhesion process. Reproduced from Reference[43].

Bacteria prefer to grow on available surfaces rather than in the surrounding aqueous phase [48, 49]. The physiochemical forces that control the initial attachment of bacteria are primarily Brownian motion, Van der Waals attraction forces, gravitational forces, electrostatic, hydration and hydrophobic interaction, followed by other short-range (< 5 nm) stereospecific interactions, such as chemical bonds, ionic and dipole interactions, hydrophobic interactions, mediate irreversible adhesion and attachment of the microorganism to a surface [50]. Fig 1-3 displays detailed information about the process of the initial surface interaction with a reversible physical phase and the attachment by specific interactions. Molecular specific reactions between bacteria and substrate surface are predominant in the short range of adhesion process, forming a stronger adhesion

between bacteria and a surface through a selective bridging function of bacterial surface polymeric structures including capsules, fimbriae/pili and slime. [44].

Bacterial adhesion is a complicated process that is affected by many factors, including the environment, the presence of serum proteins or bactericidal substances, the properties of the target surface and the intrinsic characteristics of the bacteria itself [44]. Our focus is on how the properties of surfaces influence bacterial adhesion.

Surface properties, e.g. material hydrophobicity and surface charge, influence bacterial adhesion. Generally, bacteria with hydrophobic properties prefer hydrophobic surfaces, while bacteria with hydrophilic characteristics prefer hydrophilic surfaces [44, 51]. Hydrophilic materials are more resistant to bacterial adhesion than hydrophobic materials [44, 52-54]. Bacterial adhesion is hindered by surface modification with ethylene glycol (EG) monolayer. The EG provides a template for water nucleation and forms a stable interfacial hydration layer [55, 56]. Bacteria in aqueous suspension are always negatively charged [57]. It was reported that the tested bacterial strains adhered rapidly to positively charged surfaces, although no subsequent growth of the Gram-negative strains was observed [58]. Long-range electrostatic forces may influence the initial phase of bacterial adhesion; positively charged surface can only inhibit growth of some adhered bacteria. Surfaces with bactericidal substances displayed a decreased adhesion [59-63].

Surfaces of the same materials and surface chemistry may have different bacterial attachment affinity in the same environmental conditions owing to different surface topography [45]. It has been shown that in general surfaces with higher roughness promote better bacterial adhesion owing to the greater surface area compare to smoother surface [64, 65]. However, Harris et al. [66] found that no differences between the adhesion of *S.aureus* on micro-scale rough standard titanium and smooth electropolished titanium surfaces under static conditions in vitro. Bacterial adhesion affected by micro-scale surface features has yet to be extensively studied, while few studies addressed the effect of nano-scale topography on bacterial response [67]. In an early work [68], a small increase in R_a values (0.04-1.24 μm , the surface roughness of a substratum was evaluated by laser profilometry), resulted in a significant increase of bacterial attachment,

compared to a larger increase of surface roughness ($R_a=1.86-7.89 \mu\text{m}$), although both adhesion values were higher than on smooth surfaces. A similar non-linear relationship between bacteria adhesion to the increase of roughness has been obtained by using AFM to measure the surface roughness and bacteria adhesion image [69]. More bacteria adhesion on a modified nano-scale smooth surface with an average surface roughness of 1.3 nm than the native sample surface with an average roughness of 2.1 nm was observed. This inverse relationship manifested that bacteria might be more susceptible to nano-scale surface roughness. The surface nanotopography was also found to stimulate the exerting of bacterial exopolysaccharide (EPS), which promote adhesion [70]. Furthermore, the surfaces with certain pattern or some hierarchical structure roughness might possess superhydrophobic wettability. These surfaces with self-cleaning ability demonstrated resistance to bacterial adhesion [71, 72]. Discussion of these concepts follows in later sections.

1.3 Strategies to prepare antifouling surface

Several strategies have been developed to fabricate antifouling surfaces or to overcome problems of biofouling on surfaces, such as the chemical modification involving biocidal agents and fouling release coatings, and the introduction of surface modified coatings with appropriate surface patterns and structures. Herein, methodologies towards preparing antifouling coatings are reviewed and those methods are basically categorized into two directions: 1) active methods, with intrinsic bactericidal properties such as metal and metallic oxide nanoparticles, carbon nanotubes and fullerenes, polycations (chitosan) and polysaccharide (antimicrobial peptides) and 2) passive methods, showing resistance to the adhesion of microorganisms including hydrophilic and superhydrophobic surfaces.

1.3.1 Active antifouling coatings

Metal and metallic oxide are among the most commonly studied active agents and applied for antibacterial applications [73]. The germicidal activity of metal, both as free or complexes species, is well known and has been well documented. Compared to the bulk micro-size structures, nanomaterials with size less than 100 nm possess unique properties (such as high surface-to-volume ratios, high reactivation and so forth) due to

size effects and surface phenomena at the nano-scale. A variety of metallic nanoparticles and compounds with bacteriostatic and bactericidal properties have been reported including copper [74-78], zinc oxide [79-82], magnesium oxide [59, 83], iron [84, 85], iron oxide [86-88] and titanium oxide (TiO₂) [89]. Production of reactive oxygen species (ROS) or heavy metal ions, which would result in oxidative damage to bacterial membranes, proteins and DNA, is the main mechanisms of antibacterial activity of metal oxides [59, 90, 91]. In addition, penetration of metal oxide nanoparticles into cells [59], electrostatic interactions [53] as mechanism of antibacterial activity have also been proposed. Among the metal with antibacterial properties, silver is the most promising and potent agents [81, 92].

Silver has been in use for the treatment of burns and chronic wounds for centuries in the form of metal silver, silver nitrate and silver sulfadiazine [93]. In the industrial field, silver nanoparticles and silver ions loading materials are dominated in the inorganic disinfection agent application due to its broad biocide spectrum and high efficiency. Possible mechanisms of antimicrobial action of silver ions have been suggested according to the morphological and structural changes in the bacterial cells. When silver ions are close enough to bacterial cell wall, the Coulomb attraction owing to opposite charges carried by silver ions and cell membrane, drives the coordination of silver ions to cell membrane. Thus, silver ions penetrate inside the bacterial cell and react to the thiol group proteins, resulting in the DNA molecules turn to the condensed form and lose the replication ability, eventually leading the death of cells [93]. Silver ions may also inactivate protein by acting with the sulfur containing protein [94]. As for the mechanisms of silver nanoparticles, it was demonstrated that the toxicity of various silver nanoparticles followed the dose-response pattern of bacterial exposed to silver ions [95]. It is believed that the silver ions released from silver nanoparticles exert the toxicity to bacteria instead of the silver nanoparticle itself. The antibacterial activity of silver nanoparticles can be controlled by modulating silver ions release through manipulation of oxygen availability, particle size, shape and types of coating [95].

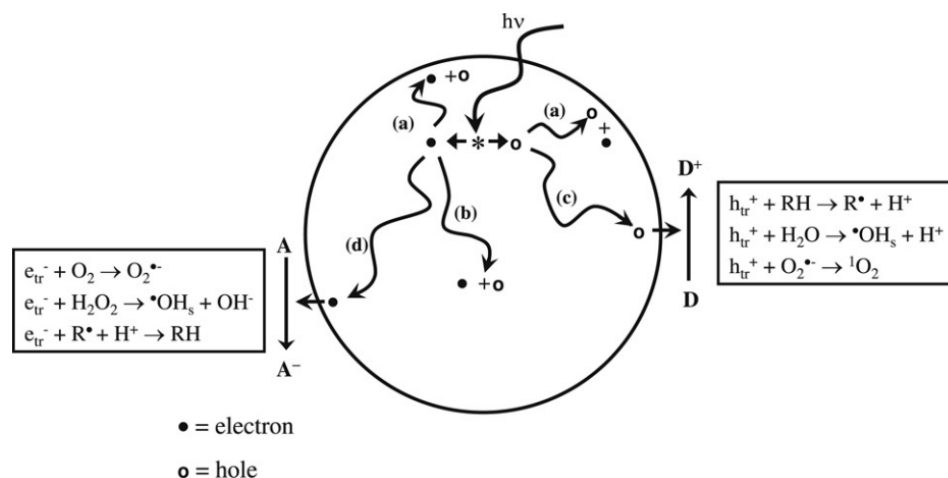


Figure 1-4: Schematic photoexcitation on TiO₂ after UV excitation. Reproduced from Reference [96].

TiO₂ is one of the most effective photocatalysts because of its strong oxidizing power, non-toxicity and long-term photostability. It is well-known that photocatalytic activity is strongly related to the physical properties including crystallinity, crystal structure, particle size, specific surface area (SSA) and morphology. As reported, TiO₂ has three main types of crystalline structures, known as anatase (tetragonal, band gap = 3.2 eV, which is equivalent to a wavelength of 388 nm), rutile (tetragonal, band gap = 3.02 eV) and brookite (orthorhombic, band gap = 2.96 eV) [97]. Anatase and brookite are thermodynamically metastable phases at lower temperatures and the bulk rutile is the most thermodynamically stable polymorph. An irreversible phase transition from brookite to anatase and to rutile usually occurs with increasing temperature [98]. Anatase and rutile phase are commonly used as photocatalysts, and most practical work has been carried out with either rutile or anatase [96]. In contrast, brookite has attracted much less interest due to the generally considered lack of photocatalytic activity, although continuing studies have shown that brookite is photocatalytically active [99].

TiO₂ as a photocatalyst has been extensively studied over recent decades for the strong oxidizing power when illuminated by UV light with wavelength <385 nm. When light absorption with energy equal to or greater than the band gap energy of the TiO₂, electron-

hole pairs are generated at the surface of the TiO_2 . Upon excitation, the photoinduced electron-hole pair is separated into a free electron and a free hole. The electron and hole either transfer to the surface of the photocatalyst or trapped there. Fig. 1-4 shows the electron-hole excitation process, characteristic surface reaction and some of the de-excitation pathways [96]. At the surface, the electron can transfer to atmospheric oxygen to form superoxide ions ($\text{O}_2^{\bullet-}$) and holes can react with adsorbed H_2O or OH^- at the catalyst/water interface to produce the highly reactive hydroxyl radicals (OH^\bullet). The photocatalytic process generates reactive oxygen species (ROS) such as hydroxyl radical (OH^\bullet), hydrogen peroxide (H_2O_2) and superoxide ($\text{O}_2^{\bullet-}$) which can oxidize and decompose many types of organic compounds and microbial organisms, such as cancer cells, viruses and bacteria [100-102]. Complete oxidation of organic compounds and whole cells to carbon dioxide can be achieved without creating secondary pollution [103]. Moreover, it also simultaneously degrades the toxic compounds released from the bacteria [104].

With excellent chemical stability, low cost and non-toxicity, TiO_2 became attractive for practical applications. Since 1985, the first report about that TiO_2 photocatalyst could kill bacterial cells in water, a variety of research works have been carried out related to the bactericidal effect of TiO_2 photocatalyst [89]. Fig. 1-5 schematically illustrates the process of photodegradation of bacterial cells. Hydroxyl radicals produced during the illumination process on TiO_2 surfaces may harm cellular macromolecules (e.g. lipids, proteins and nucleic acids) and promote other deleterious changes in bacterial cells (e.g. phospholipids peroxidation) [105]. The loss of bacterial respiratory activity owing to oxidation/reduction of the intracellular Coenzyme A (CoA) will cause bacterial death. If the TiO_2 particles are sufficiently small, they can penetrate the cell and implement the photocatalytic process inside and directly attack intracellular components [105]. Most studies reported the killing or inhibition of bacterial growth by using TiO_2 nanoparticles owing to the very large surface area and high efficiency. Lu et al. [106] have reported a possible bactericidal mechanism of the illuminated TiO_2 thin film. The cell wall was decomposed first and then the cell membrane was destroyed, resulting in the leakage of intracellular molecules and eventual cell death.

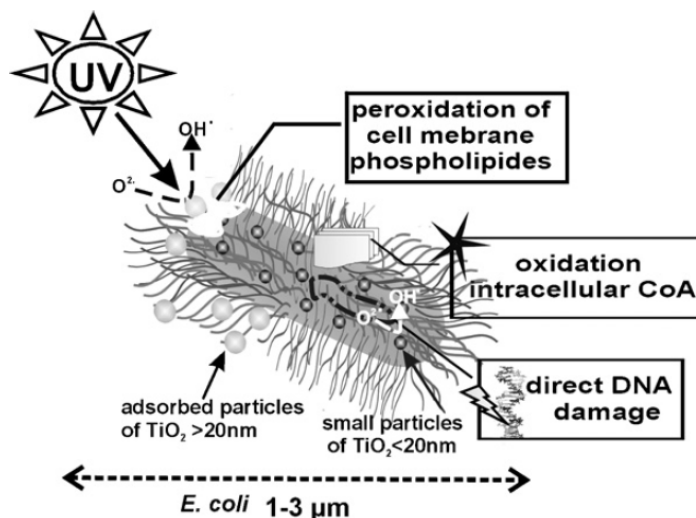


Figure 1-5: The photodegradation of bacteria. Reproduced from Reference [105].

Considering to expand the application field to indoor condition in the absence of UV-light and to utilize the solar energy efficiently, it is necessary to develop titania with photoresponse capacity within the visible range. Several methods have been used to improve the photocatalytic properties and antibacterial activities, including the reduce form of the band gap energy via surface modification with metal or another semiconductor and the generation of a defect structure to induce space-charge separation through metal or non-metal dopants. For instance, Yu et al. [107] described that 96.7% Gram positive bacterium *Micrococcus lylae* (3×10^6 CFU mL⁻¹) were killed by S-doped TiO₂ nanoparticles after 1 hour visible light illumination (100 W tungsten halogen lamp with 420nm filter). The doping of commercial TiO₂ powder with nitrogen and sulfur by direct heating the mixture of TiO₂ with thiourea showed high photocatalytic activity towards *E.coli* inactivation ($\sim 10^4$ CFU mL⁻¹) under blue light illumination [108]. Li et al reported enhanced photodisinfection of *E. coli* by using carbon and nitrogen co-doped TiO₂ [109]. The addition of noble metals such as gold and silver as electron trapper to reduce the electron-hole recombination rate also lead to the increase of photocatalytic efficiency. Wu and co-workers [110] studied the visible light induced bactericidal effect

of TiO₂ co-doped with nitrogen and silver. The resultant co-doped powder samples showed the survival fraction of *E. coli* $<10^{-5}$ within approx. 30 min irradiation, which is fastest ever reported using TiO₂ based photocatalysts.

Compared to the application of nanopowders, which in some practical applications require extra nanopowder filtration and recollection processes and have the potential environmental pollution risk, the form of a thin film is more favourable. Many techniques have been developed to coat surfaces with photocatalysts including wet methods such as sol-gel and spraying, or dry processes, such as ion-assisted electron beam evaporation, reactive sputtering, pulsed laser deposition and chemical vapour deposition [111-117]. Shieh et al. [115] developed a defective TiO₂ thin film on glass and steel substrates using radiofrequency sputter technique. They demonstrated a stronger antibacterial performance against *E. coli* than plain TiO₂ nanoparticles, with a killing efficiency of approximately 99.99% versus 50% under 5 h illumination of four 15 W fluorescent lamps. Wong et al. [114] demonstrated disinfection of various bacterial strains using nitrogen-doped TiO₂ films and carbon-doped TiO₂ films, prepared in an ion-assisted electron beam evaporation system. The study showed that nitrogen-doped TiO₂ films had better visible light photocatalytic bactericidal activity against human pathogens than TiO₂ film and carbon-doped TiO₂ films. Several pathogens also showed resistance against ROS attributed to the presence of the enzyme system. The presence of protein such as BSA or dye contaminant in the solution will inhibit the antibacterial performance. The mechanism remains to be further investigated.

Gram-negative bacteria *E. coli* and Gram-positive bacteria *S. aureus* are two common used organism models in antimicrobial tests. Although some researches claimed that *E. coli* is more easily deactivated under photocatalytic reaction than *S. aureus* caused by the thinner cell wall [118], it should be noted that *S. aureus* is more light sensitive and spontaneously exhibits a high kill rate purely from the light source [119], while Gram negative bacteria are far less susceptible to light-activated antimicrobial agents [120]. Therefore, *E. coli* is harder to kill than *S. aureus* [121]. The antibacterial activities of TiO₂ based photocatalyst are dependent on bacterial strains, light source, irradiation time, photocatalyst type, structure and the concentration. As there are no standardized

conditions for photocatalytic inactivation of bacteria, a direct comparison among the reported photosterilization activity data of TiO₂ under UV or under visible light irradiation is not realistic. However, N-doped TiO₂ is less effective than the pure TiO₂ under UV light irradiation, because the recombination sites from the dopant ions lead to the faster recombination of the electron-hole pairs, preventing the antimicrobial effects [121].

Carbon nanotubes (CNTs) and graphene have attracted great attention owing to the unique electrical properties and structural characteristics. CNTs with high surface areas and strong adsorption capacities as an effective dopant to TiO₂ based photocatalytic materials give rise to the enhanced visible light photocatalytic performance and improved bacterial inactivation [122]. CNT nanocomposites were reported to be resistant to protein adsorption [123]. Graphene-based nanomaterials (graphene oxide GO) also suppressed the growth of E.coli with mild cytotoxicity [124]. The antibacterial activity was attributed to the membrane stress induced by sharp edges of graphene nanosheets, leading to the damage of cell membranes and leakage of RNA [125].

1.3.2 Passive antifouling coatings

The surface chemistry of a solid substrate is one of key determinants of the initial adhesion, formation, stability and release of adhesion of fouling organisms to a surface [126]. Surface energy, mechanical properties and wettability also play an important role in the surface resistance to biofouling [127]. A general relationship (Baier curve) between surface tension and the relative amount of bioadhesion demonstrates that the minimal fouling is at a critical surface tension of 22-24 mN m⁻¹, which is equal to the cost for water rewet the surface [126]. One method of varying surface energy without changing the bulk materials is through surface modification by introducing materials fall above the zone of low cell adhesion defined by Baier.

In recent years, the polymer modification on various substrates to construct the antifouling surfaces has attracted much attention, especially after the development of surface initiated living radical polymerization techniques, *e.g.* reversible addition-fragmentation chain transfer (RAFT) polymerization and atom transfer radical

polymerization (ATRP). The advantages of the polymer modification include, 1) low cost of the abundant available monomers; 2) the well-defined surface chemistry of polymers; 3) the facile surface patterning as a means to construct various nanostructures on substrates; and 4) the advanced functionalities of polymers, *e.g.* stimuli-responsive polymers. In general, the adhesion strength of bioactive molecules to polymer surfaces (A) is dependent on the polymer modulus (E) and surface energy (σ), $A \sim (E\sigma)^{0.5}$ [128]. As a consequence, a number of polymers having low surface energy, including poly(ethylene glycol) (PEG), fluoride poly(methyl)acrylates, zwitterionic polymers, and polyelectrolytes, have been investigated for antifouling surface coating; besides, the low modulus polymers, *e.g.* poly(dimethylsiloxane) (PDMS) and polyurethane (PU) have been studied for the fouling release properties.

PEG with rather low polymer-water interfacial energy ($\sigma < 5 \text{ mJ m}^{-2}$) is a completely biocompatible polymer and has been widely used in biomedical industries [129]. The antifouling property of PEG modified substrates was firstly revealed in the studies of self-assembled monolayers (SAMs) of oligo (ethylene glycol) functionalized alkanethiolates on Au films by Prime and Whitesides [130]. SAMs composed of $\text{HS}(\text{CH}_2)_{11}(\text{OCH}_2\text{CH}_2)_6\text{OH}$ and $\text{HS}(\text{CH}_2)_{11}\text{CH}_3$ strongly prevented the protein adsorption on the modified substrates, when the hydrophilic thiolates reached above 60 mol. The theoretical calculation demonstrated that the chain length and grafting density of PEG on substrates played important roles in the antifouling behaviour [131]. The hydrated PEG layer acted as a kinetic “barrier” of substrate surfaces. Despite hydrophobic interaction between proteins and substrates, protein molecules approaching to the substrate surface compressed the hydrated PEG chains, resulting in a strong steric repulsion force of PEG chains and the unfavourable enthalpy. The short PEO chain with low surface coverage might lead the failure of antifouling due to the insufficient repulsion force [132, 133]. For example, using the “grafting to” approach where PEG chains were directly attached to substrates through the covalent bonding, the obtained surface could not inhibit the adsorption of bacteria [134]. Given that high surface coverage of PEG chains on substrates is required, the “grafting from” polymerization technique has been applied to *in situ* grow dense PEG chains on substrates [133, 135]. Using surface-initiated ATRP with a trimethoxysilane-based initiator, Tugulu et al. have systematically studied the

effect of PEG chain density on the nonfouling properties [135]. At high grafting density, the PEG grafts in the brush state detached from the substrate and had the highest resistance to the protein adsorption; while, the decrease of PEG grafting density that gave rise to the mushroom conformation of polymer chains on the substrate, resulted in the increase of protein attachment. However, the stability of PEG in biomedical environment limits the *in vivo* application, due to the autoxidation of PEG in the presence of transition metal ions and oxygen radicals.

The Zwitterionic polymers resembling the phospholipid design of cell membranes are composed of both positively and negatively charged repeat units. The non-fouling mechanism of Zwitterionic groups is attributed to the hydration layer of water molecules that bond to the charged terminal groups through solvation, and thus does not allow the attachment of proteins. Whitesides's group rendered the combinations of charged groups on SAMs to resist the nonspecific adsorption of proteins, using the mixed thiolates with trimethylammonium and sulfonate end groups [136]. The neutral surfaces formed by 1:1 positive and negative charge groups considerably prevented the nonspecific adsorption of proteins, while the single-component SAM with net positive or negative charged surface fully covered with monolayer of proteins. The resistance of Zwitterionic group functionalized surface to proteins presented the interesting dependence on the ionic strength and pH of solution. This suggested the possible design of stimuli-responsive protein adsorption, that is, proteins attach on surface at low ionic strength while detach at high ionic strength. Compared to the PEG surface, Zwitterionic polymers can significantly improve the stability. A number of Zwitterionic polymers based on poly(carboxybetaine) and poly(sulfobetaine) have been studied as non-fouling surfaces to protein, blood, and bacteria in recent years refer to Fig. 1-6 [137]. To avoid the complex design of Zwitterionic monomers, Chen et al. have designed the polyelectrolyte hydrogel composed of a variety of positively and negatively charged monomers [138]. The mixed charged groups (e.g. amine and carboxylic acid) formed the random network of charge distribution in nano-sized domains can substitute the Zwitterionic monomers. They demonstrated excellent antifouling properties of hydrogels from the simple, costless and commercialized monomers, similar to the ionic solvation behaviour of Zwitterionic monomers.

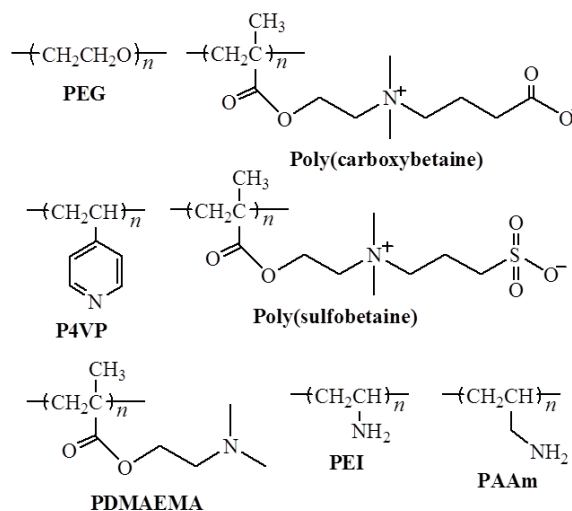


Figure 1-6: The chemical structures of polymers for antifouling coating.

Polycations are known for the antibacterial and anti-cell adhesion properties in solution due to their diffusion across the bacterial membranes and disruption of the membranes. Due to the bactericidal ability, they should be categorized as active agents for antibacterial adhesion. However, we mentioned them in this section because of their polymer intrinsic properties. A number of polymers with primary, secondary or tertiary amine groups (*e.g.* poly(4-vinyl pyridine) (P4VP), poly(2-dimethylaminoethyl methacrylate) (PDMAEMA), polyethylamine (PEI) and polyallylamine (PAAm)) have been investigated as antifouling coatings in the form of quaternary ammonium refer to Fig. 1-6 [139-141]. Lin et al reported the effect of chemical structures of quaternary ammoniated PEI on the antibacterial properties [142]. The unreacted PEI only showed a bactericidal efficiency of 14%; while the increase of chain length of alkylation on PEI quickly improved the bactericidal efficiency up to 80% for hexyl groups. It was possible due to the increase of penetration of quaternary ammoniated PEO through the hydrophobic membrane by increasing its hydrophobicity. Lee et al also demonstrated the antifouling behaviour of quaternary ammoniated PDMAEMA by using the surface-initiated ATRP [140].

Other than the low surface energy polymers, the fouling release properties of low modulus polymers are of interest in the field of bioimplants, artificial vessels and biomimic devices that serve in dynamic fluids [143-145]. The apolar surfaces of the rubbers or elastomers (*e.g.* silicone, PDMS and PU) can easily be attached by proteins or bacteria in aqueous media, whereas such surfaces have low modulus that result in the easy detaching of proteins or bacteria under hydrodynamic forces [129]. As these polymers are environmentally friendly, the possible application of these polymers for the marine bio-antifouling coating has been intensively studied. Callow et al. studied the effect of PDMS film modulus and thickness on the fouling release of spores by varying the cross-linking density of PDMS [143]. The detaching of spores only occurred at the modulus ~ 0.2 MPa. To improve the adhesion and antifouling properties of PDMS coating to substrates, the copolymers of PDMS/PU or PDMS/polyacrylates have been investigated [146, 147].

In contrast to complete wetting surface, which forms the hydrated interfacial layer, the other approach to prevent microbes coming into contact with the surfaces is developing superhydrophobic or superoleophobic surfaces.

Static contact angle θ (CA) is the primary parameter and the most straightforward method to characterize the surface wettability. The contact angle is affected both by the surface chemical nature and roughness. The affinity of a flat (atomically smooth, chemically homogeneous) surface towards a liquid is defined in terms of the “flat” (or intrinsic, or Young’s) contact angle,

$$\cos(\theta_{flat}) = \frac{\gamma_{SA} - \gamma_{SL}}{\gamma_{LA}} \quad (1)$$

where γ is the surface energy or surface tension, subscripts **S** stands for solid, **L** stands for liquid and **A** stands for air. The solid-liquid surface energy can be approximately estimated by the other two as follows [148]:

$$\gamma_{SL} = \gamma_{SA} + \gamma_{LA} - 2\sqrt{\gamma_{SA}\gamma_{LA}} \quad (2)$$

If the liquid wets the surface, the value of the static contact angle is $0 \leq \theta \leq 90^\circ$ and the corresponding surface is hydrophilic (where the prefix *hygro* means liquid in Greek, can be replaced by *hydro-*, *oleo-*, etc., depending on the wetting liquid) [149], whereas if the liquid does not wet the surface, the value of the contact angle is $90^\circ < \theta \leq 180^\circ$ and the corresponding surface is called hydrophobic. For water (surface energy $\gamma_{LA} = 73 \text{ mJ m}^{-2}$) the best non-wetting situation on a flat surface is achieved by terminated with the $-\text{CF}_3$ group, which lowers the surface energy to $\gamma_{SA} \sim 6 \text{ mJ m}^{-2}$. The value of the intrinsic (Young's) CA for water on such a surface is $\theta_{flat} \sim 120^\circ$ which is close to the estimation via Eqs.(1) and (2) [150]. By contrast, many organic liquids such as oils and alcohols have very low surface energies (e.g. $\gamma_{LA} = 27.6 \text{ mJ m}^{-2}$ for hexadecane, $\gamma_{LA} = 22.5 \text{ mJ m}^{-2}$ for methanol). Consequently, even on the chemically least energetic surface terminated with $-\text{CF}_3$ groups, the intrinsic CA for typical oils such as hexadecane is $\theta_{flat} \sim 78^\circ$. In other words, all flat solid surfaces in nature are intrinsically oleophilic (in terms of the Young's CA) no matter their chemical compositions. This circumstance has profound consequences on the design of super-oleophobic surfaces, as we describe in more detail below.

Real surfaces are always rough, which introduce a multitude of metastable states, thus one may observe different apparent contact angles for a surface. The CA at the front of the droplet (advancing contact angle) is greater than the one at the back (receding contact angle), resulting in contact angle hysteresis (CAH), which is the difference between advancing and receding contact angles due to surface roughness and heterogeneity [151]. CAH is a measurement of energy dissipation during the flow of a droplet along a solid

surface [152]. Surfaces with a CA of less than 10° are called superhydrophilic, while surfaces with both advancing and receding contact angle for liquid droplet exceed a value of 140° called superhydrophobic [153]. Such a superhydrophobic surface is also characterized by a low CAH, which has a common qualitative feature that liquid droplets do not stick to such a surface and easily roll off from the surface when the surface is tilted. The definition of superoleophobic is high CA for organic liquids with low hysteresis.

A multitude of wetting behaviours on surfaces can be divided into two major classes (1) homogenous and (2) heterogeneous. Two theoretical models are widely used to explain the wettability phenomena of surfaces. Homogenous wetting is where the liquid wets all the details of a rough surface and is described by the Wenzel's model [154] In the Wenzel's model, the roughness r ($r > 1$) of a surface is known to amplify both its hydrophobicity and hydrophilicity, comparing to a chemically identical and flat surface:

$$\cos(\theta_{rough}) = r \cos(\theta_{flat}) \quad (3)$$

According to the Eq.(3), both hydrophobicity and hydrophilicity are enhanced by roughness, $\theta_{adv} < \theta_{flat}$, in the hydrophilic case ($\theta_{flat} < 90^\circ$); and on the other side, $\theta_{adv} > \theta_{flat}$, in the hydrophobic case ($\theta_{flat} > 90^\circ$). However, the receding contact angle is very low in the Wenzel state, and consequently has a very high CAH because the liquid droplets remain pinned in the roughness valleys.

The second class of wetting behaviour is heterogeneous wetting and is described by the Cassie-Baxter model [155], where the liquid droplets only contact the top of the roughness asperities, staying in contact with a fraction f_l of the rough solid surface. The liquid does not penetrate the roughness valleys as seen in Fig.1-7. It is this relation that provides the superhydrophobic property to surfaces. In general, it is approximately described by the formula:

$$\cos(\theta_{\text{rough}}) = f_1 \cos(\theta_{\text{flat}}) - f_2 \quad \text{with} \quad f_1 + f_2 \geq 1 \quad (4)$$

where f_1 is defined as the total area of solid under the drop per unit projected area under the drop, with θ_{flat} is the CA on a smooth surface of material 1, f_2 defined in an analogous way with material 2 as air ($\theta_2 = 180^\circ$) [156].

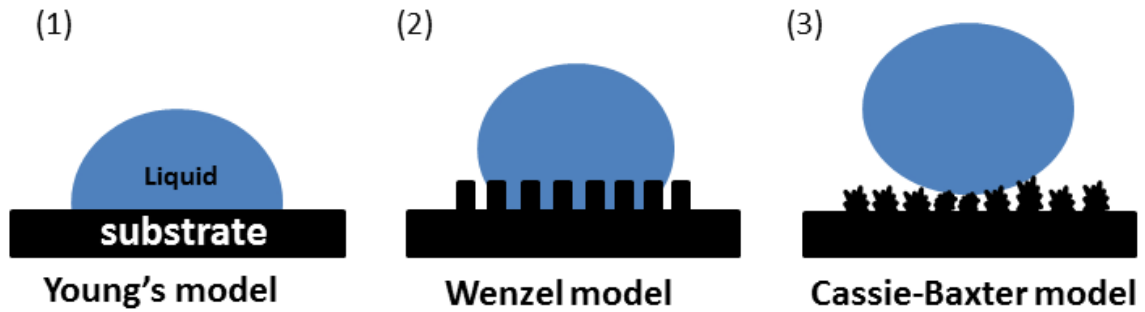


Figure 1-7: Three different wetting models. (1) Young's model, (2) Wenzel model and (3) Cassie-Baxter model.

As described in Cassie-Baxter model, one can achieve very high apparent CA with low f_1 , which implicitly assumes the CAH is low. It is easy to realize the Cassie-Baxter state in the case of water on the surfaces which are intrinsically hydrophobic ($\theta_{\text{flat}} > 90^\circ$ for water). In such a case, a hydrophobic material has higher surface energy when it is wet than when it is dry; Water does not penetrate the rough valleys because it is energetically unfavourable [157, 158]. It is not surprising that there exist a large number of known superhydrophobic surfaces discovered in nature (such as the lotus leaf [159] and water strider's leg [160]) and artificial structures [161] but superoleophobic surfaces are still extremely rare in nature [162].

It is easy to see why superoleophobic surfaces are exotic. If a surface is intrinsically hydrophilic when flat ($\theta_{\text{flat}} < 90^\circ$, which is typical for most oils on flat natural surfaces), then the condition described in Eq. (4) can not be satisfied for any roughness r . Thus, the Cassie-Baxter state can at best be metastable. If sufficiently large perturbations (such as pressure) are applied to an oil droplet, the oil will eventually wet any rough surface.

However, low-surface energy liquid droplets such as oil ($\theta_{flat} < 90^\circ$) can be kept in the metastable Cassie-Baxter state for a sufficient long time, showing that some local stability criteria for a liquid-solid contact line are met [149, 157, 163]. While a detailed description of these conditions is out of scope of the present work, here we only note that: (i) the intrinsic CA at the contact line must be equal to the value at flat surface θ_{flat} ; (ii) parts of the roughness asperities where the contact line finds a stable position must be of a convex shape. It has been shown [149, 164], that for low-surface energy oil-like liquids ($\theta_{flat} < 90^\circ$) the above conditions can be satisfied in the case when surface morphology bears some “over-hanging” or “re-entrant” features [162, 165-167]. However, to reduce the fraction f of a rough surface in contact with a liquid in Eq. (4), such a surface must possess rough features on a multiple scale, ideally like a fractal [164].

The natural lotus leaf surface is one of the most typical examples of the self-cleaning effect as a result of combined low surface energy chemicals and the micro-nano structure surface [159, 168]. Many other biological materials also exhibit excellent surface wettability [169]. Contaminant particles can be easily removed from the surface when water droplet roll off the surface. Inspired by the hierarchical structure features and mechanisms of the self-cleaning, many superhydrophobic surfaces have been developed through creating surfaces with appropriate chemical composition and hierarchical geometrical structures using top-down or bottom-up approaches or the combination of the two methods [170]. One of the most frequently applied methods is silanization of hydroxyl group bearing rough surfaces through chlorosilanes or ethoxysilanes. Other than isotropic hierarchical structures, anisotropic wetting surfaces fabricated through chemical patterning also showed superhydrophobicity.[169] Air trapped in the nanostructures of those superhydrophobic surfaces plays a key role in the self-cleaning property. Some research groups have recently reported the possibility of using superhydrophobic surfaces to resist bacteria adhesion and consequent colonization [72, 153, 171]. Ma et al. [72] studied the adhesion of biological (*P.aeruginosa*) and nonbiological particles on natural taro leaves with hierarchical structures and confirmed that the nanostructure could resist particle/bacterial adhesion under both wet and nonwet conditions. However, in the bacterial adhesion experiment process, 30 min immersion period in bacterial solution is quite short. Recently Fadeeva et al. reported that *S.aureus* was shown to be able to

colonize on the lotus-like Ti surfaces [172]. Truong et al. also found four different bacteria attached to the lotus-like Ti surfaces after 1 h immersion period due to the replacement of trapped air by the incubation medium [173].

Compared to superhydrophobic surface, superoleophobic surface is relative harder to achieve owing to critical requirement on the structure parameters. Some superoleophobic surfaces have been developed by the creation of re-entrant or overhanging features and multi-scale hierarchical structures [162, 165-167, 174-179]. Most of these research focused on propose fabrication processes and few studies have considered the applications such as antifouling from biological and organic contaminants.

1.4 Scope of the thesis

The overall objectives of the research work presented in this thesis are to develop strategies and methodologies to fabricate nanostructured materials and composite materials which have the ability to resist bacterial adhesion. TiO_2 is identified as a unique material with significant potential owing to its excellent photocatalytic ability, chemical inert property and because it is environmentally friendly. The self-sterilizing property also gives TiO_2 materials have many fascinating applications. In particularly, we have synthesized active antibacterial TiO_2 nanomaterials that kill bacteria under UV illumination or in the dark. A green and low-cost method to involve silver nanoparticles in TiO_2 nanothin film matrix to enhance the antibacterial property has been investigated. Furthermore, we have synthesised nitrogen doped TiO_2 nanomaterials (nanoparticles and nanothin film) to promote the antibacterial properties to visible light range. By applying liquid phase deposition (LPD) method through the control of nucleation process by adding seed, TiO_2 coatings with controllable structures have been achieved. More importantly, we have designed, fabricated and characterized durable superoleophobic composite surfaces based on polymer matrix and nanoparticles. We have demonstrated a novel method that has a potential to develop a number of polymer-nanoparticle composites with multiple functions. The study of antibacterial adhesion and protein adsorption of the resultant polymer-nanoparticles composite coatings with superoleophobicity showed excellent antifouling properties, which have the potential to apply in the biomedical field.

In Chapter 2 and Chapter 3, active component was involved to fabricate antifouling surfaces. We developed a strategy to prepare TiO₂ nanothin film on silicon wafers with various silver content. Nitrogen doped TiO₂ nanomaterials have also been prepared to expand the application field to visible light range and to utilize the solar energy efficiently. The morphology of the resultant nanomaterials was controllable by tuning the molar ratio composition in the precursor solution. Different characterization methods were used to analyze the prepared films and nanoparticles. The antibacterial ability of the obtained thin films and nanoparticles on Gram-negative bacteria was tested.

In Chapter 4, TiO₂ coatings were deposited on the interested substrates, such as butyl rubber, silicon wafer and cotton sheet, at mild environmental conditions by using the LPD approach. SEM and AFM have been used to observe the surface morphology of the resultant coatings. The morphology of the thin film can be controlled by tuning the solution composition which, in principle, tunes the formation mechanism of TiO₂ film. After surface fluorination treatment, the TiO₂ coatings with hierarchical structure became superoleophobic. Furthermore, preliminary results on antibacterial adhesion have been explored.

In Chapter 5, we described an easy method to fabricate superoleophobic and conductive dual-functional coatings which are also flexible and stretchable. The durability of the resultant nanocomposite coatings have been tested by tape test. The conductivity and wettability as the function of stretch was measured. In the work described in Chapter 6, the same design principle of superoleophobic surface was applied to involving TiO₂ as another nanoparticle loading. The formed structures were characterized and process was optimized. The distribution of the nanofillers and surface roughness of the resultant composite coatings was further investigated. The resultant superoleophobic surfaces are evaluated regarding their non-fouling performance by resisting protein adsorption as well as bacterial adhesion.

Finally, a general discussion and some future work are presented in Chapter 7.

1.5 Literature citations

- [1] Brash JL. Exploiting the current paradigm of blood-material interactions for the rational design of blood-compatible materials. *J Biomater Sci-Polym Ed.* 2000;11:1135-46.
- [2] Ratner BD. THE BLOOD COMPATIBILITY CATASTROPHE. *J Biomed Mater Res.* 1993;27:283-7.
- [3] Wisniewski N, Reichert M. Methods for reducing biosensor membrane biofouling. *Colloid Surf B-Biointerfaces.* 2000;18:197-219.
- [4] Falconnet D, Csucs G, Grandin HM, Textor M. Surface engineering approaches to micropattern surfaces for cell-based assays. *Biomaterials.* 2006;27:3044-63.
- [5] Donlan RM, Costerton JW. Biofilms: Survival mechanisms of clinically relevant microorganisms. *Clin Microbiol Rev.* 2002;15:167-+.
- [6] Diekema DJ, Pfaller MA, Schmitz FJ, Smayevsky J, Bell J, Jones RN, et al. Survey of infections due to *Staphylococcus* species: Frequency of occurrence and antimicrobial susceptibility of isolates collected in the United States, Canada, Latin America, Europe, and the Western Pacific region for the SENTRY Antimicrobial Surveillance Program, 1997-1999. *Clin Infect Dis.* 2001;32:S114-S32.
- [7] Huebner J, Goldman DA. Coagulase-negative staphylococci: Role as pathogens. *Annu Rev Med.* 1999;50:223-36.
- [8] Dankert J, Hogt AH, Feijen J. Biomedical Polymers - Bacterial Adhesion, Colonization, and Infection. *Crit Rev Biocompat.* 1986;2:219-301.
- [9] Barber M. Methicillin-resistant staphylococci. *J Clin Pathol.* 1961;14:385-393.
- [10] Costerton JW, Stewart PS, Greenberg EP. Bacterial biofilms: A common cause of persistent infections. *Science.* 1999;284:1318-22.
- [11] Garcia-Fulgueiras A, Navarro C, Fenoll D, Garcia J, Gonzalez-Diego P, Jimenez-Bunuales T, et al. Legionnaires' disease outbreak in Murcia, Spain. *Emerging Infectious Diseases.* 2003;9:915-21.
- [12] Herrmann M, Vaudaux PE, Pittet D, Auckenthaler R, Lew PD, Schumacherperdreau F, et al. Fibronectin, fibrinogen, and laminin act as mediators of adherence of clinical staphylococcal isolates to foreign material. *Journal of Infectious Diseases.* 1988;158:693-701.
- [13] Chapman RG, Ostuni E, Liang MN, Meluleni G, Kim E, Yan L, et al. Polymeric thin films that resist the adsorption of proteins and the adhesion of bacteria. *Langmuir.* 2001;17:1225-33.

- [14] Andrade JD, Hlady V, Wei AP. ADSORPTION OF COMPLEX PROTEINS AT INTERFACES. Pure and Applied Chemistry. 1992;64:1777-81.
- [15] Rabe M, Verdes D, Seeger S. Understanding protein adsorption phenomena at solid surfaces. Adv Colloid Interface Sci. 2011;162:87-106.
- [16] Brash John L, Horbett Thomas A. Proteins at Interfaces. Proteins at Interfaces II: American Chemical Society; 1995. p. 1-23.
- [17] Norde W, Giacomelli CE. BSA structural changes during homomolecular exchange between the adsorbed and the dissolved states. Journal of Biotechnology. 2000;79:259-68.
- [18] Norde W, Haynes CA. Reversibility and the mechanism of protein adsorption. In: Horbett TA, Brash JL, editors. Proteins at Interfaces II: Fundamentals and Applications 1995. p. 26-40.
- [19] Norde W. Driving forces for protein adsorption at solid surfaces. Macromol Symp. 1996;103:5-18.
- [20] Rabe M, Verdes D, Seeger S. Understanding protein adsorption phenomena at solid surfaces. Adv Colloid Interface Sci. 2011;162:87-106.
- [21] Andrade JD, Hlady V. Plasma-protein adsorption - the big 12. Annals of the New York Academy of Sciences. 1987;516:158-72.
- [22] Hlady V, Buijs J, Jennissen HP. Methods for studying protein adsorption. Amyloid, Prions, and Other Protein Aggregates. 1999;309:402-29.
- [23] Prime KL, Whitesides GM. Adsorption of proteins onto surfaces containing end-attached oligo(ethylene oxide) - a model system using self-assembled monolayers. Journal of the American Chemical Society. 1993;115:10714-21.
- [24] Anand G, Jamadagni SN, Garde S, Belfort G. Self-Assembly of TMAO at Hydrophobic Interfaces and Its Effect on Protein Adsorption: Insights from Experiments and Simulations. Langmuir : the ACS journal of surfaces and colloids. 2010;26:9695-702.
- [25] Anand G, Sharma S, Dutta AK, Kumar SK, Belfort G. Conformational Transitions of Adsorbed Proteins on Surfaces of Varying Polarity. Langmuir : the ACS journal of surfaces and colloids. 2010;26:10803-11.
- [26] Koehler JA, Ulbricht M, Belfort G. Intermolecular forces between proteins and polymer films with relevance to filtration. Langmuir : the ACS journal of surfaces and colloids. 1997;13:4162-71.

- [27] Koehler JA, Ulbricht M, Belfort G. Intermolecular forces between a protein and a hydrophilic modified polysulfone film with relevance to filtration. *Langmuir : the ACS journal of surfaces and colloids*. 2000;16:10419-27.
- [28] Nabe A, Staude E, Belfort G. Surface modification of polysulfone ultrafiltration membranes and fouling by BSA solutions. *Journal of Membrane Science*. 1997;133:57-72.
- [29] Sethuraman A, Han M, Kane RS, Belfort G. Effect of surface wettability on the adhesion of proteins. *Langmuir : the ACS journal of surfaces and colloids*. 2004;20:7779-88.
- [30] Lee NK, Vilgis TA. Preferential adsorption of hydrophobic-polar model proteins on patterned surfaces. *Physical Review E*. 2003;67.
- [31] Muller B, Riedel M, Michel R, De Paul SM, Hofer R, Heger D, et al. Impact of nanometer-scale roughness on contact-angle hysteresis and globulin adsorption. *Journal of Vacuum Science & Technology B*. 2001;19:1715-20.
- [32] Galli C, Coen MC, Hauert R, Katanaev VL, Wymann MP, Groning P, et al. Protein adsorption on topographically nanostructured titanium. *Surface Science*. 2001;474:L180-L4.
- [33] Galli C, Coen MC, Hauert R, Katanaev VL, Groning P, Schlapbach L. Creation of nanostructures to study the topographical dependency of protein adsorption. *Colloid Surf B-Biointerfaces*. 2002;26:255-67.
- [34] Cai KY, Bossert J, Jandt KD. Does the nanometre scale topography of titanium influence protein adsorption and cell proliferation? *Colloid Surf B-Biointerfaces*. 2006;49:136-44.
- [35] Han M, Sethuraman A, Kane RS, Belfort G. Nanometer-scale roughness having little effect on the amount or structure of adsorbed protein. *Langmuir : the ACS journal of surfaces and colloids*. 2003;19:9868-72.
- [36] Rechendorff K, Hovgaard MB, Foss M, Zhdanov VP, Besenbacher F. Enhancement of protein adsorption induced by surface roughness. *Langmuir : the ACS journal of surfaces and colloids*. 2006;22:10885-8.
- [37] Dolatshahi-Pirouz A, Pennisi CP, Skeldal S, Foss M, Chevallier J, Zachar V, et al. The influence of glancing angle deposited nano-rough platinum surfaces on the adsorption of fibrinogen and the proliferation of primary human fibroblasts. *Nanotechnology*. 2009;20.
- [38] Lundqvist M, Sethson I, Jonsson BH. Protein adsorption onto silica nanoparticles: Conformational changes depend on the particles' curvature and the protein stability. *Langmuir : the ACS journal of surfaces and colloids*. 2004;20:10639-47.

- [39] Vertegel AA, Siegel RW, Dordick JS. Silica nanoparticle size influences the structure and enzymatic activity of adsorbed lysozyme. *Langmuir : the ACS journal of surfaces and colloids*. 2004;20:6800-7.
- [40] Roach P, Farrar D, Perry CC. Surface tailoring for controlled protein adsorption: Effect of topography at the nanometer scale and chemistry. *Journal of the American Chemical Society*. 2006;128:3939-45.
- [41] Black JG. *Microbiology : principles and explorations*. 4th ed. Upper Saddle River, N.J.: Prentice Hall; 1999.
- [42] Zhang YM, Rock CO. Membrane lipid homeostasis in bacteria. *Nature Reviews Microbiology*. 2008;6:222-33.
- [43] Ploux L, Ponche A, Anselme K. Bacteria/Material Interfaces: Role of the Material and Cell Wall Properties. *Journal of Adhesion Science and Technology*. 2010;24:2165-201.
- [44] An YH, Friedman RJ. Concise review of mechanisms of bacterial adhesion to biomaterial surfaces. *J Biomed Mater Res*. 1998;43:338-48.
- [45] Hall-Stoodley L, Costerton JW, Stoodley P. Bacterial biofilms: From the natural environment to infectious diseases. *Nature Reviews Microbiology*. 2004;2:95-108.
- [46] Van Houdt R, Michiels CW. Role of bacterial cell surface structures in *Escherichia coli* biofilm formation. *Research in Microbiology*. 2005;156:626-33.
- [47] Fux CA, Costerton JW, Stewart PS, Stoodley P. Survival strategies of infectious biofilms. *Trends in Microbiology*. 2005;13:34-40.
- [48] An YH, Friedman RJ. *Handbook of bacterial adhesion : principles, methods, and applications*. Totowa, N.J.: Humana Press; 2000.
- [49] Ofek I, Hasty DL, Doyle RJ. *Bacterial adhesion to animal cells and tissues*. Washington, D.C.: ASM Press; 2003.
- [50] Ong YL, Razatos A, Georgiou G, Sharma MM. Adhesion forces between *E-coli* bacteria and biomaterial surfaces. *Langmuir : the ACS journal of surfaces and colloids*. 1999;15:2719-25.
- [51] Satou N, Satou J, Shintani H, Okuda K. Adherence of streptococci to surface-modified glass. *Journal of General Microbiology*. 1988;134:1299-305.
- [52] Balazs DJ, Triandafillu K, Chevolut Y, Aronsson BO, Harms H, Descouts P, et al. Surface modification of PVC endotracheal tubes by oxygen glow discharge to reduce bacterial adhesion. *Surf Interface Anal*. 2003;35:301-9.

- [53] Li BK, Logan BE. Bacterial adhesion to glass and metal-oxide surfaces. *Colloid Surf B-Biointerfaces*. 2004;36:81-90.
- [54] Chandra J, Patel JD, Li J, Zhou GY, Mukherjee PK, McCormick TS, et al. Modification of surface properties of biomaterials influences the ability of *Candida albicans* to form biofilms. *Applied and environmental microbiology*. 2005;71:8795-801.
- [55] Harris JM, Zalipsky S, American Chemical Society. Division of Polymer Chemistry., American Chemical Society. Meeting. Poly(ethylene glycol) : chemistry and biological applications. Washington, DC: American Chemical Society; 1997.
- [56] Tegoulia VA, Cooper SL. Staphylococcus aureus adhesion to self-assembled monolayers: effect of surface chemistry and fibrinogen presence. *Colloid Surf B-Biointerfaces*. 2002;24:217-28.
- [57] Hogt AH, Dankert J, Feijen J. Adhesion of staphylococcus-epidermidis and staphylococcus-saprophyticus to a hydrophobic biomaterial. *Journal of General Microbiology*. 1985;131:2485-91.
- [58] Gottenbos B, Grijpma DW, van der Mei HC, Feijen J, Busscher HJ. Antimicrobial effects of positively charged surfaces on adhering Gram-positive and Gram-negative bacteria. *J Antimicrob Chemother*. 2001;48:7-13.
- [59] Makhluif S, Dror R, Nitzan Y, Abramovich Y, Jelinek R, Gedanken A. Microwave-assisted synthesis of nanocrystalline MgO and its use as a bactericide. *Advanced Functional Materials*. 2005;15:1708-15.
- [60] Xi YY, Huang BQ, Djurasic AB, Chan CMN, Leung FCC, Chan WK, et al. Electrodeposition for antibacterial nickel-oxide-based coatings. *Thin Solid Films*. 2009;517:6527-30.
- [61] Stobie N, Duffy B, Hinder SJ, McHale P, McCormack DE. Silver doped perfluoropolyether-urethane coatings: Antibacterial activity and surface analysis. *Colloid Surf B-Biointerfaces*. 2009;72:62-7.
- [62] Shao W, Zhao Q. Influence of reducers on nanostructure and surface energy of silver coatings and bacterial adhesion. *Surf Coat Technol*. 2010;204:1288-94.
- [63] Chen W, Liu Y, Courtney HS, Bettenga M, Agrawal CM, Bumgardner JD, et al. In vitro anti-bacterial and biological properties of magnetron co-sputtered silver-containing hydroxyapatite coating. *Biomaterials*. 2006;27:5512-7.
- [64] Scheuerman TR, Camper AK, Hamilton MA. Effects of substratum topography on bacterial adhesion. *Journal of colloid and interface science*. 1998;208:23-33.
- [65] Harris LG, Tosatti S, Wieland M, Textor M, Richards RG. Staphylococcus aureus adhesion to titanium oxide surfaces coated with non-functionalized and peptide-

functionalized poly(L-lysine)-grafted-poly(ethylene glycol) copolymers. *Biomaterials*. 2004;25:4135-48.

[66] Harris LG, Richards RG. Staphylococcus aureus adhesion to different treated titanium surfaces. *J Mater Sci-Mater Med*. 2004;15:311-4.

[67] Anselme K, Davidson P, Popa AM, Giazon M, Liley M, Ploux L. The interaction of cells and bacteria with surfaces structured at the nanometre scale. *Acta biomaterialia*. 2010;6:3824-46.

[68] Taylor RL, Verran J, Lees GC, Ward AJP. The influence of substratum topography on bacterial adhesion to polymethyl methacrylate. *J Mater Sci-Mater Med*. 1998;9:17-22.

[69] Boyd RD, Verran J, Jones MV, Bhakoo M. Use of the atomic force microscope to determine the effect of substratum surface topography on bacterial adhesion. *Langmuir : the ACS journal of surfaces and colloids*. 2002;18:2343-6.

[70] Crawford RJ, Webb HK, Truong VK, Hasan J, Ivanova EP. Surface topographical factors influencing bacterial attachment. *Adv Colloid Interface Sci*. 2012;179:142-9.

[71] Crick CR, Ismail S, Pratten J, Parkin IP. An investigation into bacterial attachment to an elastomeric superhydrophobic surface prepared via aerosol assisted deposition. *Thin Solid Films*. 2011;519:3722-7.

[72] Ma JW, Sun YK, Gleichauf K, Lou J, Li QL. Nanostructure on Taro Leaves Resists Fouling by Colloids and Bacteria under Submerged Conditions. *Langmuir : the ACS journal of surfaces and colloids*. 2011;27:10035-40.

[73] Mohamed GG, Soliman MH. Synthesis, spectroscopic and thermal characterization of sulphur complexes of iron, manganese, copper, cobalt, nickel, and zinc salts. Antibacterial and antifungal activity. *Spectrochimica Acta Part a-Molecular and Biomolecular Spectroscopy*. 2010;76:341-7.

[74] Cioffi N, Torsi L, Ditaranto N, Tantillo G, Ghibelli L, Sabbatini L, et al. Copper nanoparticle/polymer composites with antifungal and bacteriostatic properties. *Chem Mat*. 2005;17:5255-62.

[75] Sheikh FA, Kanjwal MA, Saran S, Chung WJ, Kim H. Polyurethane nanofibers containing copper nanoparticles as future materials. *Appl Surf Sci*. 2011;257:3020-6.

[76] Zhang XY, Huang XB, Jiang L, Ma Y, Fan AL, Tang B. Surface microstructures and antimicrobial properties of copper plasma alloyed stainless steel. *Appl Surf Sci*. 2011;258:1399-404.

[77] Chatterjee AK, Sarkar RK, Chattopadhyay AP, Aich P, Chakraborty R, Basu T. A simple robust method for synthesis of metallic copper nanoparticles of high antibacterial potency against E. coli. *Nanotechnology*. 2012;23.

- [78] Ramyadevi J, Jeyasubramanian K, Marikani A, Rajakumar G, Rahuman AA. Synthesis and antimicrobial activity of copper nanoparticles. *Materials Letters*. 2012;71:114-6.
- [79] Applerot G, Perkas N, Amirian G, Girshevitz O, Gedanken A. Coating of glass with ZnO via ultrasonic irradiation and a study of its antibacterial properties. *Appl Surf Sci*. 2009;256:S3-S8.
- [80] Joshi P, Chakraborti S, Chakrabarti P, Haranath D, Shanker V, Ansari ZA, et al. Role of Surface Adsorbed Anionic Species in Antibacterial Activity of ZnO Quantum Dots Against *Escherichia coli*. *Journal of nanoscience and nanotechnology*. 2009;9:6427-33.
- [81] Aruguete DM, Hochella MF. Bacteria-nanoparticle interactions and their environmental implications. *Environmental Chemistry*. 2010;7:3-9.
- [82] Premanathan M, Karthikeyan K, Jeyasubramanian K, Manivannan G. Selective toxicity of ZnO nanoparticles toward Gram-positive bacteria and cancer cells by apoptosis through lipid peroxidation. *Nanomedicine-Nanotechnology Biology and Medicine*. 2011;7:184-92.
- [83] Stoimenov PK, Klinger RL, Marchin GL, Klabunde KJ. Metal oxide nanoparticles as bactericidal agents. *Langmuir : the ACS journal of surfaces and colloids*. 2002;18:6679-86.
- [84] Rogers HJ. Ferric iron and antibacterial effects of horse 7s antibodies to *Escherichia coli* 0111. *Immunology*. 1976;30:425-33.
- [85] Ward CG, Hammond JS, Bullen JJ. Effect of iron compounds on antibacterial function of human polymorphs and plasma. *Infection and Immunity*. 1986;51:723-30.
- [86] Touati D. Iron and oxidative stress in bacteria. *Archives of Biochemistry and Biophysics*. 2000;373:1-6.
- [87] Subbiandoss G, Sharifi S, Grijpma DW, Laurent S, van der Mei HC, Mahmoudi M, et al. Magnetic targeting of surface-modified superparamagnetic iron oxide nanoparticles yields antibacterial efficacy against biofilms of gentamicin-resistant staphylococci. *Acta biomaterialia*. 2012;8:2047-55.
- [88] Iconaru SL, Prodan AM, Le Coustumer P, Predoi D. Synthesis and Antibacterial and Antibiofilm Activity of Iron Oxide Glycerol Nanoparticles Obtained by Coprecipitation Method. *Journal of Chemistry*. 2013.
- [89] Matsunaga T, Tomoda R, Nakajima T, Wake H. Photoelectrochemical sterilization of microbial-cells by semiconductor powders. *FEMS microbiology letters*. 1985;29:211-4.

- [90] Weir E, Lawlor A, Whelan A, Regan F. The use of nanoparticles in anti-microbial materials and their characterization. *Analyst*. 2008;133:835-45.
- [91] Li QL, Mahendra S, Lyon DY, Brunet L, Liga MV, Li D, et al. Antimicrobial nanomaterials for water disinfection and microbial control: Potential applications and implications. *Water research*. 2008;42:4591-602.
- [92] Marambio-Jones C, Hoek EMV. A review of the antibacterial effects of silver nanomaterials and potential implications for human health and the environment. *Journal of Nanoparticle Research*. 2010;12:1531-51.
- [93] Rai M, Yadav A, Gade A. Silver nanoparticles as a new generation of antimicrobials. *Biotechnol Adv*. 2009;27:76-83.
- [94] Feng QL, Wu J, Chen GQ, Cui FZ, Kim TN, Kim JO. A mechanistic study of the antibacterial effect of silver ions on *Escherichia coli* and *Staphylococcus aureus*. *J Biomed Mater Res*. 2000;52:662-8.
- [95] Xiu ZM, Zhang QB, Puppala HL, Colvin VL, Alvarez PJJ. Negligible Particle-Specific Antibacterial Activity of Silver Nanoparticles. *Nano letters*. 2012;12:4271-5.
- [96] Fujishima A, Zhang XT, Tryk DA. TiO₂ photocatalysis and related surface phenomena. *Surf Sci Rep*. 2008;63:515-82.
- [97] Dastjerdi R, Montazer M. A review on the application of inorganic nano-structured materials in the modification of textiles: Focus on anti-microbial properties. *Colloid Surf B-Biointerfaces*. 2010;79:5-18.
- [98] Gateshki M, Yin S, Ren Y, Petkov V. Titania polymorphs by soft chemistry: Is there a common structural pattern? *Chem Mat*. 2007;19:2512-8.
- [99] Liu G, Yu JC, Lu GQ, Cheng HM. Crystal facet engineering of semiconductor photocatalysts: motivations, advances and unique properties. *Chemical Communications*. 2011;47:6763-83.
- [100] Fujishima A, Cai RX, Otsuki J, Hashimoto K, Itoh K, Yamashita T, et al. Biochemical application of photoelectrochemistry-photokilling of malignant-cells with TiO₂ powder. *Electrochimica Acta*. 1993;38:153-7.
- [101] Cai RX, Kubota Y, Shuin T, Sakai H, Hashimoto K, Fujishima A. Induction of cytotoxicity by photoexcited TiO₂ particles. *Cancer research*. 1992;52:2346-8.
- [102] Mills A, LeHunte S. An overview of semiconductor photocatalysis. *J Photochem Photobiol A-Chem*. 1997;108:1-35.
- [103] Jacoby WA, Maness PC, Wolfrum EJ, Blake DM, Fennell JA. Mineralization of bacterial cell mass on a photocatalytic surface in air. *Environmental science & technology*. 1998;32:2650-3.

- [104] Sunada K, Kikuchi Y, Hashimoto K, Fujishima A. Bactericidal and detoxification effects of TiO₂ thin film photocatalysts. *Environmental science & technology*. 1998;32:726-8.
- [105] Markowska-Szczupak A, Ulfig K, Morawski AW. The application of titanium dioxide for deactivation of bioparticulates: An overview. *Catal Today*. 2011;169:249-57.
- [106] Lu ZX, Zhou L, Zhang ZL, Shi WL, Xie ZX, Xie HY, et al. Cell damage induced by photocatalysis of TiO₂ thin films. *Langmuir : the ACS journal of surfaces and colloids*. 2003;19:8765-8.
- [107] Yu JC, Ho WK, Yu JG, Yip H, Wong PK, Zhao JC. Efficient visible-light-induced photocatalytic disinfection on sulfur-doped nanocrystalline titania. *Environmental science & technology*. 2005;39:1175-9.
- [108] Rengifo-Herrera JA, Mielczarski E, Mielczarski J, Castillo NC, Kiwi J, Pulgarin C. Escherichia coli inactivation by N, S co-doped commercial TiO₂ powders under UV and visible light. *Appl Catal B-Environ*. 2008;84:448-56.
- [109] Li Q, Xie RC, Li YW, Mintz EA, Shang JK. Enhanced visible-light-induced photocatalytic disinfection of E-coli by carbon-sensitized nitrogen-doped titanium oxide. *Environmental science & technology*. 2007;41:5050-6.
- [110] Wu PG, Xie RC, Imlay K, Shang JK. Visible-Light-Induced Bactericidal Activity of Titanium Dioxide Codoped with Nitrogen and Silver. *Environmental science & technology*. 2010;44:6992-7.
- [111] Shen H, Mi L, Xu P, Shen W, Wang P-N. Visible-light photocatalysis of nitrogen-doped TiO₂ nanoparticulate films prepared by low-energy ion implantation. *Appl Surf Sci*. 2007;253:7024-8.
- [112] Suda Y, Kawasaki H, Ueda T, Ohshima T. Preparation of high quality nitrogen doped TiO₂ thin film as a photocatalyst using a pulsed laser deposition method. *Thin Solid Films*. 2004;453:162-6.
- [113] Yang TS, Yang MC, Shiu CB, Chang WK, Wong MS. Effect of N² ion flux on the photocatalysis of nitrogen-doped titanium oxide films by electron-beam evaporation. *Appl Surf Sci*. 2006;252:3729-36.
- [114] Wong MS, Chu WC, Sun DS, Huang HS, Chen JH, Tsai PJ, et al. Visible-light-induced bactericidal activity of a nitrogen-doped titanium photocatalyst against human pathogens. *Applied and environmental microbiology*. 2006;72:6111-6.
- [115] Shieh KJ, Li M, Lee YH, Sheu SD, Liu YT, Wang YC. Antibacterial performance of photocatalyst thin film fabricated by defect effect in visible light. *Nanomedicine : nanotechnology, biology, and medicine*. 2006;2:121-6.

- [116] Chen SZ, Zhang PY, Zhuang DM, Zhu WP. Investigation of nitrogen doped TiO₂ photocatalytic films prepared by reactive magnetron sputtering. *Catal Commun.* 2004;5:677-80.
- [117] Pelaez M, Falaras P, Likodimos V, Kontos AG, de la Cruz AA, O'Shea K, et al. Synthesis, structural characterization and evaluation of sol-gel-based NF-TiO₂ films with visible light-photoactivation for the removal of microcystin-LR. *Appl Catal B-Environ.* 2010;99:378-87.
- [118] Blanco-Galvez J, Fernandez-Ibanez P, Malato-Rodriguez S. Solar photocatalytic detoxification and disinfection of water: Recent overview. *J Sol Energy Eng Trans-ASME.* 2007;129:4-15.
- [119] Maclean M, MacGregor SJ, Anderson JG, Woolsey G. High-intensity narrow-spectrum light inactivation and wavelength sensitivity of *Staphylococcus aureus*. *FEMS microbiology letters.* 2008;285:227-32.
- [120] Decraene V, Pratten J, Wilson M. Cellulose acetate containing toluidine blue and rose bengal is an effective antimicrobial coating when exposed to white light. *Applied and environmental microbiology.* 2006;72:4436-9.
- [121] Dunnill CW, Parkin IP. Nitrogen-doped TiO₂ thin films: photocatalytic applications for healthcare environments. *Dalton Trans.* 2011;40:1635-40.
- [122] Akhavan O, Azimirad R, Safa S, Larijani MM. Visible light photo-induced antibacterial activity of CNT-doped TiO₂ thin films with various CNT contents. *J Mater Chem.* 2010;20:7386-92.
- [123] Upadhyayula VKK, Gadhamshetty V. Appreciating the role of carbon nanotube composites in preventing biofouling and promoting biofilms on material surfaces in environmental engineering: A review. *Biotechnol Adv.* 2010;28:802-16.
- [124] Hu WB, Peng C, Luo WJ, Lv M, Li XM, Li D, et al. Graphene-Based Antibacterial Paper. *ACS nano.* 2010;4:4317-23.
- [125] Akhavan O, Ghaderi E. Toxicity of Graphene and Graphene Oxide Nanowalls Against Bacteria. *ACS nano.* 2010;4:5731-6.
- [126] Magin CM, Cooper SP, Brennan AB. Non-toxic antifouling strategies. *Mater Today.* 2010;13:36-44.
- [127] Sigal GB, Mrksich M, Whitesides GM. Effect of surface wettability on the adsorption of proteins and detergents. *Journal of the American Chemical Society.* 1998;120:3464-73.
- [128] Brady RF, Singer IL. Mechanical factors favoring release from fouling release coatings. *Biofouling.* 2000;15:73-81.

- [129] Krishnan S, Weinman CJ, Ober CK. Advances in polymers for anti-biofouling surfaces. *J Mater Chem*. 2008;18:3405-13.
- [130] Prime KL, Whitesides GM. Self-Assembled Organic Monolayers - Model Systems for Studying Adsorption of Proteins at Surfaces. *Science*. 1991;252:1164-7.
- [131] Jeon SI, Lee JH, Andrade JD, Degennes PG. Protein Surface Interactions in the Presence of Polyethylene Oxide .1. Simplified Theory. *Journal of colloid and interface science*. 1991;142:149-58.
- [132] Sofia SJ, Premnath V, Merrill EW. Poly(ethylene oxide) grafted to silicon surfaces: Grafting density and protein adsorption. *Macromolecules*. 1998;31:5059-70.
- [133] Hucknall A, Rangarajan S, Chilkoti A. In Pursuit of Zero: Polymer Brushes that Resist the Adsorption of Proteins. *Adv Mater*. 2009;21:2441-6.
- [134] Kingshott P, Wei J, Bagge-Ravn D, Gadegaard N, Gram L. Covalent attachment of poly(ethylene glycol) to surfaces, critical for reducing bacterial adhesion. *Langmuir : the ACS journal of surfaces and colloids*. 2003;19:6912-21.
- [135] Tugulu S, Klok HA. Stability and nonfouling properties of poly(poly(ethylene glycol) methacrylate) brushes-under cell culture conditions. *Biomacromolecules*. 2008;9:906-12.
- [136] Holmlin RE, Chen XX, Chapman RG, Takayama S, Whitesides GM. Zwitterionic SAMs that resist nonspecific adsorption of protein from aqueous buffer. *Langmuir : the ACS journal of surfaces and colloids*. 2001;17:2841-50.
- [137] Jiang SY, Cao ZQ. Ultralow-Fouling, Functionalizable, and Hydrolyzable Zwitterionic Materials and Their Derivatives for Biological Applications. *Adv Mater*. 2010;22:920-32.
- [138] Chen SF, Jiang SY. A new avenue to nonfouling materials. *Adv Mater*. 2008;20:335-+.
- [139] Tiller JC, Liao CJ, Lewis K, Klibanov AM. Designing surfaces that kill bacteria on contact. *Proceedings of the National Academy of Sciences of the United States of America*. 2001;98:5981-5.
- [140] Lee SB, Koepsel RR, Morley SW, Matyjaszewski K, Sun YJ, Russell AJ. Permanent, nonleaching antibacterial surfaces. 1. Synthesis by atom transfer radical polymerization. *Biomacromolecules*. 2004;5:877-82.
- [141] Karamdoust S, Yu BY, Bonduelle CV, Liu Y, Davidson G, Stojcevic G, et al. Preparation of antibacterial surfaces by hyperthermal hydrogen induced cross-linking of polymer thin films. *J Mater Chem*. 2012;22:4881-9.

- [142] Lin J, Qiu SY, Lewis K, Klibanov AM. Bactericidal properties of flat surfaces and nanoparticles derivatized with alkylated polyethylenimines. *Biotechnol Progr.* 2002;18:1082-6.
- [143] Chaudhury MK, Finlay JA, Chung JY, Callow ME, Callow JA. The influence of elastic modulus and thickness on the release of the soft-fouling green alga *Ulva linza* (syn. *Enteromorpha linza*) from poly(dimethylsiloxane) (PDMS) model networks. *Biofouling.* 2005;21:41-8.
- [144] Hoipkemeier-Wilson L, Schumacher J, Carman M, Gibson A, Feinberg A, Callow M, et al. Antifouling potential of lubricious, micro-engineered, PDMS elastomers against zoospores of the green fouling alga *Ulva* (*Enteromorpha*). *Biofouling.* 2004;20:53-63.
- [145] Sommer S, Ekin A, Webster DC, Stafslie SJ, Daniels J, VanderWal LJ, et al. A preliminary study on the properties and fouling-release performance of siloxane-polyurethane coatings prepared from poly(dimethylsiloxane) (PDMS) macromers. *Biofouling.* 2010;26:961-72.
- [146] Ekin A, Webster DC, Daniels JW, Stafslie SJ, Casse F, Callow JA, et al. Synthesis, formulation, and characterization of siloxane-polyurethane coatings for underwater marine applications using combinatorial high-throughput experimentation. *J Coat Technol Res.* 2007;4:435-51.
- [147] Pieper RJ, Ekin A, Webster DC, Casse F, Callow JA, Callow ME. Combinatorial approach to study the effect of acrylic polyol composition on the properties of crosslinked siloxane-polyurethane fouling-release coatings. *J Coat Technol Res.* 2007;4:453-61.
- [148] Israelachvili J. *Intermolecular and Surface Forces.* London: Academic Press; 1991.
- [149] Marmur A. From hydrophilic to superhydrophobic: Theoretical conditions for making high-contact-angle surfaces from low-contact-angle materials. *Langmuir : the ACS journal of surfaces and colloids.* 2008;24:7573-9.
- [150] Nishino T, Meguro M, Nakamae K, Matsushita M, Ueda Y. The lowest surface free energy based on -CF₃ alignment. *Langmuir : the ACS journal of surfaces and colloids.* 1999;15:4321-3.
- [151] Extrand CW. Model for contact angles and hysteresis on rough and ultraphobic surfaces. *Langmuir : the ACS journal of surfaces and colloids.* 2002;18:7991-9.
- [152] Bhushan B, Jung YC, Koch K. Micro-, nano- and hierarchical structures for superhydrophobicity, self-cleaning and low adhesion. *Philosophical Transactions of the Royal Society a-Mathematical Physical and Engineering Sciences.* 2009;367:1631-72.
- [153] Genzer J, Efimenko K. Recent developments in superhydrophobic surfaces and their relevance to marine fouling: a review. *Biofouling.* 2006;22:339-60.

- [154] Wenzel RN. Resistance of solid surfaces to wetting by water. *Industrial & Engineering Chemistry*. 1936;28:988-94.
- [155] Cassie ABD, Baxter S. Wettability of porous surfaces. *Transactions of the Faraday Society*. 1944;40:546-51.
- [156] Milne AJB, Amirfazli A. The Cassie equation: How it is meant to be used. *Adv Colloid Interface Sci*. 2012;170:48-55.
- [157] Quere D. Non-sticking drops. *Rep Prog Phys*. 2005;68:2495-532.
- [158] Nosonovsky M. Multiscale roughness and stability of superhydrophobic biomimetic interfaces. *Langmuir : the ACS journal of surfaces and colloids*. 2007;23:3157-61.
- [159] Barthlott W, Neinhuis C. Purity of the sacred lotus, or escape from contamination in biological surfaces. *Planta*. 1997;202:1-8.
- [160] Gao XF, Jiang L. Water-repellent legs of water striders. *Nature*. 2004;432:36-.
- [161] Feng XJ, Jiang L. Design and creation of superwetting/antiwetting surfaces. *Adv Mater*. 2006;18:3063-78.
- [162] Tuteja A, Choi W, Ma ML, Mabry JM, Mazzella SA, Rutledge GC, et al. Designing superoleophobic surfaces. *Science*. 2007;318:1618-22.
- [163] Joly L, Biben T. Wetting and friction on superoleophobic surfaces. *Soft Matter*. 2009;5:2549-57.
- [164] Herminghaus S. Roughness-induced non-wetting. *Europhysics Letters*. 2000;52:165-70.
- [165] Tuteja A, Choi W, Mabry JM, McKinley GH, Cohen RE. Robust omniphobic surfaces. *Proceedings of the National Academy of Sciences of the United States of America*. 2008;105:18200-5.
- [166] Ahuja A, Taylor JA, Lifton V, Sidorenko AA, Salamon TR, Lobaton EJ, et al. Nanonails: A simple geometrical approach to electrically tunable superlyophobic surfaces. *Langmuir : the ACS journal of surfaces and colloids*. 2008;24:9-14.
- [167] Cao LL, Price TP, Weiss M, Gao D. Super water- and oil-repellent surfaces on intrinsically hydrophilic and oleophilic porous silicon films. *Langmuir : the ACS journal of surfaces and colloids*. 2008;24:1640-3.
- [168] Feng L, Li SH, Li YS, Li HJ, Zhang LJ, Zhai J, et al. Super-hydrophobic surfaces: From natural to artificial. *Adv Mater*. 2002;14:1857-60.

- [169] Liu KS, Yao X, Jiang L. Recent developments in bio-inspired special wettability. *Chemical Society reviews*. 2010;39:3240-55.
- [170] Li XM, Reinhoudt D, Crego-Calama M. What do we need for a superhydrophobic surface? A review on the recent progress in the preparation of superhydrophobic surfaces. *Chemical Society reviews*. 2007;36:1350-68.
- [171] Scardino AJ, de Nys R. Mini review: Biomimetic models and bioinspired surfaces for fouling control. *Biofouling*. 2011;27:73-86.
- [172] Fadeeva E, Truong VK, Stiesch M, Chichkov BN, Crawford RJ, Wang J, et al. Bacterial Retention on Superhydrophobic Titanium Surfaces Fabricated by Femtosecond Laser Ablation. *Langmuir : the ACS journal of surfaces and colloids*. 2011;27:3012-9.
- [173] Truong VK, Webb HK, Fadeeva E, Chichkov BN, Wu AHF, Lamb R, et al. Air-directed attachment of coccoid bacteria to the surface of superhydrophobic lotus-like titanium. *Biofouling*. 2012;28:539-50.
- [174] Tsujii K, Yamamoto T, Onda T, Shibuichi S. Super oil-repellent surfaces. *Angew Chem Int Edit*. 1997;36:1011-2.
- [175] Xi JM, Feng L, Jiang L. A general approach for fabrication of superhydrophobic and superamphiphobic surfaces. *Appl Phys Lett*. 2008;92.
- [176] Leng BX, Shao ZZ, de With G, Ming WH. Superoleophobic Cotton Textiles. *Langmuir : the ACS journal of surfaces and colloids*. 2009;25:2456-60.
- [177] Steele A, Bayer I, Loth E. Inherently Superoleophobic Nanocomposite Coatings by Spray Atomization. *Nano letters*. 2009;9:501-5.
- [178] Wu WC, Wang XL, Wang DA, Chen M, Zhou F, Liu WM, et al. Alumina nanowire forests via unconventional anodization and super-repellency plus low adhesion to diverse liquids. *Chemical Communications*. 2009:1043-5.
- [179] Srinivasan S, Chhatre SS, Mabry JM, Cohen RE, McKinley GH. Solution spraying of poly(methyl methacrylate) blends to fabricate microtextured, superoleophobic surfaces. *Polymer*. 2011;52:3209-18.

Chapter 2

2 Synthesis of Ag-TiO₂ composite nano-thin film for antimicrobial application

2.1 Introduction

Researchers have shown constant interest in developing antimicrobial materials containing various organic chemical antibiotics and inorganic substances. Among these fine structural functional materials, nanosized organic and inorganic particles have attracted increasing attention in medical applications due to their unique properties and amenability to biological functionalization [1-3]. Compared with the organic antimicrobial materials, the key advantages of inorganic antibacterial agents are improved safety and stability. Titanium dioxide (TiO₂) is one of the most effective photocatalysts currently in use due to its strong oxidizing power, non-toxicity and long-term physical and chemical stability. It has been widely used for the decomposition of organic compounds and microbial organisms, such as cancer cells, viruses and bacteria as well as its potential application in sterilization of medical devices and air-conditioning filters owing to its self-sterilizing property [4-7]. When irradiated with near UV light, TiO₂ exhibits strong bactericidal activity [8]. The photo-generated holes and electrons react with water and oxygen respectively to form hydroxyl radicals ($\cdot\text{OH}$) and other reactive oxygen species, such as singlet oxygen ($\text{O}_2^{\cdot-}$), and hydrogen peroxide (H_2O_2) [9]. Thus, TiO₂ and TiO₂-deposited materials could kill bacteria and also simultaneously degrade the toxic compounds exhausted from the bacteria [7]. Complete oxidation of organic compounds and the whole cells to carbon dioxide can be achieved [10]. However, its drawbacks of the low quantum yields and the lack of visible-light utilization hinder its practical application. To overcome these problems, numerous studies have been recently performed to enhance the photocatalytic efficiency and antibacterial activities, such as doping noble metals [11-14]. It is reported [15-17] that loading of silver nanoparticles highly enhances the photocatalytic activity of TiO₂. The enhancement is attributed to its ability to trap electrons at Schottky barriers at each Ag-TiO₂ contact region, which reduces the recombination of light generated e^-h^+ at TiO₂ surface.

Therefore charge separation is promoted and more electron transfer occurs, and consequent longer electron-hole pair lifetimes.

Silver metal and silver solutions have been known as effective antimicrobial agents for centuries, owing to a broad spectrum of antibacterial activity as well as low toxicity towards cells [18]. Several studies have been reported to explain the inhibitory effect of silver on bacteria. In general, it is believed that silver ions interact with proteins by reacting with the SH groups present in bacteria, leading the inactivation of the proteins [19]. Moreover, silver ions can interact with DNA of bacteria preventing the cell reproduction [20]. Both effects lead to the death of the bacterial cells. In contrast to the use of silver ions, silver nanoparticles are long lasting, stable and are subject to controlled release. Especially with decreasing of the silver crystal size, there are more chemical reaction sites available. Silver-doped materials are chemically durable and release silver ions for a long period time. It is promising to fix silver nanoparticles on various supports [21-24], to perform as an excellent antibacterial coating in the food industry, water disinfection and other disinfection related fields.

The importance of silver in medical applications and antibacterial activity of TiO_2 together led researchers to think about the manufacture of systems combining both titania and embedded silver compounds or silver nanoparticles, to expand the nanomaterial's antibacterial functions to a wider variety of working conditions. Synthesis of TiO_2/Ag nanocomposites has been carried out through different synthetic techniques. In the literature, a solvothermal method is commonly used to obtain the nanoparticles. But for practical applications, the sol-gel process is the most attractive method to introduce foreign metal ions into TiO_2 particles and films; for example, the photoreduction under UV exposure of Ag^+ containing films [25-28], and direct calcination of the sol-gel material [29-31]. However, photoreduced silver cannot be highly dispersed into the depth beneath the surface of TiO_2 , especially when the adhesion force is weak for the coating surface. Moreover, for the direct annealing methods, because of aggregation, agglomeration and other factors, the resultant composites showed a broad size distribution and non-uniform allocation of metal nanoparticles [25, 31]. Fortunately, these drawbacks could be suppressed by the use of sonochemical method. Since the early

1980s, sol-gel processes in which precursor-water mixtures are exposed to intense ultrasonic vibration have been investigated [32]. It has been demonstrated that the irradiated solution will result in higher density gel and less shrink during the following annealing process. Sonochemistry has been used not only for the preparation of the mesoporous materials, but also for the insertion of nanoparticles into the mesopores [33].

In this study, TiO₂ thin films with different silver content deposited on silicon wafers were prepared by a template sol-gel method. We could control the morphology of the composite film by tuning the molar ratio of water to Ti when introducing the silver ion. The interaction between the TiO₂ grains and the nanosized silver particles was enhanced by forming more hetero-junctions, such as Ag/anatase in the Ag-TiO₂ multiphase nanocomposite films. A low-intensity ultrasonic cleaning bath was used to help disperse the silver ions. Different characterization methods were used to analyze the resultant films. The antibacterial effect of the obtained thin films on Gram-negative bacteria was tested.

2.2 Materials and methods

2.2.1 Materials

Titanium (IV) isopropoxide (TTIP), AgNO₃, acetylacetone, Poly(propylene glycol)-*block*-poly(ethylene glycol)-*block*-poly(propylene glycol) (P123, M_n ~ 4,400) were all purchased from Sigma-Aldrich Chemical Co. The anhydrous ethanol was a commercial product and was used as received without further purification. Ultrapure Milli-Q water was used in all experiments. Gram-negative bacteria (*Escherichia coli* ATCC 29425) were used to test the antimicrobial activity of the resultant films. The strains were cultured in Nutrient Broth (BD Difco™) and Standard Methods Agar (BD Difco™) using the appropriate times and temperatures of incubation.

2.2.2 Preparation of silicon wafer supported TiO₂ and Ag-TiO₂ films

TiO₂ thin films were synthesized by a surfactant-templating method using a triblock copolymer (P123) as a template [34-36]. In a typical synthesis, 15 mL titanium isopropoxide was added drop-wise to a template solution prepared by dissolving 10 g of P123 in 100 mL of absolute ethanol. Then 5 mL acetylacetone was added to control the polymerization via the condensation rate. After stirring vigorously for 1 h at room temperature, 1 mL of water was added drop-wise to the solution under vigorous stirring. To form Ag nanoparticles embedded within the TiO₂ composite films, a solution B composed of an appropriate amount of AgNO₃ (the molar ratio of Ti to Ag was varied from 50:1 to 5:1) and 1 mL deionized water was added drop-wise into the precursor solution under stirring. The mixture was sonicated at room temperature for 30 min using a low-intensity ultrasonic cleaner bath (Fisher FS 30 50/60HZ 130W). Then the resultant alkoxide solution was kept standing at room temperature for hydrolysis reaction for 1h. The vigorous chemical reduction yields a brownish dispersion; there is a change of color (from yellow to brownish). All reactions containing AgNO₃ were conducted in amber glassware to prevent photoreduction of the silver ions. Samples with varying molar composition of Ti⁴⁺ to Ag⁺ as 50:1, 20:1, 10:1 and 5:1, were named SG1, SG2, SG3 and SG4, respectively. The sample without the addition of silver nitrate was labeled as SG0.

The as-prepared sol could be applied onto different substrates by various techniques, such as dip-coating, a spraying process and spin coating. In our study, a spin processor (Laurell Technologies Corporation, PA) was used for the deposition of the solution onto washed silicon wafer. The silicon wafer substrates were cleaned in a piranha solution (7:3 concentrated H₂SO₄/H₂O₂) for 1 h at 90 °C, followed by thorough rinsing with distilled water and dried under a stream of nitrogen. A number of 100 µl of precursor solution, prepared according to the procedure described above, were applied onto modified silicon wafer (160 × 160 mm²) by spin-coating at 2500 rpm for 30 s. The obtained films were typically dried at 100°C for 30 min and then heat-treated at 500°C for 1 h (1°C min⁻¹) and cooled to ambient temperature. The thickness of the resultant films was controlled by

repeating the cycle three times from spinning to heat treatment. Silver only samples were also prepared through the same process without adding TTIP.

2.2.3 Materials characterization

The crystalline structures of the Ag-TiO₂ and TiO₂ films were determined by x-ray diffraction (XRD) with Co ($\lambda = 1.79026 \text{ \AA}$) radiation operated at 45 kV and 160 mA with a rotating anode x-ray generator (Rigaku Rotaflex RTP 30). The scanning range was from 20° to 75°. The surface compositions were characterized by x-ray photoelectron spectroscopy (XPS; Kratos Axis Ultra spectrometer, Surface Science) using Al K α ($E = 1486.6 \text{ eV}$). All the binding energies were referenced to the C 1s peak at 284.8 eV of the surface adventitious carbon. The as-deposited surface was etched by Ar ion sputtering at energy of 4 keV for 5 min to analyze the chemical state of the Ag-TiO₂ films. Survey scan analyses were carried out with an analysis area of 300 $\mu\text{m} \times 700 \mu\text{m}$. The surface morphology of the films was assessed by scanning electron microscopy (SEM, HITACHI S-4500) with an energy-dispersive x-ray spectrometer (EDX). The cross-section of the samples was covered by a Pt layer to increase the conductivity. The surfaces were further visualized by an atomic force microscopy (AFM). Images were obtained by scanning a surface of 1 $\mu\text{m} \times 1 \mu\text{m}$ in a tapping mode using silicon nitric cantilevers with a spring constant of 40 N m⁻¹ at ambient conditions.

2.2.4 Measurements of photoinduced super-hydrophilicity

The surface wettability was measured in ambient air at room temperature using a contact angle meter (Model 100-00 contact angle goniometer) based on the sessile drop method. The photoinduced hydrophilicity of the resultant films was also evaluated by the water contact angle difference before and after illumination with an 8 W UV lamp (emission in 340nm-400nm, with a peak at 365nm UVP, Inc. Upland, CA, USA). The droplet size used for the measurements was 8 μl . At least five measurements on each sample were recorded and the average value was adopted as the static contact angle.

2.2.5 Antibacterial activity evaluation

The bacteria was cultivated in Nutrient Broth medium at 37°C for 18-24 h, and then harvested by centrifugation at 3000 rpm for 10 min. After removing the supernatant, the cells were washed with phosphate buffer solution (PBS) twice and were resuspended with the same PBS solution. The final concentration of bacterial cells was diluted to approximately 2×10^6 - 2×10^5 CFU mL⁻¹ with PBS solution. The antibacterial activity of the coatings against *E.coli* was determined by two different methods: (i) qualitative evaluation using the zone of inhibition method and (ii) quantitative evaluation.

For the qualitative evaluation (zone of inhibition test), 20 mL liquid nutrient agar was poured onto disposable sterilized Petri dishes and allowed to solidify. Then 100 µL of the bacterial PBS solution (10^6 CFU mL⁻¹) was streaked over the plate and spread uniformly. Both the silicon wafer substrates coated with Ag-TiO₂ and pure TiO₂ films were gently placed over the solidified agar gel in different Petri dishes. The plates were incubated at 37°C for 24 h and the antagonistic activity was estimated by a clear zone of inhibition around the coated substrate. Uncoated silicon wafers were also tested as negative controls.

In order to quantitatively evaluate the antibacterial activity, samples were investigated both under the low-intensity UV light and in the dark. For the antibacterial evaluation under the UV light, an 8 W UV lamp (emission in 340nm-400nm, with a peak at 365nm UVP, Inc. Upland, CA, USA) was used as the light source. The sample was placed in a sterilized Petri dish. Then 100 µL of PBS solution containing bacteria was added drop-wise onto the surface of each sample. The Petri dish was sealed and illuminated with UV light from above. The light intensity at the working films was 0.6 mW cm⁻² measured by a UV intensity meter (Model 1000 SUSS Micro Tec, Inc.). To measure the antibacterial activity in the dark, the experiment was carried out under similar conditions without illumination. After a certain period the bacteria liquid drops were washed from the surface of the sample by using 10 mL PBS in the sterilized Petri dish. Then 100 µL of each bacteria suspension was dispersed on the plate count agar. The number of surviving bacterial colonies on the Petri dish was counted after incubation for 24 h at 37°C. The counts on three plates corresponding to a particular sample were averaged.

2.3 Results and discussion

2.3.1 Characterization of the TiO₂ and Ag-TiO₂ films

2.3.1.1 XRD and XPS analysis

The x-ray diffraction patterns of the resultant films (Fig.2-1) showed the six typical TiO₂ peaks can be attributed to the (101), (004), (200), (105), (211) and (204) crystal planes, respectively. This indicated that all the resultant films exhibit a pure anatase phase structure. For all the composite films after heat treatment at 500°C for 1 h, no crystalline phase of metallic silver formation was detected. This may due to the uniform distribution of silver nanoparticles in the titanium matrix, or the peak of silver at $2\theta = 44.3^\circ$ was covered by the peak of TiO₂ at $2\theta = 44.47^\circ$ owing to the low content of silver. Similar behavior was also reported by Chang et al. [37]. Different from the previous study [31], the presence of silver content does not lead to apparent varieties on crystalline structure. There is no significant reduction in particle size observed with the increase of silver amount.

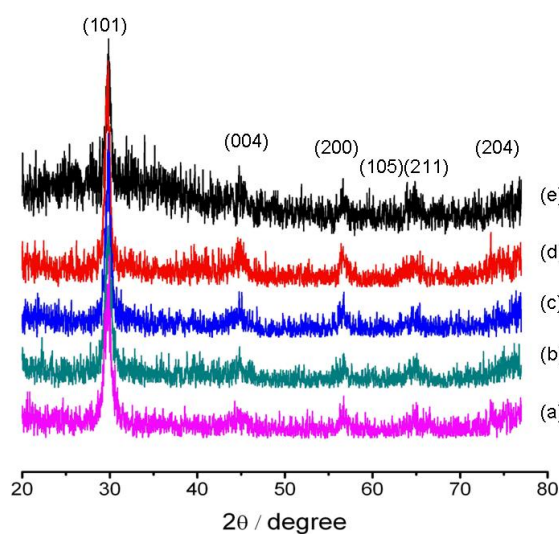


Figure 2-1: Wide-angle x-ray scattering patterns of the result films with different Ag contents: sample SG0-SG4 is labeled as (a)-(e) in sequence.

To confirm the metallic state of the silver on the surface of these samples, the resultant film samples were further characterized by XPS measurement. Fig. 2-2 shows the XPS profiles of the prepared TiO_2 and Ag-TiO_2 composite films. The peak position of 368.5 eV for Ag^0 was taken as reference values. The Ag element clearly appeared on the surface of Ag-TiO_2 composite thin films. The XPS spectra of Ag $3d_{5/2}$ of the fresh SG4 sample right after the calcination process were recorded. As shown in Fig.2-3, XPS spectra of the fresh SG4 samples before and after 8 W UV lamp exposure were fitted with a nonlinear least-squares fitting program. The Ag $3d_{5/2}$ peak appeared at a binding energy of 368.5 eV. This binding energy indicated that the silver was of metallic nature [38]. After 0.6 mW cm^{-2} UV exposure for 1 h, the XPS spectra of Ag $3d_{5/2}$ indicated that there were two components after deconvolution, ascribed to Ag_2O (367.9 eV) and Ag^0 (368.6 eV) respectively [38]. The Ag species mainly exist as Ag_2O after UV exposure, while there is still Ag^0 on the surface. Thus we may conclude that metallic silver is oxidized due to the strong oxidation ability of TiO_2 matrix under UV exposure.

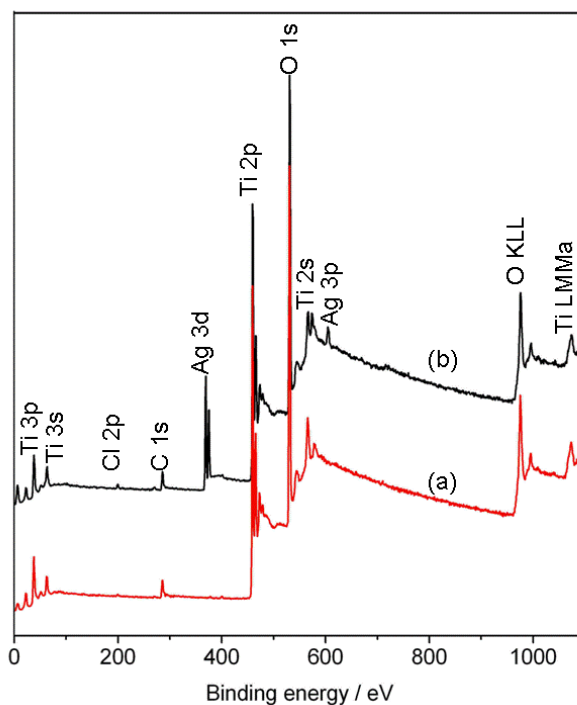


Figure 2-2: XPS spectra of TiO_2 (a) and Ag-TiO_2 (b) composite films of SG4.

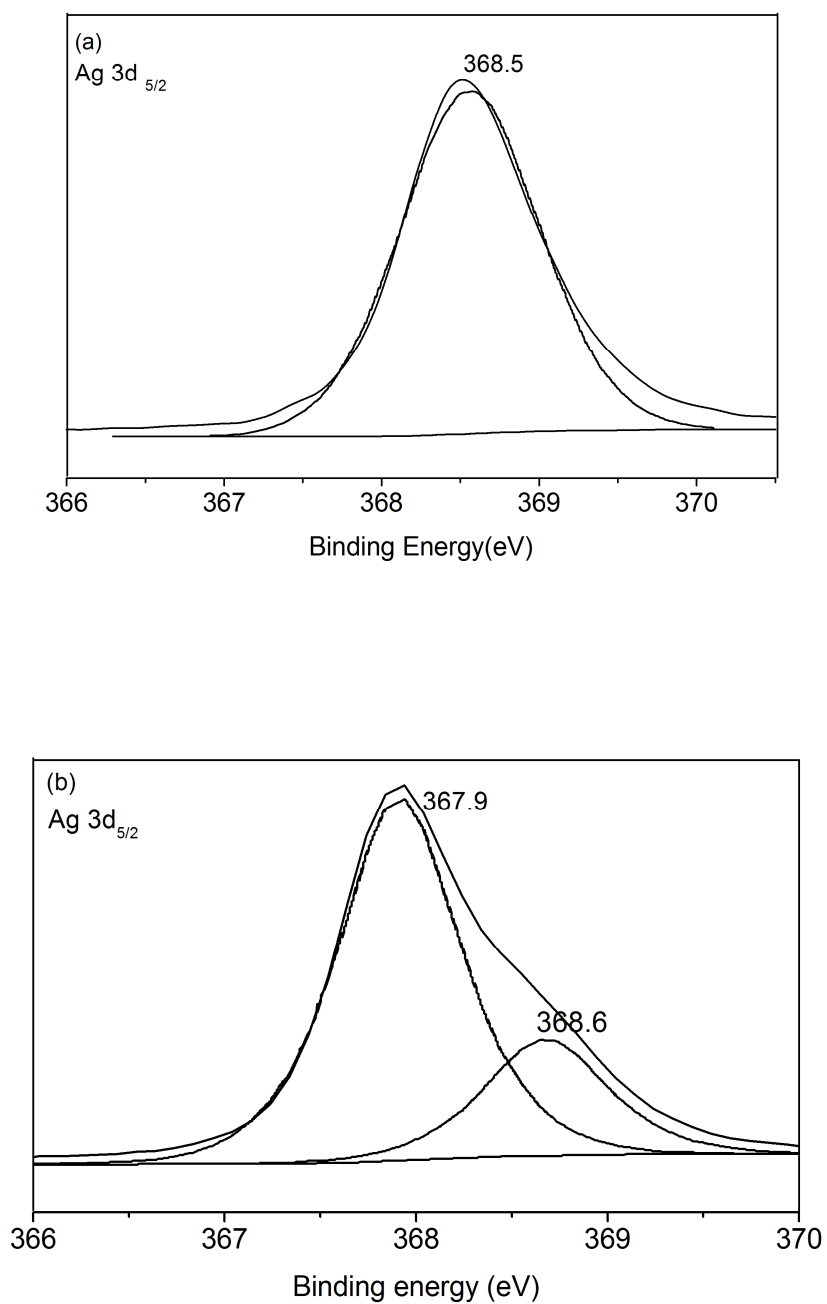


Figure 2-3: High-resolution XPS spectra of Ag 3d_{5/2} in Ag-TiO₂ composite film SG4. (a) before UV exposure and (b) after 0.6 mW cm⁻² UV exposure for 1 h.

2.3.1.2 SEM/EDX analysis

SEM images of the pure TiO₂ and the composite films with different silver content are presented in Fig. 2-4. While all the films were sintered at 500°C, the morphology of the constituted grains seems to be different dependent on the Ag content. The image of the pure TiO₂ film (Fig.2-4 (a)) illustrates an extremely smooth and dense surface. There are no defects observed, and the average size of the TiO₂ granular structure is approximately 20 nm in diameter. Considering that heavy element (e.g. Ag) backscatter electrons more strongly than light elements (e.g. O, Ti), the metallic silver appears brighter in the image. At low AgNO₃ concentrations, the bright Ag nanoparticles with a diameter around 20-30 nm were well dispersed as shown in Fig. 2-4 (b) and (c). The surface of the SG1 is very similar to that of SG2; and the density of Ag nanoparticles was increased with respect to SG2 due to the Ag⁺ concentration being increased in the sol solution. The TiO₂ substrate films are still smooth and worm-like TiO₂ grains appear. For a higher silver concentration, the Ag nanoparticles became gradually aggregated but still remained roughly uniform on the surface as shown in Fig.2-4 (d)-1. Instead of having a smooth surface, the Ag-TiO₂ composite films displayed a rough surface morphology. The addition of silver salt results in more mesoporous TiO₂ matrix (Fig.2-4 (d)-2), which included TiO₂ crystallites of 10-20 nm in size and small Ag nanoparticles (white spots) with various size ranging from 10 to 30 nm. Finally, when the concentration increased further, no obvious aggregation was observed on the surface (Fig.2-4 (e)-1). The enlarged image (Fig.2-4 (e)-2) shows the smaller Ag nanoparticles more uniformly distributed in the TiO₂ matrix. Although the size of the silver particles is smaller with diameter around 10 nm, there are more nano-pores detected in the thin film. It is reported that heating promotes aggregation of Ag atoms. As the radius of Ag⁺ ions (ca.126 pm) is much larger than that of Ti⁴⁺ (ca.68 pm), the Ag⁺ ions introduced by the sol-gel process would not enter into the lattice of TiO₂ anatase phase [40]. When the samples were heat-treated to a certain temperature, the reduction of Ag⁺ to Ag⁰ took place as the AgNO₃ decomposed. During the calcination process, these uniformly dispersed Ag⁺ ions would gradually migrate along with the anatase grain boundaries to the surface of TiO₂ film, while TiO₂ anatase grains would grow at the same time. Finally, the Ag⁺ ions probably exist on the

surface of the anatase grains by forming Ag–O–Ti bonds. In our present study, the movement of the resulting nanoparticles in the TiO₂ matrix could also be restricted by tuning the molar ratio of water to Ti when adding the Ag⁺ preparing sol, and hence particle aggregation is controlled. The anatase grain growth is thereby depressed and the specific surface area increase. The porous feature of the film indicates that it should have a rough surface.

Spin-coating resulted in TiO₂ and Ag-TiO₂ thin films with a thickness of approximately 370 nm as determined from the cross-section images (Fig.2-4 (f)). From spin-coating theory, the resultant film thickness is mainly decided by two factors: liquid viscosity and rotating speed. In our case, rotating speed was kept the same and the viscosity of the precursor solution did not change much as silver concentration changes. Hence the film thickness could be kept as the same.

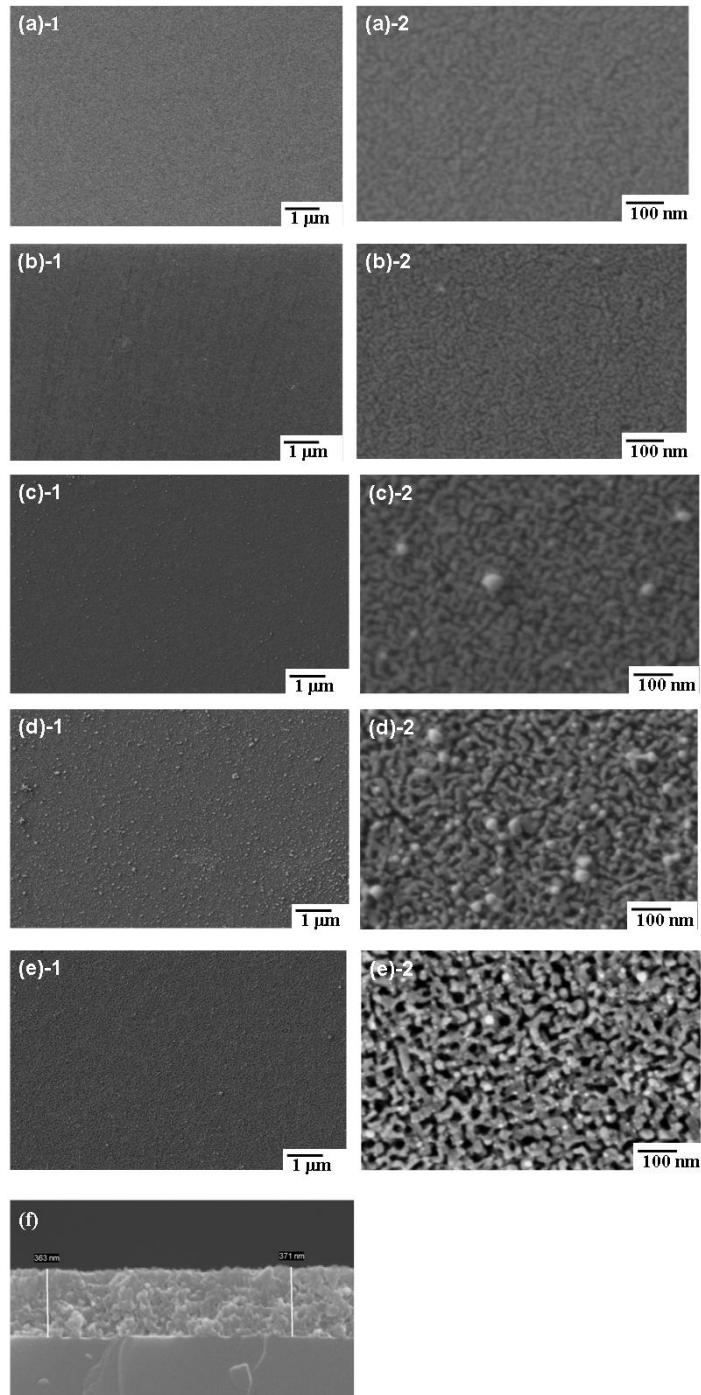


Figure 2-4: Scanning electron micrographs of the (a) the neat TiO₂ film surface of SG0, (b) SG1, (c) SG2, (d) SG3 and (e) SG4 Ag-TiO₂ composite film surfaces. (a)-2, (b)-2, (c)-2, (d)-2 and (e)-2 are enlarged images of (a), (b), (c), (d) and (e) respectively. (f) The thickness of the films is about 370 nm as determined by the cross-section image.

EDX spectra of the film showed the presence of a small amount of silver within the surface. Quantification of the spectra indicates that the silver content varies with the different AgNO_3 amount and the molar ratio of Ti to Ag are around 4.5:1, 13:1 in SG4 and SG3, respectively, (Table 2-1). This is in good agreement with theoretically calculated values of the precursor solution composite.

Table 1: Composition of Ag-TiO₂ composite films according to EDX analysis

samples	O	Si	Ti	Ag
SG0	31.48	58.98	9.54	-
SG3	34.94	53.06	11.16	0.85
SG4	31.01	56.49	10.21	2.28

2.3.1.3 AFM

AFM was used to characterize the morphology and surface roughness of the samples. Fig. 2-5 shows the representative top view images and angle view images of the surface morphology of scan area $1\ \mu\text{m} \times 1\ \mu\text{m}$ of the Ag-TiO₂ composite films on silicon wafer by three spin-coating cycles. It is clear to see from the height images that the surface of SG2 is smooth with an rms roughness of 1.22 nm. The AFM image confirms the results obtained by SEM since the surface of SG3 is covered with some silver particles with diameter around 30 nm. The statistical mean roughness of the surface is about 3.44 nm, while the maximum height within this area is about 30 nm. As for the sample SG4 with the highest silver content, no obvious silver aggregation was observed, indicating that silver nanoparticles uniformly dispersed in the matrix without aggregation. This result is in general agreement with the SEM observation. The height image of SG4 shows a mesoporous surface structure with the rms about 8.57 nm. The grain size of TiO₂

estimated from AFM images was quite large, which may be due to the worm-like structure as shown in SEM image and the silver nanoparticles embedded within the TiO_2 matrix. The average roughness (R_a) and mean square roughness (R_q) of the resultant films are listed in Table 2-2.

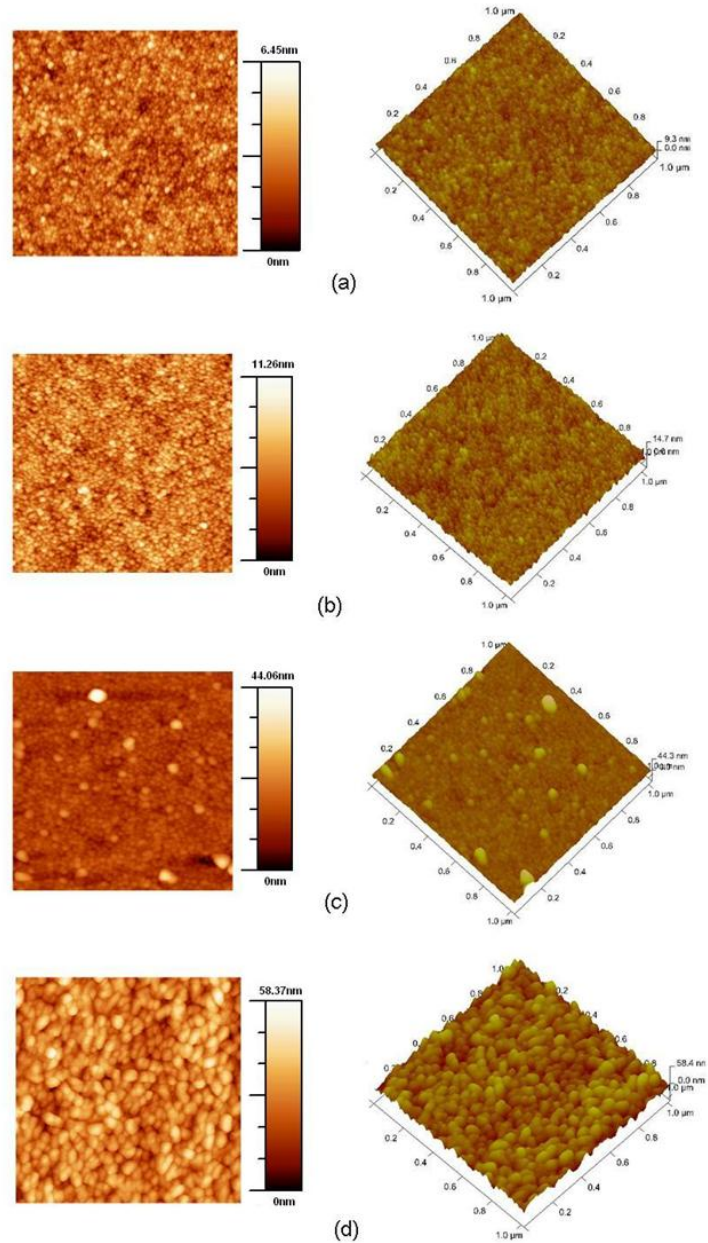


Figure 2-5: AFM top view images (left) and AFM angle view images(right) of the composite films: (a) SG0, (b) SG2, (c) SG3, (d) SG4.

Table 2-2: Surface roughness of the resultant films with different silver content.

samples	Rq ^a	Ra ^b
SG0	0.859	0.677
SG2	1.222	0.965
SG3	3.440	2.020
SG4	8.570	6.710

^a Mean square roughness of resultant films

^b Average roughness of resultant films

2.3.2 Hydrophilicity

The photoinduced hydrophilicity of TiO₂ via UV light irradiation is well known. It is assumed that photogenerated holes lead to the oxidation of the bridging oxygen (O₂⁻) to oxygen and generate oxygen vacancies simultaneously. The adsorption of water molecules on the surface was dissociated via the oxygen vacancies under UV illumination. This process created hydrophilic OH group on the illuminated TiO₂ surface [40]. Prior to UV light irradiation, the freshly prepared neat TiO₂ film showed a highly hydrophilic property, with the water contact angle around $15^{\circ} \pm 2^{\circ}$. It was observed that the water contact angle of the composite films were $20^{\circ} \pm 2^{\circ}$ for SG1 and SG2, $25^{\circ} \pm 2^{\circ}$ for SG3 and SG4 respectively. However, the water contact angle of all the resultant films could drop to $5^{\circ} \pm 2^{\circ}$ after 2 h UV irradiation of 0.6 mW cm^{-2} in ambient conditions. It is known that the wettability of a solid surface is influenced by both surface energy and the geometrical microstructure of the surface. It is expected that the initial water contact angle varies with the composite films of different roughness. The loading of silver has no effect on the photoinduced hydrophilicity of TiO₂. Moreover, the composite films of higher silver loading showed higher hydrophilicizing rate. The water contact angle tended

to increase up to a certain angle due to gradual adsorbing of contaminants on the surface, which make the surface more hydrophobic. However, the water contact angle could be recovered by UV illumination again. In our case, the water contact angle would drop from 40° - 25° to 8° .

2.3.3 Antibacterial activity evaluation

The antibacterial activity is evidenced by an inhibition zone of bacteria (*E.coli*) growth around the resultant substrates as shown in Fig.2-6 as a typical result. No bacterial growth was observed on the top of and adjacent to the Ag-TiO₂ coatings. The result demonstrates that all composite films could inhibit the bacterial growth. Bacterial growth was seen around and on the top of the neat TiO₂ coated substrate without UV exposure, as indicated by the presence of colonies. Table 2-3 presents the experimental results for the qualitative evaluation. The diameter of the inhibition zone increases from 0.3 to 0.7 cm with the growing silver loaded in the composite films. This result was expected, because the driving force of silver ion diffusion from the bulk to the surface is larger for films with higher silver content. Ag only samples without the TiO₂ matrix with the same silver content in solution as their counterparts of the composite films SG2 and SG4 did not show clear inhibition zones. For the present method of material synthesis, the silver only samples appeared as bulk silver or silver crystal aggregations, which led to very limited silver ion diffusion. While in the Ag-TiO₂ composite films the silver appeared as 10–30 nm nanoparticles and was well dispersed in the TiO₂ matrix, the Ag-TiO₂ composite films exhibited much larger inhibition zones. These results indicate that the diffusion of silver ions may depend on the formation of silver in the nanofilms. In this work, silver ion diffusion has been evaluated in the sample SG4 by ICP-AES (inductively coupled plasma atomic emission spectroscopy). To avoid the possible formation of insoluble salt crystals on the coating surface in the saline solution, we chose deionized water as test fluid to evaluate the silver ion release. Non-cumulative release of silver ions into 50 mL of deionized water from 10 cm² and 370 nm thick SG4 Ag-TiO₂ composite film was recorded, whose concentration was 0.4 ppm, 0.26 ppm and 0.005 ppm for 1 h, 24 h and 7 days after immersion, respectively.

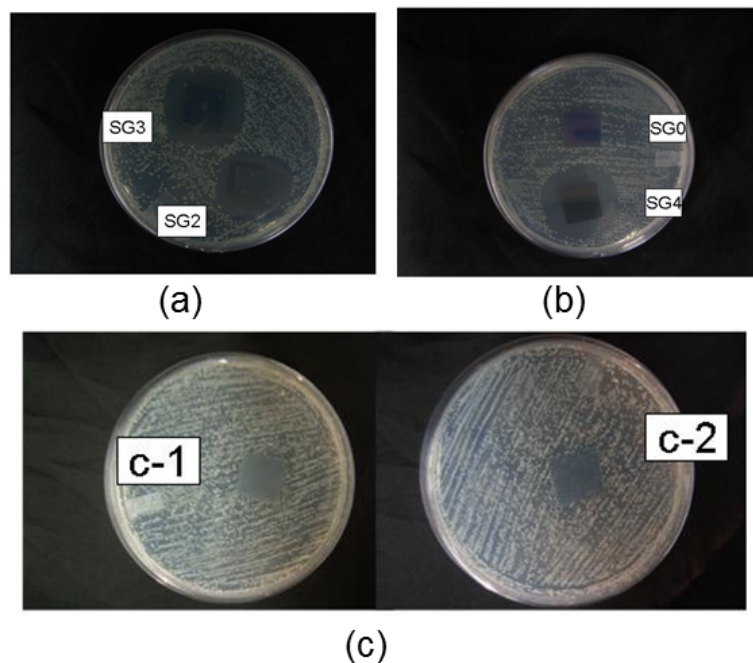


Figure 2-6: Zone of inhibition test results. Comparison of the composite Ag-TiO₂ film and the neat TiO₂ film for E.coli with agar plating.

Table 2-3: The antibacterial test result of the composite films with different silver content against E. coli.

Samples	Diameter of inhibition zone(cm) ^{a,b}
SG0	0
SG1	0.25(0.05)
SG2	0.50(0.05)
SG3	0.65(0.05)
SG4	0.7(0.06)

^a Duplicate experiments gave similar results

^b Standard deviations are given in parentheses

As expected, the composite film with the highest silver loading (SG4) showed the most notable antibacterial effect and the inhibition zone diameter increased about three times compared to SG1. The actual antibacterial mechanism of silver nanoparticles is still under debate. Some research suggested the silver may be used as a metal, but the active agent appears to be the ions produced. In the presence of water and oxygen, elemental silver particles release small amounts of silver ions [41], which induce the cell death. While a study by Panacek [42] suggested that the silver nanoparticles might attach on the surface of the cell membrane, affecting the permeability and respiration. The interactions of silver nanoparticles with the bacteria are dependent on the size and shape of the nanoparticles. In our experiment, the observed inhibition zone is a result of the leaching of active biocidal Ag^+ ions from the embedded silver nanoparticles present in the composite coating matrix into the surrounding aqueous medium, which cause the bacteria death.

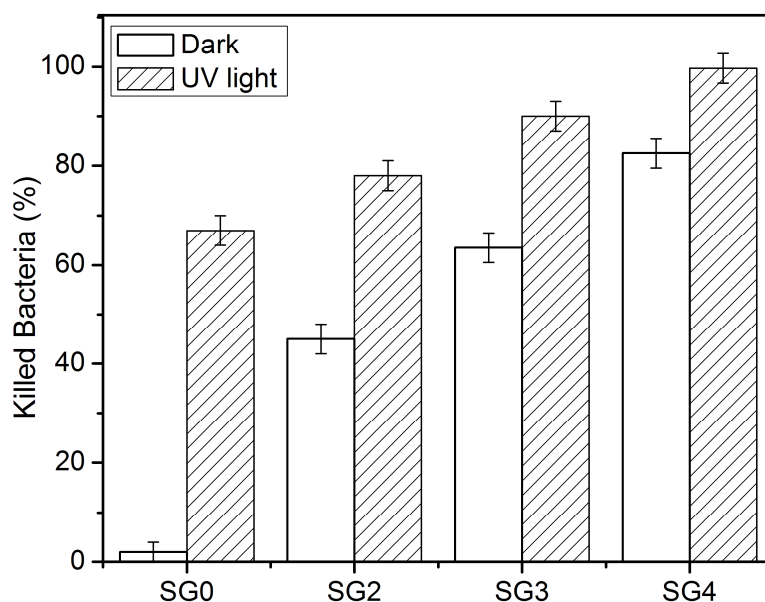


Figure 2-7: Killing ratio of E.coli in the liquid film on Ag-TiO₂ composite film and neat TiO₂ film under 1h UV light illumination (0.6mW cm^{-2}) and in the dark for 1h. For the blank silicon wafer, the killing ratio is $18\pm 5\%$ under the same UV-irradiation.

On the basis of the qualitative results, quantitative tests were carried out on the films of SG0, SG2, SG3 and SG4. Fig.2-7 shows the bacteria killing ratio under UV light illumination and in the dark. After 1 h UV exposure the viable count for *E. coli* showed almost 100% bacterial killing by the sample SG4, while under the same conditions the neat TiO₂ (SG0) film showed a decrease of about 60% only. The samples SG2 and SG3 with less silver content showed decrease of 78% and 90%, respectively. The bactericidal effect of TiO₂ under UV irradiation has been well documented [7]; the ultraviolet A (UVA) light intensity, the extent of irradiation and the catalyst concentration play an important role in disinfection properties. It is reported that anatase TiO₂ film exhibits a strong photocatalytic reaction under UVA illumination and the bactericidal activity of TiO₂ is directly related to ultraviolet light absorption and the formation of various reactive species such as superoxide radicals and hydroxyl radicals [11], so in the dark TiO₂ particles present no bactericide activity. Furthermore, silver ions are also photoactive in the presence of UVA and the photochemical reaction of silver-cysteine complex hinders the enzymatic function of the affected protein, leading to enhanced inactivation of bacteria [43]. The silver only film prepared from the highest silver nitrate concentration showed $63 \pm 15\%$ decrease after 1 h UV of illumination and $39 \pm 16\%$ decrease in the dark respectively. The Ag-TiO₂ composite film SG4 with richest content of silver nanoparticles also showed the highest antimicrobial activity against *E.coli* in the dark and at least 80% of decrease in terms of the number of grown bacterial colonies was found, while SG2 and SG3 showed decreases of 45%, and 63.5%, respectively, after 1 h interaction. For the neat TiO₂ coating, the decrease of the number of viable cells by 5% is caused by natural apoptosis. In our study, 0.6 mW cm^{-2} UV light intensity was chosen and the blank washed silicon under the same UV illumination was considered as blank control. The control result showed around 13% inactivation of *E.coli* after 1h UV irradiation. This could be explained by the exposure to long wavelength UV light, which damaged organisms by the exposure to long wavelength UV light, which damaged organisms by exciting photosensitive molecules within the cell to produce active species to damage the genome and other intracellular molecules [44].

The above results demonstrated that all the Ag-TiO₂ composite films have antibacterial activity even when no light is present, indicating that silver nanoparticles were

responsible for the antimicrobial effect of the coatings in the dark. The higher antibacterial activity of the composite films under the UV light is due to the synergistic antibacterial effects of the photocatalytic reaction of the TiO₂ coating and silver nanoparticles in the matrix. After storing for two months in the dark in an atmospheric environment, the Ag-TiO₂ composite film SG2 showed $76.7 \pm 3\%$ and SG4 showed $99.7 \pm 2\%$ inactivation of *E. coli* after 1 h UV exposure. This indicated the stability of the Ag-TiO₂ composite film. The advantage of Ag-TiO₂ nanocomposite is to expand the antibacterial nanomaterial's functions to a wider variety of working conditions. Thus, the present Ag-TiO₂ composite films are effective in diminishing the living cells and are promising as antibacterial coatings. More detailed silver ion release tests combined with antimicrobial dynamic tests and anti-biofilm properties of the resultant films will be studied in further work.

2.4 Conclusions

Mesoporous TiO₂ thin films of polycrystalline anatase containing silver nanoparticles were prepared by the template sol-gel method on silicon substrates. The morphology of the obtained films could be tuned by changing the ratio of water to Ti in the precursor solution. Silver nanoparticles can be uniformly distributed and strongly attached to the mesoporous TiO₂ matrix. The inactivation results of *E. coli* in the dark and under UVA illumination of the composite films with different silver loadings were compared. The composite films display excellent antibacterial activity and better antibacterial effect with increase of the silver content of the samples. A similarly strong antimicrobial property was observed even after the composite films stored for long periods. The synthesis process is simple, convenient and low cost. It may be reasonably presumed that such mesoporous TiO₂ substrates with silver loaded composite films will prolong the release time of silver ions and preserve the sustained antibacterial behavior. However, further studies must be conducted to examine silver ion release kinetics combined with antimicrobial efficacy test and the cytotoxicity of the composite films. Such mesoporous TiO₂ substrate structures with silver loading could have promising applications as antibacterial materials for biomedical use and in the water treatment field.

2.5 References

- [1] Shi Z L, Neoh K G, Kang E T and Wang W 2006 *Biomaterials* 27 2440-2449
- [2] Cioffi N, Torsi L, Ditaranto N, Tantillo G, Ghibelli L, Sabbatini L, Bleve-Zacheo T, D'Alessio M, Zambonin P G and Traversa E 2005 *Chem.Mater.* 17 5255-5262
- [3] Vigneshwaran N, Kumar S, Kathe A A, Varadarajan P V and Prasad V 2006 *Nanotechnology* 17 5087-5095
- [4] Sunada K, Watanabe T and Hashimoto K J 2003 *J. Photochem. Photobiol. A* 156 227-233
- [5] Blake D M, Maness P C, Huang Z, Wolfrum E J and Huang J 1999 *Sep. Purif. Methods* 28 1-50
- [6] Nonami T, Hase H and Funakoshi K 2004 *Catalysis Today* 96 113-118
- [7] Sunda K, Kikuchi Y, Hashimoto K and Fujishima A 1998 *Environ. Sci. Technol.* 32 726-728
- [8] Fujishima A, Rao T N and Tryk D A 2000 *J. Photochem. Photobiol. C* 1 1-21
- [9] Mills A and Hunte S Le 1997 *J. Photochem. Photobiol. A* 108 1-35
- [10] Jacoby W A, Maness P C, Wolfrum E J, Blanke D M and Fennel J A 1998 *Environ. Sci. Technol.* 32 2650-2653
- [11] Fu G F, Vary P S and Lin C T 2005 *J. Phys. Chem. B* 109 8889-8898
- [12] Choi W, Termin A and Hoffmann M R 1994 *J. Phys. Chem.* 98 13669-13679
- [13] Cozzoli P D, Comparelli R, Fanizza E, Curri M L, Agostiano A and Laub D 2004 *J. Am. Chem. Soc.* 126 3868-3879
- [14] Mayya K S, Gittins D I and Garuso F 2001 *Chem. Mater.* 13 3833-3836

- [15] Zhao G, Kozuka H and Yoko T 1996 *Thin Solid Films* 277 147-154
- [16] Coleman HM, Chiang K and Amal R 2005 *Chem.Eng.J.* 113 65-73
- [17] Tada H, Teranishi K, Inubushi Y I and Ito S 2000 *Langmuir* 16 3304-3309
- [18] Berger T J, Spadaro J A, Chapin S E, Becker R O 1976 *Antimicrob. Agents Chemother.* 9 357-358
- [19] Lehninger A L, Nelson D L and Cox M M 1993 *Principles of biochemistry*. 2nd Ed. (New York: Worth Publishers)
- [20] Feng Q L, Wu J, Chen G Q, Cui F Z, Kim T N and Kim J O 2000 *J. Biomed. Mater. Res. A* 52 662-668
- [21] Dai J and Bruening M L 2002 *Nano Lett.* 2 497-501
- [22] Hyung J J, Sung C Y and Seong G O 2003 *Biomaterials* 24 4921-4928
- [23] Yuranova T, Rincon A G, Pulgarin C, Laub D, Xantopoulos N, Mathieu H J and Kiwi J 2006 *J. Photochem. Photobiol. A* 181 363-369
- [24] Lv Y H, Liu H, Wang Z, Liu S J, Hao L J, Sang Y H, Liu D, Wang J Y and Boughton R I 2009 *J. Membr. Sci.* 331 50-56
- [25] Hermann J M, Tahiri H, Ait-Ichou Y, Lassaletta G, González-Elipse A R and Fernández A 1997 *Appl. Catal. B* 13 219-228
- [26] Naoi K, Ohko Y and Tatsuma T 2005 *Chem. Commun.* 10 1288-1290
- [27] Kubo W and Tatsuma T 2005 *J. Mater. Chem.* 15 3104-3108
- [28] Xin B F, Jing L Q, Ren Z Y, Wang B Q and Fu H G 2005 *J. Phys. Chem. B* 109 2805-2809
- [29] He C, Yu Y, Hu X F and Larbot A 2002 *Appl. Surf. Sci.* 200 239-247

- [30] Sen S, Mahanty S, Roy S, Heintz O, Bourgeois S and Chaumont D 2005 Thin solid films 474 245-249
- [31] Seery M K, George R, Floris P and Pillai S C 2007 J. Photochem. Photobiol. A 189 258-263
- [32] De la Rosa-Fox N, Esquivias E and Pinero M 2001 In: Nalwa HS (ed) Handbook of organic-inorganic hybrid materials and nanocomposites, vol 1. (Los Angeles: Academic Press, Stanford Scientific Corp)
- [33] Yu J C, Wang X C, Wu L, Ho W K, Zhang L Z and Zhou G T 2004 Adv. Funct. Mater. 14 1178-1183
- [34] Yang P D, Deng T, Zhao D Y, Feng P Y, Chmelka B F, Whitesides G M and Stucky G D 1998 Science 282 2244-2246
- [35] Frindell K L, Bartl M H, Popitsch A, Stucky G D 2004 Angew. Chem. Int. Edn 41 959-962
- [36] Yu J C, Wang X C and Fu X Z 2004 Chem. Mater. 16 1523-1530
- [37] Chang C C, Chen J Y, Hsu T L, Lin C K and Chan C C 2008 Thin Solid Films 516 1743-1747
- [38] Moulder J F, Stickle W F, Sobol P E and Bomben K D 1992 Handbook of X-ray Photoelectron Spectroscopy. (Perkin-Elmer Corp., Eden Prairie, MN, 1992)
- [39] Kingery W D, Bowen H K and Uhlmann D R 1976 Introduction to Ceramics (New York: Wiley)
- [40] Sakai N, Fujishima A, Watanabe T and Hashimoto K 2001 J. Phys. Chem. B 105 3023-3026
- [41] Hu C, Lan Y Q, Qu J H, Hu X X and Wang A M 2006 J. Phys. Chem. B 110 4066-4072

- [42] Panacek A, Kvitek L, Pucek R, Kolar M, Vecerova R, Pizurova N, Sharma V K, Nevecna T and Zboril R 2006 J. Phys. Chem. B 110:16248-16253
- [43] Kim JY, Lee C, Cho M, Yoon J 2008 Water Res. 42 356-362
- [44] Oguma K, Katayama H and Ohgaki S 2002 Appl. Environ. Microbiol. 68 6092-6035

Chapter 3

3 Preparation and characterization of Nitrogen doped TiO₂ photocatalyst with high crystallinity and enhanced photoinactivation

3.1 Introduction

Titanium dioxide (TiO₂) has attracted much attention as one of the best semiconductor photocatalysts due to its strong redox power in the presence of oxygen and water, non-toxicity, outstanding stability and low cost. It has been frequently used in practical applications such as self-cleaning coating, air purification and water sterilization. However, TiO₂ only exhibits photocatalytic properties under ultraviolet (UV) range (< 385 nm) and only 5% of the total irradiated natural sunlight has sufficient energy to generate effective photosensitization [1]. The indoor applications were limited in the absence of UV-light. To expand the application field and to utilize the solar energy efficiently, it is necessary to develop titania with photoresponse capacity under visible light.

Recently, extensive research efforts have been directed toward the synthesis and characterization of cation doped (e.g. Pt, Cu, and Fe) [1-4] and anion doped (e.g. N, F, C, and S) [5-12] TiO₂ photocatalysts. The enhanced photocatalytic activity under visible light illumination has been observed, which is attributed to band-gap narrowing after doping [2-12].

Compared to using cations as doping agents, anion doping avoids the risk caused by thermal instability and possible toxic leakage resulting in adverse effect when exposure to ecosystem or humans. Among various approaches of anion doping, doping TiO₂ with nitrogen is one of the most effective approaches to improving photocatalytic activity of TiO₂ in visible light range and enhancing the hydrophilicity [5, 10]. Nitrogen doped TiO₂ (N-TiO₂) nanomaterials have been prepared by a number of physical and chemical techniques. The physical techniques used to dope nitrogen atoms into substitutional sites in the crystal structure of TiO₂ include heat treatment in ammonia atmosphere [13-15]

and sputtering and implantation [16-18], which need expensive special equipment, involving sophisticated vacuum apparatus, limited the large-scale application. The wet chemical route is a simple one-step process to synthesize nanomaterial; it is convenient for scaling up application. Particularly, the sol-gel method [19, 20] is most widely employed in nanomaterial preparation due to its inexpensive equipment requirements and easy fabrication procedure. And the produced nanomaterial is pure and homogeneous.

When utilizing the sol-gel method, N-TiO₂ powder is generally prepared by the precipitation of titanium hydroxide by the hydrolysis of the titanium compound such as titanium tetra-isopropoxide with urea or other nitrogen-containing compounds and the following thermal decomposition process [21-23]. Compared to nanopowders, in some practical applications such as water disinfection, the form of a thin film is greatly favoured, which requires no extra nanopowder filtration and recollection process and reduces the potential environment pollution. However, the precipitation produced by most sol-gel methods cannot be employed for the preparation of nano thin film by dip-coating or spin-coating procedures which require stable sols.

It is known that the efficiency of titania photocatalysts strongly depends on several factors, including crystallite phase, crystallite size, surface area, amount of dopants and methods of preparation. Simple operation variables as solvent selection, catalysis amount and the use of stabilizing agent can influence the properties of the final product. In this paper, the effect of water amount and the pH value on the sol-gel system, final crystal structures and composition of the resultant nanomaterial were investigated in the presence of urea as doping agent, by the characterization methods of x-ray powder diffraction (XRD), specific surface area and x-ray photoelectron spectra (XPS). The morphology of the produced nanomaterials was further characterized by transmission electron microscopy (TEM) and atomic force microscopy (AFM). The synthesis conditions of N-TiO₂ catalyst were optimized and the catalytic activity of N-TiO₂ catalyst for degradation of methyl blue and photo inactivation of bacteria solution under variable light source were compared with that of pure TiO₂ and commercial product P25.

3.2 Materials and methods

3.2.1 Chemicals and materials

Titanium (IV) isopropoxide (TTIP) and urea purchased from Sigma-Aldrich were used in this study as precursors to provide titanium and nitrogen sources respectively. Isopropanol, and nitric acid were commercial products and used as received without further purification. Methylene blue (MB) was used as target degradation dye under visible light irradiation. Ultrapure Milli-Q water was used in all experiments. Gram-negative (*Escherichia coli* ATCC 29425) bacteria were used to test the anti-microbial activity of the resultant nanomaterials. The strains were cultured in Nutrient Broth (BD Difco™) and Standard Methods Agar (BD Difco™) using the appropriate times and temperatures of incubation. The silicon wafers and glass slides were cleaned with freshly prepared piranha solution ($\text{H}_2\text{O}_2:\text{H}_2\text{SO}_4 = 3:7$) for 1h, followed by rinsing with excess of water. The cleaned silicon wafers and glass slides were stored in ultrapure water until further use.

3.2.2 Preparation of materials

The TiO_2 sols were prepared by sol-gel process using acid catalyst. The hydrolysis and polycondensation reaction of TTIP were carried out at room temperature with different molar ratio of catalyst/TTIP. Generally, the molar ratio of isopropanol to TTIP was 120. The concentration of TTIP in the solution was 0.2 mol L^{-1} . Firstly, TTIP was added dropwise to isopropanol under vigorous stirring, forming solution A. Secondly, a certain amount of urea were mixed with deionized water (the molar ratio of H_2O to TTIP was varied from 10:1 to 100:1) containing a certain amount of nitric acid with different pH values, forming solution B. Then the acid urea solution was dropped under stirring into the transparent solution A to promote hydrolysis. Rapid precipitation was observed when large amounts of water was added to the TTIP isopropyl alcohol solution. The obtained stable sol was further aged until transparent gel was obtained. The gel was dried at room temperature and ground to fine powder and subsequently heat-treated in air for 4 h at 400

°C. The precipitation produced by adding large amount of water was collected and dried at room temperature, followed by the same grind and heat-treatment process.

To prepare the N-TiO₂ thin film samples, piranha solution washed glasses and silicon wafers were chosen as substrates. The resultant stable TiO₂ sols were spin-coated on treated glasses and silicon wafers, then dried at 80 °C and annealed at 400 °C in air for 4 h. For comparison, pure TiO₂ was prepared by the same process without adding urea. The powder samples were prepared by grinding the dry gel into a fine powder in a mortar and heated in air for 4h.

3.2.3 Characterization methods

The structure of the samples were determined by XRD with Co ($\lambda=1.79026 \text{ \AA}$) radiation operated at 45 kV and 160 mA with a rotating anode x-ray generator (Rigaku Rotaflex RTP 30). The scanning range was from 20° to 75°. The surface composition was characterized by XPS (Kratos Axis Ultra spectrometer, Surface Science) using Al K α source (15mA, 14kV). Survey scan analyses were carried out with an analysis area of 300 $\mu\text{m} \times 700 \mu\text{m}$, a pass energy of 160 eV. High resolution analyses were carried out with an analysis area of 300 $\mu\text{m} \times 700 \mu\text{m}$ and a pass energy of 20 eV. All the binding energies were referenced to the C 1s peak at 284.8 eV of the surface adventitious carbon. Spectra were analyzed using CasaXPS software (version 2.3.14). Specific surface area was measured using nitrogen adsorption-desorption at 78 K via Micrometircs ASAP 2010 Surface Area Analyzer instrument and calculated by the Brunauer-Emmett-Teller (BET) method. The UV-vis absorption spectra of the resultant powder samples were recorded on a Cary 100 Scan UV/Vis spectrophotometer from Varian equipped with a DRA-CA-301 Labsphere diffuse reflectance cell referenced to BaSO₄. AFM measurements were carried out under ambient conditions using a Dimension V AFM equipped with Nanoscope controller V (Veeco, Inc.) in tapping mode. The samples were probed at three different random locations with scanned areas of 25 μm^2 .

3.2.4 Photocatalytic activity measurement

The photocatalytic activity of obtained N-TiO₂ nanoparticles was evaluated by measuring the photodegradation of the aqueous methylene blue solution under visible light irradiation. A 300 W halogen lamp was used as the light source in the homemade photoreactor. Running water was circulated at the outer wall through the jacket to ensure constant temperature of the reaction mixture. The temperature of the photocatalytic reaction was kept around 25°C. A 400 nm cut-off glass optical filter was placed in front of the reactor. The distance between the lamp and the center of the glass tube was 25 cm. For a typical photocatalytic experiment, a total of 20 mg of nanoparticles was added to a glass tube with 20 mL of methylene blue solution. Prior to irradiation, the suspensions were magnetically stirred in the dark for 1 h to ensure the establishment of an adsorption/desorption equilibrium. Varian CARY 100 UV-Vis spectrophotometer was used for recording absorption spectra. According to the standard curve of absorption to concentration, the value of $\Delta C/C_0$ was calculated to indicate the decomposition efficiency.

3.2.5 Antibacterial activity evaluation

Escherichia coli ATCC 29425 were used in the photocatalytic inactivation experiment. Before the experiment, bacteria were long-term stored at -80 °C in glycerol solution. From the frozen stock, a sample was inoculated on Tryptic Soy Agar plates for short-term storage in the refrigerator at 2-8°C. Two bacteria colonies were precultured in 20 mL of Nutrient Broth medium in the incubator at 37°C overnight and then harvested by centrifugation at 3000 rpm for 10 min. After removing the supernatant, the cells were washed with phosphate buffer solution (PBS) twice and were resuspended in PBS solution. The final concentration of bacterial cells was diluted to approximately 3×10^5 CFU mL⁻¹ in PBS solution.

Powder samples were mixed with the *E. coli* suspension at a fixed concentration of 1 mg mL⁻¹. The covered petri dish containing nanoparticles and bacterial suspension were illuminated by a halogen lamp with a 400 nm cut-off filter, which was used as the visible

light source. During the exposure period, samples (50 μ l) were taken at different time interval and diluted in PBS. After serial dilutions, 100 μ l of bacteria suspension was spread on the plate count agar. The number of surviving bacterial colonies on the Petri dish was counted after incubation for 24 h at 37°C. The counts on three plates corresponding to a particular sample were averaged.

For the antibacterial evaluation of resultant N-TiO₂ thin film samples, a 13 W fluorescent lamp with the 400 nm cut-off filter was also used as the light source. In a typical experiment, 100 μ l of PBS solution containing bacteria was spread on the N-TiO₂ thin film samples with an area of 2.25cm² in a sterilized Petri dish. The Petri dish was sealed and illuminated for 18 h. The light intensity at the working films was 5000 lux (luminous flux per unit area) measured by a light meter. The control samples of photocatalytic thin film were placed in the dark under similar conditions without illumination. The bacteria containing drops were washed from the surface by using 10 mL of PBS in the sterilized Petri dish. After appropriate dilution, the same colonies counting method was used to verify the bacteria viability. The counts on the three plates were averaged. All results were calculated from the data of three independent experiments. When comparing two data sets, unpaired, two-tailed T tests were used to assess the statistical significance of difference in results of antimicrobial effects. A *P* value of less than 0.05 was considered significant.

3.3 Results and discussion

3.3.1 Characterization of N-TiO₂

The crystal phase, particle size and surface structure of the sol-gel derived TiO₂ nanomaterial highly depend on the fabrication methods, anneal temperature and precursor solution composition. In the sol-gel process, TiO₂ colloids were formed through two simultaneous hydrolysis and polycondensation reactions of titanium alkoxides with water. The molar ratio of catalyst/Ti and Ti/H₂O controlled the hydrolysis/condensation rate and phase transformation, which result in different photocatalytic activity [24-29]. High molar ratio of water-to-titanium ($r = [\text{H}_2\text{O}]/[\text{Ti}]$) is of great interest owing to the

small size of particles obtained under these conditions [26]. However, the higher r value produced large numbers of TiO_2 colloids to aggregate, resulting in precipitation. Fig. 3-1 shows the XRD patterns of powder samples obtained at various pH value with $r = 100$. The heat-treated powder samples appeared to be crystalline with distinctive diffraction peaks of anatase in all the samples. When the pH value is 1, the plane of brookite (121) at 35.8° appeared for both powder samples with urea as doping agent. When the pH value increased to 3, the (121) peak of brookite appeared only in the powder samples without urea. It is also noted that when pH increased from 1 to 3, the intensity of the peak around 35.8° became weaker. In contrast, the intensity of anatase as shown at 29.7° increased with the increase of pH. The powder sample prepared at pH = 3 with urea showed highest anatase crystallinity.

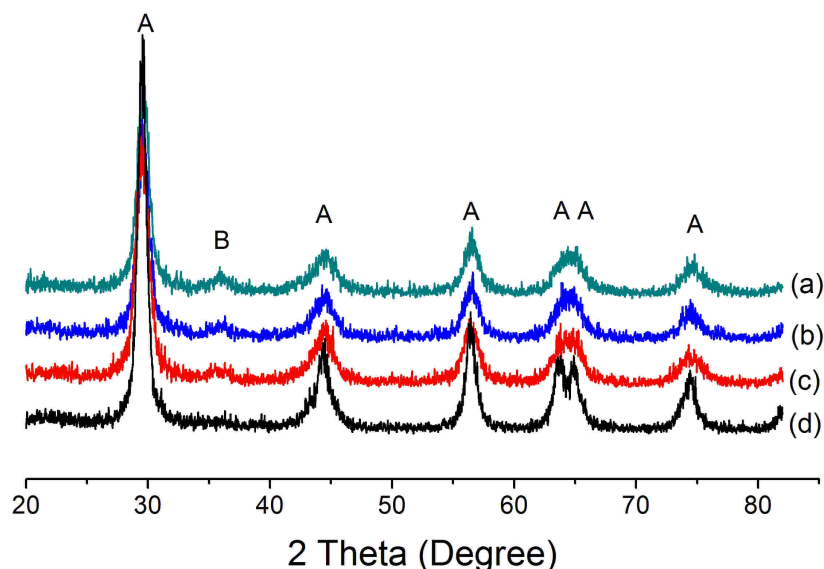


Figure 3-1: XRD patterns of the doped and undoped TiO_2 nanoparticles prepared at different pH with $r = 100$, (a) pH = 1, without urea, (b) pH = 1, with urea, (c) pH = 3, without urea, (d) pH = 3, with urea. A represents anatase phase and B represents brookite phase. All the powder samples have been annealed at 400°C for 4 h.

We decreased the ratio of water-to-titanium to 10 and kept the pH value equal to 3 to obtain stable solution for further study. And the XRD patterns of N- TiO_2 and pure TiO_2

powders under these preparation conditions were shown in Fig. 3-2. Samples with varying molar composition of urea to TTIP as 1:1, 2:1, 3:1 and 4:1 were named NT1, NT2, NT3 and NT4, respectively. Label (e) was homemade pure TiO₂ powder, denoted as NT0. XRD results demonstrated that the doped TiO₂ powders were of homogeneous anatase structure with high crystallinity, and the average grain sizes were between 22-35 nm calculated from Scherer equation (crystallite size, $d = 0.94\lambda/\beta_{1/2}\cos\theta$, where λ is the characteristic x-ray wavelength applied (1.79026 Å), β is the half width of the peak at the 2θ value at the peak of 29.7°. The crystallite size decreased with the increase of the urea concentration. The NT4 sample had the lowest crystallite size of 22 nm, while the NT1, NT2, NT3 sample had crystallite size of 35, 26 and 23 nm, respectively. Home prepared pure TiO₂ powders displayed the lowest crystallite size of 14nm. The particle size of homemade pure TiO₂ was smaller than the N-doped ones. The presence of urea affected the phase transformation from anatase to rutile. Titania powders prepared with urea raised the transformation temperature of anatase to rutile to higher temperature. All the doped samples showed a pure anatase phase, including the one which calcinated at 600°C for 4 h (data not shown).

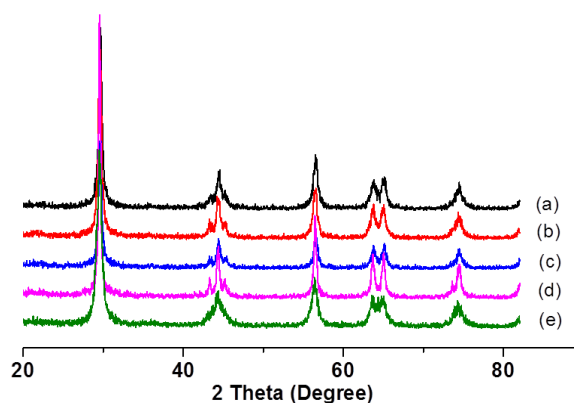


Figure 3-2: XRD patterns of TiO₂ powder samples prepared with molar ratio of water to TTIP at 10 and pH = 3 in the presence of various content of urea, (a) NT4, (b) NT3, (c) NT2, (d) NT1 and (e) NT0.

TEM analysis was used to examine the microstructure of nanoparticles. As shown in Fig 3-3, the primary particles size of N-TiO₂ nanoparticles (NT3) is consistent with the XRD result.

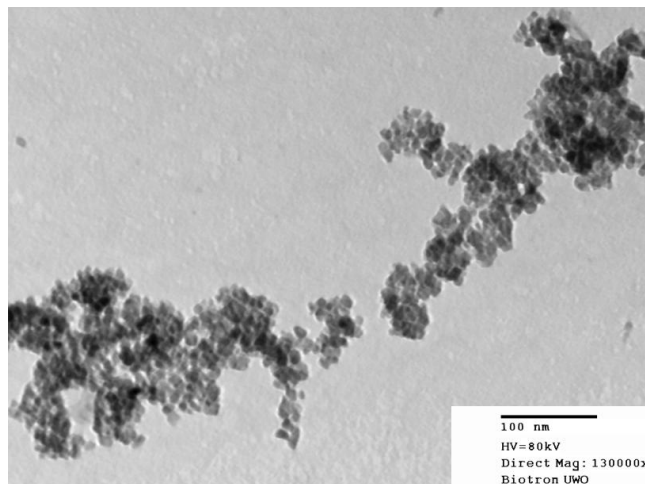


Figure 3-3: TEM image of typical TiO₂ powder (sample NT3).

To evaluate the chemical composition of the prepared materials, XPS studies have been carried out. Fig. 3-4 shows the representative XPS survey spectra of N-TiO₂ powders (NT3) calcinated at 400 °C in air. The characteristic peaks of C 1s (284.6 eV), Ti 2p (458.5 eV), O 1s (530.2 eV) and N 1s peak (400 eV) can be recognized clearly. It confirmed the existence of O and Ti in these powders. The status of doping N in TiO₂ nanoparticles was examined by measuring of the N 1s binding energy. High-resolution XPS spectra of N 1s shown in Fig. 3-4 (c) revealed the corresponding N 1s spectra of the N-doped TiO₂ (NT3) sample, which consisted of two peaks: one was centered at 399.97 eV and the other one was centered at 398.30 eV. The assignment of XPS features in N-TiO₂ and the position of N 1s responsible for the band gap narrowing remained debatable according to previous reports [30, 31]. The binding energy of N 1s was observed in the range of 396-404 eV in different studies and assigned as substitutional and interstitial states of nitrogen in TiO₂ lattice, depending on specific preparing method and ingredient used in the preparation process [32, 33]. It is now generally accepted that substitutional doped nitrogen exhibits the binding energy at 397 eV [5, 15] and the interstitial N shows

a binding energy around 400 eV [34, 35]. Substitutional doping involves oxygen replacement in the TiO_2 lattice forming $\text{TiO}_{2-x}\text{N}_x$, while the interstitial doping involves the formation of TiO_2N_x . High nitrogen concentration is likely to result in substitutional doping at lower binding energy to form O-Ti-N and Ti-N structures. Lower nitrogen concentration favors to form interstitial doping at higher binding energy. In fact, the species of $\text{TiO}_{2-x}\text{N}_y$ ($x < y$) often formed in nitrogen doping nanomaterial. Both doping states can result in the visible light activity of nitrogen-doped TiO_2 . In our samples, the two features of 398.3 eV were attributed to the Ti-O-N binding, and the N 1s peak at 399.97 eV indicated the interstitial nitrogen content [16, 36]. No appreciable signal related to substitutional N doping was observed, which might correspond to the low amount of nitrogen doping.

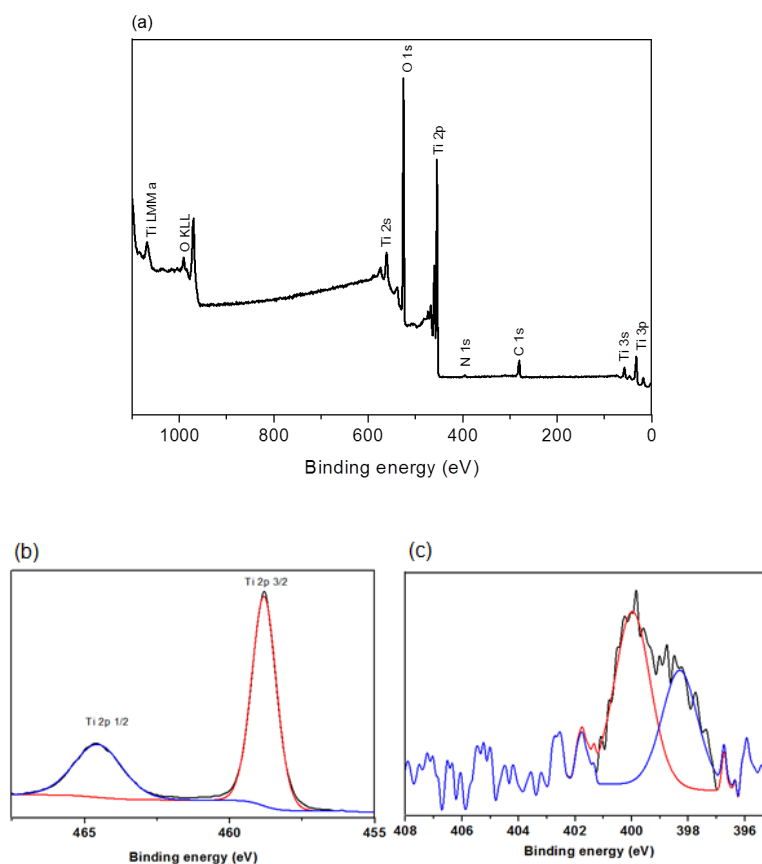


Figure 3-4: (a) The XPS spectra of N-TiO₂ (NT3). (b) Ti 2p of N-TiO₂ XPS region; (c) N 1s of N-TiO₂ XPS region.

In order to determine the specific surface areas (SSAs) of the N-TiO₂, BET experiments were carried out. Doped materials presented a decrease of their surface area with increase of nitrogen doping content, as given in Fig. 3-5. Home-made pure TiO₂ had a SSA around 116 m² g⁻¹ and the total pore volume and average pore size of 0.1728 cm³ g⁻¹ and 5.94 nm, respectively. N-doped powder NT3 presented a smaller SSA of 76 m² g⁻¹ and less total pore volume and average pore size of 0.0849 cm³ g⁻¹ and 4.49 nm, respectively. The measured surface area of P25 as reference was about 50.5 m² g⁻¹, which is consistent with the report data. It can be clearly seen that the prepared powder samples are mesoporous in nature. The surface area of photocatalysts decreases with increasing of crystallite/particle sizes, as discussed below.

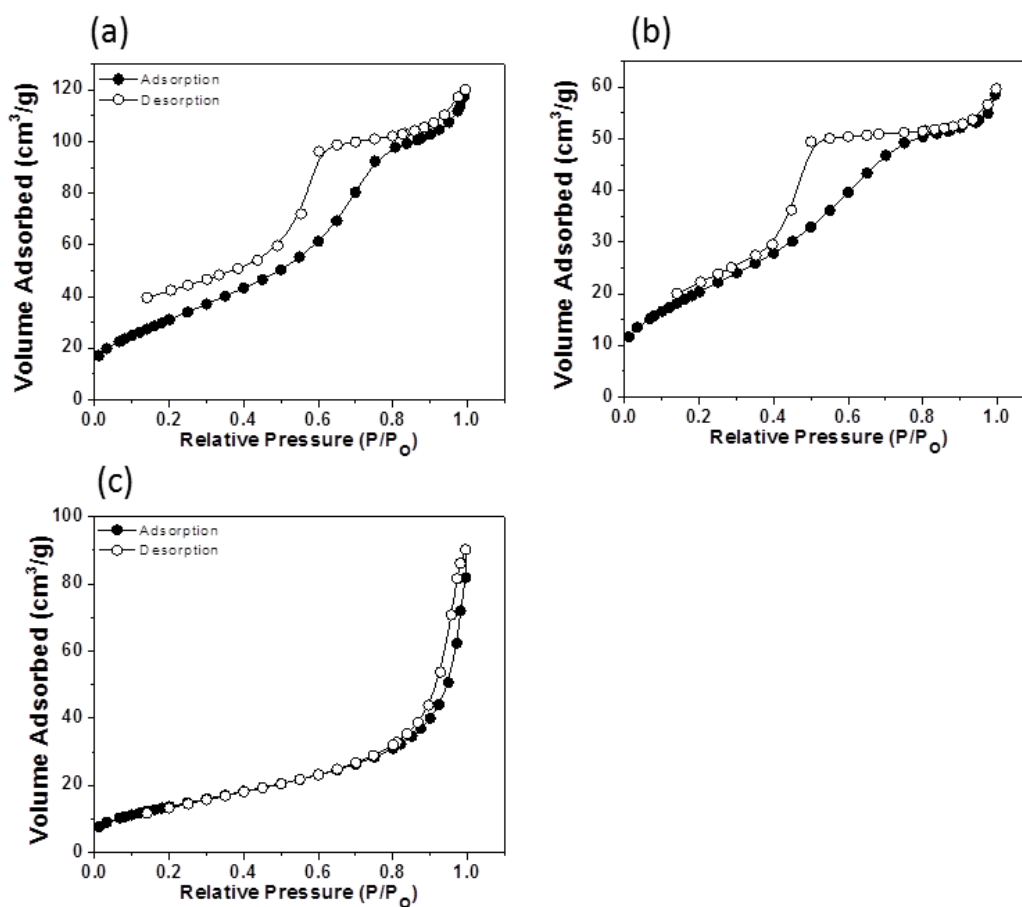


Figure 3-5: N₂ adsorption-desorption isotherm of (a) homemade pure TiO₂, (b) N-doped TiO₂ (NT3) and (c) P25.

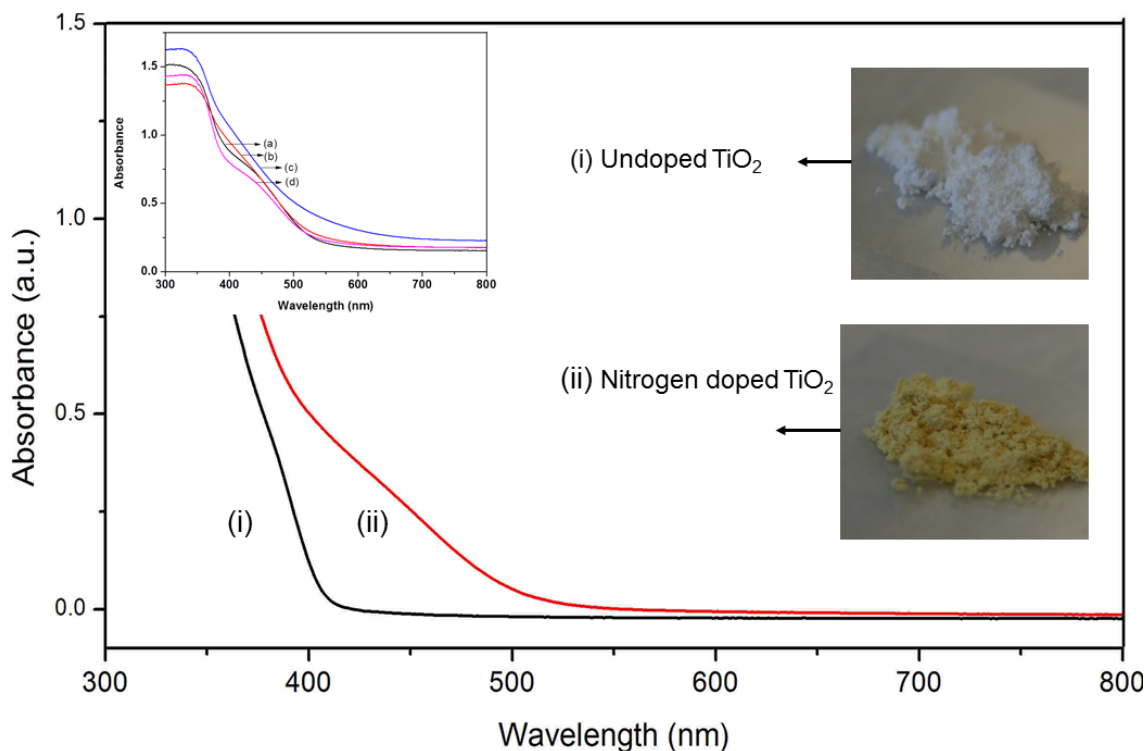


Figure 3-6: UV-visible diffuse reflectance spectra of the N-TiO₂ with various content of urea in the precursor solution as well as the undoped TiO₂ samples. (a) NT1, (b) NT2, (c) NT3 and (d) NT4. The insets on the right side show the pictures of (i) undoped and (ii) N-TiO₂ sample (NT3).

The surface spectral properties of the derived photocatalysts are fundamental to their photocatalytic activity. The optical properties of the home made N-TiO₂ and pure TiO₂ samples were investigated by UV-visible diffuse reflectance spectroscopy, and the results are shown in Fig. 3-6. It is clear that the pure TiO₂ nanoparticles have the absorption below 410 nm, which is consistent with the well-known band gap of anatase TiO₂ bulk. The absorbance shoulder of nitrogen doped samples obviously shifted into the visible-light region compared with the undoped TiO₂, and this enables the nitrogen doped samples to have an extensive absorbance from 400 to 550 nm. It is obvious that N-doped powders possessed two absorption edges around 410 and 530 nm, which indicate the interstitial doping of nitrogen. The first absorption edge around 410 nm was related to the

original structure of TiO_2 . The second absorption edge was attributed to the formed N 1s orbits after nitrogen doping in the molecular structure. The shift in the absorption band edges of the doped TiO_2 samples indicates that the optical band gap decreased, compared to the pure TiO_2 . From the insets of Fig. 3-6, one can see that the undoped TiO_2 sample is white colored, while the nitrogen doped sample is yellow. A comparison study revealed that the visible light absorption characteristic was obtained only after the sample was heat-treated below the temperature of 600°C .

3.3.2 Photocatalytic degradation of Methyl blue under visible light

The photocatalytic activity of the prepared samples was evaluated by the degradation of the methylene blue (MB) aqueous solution under visible light ($\lambda > 400 \text{ nm}$) irradiation, and the results have been compared with the degradation result by using Degussa P25 as the photocatalyst and the result of MB photolysis (without photocatalyst). The concentration of photocatalyst was 1 g L^{-1} . It should be pointed out that the physical adsorption can occur during the degradation process. In our experiments, it took 1 h to reach the adsorption saturation in the dark, where approximately 15% of MB disappeared. And the concentration of MB solution after 1 h interaction was reset as the initial concentration for measuring the photocatalytic degradation efficiency. The degradation of MB solution under visible light radiation over N-doped samples with different nitrogen content is as shown in Fig. 3-7. It can be seen that the highest percentage degradation was observed in the case of NT3 followed by NT2 and NT1. The visible light induced higher photocatalytic activity is due to several reasons. Crystallite phase, crystallite size, surface area and porosity of N-doped TiO_2 could significantly influence the photocatalytic activity. It is also suggested that the most important cause of the photocatalytic activity enhancement is the absorption shift to visible light region due to the interstitial nitrogen doping. The comparison of the photocatalytic activity among N-doped samples with different nitrogen doping content revealed that the decreased crystallite size, as evident from XRD studies, increased the exposed surface area which thereby enhanced the quantum yield for photon absorption. The amount of degradation

has been observed to increase with the increase of nitrogen concentration. It also showed that with the increase of the nitrogen amount in the resultant nanomaterial, the visible-light photocatalytic activity would also be enhanced, which confirmed the role of nitrogen in the lattice for improvement of the visible-light response of N-TiO₂. The presence of optimal nitrogen content is crucial because excessive nitrogen may act as recombination center, which is detrimental to the photocatalytic activity [37]. In view of this, it is important to adjust the urea and TiO₂ composition to a proper ratio in order to acquire the optimum photodegradation efficiency. Thus, further studies were carried out by using NT3 as photocatalyst.

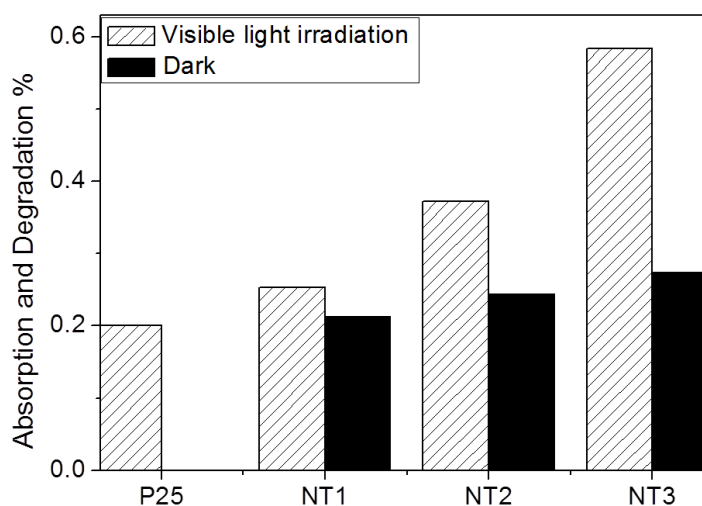


Figure 3-7: Comparison of percentage degradation of methylene blue aqueous solution by Degussa P25, N-TiO₂ (NT1, NT2, and NT3) under the visible light irradiation and in the dark condition.

The intensity of the MB absorption peak at 664 nm is plotted versus the exposure time as shown in Fig. 3-8. It was observed that the direct light-degradation of MB under the visible light irradiation was not obvious, and the MB solution also cannot be degraded under the dark conditions in the presence of the photocatalyst. The degradation of MB (~60%) by using NT3 under the visible illumination is three times compared to that of P25 (~20%) after 4 h of reaction. It should be noted that P25 contains rutile phase, and

rutile phase absorbs blue light in the range of 400-420 nm. It is evident that the degradation amount of MB increased with increasing exposure time. However, the decomposition rate (taken from the slope of curves) decreased with increasing reaction time. The rapid conversion of MB is found at the first 2 h irradiation.

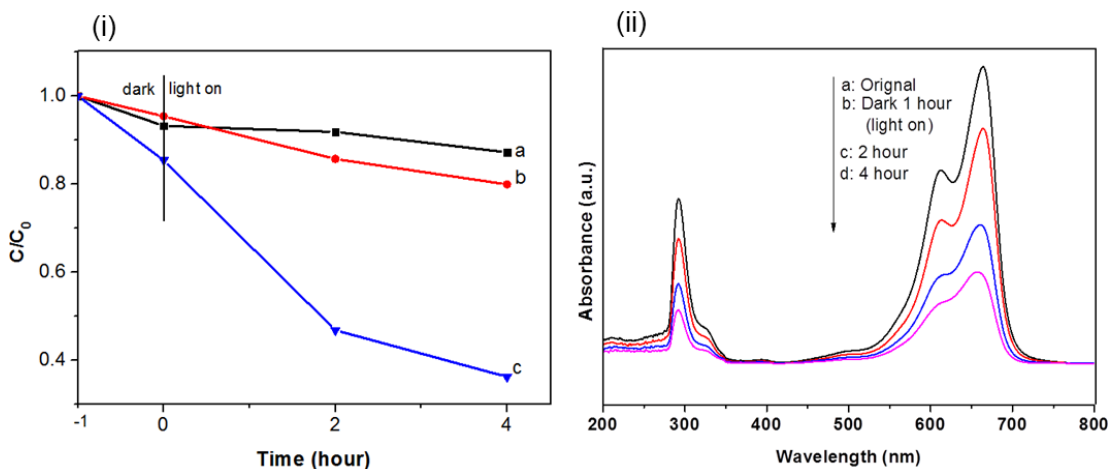


Figure 3-8: (i) adsorption followed by photocatalytic degradation of MB over various photocatalysts under visible light ($\lambda > 400$ nm) irradiation. (a) no catalyst (b) Degussa P25 (c) N-TiO₂ powders (NT3). (ii) the UV visible spectroscopic changes of the MB solution over the N-TiO₂ sample (NT3).

It is reported that photoreactions take place at or near the catalyst surface, surface adsorption is critical for efficient interfacial charge transfer to and from the target molecules.[38] To enhance the degradation rate or photocatalytic activity in the sample, it is necessary that more charge carriers (electrons and holes) should be available for the photocatalytic reactions. The charge carriers under visible light irradiation can be increased by shifting the absorption edge to longer wavelength side. Under exposure to visible irradiation more charge carriers are generated. Optical studies (Fig. 3-6 UV-vis diffuse reflectance) indicated the lower band energy level. The comparison between the results in the dark and under illumination suggested that the degradation of MB under

visible light was enhanced by simultaneous adsorption, which is favourable for charge transfer during photodegradation process. UV-visible spectroscopic changes of the MB aqueous solution over the photocatalyst were included in Fig. 3-8 (ii). It is clearly noted that the MB absorption peak at 664 nm shifted to shorter wavelength. This hypsochromic effect of irradiation on the MB in the presence of photocatalysts is attributed to N-demethylation upon dye breakdown. In contrast, no blue shift was observed during the dark adsorption stage. While no significant blue shift was observed in the MB absorption using P25. To further investigate the visible-light activity, the photocatalytic inactivation of E coli under visible light was also carried out.

3.3.3 Antibacterial activity evaluation

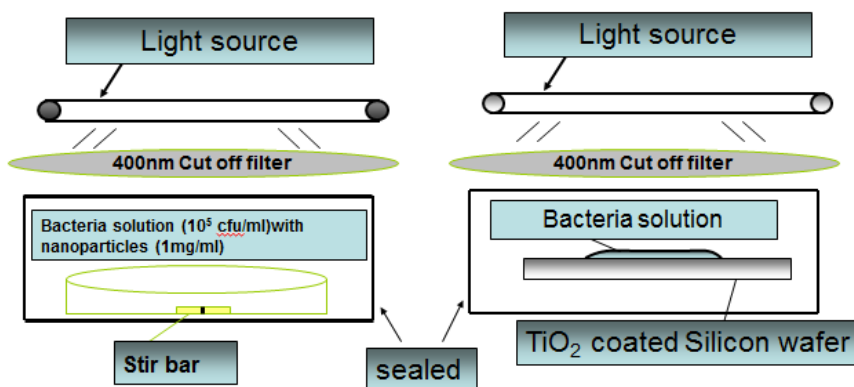


Figure 8-9: Schematic illustrations of the photodisinfection test.

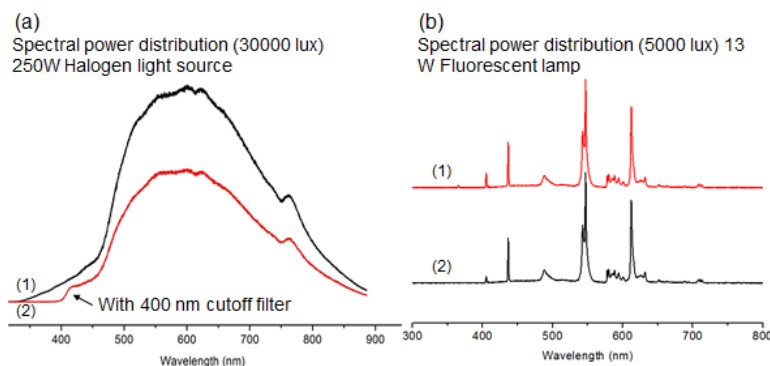


Figure 3-10: Emission spectrum of (a) halogen lamp and (b) 13 W fluorescent lamp used in the visible light photo disinfection measurement, (1) without filter, (2) with 400 nm cut off filter.

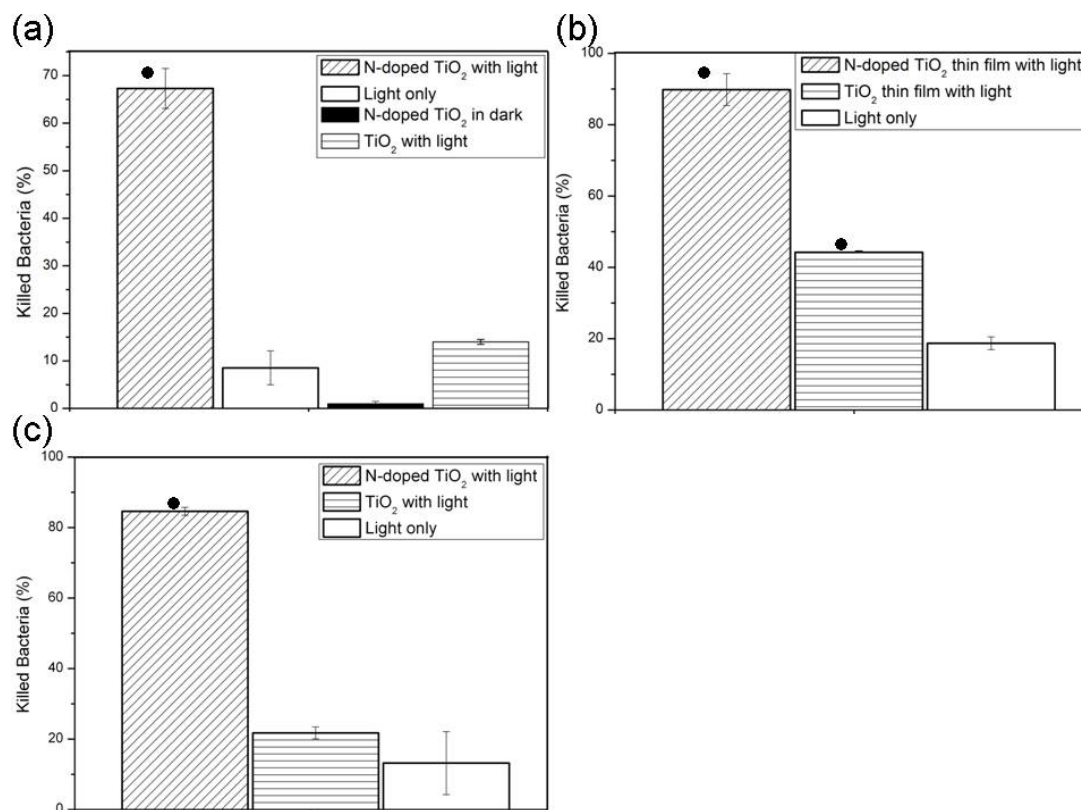


Figure 3-11: Killing ratio of *E.coli* (10^5 CFU mL^{-1}) in the presence of N-doped TiO_2 nano material and pure TiO_2 nano material after exposure to the halogen lamp and fluorescent lamp source. (a) Illumination was carried out under halogen lamp at a light density of 3×10^4 lux for 1 h with nanoparticles (b) Illumination was carried out under halogen lamp at a light density of 3×10^4 lux for 15 min with nanothin film (c) Illumination was carried out under fluorescent lamp at a light density of 5000 lux for 18 h with nanothin film. Bacterial solution alone under various light illumination was chosen as control. Bars indicate average value from three independent experiment data. (• $p < 0.05$)

To evaluate the bactericidal activities of resultant TiO_2 nanomaterials, we first add 1 mg mL^{-1} nanoparticles into 3×10^5 CFU mL^{-1} *E.coli* PBS solution in petri dish. The solution was kept stirring and irradiated with 3×10^4 lux for 1 h. After irradiation, bacteria solution was diluted and the number of surviving bacteria was determined by standard plant count

method. Pure TiO₂ with irradiation and bacterial solution without irradiation were used as control. As expected, the N-TiO₂ nanoparticles exhibited a significant higher bactericidal effect compare to pure TiO₂. Around 70% *E. coli* was killed in the presence of N-TiO₂ nanoparticles, while about 20% *E.coli* was killed by pure TiO₂. Further investigation on the bactericidal ability of doped TiO₂ nanothin film, 3×10⁵ CFU mL⁻¹ *E.coli* PBS solution was placed on the silicon wafer surface with TiO₂ nano-film. Bacterial solution on a bare silicon wafer surface was chosen as control. The solution was irradiated with 3×10⁴ lux for 15 min. The killing efficiency of N-doped TiO₂ nano film is around 90%. It is higher than the efficiency of nanoparticles with less dose irradiation, which might be due to the absorption of the irradiation by the silicon wafer substrate which produced heat. The irradiation only sample also showed higher killing efficiency. In order to expand the application field in public area, we chose the fluorescent lamp which is commonly used in hospital as light source. No significant differences in bactericidal ability was observed on the TiO₂ thin films samples incubated in the dark compared with those exposed to 13W fluorescent lamp at 5000 lux for 1.5 h, which is the same dose as compared with irradiation under 3×10⁴ lux for 15 min. Further increased the irradiation exposure time to 18 h allows 85% of *E.coli* killing efficiency on the N-doped TiO₂ film, while 20% of *E.coli* was killed on the pure TiO₂ film sample under the same irradiation conditions. For all irradiation sources used in the study, the N-doped TiO₂ nanomaterial showed higher bacterial inactivation property due to the relatively decreased band gap and consequently visible light absorption ability. Though the bacterial inactivation efficiency of N-doped TiO₂ nanomaterial under visible-light irradiation is quite low compared with UV irradiation and other chemical bactericide agent, the visible-light activated TiO₂ nanomaterials offer broad application field. The nontoxic, stable and inert chemical property of TiO₂ allow continuous act as antimicrobial material when illuminated by light. It has the potential to be used in hospital or other public environment.

3.4 Conclusions

In conclusion, we have prepared N-doped TiO₂ nanomaterial by the sol-gel technique. All the prepared nano materials with lower water ratio in the precursor solution exhibited anatase-phase TiO₂ as determined by XRD characterization. Large water ratio in

precursor solution produced TiO₂ nanoparticles both with anatase and brookite phase. The addition of urea in the precursor solution inhibited the appearance of brookite phase. The prepared N-doped TiO₂ nanoparticles have size distribution in the nanometer range. And the nanocrystallite size decreased with the increase of the doping amount. The N-doped TiO₂ nanoparticles showed excellent visible-light absorption and high photocatalytic ability for the methyl blue under visible light irradiation. Meanwhile, N-doped TiO₂ thin films were obtained by spin coating. The evidence for the presence of nitrogen and the interstitial doping states of nitrogen is demonstrated by UV-visible spectra and XPS characterization. The N-doped titanium nanomaterials were applied to bacterial inactivation. The enhanced photoactivity was attributed to the dopant induced elevated and extended light absorption into the visible range. Based on the above experiment results, this study facilitated the development of a visible active photocatalyst with improved photoactivity. A large range of pathogenic microorganisms need to be tested to evaluate the microbial inactivation property for real applications. Our method of narrowing the band gap has the advantage of low cost, simple processing, easy large-scale production and is environmentally friendly.

3.5 References

- [1] Wilke K, Breuer HD. The influence of transition metal doping on the physical and photocatalytic properties of titania. *Journal of Photochemistry and Photobiology A: Chemistry*. 1999;121:49-53.
- [2] Umebayashi T, Yamaki T, Itoh H, Asai K. Analysis of electronic structures of 3d transition metal-doped TiO₂ based on band calculations. *J Phys Chem Solids*. 2002;63:1909-20.
- [3] Sakthivel S, Shankar MV, Palanichamy M, Arabindoo B, Bahnemann DW, Murugesan V. Enhancement of photocatalytic activity by metal deposition: characterisation and photonic efficiency of Pt, Au and Pd deposited on TiO₂ catalyst. *Water research*. 2004;38:3001-8.

- [4] Kim S, Hwang SJ, Choi W. Visible light active platinum-ion-doped TiO₂ photocatalyst. *The journal of physical chemistry B*. 2005;109:24260-7.
- [5] Asahi R, Morikawa T, Ohwaki T, Aoki K, Taga Y. Visible-light photocatalysis in nitrogen-doped titanium oxides. *Science*. 2001;293:269-71.
- [6] Umebayashi T, Yamaki T, Itoh H, Asai K. Band gap narrowing of titanium dioxide by sulfur doping. *Appl Phys Lett*. 2002;81:454-6.
- [7] Yu JC, Yu JG, Ho WK, Jiang ZT, Zhang LZ. Effects of F- doping on the photocatalytic activity and microstructures of nanocrystalline TiO₂ powders. *Chem Mat*. 2002;14:3808-16.
- [8] Sakthivel S, Kisch H. Daylight photocatalysis by carbon-modified titanium dioxide. *Angew Chem-Int Edit*. 2003;42:4908-11.
- [9] Burda C, Lou YB, Chen XB, Samia ACS, Stout J, Gole JL. Enhanced nitrogen doping in TiO₂ nanoparticles. *Nano letters*. 2003;3:1049-51.
- [10] Diwald O, Thompson TL, Zubkov T, Goralski EG, Walck SD, Yates JT. Photochemical activity of nitrogen-doped rutile TiO₂ (111) in visible light. *J Phys Chem B*. 2004;108:6004-8.
- [11] Li D, Haneda H, Labhsetwar NK, Hishita S, Ohashi N. Visible-light-driven photocatalysis on fluorine-doped TiO₂ powders by the creation of surface oxygen vacancies. *Chem Phys Lett*. 2005;401:579-84.
- [12] Park JH, Kim S, Bard AJ. Novel carbon-doped TiO₂ nanotube arrays with high aspect ratios for efficient solar water splitting. *Nano letters*. 2006;6:24-8.
- [13] Vitiello RP, Macak JM, Ghicov A, Tsuchiya H, Dick LFP, Schmuki P. N-Doping of anodic TiO₂ nanotubes using heat treatment in ammonia. *Electrochem Commun*. 2006;8:544-8.

- [14] Yates HM, Nolan MG, Sheel DW, Pemble ME. The role of nitrogen doping on the development of visible light-induced photocatalytic activity in thin TiO₂ films grown on glass by chemical vapour deposition. *J Photochem Photobiol A-Chem.* 2006;179:213-23.
- [15] Chen HY, Nambu A, Wen W, Graciani J, Zhong Z, Hanson JC, et al. Reaction of NH₃ with titania: N-doping of the oxide and TiN formation. *J Phys Chem C.* 2007;111:1366-72.
- [16] Diwald O, Thompson TL, Goralski EG, Walck SD, Yates JT. The effect of nitrogen ion implantation on the photoactivity of TiO₂ rutile single crystals. *J Phys Chem B.* 2004;108:52-7.
- [17] Kitano M, Funatsu K, Matsuoka M, Ueshima M, Anpo M. Preparation of nitrogen-substituted TiO₂ thin film photocatalysts by the radio frequency magnetron sputtering deposition method and their photocatalytic reactivity under visible light irradiation. *J Phys Chem B.* 2006;110:25266-72.
- [18] Chen SZ, Zhang PY, Zhuang DM, Zhu WP. Investigation of nitrogen doped TiO₂ photocatalytic films prepared by reactive magnetron sputtering. *Catal Commun.* 2004;5:677-80.
- [19] Lakshmi BB, Dorhout PK, Martin CR. Sol-gel template synthesis of semiconductor nanostructures. *Chem Mat.* 1997;9:857-62.
- [20] Lakshmi BB, Patrissi CJ, Martin CR. Sol-gel template synthesis of semiconductor oxide micro- and nanostructures. *Chem Mat.* 1997;9:2544-50.
- [21] Livraghi S, Paganini MC, Giamello E, Selloni A, Di Valentin C, Pacchioni G. Origin of photoactivity of nitrogen-doped titanium dioxide under visible light. *J Am Chem Soc.* 2006;128:15666-71.
- [22] Reyes-Garcia EA, Sun YP, Reyes-Gil K, Raftery D. N-15 solid state NMR and EPR characterization of N-doped TiO₂ photocatalysts. *J Phys Chem C.* 2007;111:2738-48.

- [23] Yin S, Aita Y, Komatsu M, Wang JS, Tang Q, Sato T. Synthesis of excellent visible-light responsive $\text{TiO}_2\text{-xNy}$ photocatalyst by a homogeneous precipitation-solvothermal process. *J Mater Chem*. 2005;15:674-82.
- [24] Shin HH, Jung HS, Hong KS, Lee JK. Crystallization process of TiO_2 nanoparticles in an acidic solution. *Chem Lett*. 2004;33:1382-3.
- [25] Watson SS, Beydoun D, Scott JA, Amal R. The effect of preparation method on the photoactivity of crystalline titanium dioxide particles. *Chem Eng J*. 2003;95:213-20.
- [26] Vorkapic D, Matsoukas T. Effect of temperature and alcohols in the preparation of titania nanoparticles from alkoxides. *J Am Ceram Soc*. 1998;81:2815-20.
- [27] Ding XZ, Qi ZZ, He YZ. EFFECT OF HYDROLYSIS WATER ON THE PREPARATION OF NANO-CRYSTALLINE TITANIA POWDERS VIA A SOL-GEL PROCESS. *J Mater Sci Lett*. 1995;14:21-2.
- [28] Sugimoto T, Zhou XP, Muramatsu A. Synthesis of uniform anatase TiO_2 nanoparticles by gel-sol method - 1. Solution chemistry of $\text{Ti}(\text{OH})(n)((4-n)^+)$ complexes. *Journal of colloid and interface science*. 2002;252:339-46.
- [29] Sugimoto T, Zhou XP. Synthesis of uniform anatase TiO_2 nanoparticles by the gel-sol method - 2. Adsorption of OH^- ions to $\text{Ti}(\text{OH})(4)$ gel and TiO_2 particles. *Journal of colloid and interface science*. 2002;252:347-53.
- [30] Gopinath CS. Comment on "Photoelectron spectroscopic investigation of nitrogen-doped titania nanoparticles". *J Phys Chem B*. 2006;110:7079-80.
- [31] Burda C, Gole J. Reply to "Comment on "Photoelectron spectroscopic investigation of nitrogen-doped titania nanoparticles". *J Phys Chem B*. 2006;110:7081-2.
- [32] Di Valentin C, Finazzi E, Pacchioni G, Selloni A, Livraghi S, Paganini MC, et al. N-doped TiO_2 : Theory and experiment. *Chem Phys*. 2007;339:44-56.

- [33] Cong Y, Zhang JL, Chen F, Anpo M. Synthesis and characterization of nitrogen-doped TiO₂ nanophotocatalyst with high visible light activity. *J Phys Chem C*. 2007;111:6976-82.
- [34] Ananpattarachai J, Kajitvichyanukul P, Seraphin S. Visible light absorption ability and photocatalytic oxidation activity of various interstitial N-doped TiO₂ prepared from different nitrogen dopants. *Journal of hazardous materials*. 2009;168:253-61.
- [35] Peng F, Cai LF, Yu H, Wang HJ, Yang J. Synthesis and characterization of substitutional and interstitial nitrogen-doped titanium dioxides with visible light photocatalytic activity. *J Solid State Chem*. 2008;181:130-6.
- [36] Thompson TL, Yates JT. Surface science studies of the photoactivation of TiO₂-new photochemical processes. *Chem Rev*. 2006;106:4428-53.
- [37] Irie H, Watanabe Y, Hashimoto K. Nitrogen-concentration dependence on photocatalytic activity of TiO₂-xNx powders. *J Phys Chem B*. 2003;107:5483-6.
- [38] Cheng YH, Huang YZ, Kanhere PD, Subramaniam VP, Gong DG, Zhang S, et al. Dual-Phase Titanate/Anatase with Nitrogen Doping for Enhanced Degradation of Organic Dye under Visible Light. *Chem-Eur J*. 2011;17:2575-8.

Chapter 4

4. Characterization and antibacterial adhesion performance of TiO₂ coatings prepared by liquid phase deposition

4.1 Introduction

High-performance polymers and polymer-matrix composites are increasingly used in demanding applications. For example, butyl rubber with outstanding features such as low gas and water permeability and low resilience, is an important large-volume commercial product, ranging from inner-tubes in automobile tires to diaphragms in artificial heart pumps. Unfortunately, microbial surface adhesion and the formation of a biofilm at the interface between the material and the biological environment can cause clinical failure in many applications. Recent research has focused on surface modification, including grafting polymers with good biocompatibility [1-3], introducing an inorganic barrier, for example mineral oxide films [4, 5]. Titanium dioxide (TiO₂) is one of the most effective photocatalysts currently in use due to its strong oxidizing power, non-toxicity and long-term photostability [6]. It has been widely used for sensors, photocatalysis, photovoltaic devices, etc. In addition, self-sterilizing property of TiO₂ has also been reported [7], which can kill bacteria on its surface under ultraviolet (UV) illumination [8, 9]. However, the traditional techniques to fabricate TiO₂ related nanomaterial coatings such as chemical vapour deposition, sputtering and some other physical processes usually required surface roughness to support the stringent reaction condition [10]; while, for wet chemistry method, such as hydrolyzing titanate precursors (sol-gel and reverse micelle method), required the following heat treatment at very high temperature, usually above 500°C, which is much higher than the degradation temperature of most polymers [11-13]. Therefore, a milder preparation method is desired to achieve the TiO₂ coating on polymer surface.

Liquid phase deposition (LPD) is commonly used to make silica films [14, 15] and this strategy is being increasingly used recently to produce single oxides such as titanium [16, 17], tin oxide [18], iron oxide [19] and multicomponent films [17, 20]. The oxide thin film by LPD method is formed by oxide precipitates from the hydrolysis of an aqueous

solution of a metal inorganic salt [17]. For the formation of TiO_2 film, the aqueous solution of titanium inorganic salts ($(\text{NH}_4)_2\text{TiF}_6$, TiF_4 , and TiCl_4) were hydrolyzed by the addition of boric acid or aluminum metal as F^- scavengers at low temperature ($50\text{ }^\circ\text{C}$) [21]. The whole process is low-cost and environmentally friendly, and requires neither vacuum nor high temperature. Masuda *et al.* explored in detail the mechanism of anatase TiO_2 deposition on several of self-assembled monolayers in an aqueous solution [22]. The solution composition, temperature, and pH had great influence on the morphology and growth rate of the resulting film [17, 23]. Since the TiO_2 layer deposited on the surface will not destroy the bulk properties, LPD is a potentially general approach to introducing oxides films as a method to improve thermo-oxidative and antibacterial stability of polymers. Although the deposition solution chemistry and film nucleation processes are well investigated, the control of the derived film structure as desired has not been studied in detail.

In this chapter, using the LPD approach, TiO_2 thin coatings were deposited on the substrates of interest, e.g. butyl rubber, silicon wafer and cotton sheet. The morphology, chemical composition, and the water contact angles of the deposited coatings were investigated. The morphology of the deposited coatings can be controlled by tuning the solution composition. Smooth TiO_2 films with good adhesion or loosely packed TiO_2 coatings with hierarchical structures can be achieved as desired. After surface fluorination treatment, the TiO_2 coatings with hierarchical structures showed the superoleophobic property. Furthermore, preliminary results on the antibacterial adhesion have been explored.

4.2. Methodology

4.2.1 Chemicals and materials

Ammonium hexafluorotitanate ($(\text{NH}_4)_2\text{TiF}_6$, 99.99%), boric acid (H_3BO_3 , 99%), hydrochloric acid, poly(acrylic acid) (PAA) with a molecular weight of $450,000\text{ g mol}^{-1}$ and polyethylenimine (PEI) with a molecular weight of $750,000\text{ g mol}^{-1}$ were purchased from Aldrich Chemical Company and used as received unless otherwise noted.

1H,1H,2H,2H-Perfluorodecyltrichlorosilane (PFTS) was obtained from Alfa Aesar. Butyl rubber films were received as a gift from Lanxess Company. Silicon wafer and cotton sheets were commercial products. All reagents were of analytical grade and used as-received form without further purification.

4.2.2 Preparation of seeds

To acquire the desired morphologies and examine the effect of seeds on the morphologies of TiO₂ coating film, various nanoparticles with different sizes and shapes were studied as initial seeds. TiO₂ particles with diameter of 25 nm were suspended in DI water to get 2 mg mL⁻¹ dispersion solution; homemade SiO₂ rod with the 3 μm length and 150 nm width dispersed in DI water was also chosen as seed solution. PEI and PAA aqueous solution of concentration around 0.05 wt% were prepared respectively, and followed by adding certain amount of seed at a concentration of 0.25 wt% with shaking for 24 h under ambient condition to achieve equilibrium.

4.2.3 Preparation of TiO₂ coating

The (NH₄)₂TiF₆ and H₃BO₃ were separately dissolved in deionized water and then mixed to form a homogenous solution containing 0.05 M of (NH₄)₂TiF₆ and 0.15 M of H₃BO₃. The solution pH was then adjusted to 2.88 by the addition of 1 M of hydrochloride acid. Subsequently, a predetermined amount of the prepared seed dispersion mentioned above was added to the homogenous solution and mixed under ultrasonication for 5 min to obtain the precursor solution. In the meanwhile, the substrates of butyl rubber films were treated by UV/ozone cleaner for 20 min to remove any organic contamination and convert the hydrophobic surface to hydrophilic through formation of oxygen-containing functional group. The silicon wafer substrates were cleaned by Piranha etching solution by immersed into a piranha solution (concentrated H₂SO₄/H₂O₂ 70:30 vol%) at 90 °C for 30 min, and followed by thorough rinsing with distilled water. The fresh activated butyl rubber, silicon wafer and cotton sheet substrates were placed upside down in 100 mL of precursor solutions to avoid the deposition of TiO₂ particles by gravity. The deposition was operated at 50 °C for variable reaction time from 3 to 24 h. When the reaction was

completed, the substrates with TiO₂ coating were cooled down to room temperature and washed with distilled water three times and dried under a N₂ atmosphere.

4.2.4 Surface characterization

The crystallinity of the resultant TiO₂ films were determined by x-ray diffraction (XRD) with Co radiation ($\lambda=1.79026 \text{ \AA}$) operated at 45 kV and 160 mA and a rotating anode x-ray generator (Rigaku Rotaflex RTP 30). The scanning range was from 2° to 82° in the increment of 0.02°. Atomic force microscopy (AFM) measurements were carried out with Nano-scope dimension V controller. Tapping-mode scans were performed with silicon nitric cantilever/tips (Digital Instruments) at ambient conditions using 1 μm^2 x-y range scanner. The surface morphology of samples was assessed by scanning electron microscopy (SEM, HITACHI S-4500) with an energy-dispersive x-ray spectrometer (EDX). The samples were coated by a thin layer of Pt to increase the conductivity.

4.2.5 Tape test

A piece of 3M Scotch adhesive tape was used for the adhesive tape peeling test. Scotch tape was placed on the deposited film, pressed gently to achieve a homogeneous contact between the tape and the coating film, and then peeled off quickly. The morphology of the coating on butyl rubber after tape test was observed by optical microscopy.

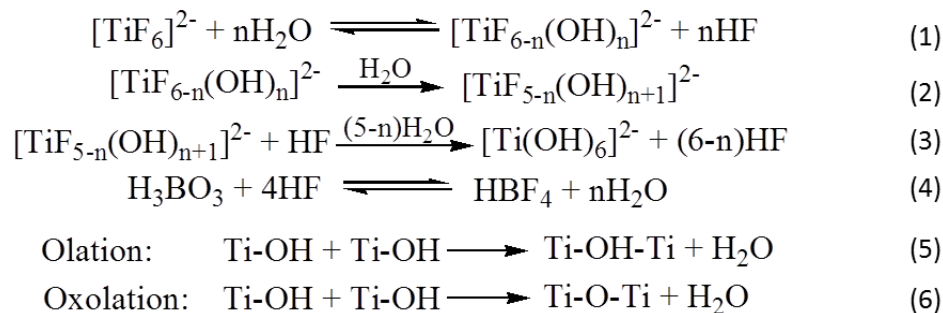
4.2.6 Bacterial adhesion test

Substrates with various coatings were immersed into bacterial solution (E.coli) with 10⁸ CFU mL⁻¹ for 6 h at ambient environment in static growth condition. Then the substrates were taken out and dipped in sterile PBS solution three times. Sterilized filter paper was used to wick the moisture from the substrate surface; after that the substrates were characterized by SEM.

4.3 Results and Discussion

4.3.1 Reaction mechanism of LPD-derived TiO₂ coating

In a typical LPD process, metal oxide or hydroxide thin films are formed by a ligand-exchange equilibrium reaction (hydrolysis) between the metal-fluoro complex ion and metal oxide or metal hydroxides in an aqueous solution [14, 15, 19]. By the addition of boric acid, as F⁻ ions scavenger to give the more stable BF₄⁻ ion, the equilibrium reaction of hydrolysis of soluble titanium fluoride complex [TiF₆]²⁻ is shifted from left to the right hand side (as depicted in Scheme 1, eqs 1-4) [17, 21, 24-26]. It also can be seen that high concentration of H⁺ would suppress the deposition of TiO₂ (Scheme 1, eq1). As a fluoride scavenger to shift hydrolysis to the right, the hydrolyzed titanium complex ion, [TiF_{6-n}(OH)_n]²⁻, leads to a hydrous oxide precipitation by condensation reaction through both olation and oxolation (Scheme 1, eqs 5-6) [21].



Scheme 1: reaction mechanism for LPD [16, 17, 21, 25, 26]

Various methods with differences in solution composition, pH, and temperature have been reported to form the supersaturation of the solution to form TiO₂ film on different substrates. The degree of supersaturation of the deposition solution, nucleation density and growth rate are deliberately controlled by solution concentration, temperature and pH, significantly influencing the crystallinity and morphology of LPD-derived TiO₂ thin films [16, 23, 27]. Ozawa [28] et al. has investigated the effect of seed crystal and composition of the aqueous solution on the formation of TiO₂ thin film from the

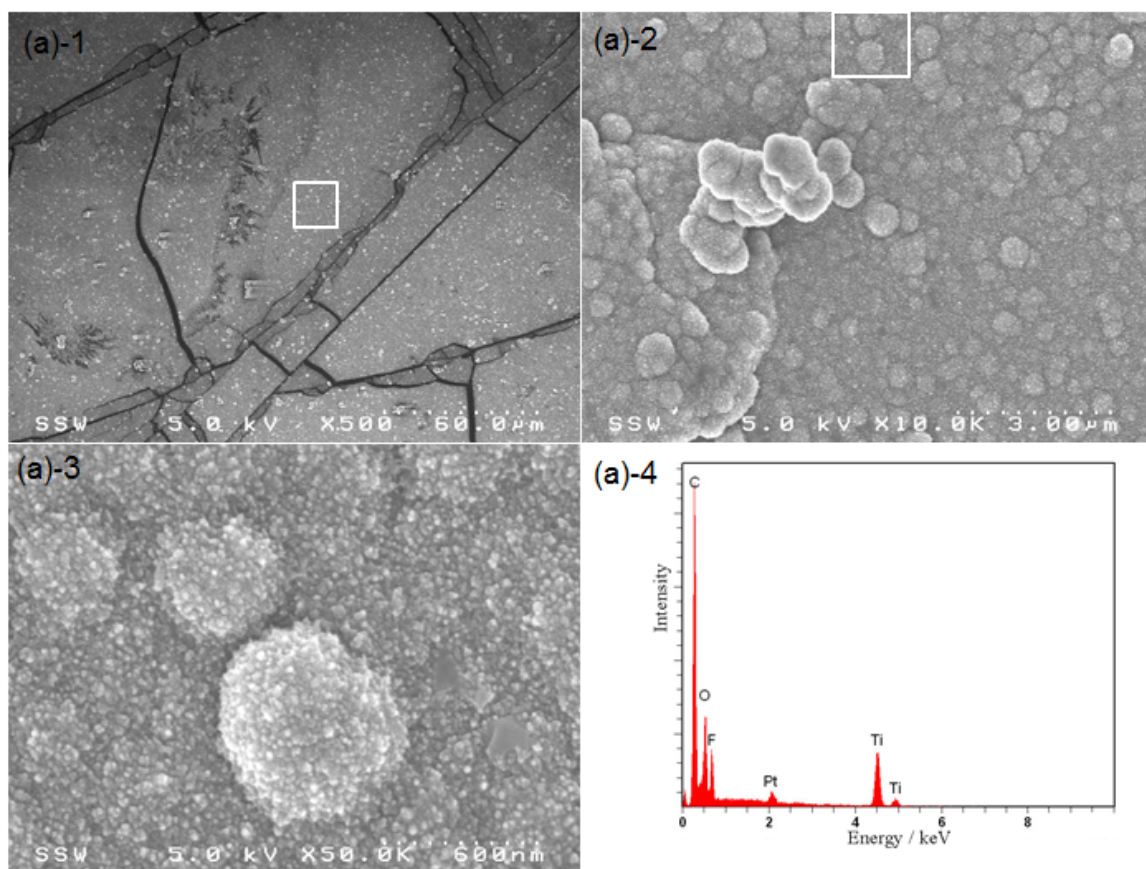
hydrolysis reaction of titanium fluoro-complex solution. The structure of the derived TiO₂ coating could be tailored as requested by the addition of various seed crystal.

4.3.2 Characterization of LPD-derived TiO₂ coating on different substrates

The morphology and adherence of the resultant film on substrate by LPD method was also affected by the surface functionality of the substrate [23]. In order to ensure uniform film growth using LPD method, surface treatments are usually required, which include the pre-deposition or self-assembly of a seed layer [29], and the surface formation of hydroxides [30]. In this chapter, pristine butyl rubber surface was treated by UV/Ozone for 20 min. Long-time exposure to UV/ozone would lead rubber age and degradation. The surface contact angle measurement results showed that the contact angle to water droplets decrease to 40° compared to a value of 90° for pristine unmodified butyl rubber surface, which revealed the surface was more hydrophilic after UV exposure due to the formation of oxygen-containing functional group. Comparing to UV/ozone treated butyl rubber surface, the fresh piranha solution treated silicon wafer exhibited superhydrophilic property with the contact angle around 5°. Furthermore, piranha solution treated silicon wafer and cotton sheet were chosen as the substrates to understand the formation of LPD-derived TiO₂ coating.

The surface morphology and grain size of the LPD derived TiO₂ thin films on UV/Ozone treated butyl rubber, silicon wafer and pristine cotton sheet were firstly characterized by SEM. Fig. 4-1 presents the representative SEM images of the derived TiO₂ coating from the top views at different magnifications. Overall, smooth surface of the coated butyl rubber without obvious aggregates of TiO₂ was observed. The formation of visible cracks appeared on the top of TiO₂ films (Fig. 4-1a) was ascribed to the capillary stress as a result of the shrinkage of films during dry process [31]. More visible cracks appeared on the silicon wafer surface, while crack-free TiO₂ coating morphology was observed on cotton sheet surface. This phenomena indicated the stress mismatch of the LPD-coating with the substrate had great effect on the surface morphology. In general, TiO₂ particles consisted of crystallines with diameter around 60 nm fully covered the substrate. The

appeared larger domains were due to the surface roughness of butyl rubber and the small TiO_2 particles incorporated together regardless to the surface fluctuation in high magnification 50,000 \times . The resultant film demonstrated a dense and defect-free morphology at high magnification (Fig. 4-1(a)-3). The energy dispersive x-ray (EDX) spectra of the surface showed in Fig. 4-1(a)-4 clearly indicate the existence of Ti and O. The appeared signal of C was from the substrate of butyl rubber and F was originated from precursor in the LPD solution that might improve the photocatalytic activity of TiO_2 [32, 33].



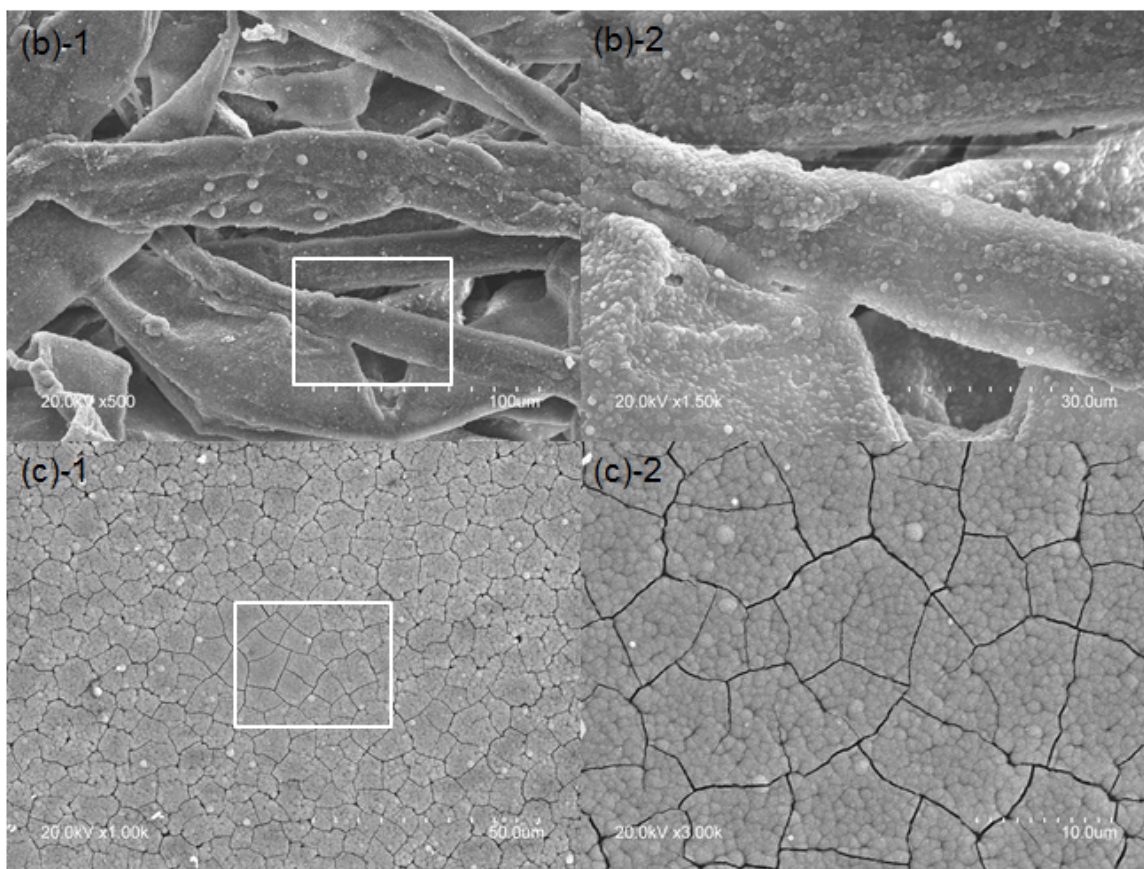


Figure 4-1: SEM images of TiO₂ coated on various substrates with different magnification. (a) LPD-derived TiO₂ coating on UV/Ozone treated butyl rubber; (a)-2 zoom in picture in the white square area of (a); (b) LPD-derived TiO₂ coating on pristine cotton sheet; (b)-2 zoom in picture in the white square area of (b); (c) LPD-derived TiO₂ coating on prianha solution treated silicon wafer; (c)-2 zoom in picture in the white square area of (c); (a)-4 EDX result corresponding to (a)-2, carbon comes from the butyl rubber substrate, and fluorine comes from the LPD solution, Pt comes from the deposited conductive Pt layer.

The LPD-derived TiO₂ coating presented good adhesion to the rubber substrate. The optical microscopy image shown in Fig. 4-2 displays the morphology changes after tape test for two cycles. A large part of the TiO₂ coating film showed integrity after tape test except the white circle area marked in the picture.

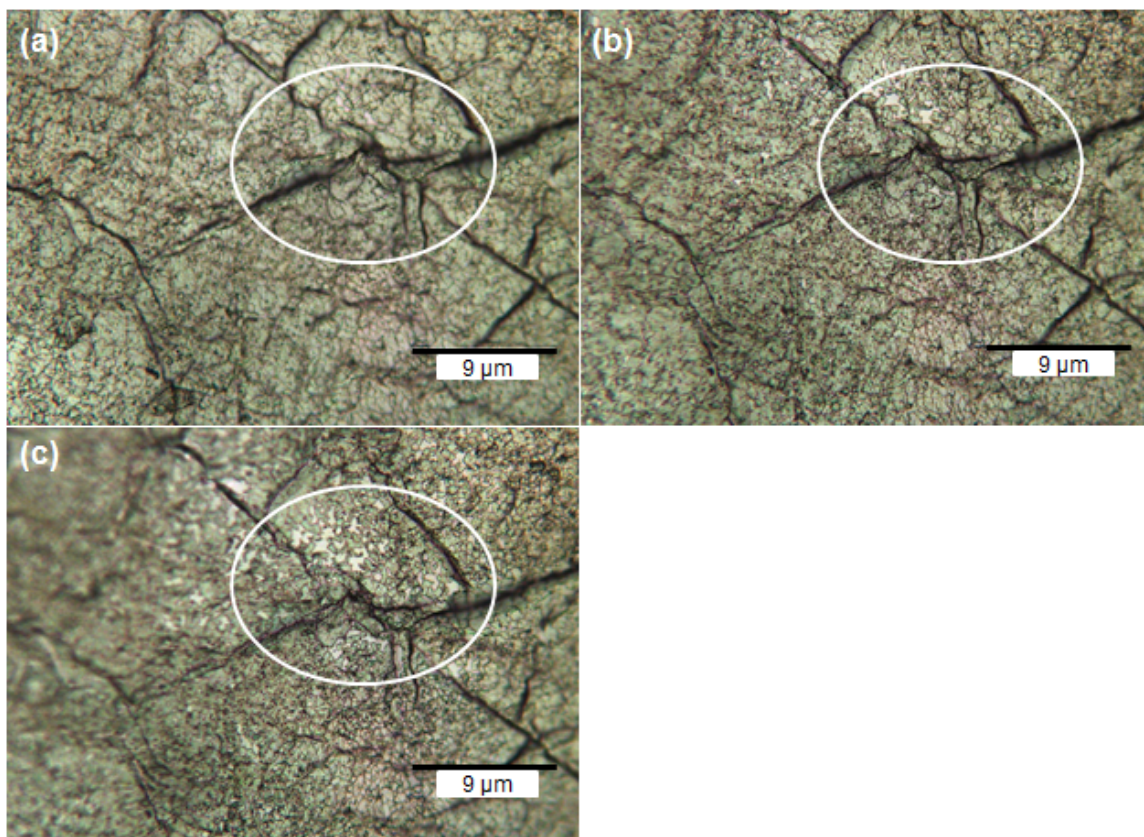


Figure 4-2: Optical microscopy of TiO₂ coated on butyl rubber substrates after tape test. (a) LPD-derived TiO₂ coating on UV/Ozone treated butyl rubber, (b) after tape test once, (c) after tape test twice. The circle area showed the changes after tape test.

The XRD patterns of the TiO₂ coating films on butyl rubber surface are presented in Fig. 4-3. As shown in Fig. 4-3 (a), the pattern presented well-defined peaks for both butyl rubber and TiO₂ coating film. The broad peak of 2θ around 17° was attributed to the amorphous phase of butyl rubber [34]. The two diffraction peaks at 30° and 44.4° were assigned to the anatase (101) facets and (004) facets, respectively, indicating that the crystalline of TiO₂ formed on the butyl rubber surface is in anatase structure [35]. To confirm the crystal structure, the XRD pattern of precipitates collected from precursor solution after reaction also was given in Fig. 4-3 (b). The diffraction peaks of the precipitates identified the obtained TiO₂ as anatase crystal.

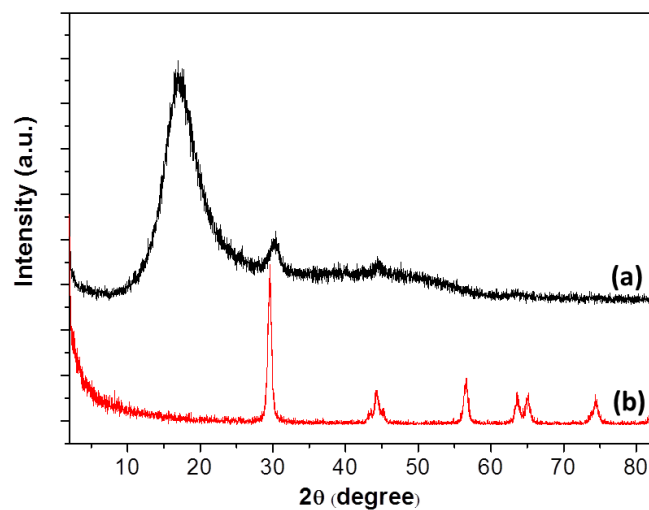


Figure 4-3: The XRD patterns of (a)TiO₂ coating on butyl rubber surface and (b) TiO₂ powders collected from precipitates from LPD method.

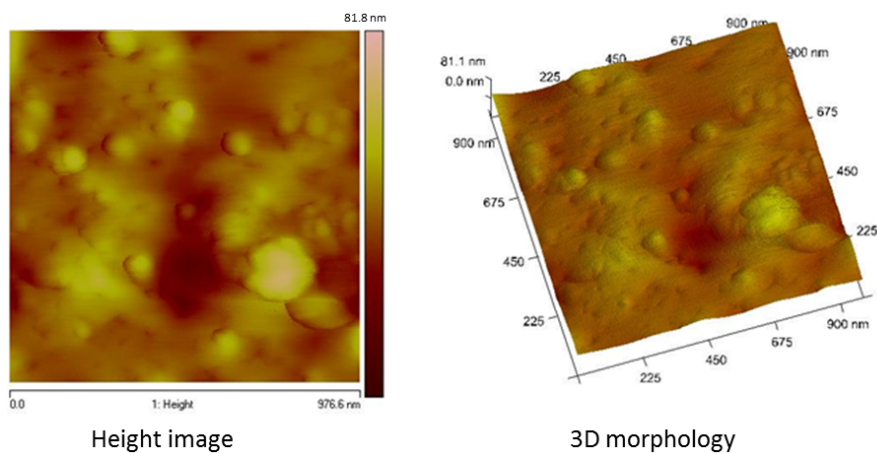


Figure 4-4: AFM images of 3D morphology and height images of the TiO₂ coating on a butyl rubber surface deposited by the LPD method.

The film morphology was further characterized by AFM. 3D morphology images of the TiO₂ thin film deposited on butyl rubber showed a uniform film coating composed of

densely packed sphere-like particles. It is consistent with the SEM results in higher magnification. The surface roughness, root mean square roughness was obtained from the AFM result. For the measured area of $1\mu\text{m}\times 1\mu\text{m}$, the R_q was as low as 3-9 nm. The LPD derived TiO_2 thin film by current deposition parameter showed quite smooth surface morphology.

4.3.3 Morphology control by addition of seeds

Fig. 4-5 shows a set of SEM images of TiO_2 crystallites grown on the silicon wafer surface in the presence of seed at a concentration of $0.3\mu\text{g mL}^{-1}$. At the early growth period (6h), sphere-like TiO_2 crystallites with diameter of $1.2\mu\text{m}$ attached on the substrate. As the reaction continued, the number of the sphere-like islands increased and the TiO_2 crystallites merged together to form the monolayer structure. But they did not cover the whole surface. It was also seen that individual hemisphere TiO_2 crystallites randomly distributed on the top of first monolayer. The hemispherical deposition on substrate surface has been observed in LPD-derived TiO_2 film by other researchers when nucleation sites density on the substrate is low [27]. No uniform film coating was observed after 12 h reaction. It is noticed that the deposition solution became cloudy after the reaction occurs and TiO_2 particles precipitated in bulk in the reaction solution. The sedimentation of TiO_2 particles formed cluster in the presence of seed also reduced the film formation on the substrate surface.

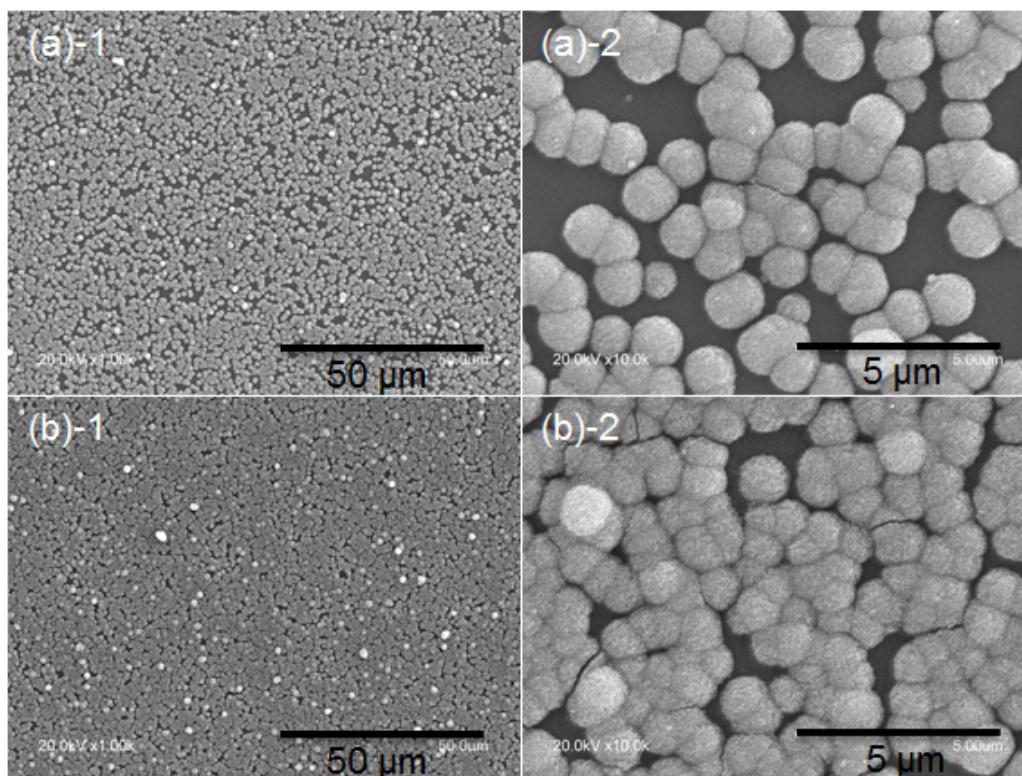


Figure 4-5: SEM micrographs of the silicon wafer surface immersed in 0.05 M $(\text{NH}_4)_2\text{TiF}_6$ and 0.15 M H_3BO_3 solution with seed of $0.3 \mu\text{g mL}^{-1}$ at 50°C after (a) 6 h and (b) 12 h.

4.3.4 Effect of the amount of additives

Fig. 4-6 compared the SEM micrographs of the silicon wafer surface immersed in 0.05 M $(\text{NH}_4)_2\text{TiF}_6$ and 0.15 M H_3BO_3 solution at $\text{pH} = 2.88$ with and without various seed concentration for 12 h. It is observed that closely packed TiO_2 particles formed coatings on the substrate surface in the solution without adding any seeds. While for the deposition solution with seed, no film but isolated islands with the diameter around $1.2 \mu\text{m}$ appeared which is similar to the morphology observed in Fig. 4-4 (b). It is noticed that the excellent monodispersed sphere-like TiO_2 particles appeared on the substrate immersed in the solution with $0.4 \mu\text{g mL}^{-1}$ seed. No noticeable differences on the surface morphology have been observed by increased the seed concentration from $0.4 \mu\text{g mL}^{-1}$ to

$3 \mu\text{g mL}^{-1}$. However, it is reported that excess addition of the seed would cause the agglomeration of the seed crystals and reduce the amount of deposition [28].

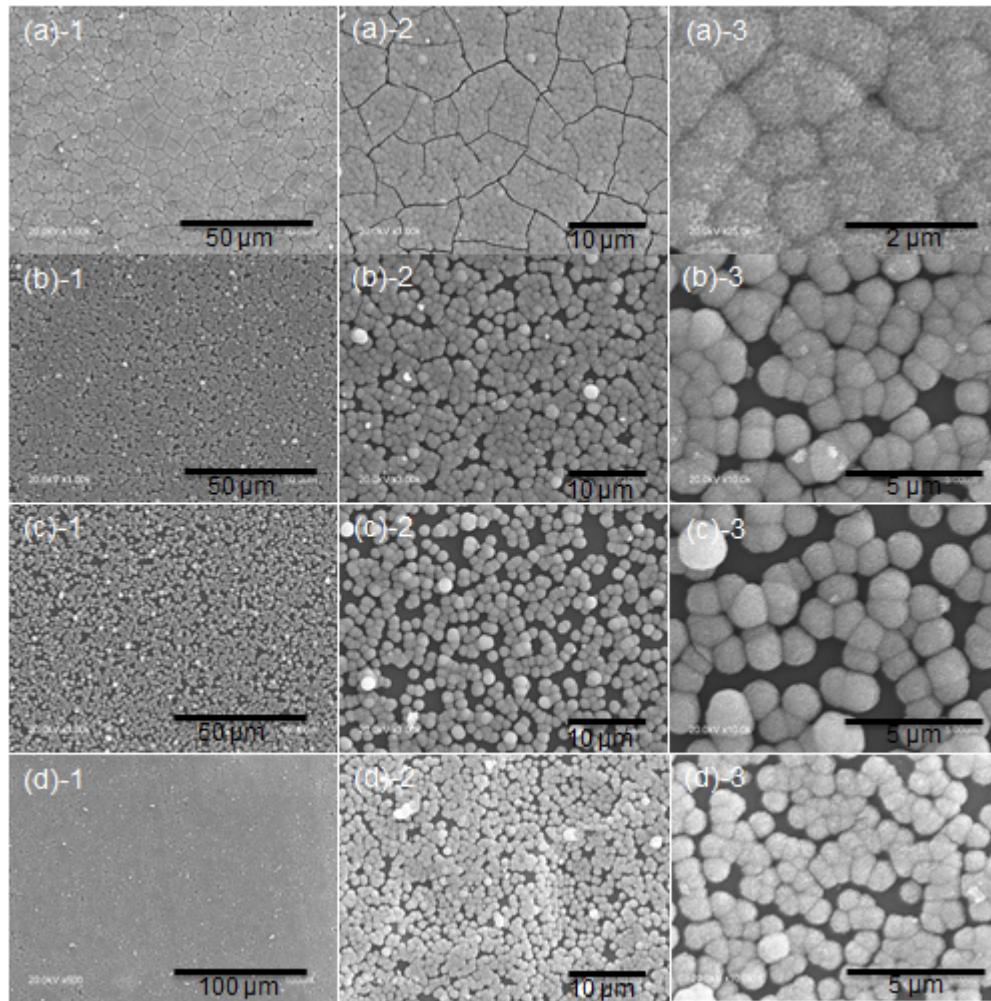


Figure 4-6: SEM micrographs of the silicon wafer substrates immersed in 0.05 M $(\text{NH}_4)_2\text{TiF}_6$ and 0.15 M H_3BO_3 solution at 50 °C for 12 h with or without various concentration of seed (a) without seed, (b) with seed $0.15 \mu\text{g mL}^{-1}$, (c) with seed $0.4 \mu\text{g mL}^{-1}$, (d) with seed $3 \mu\text{g mL}^{-1}$.

4.3.5 Effect of the surface property of additives

LPD derived TiO_2 film on substrate depended heavily on the wettability and surface charge of the substrate. For hydrophilic surface, due to the large number of nuclei growth density, TiO_2 nuclei gradually grew up to form a layer of particles contacting to each other and then formed film. In contrast, isolated particles distributed on the substrate due to low nuclei growth density on the hydrophobic substrate surface. It is also reported that LPD-derived TiO_2 coating formed excellent adherence on negatively charged surfaces [23]. TiO_2 crystallites formed by LPD method at $\text{pH}=2.88$ have positive surface charge density [23] which favour to adhere to surfaces with negative surface charge due to electrostatic attraction. In current paper, all the piranha solution treated silicon wafer surfaces were blown dry in N_2 atmosphere before soaked in the deposition solution. No uniform TiO_2 film was observed on the surface in the presence of seeds. Instead, silicon substrates were partially covered by hemispherical TiO_2 crystallites. The addition of seeds to the deposition solution increased the solid-liquid interfaces in the reaction solution, which enhanced the nucleation of TiO_2 in the solution and reduced the nuclei growth on the substrate surfaces. We further investigated the surface morphology of the derived coating in the presence of modified seed in the deposition solution with the same solution concentration. It can be observed that the silicon wafer substrate was almost fully covered by LPD-derived TiO_2 film in the deposit solution with PEI modified seed. While for the substrate exposed to the solution with PAA modified seed, sphere-like TiO_2 particles with the diameter around $1 \mu\text{m}$ distributed on the surface. PEI modified seeds contained positive surface charge, which facilitated the attachment of nucleation on the substrate surface. In contrast, PAA modified seeds contained negative surface charge which enriched the nucleation sites on seed surface, resulting in less film coating on the substrate. Fig.4-7 showed the surface morphology of the LPD derived coating with the addition of seed modified by basic polymer PEI and acid polymer PAA, respectively.

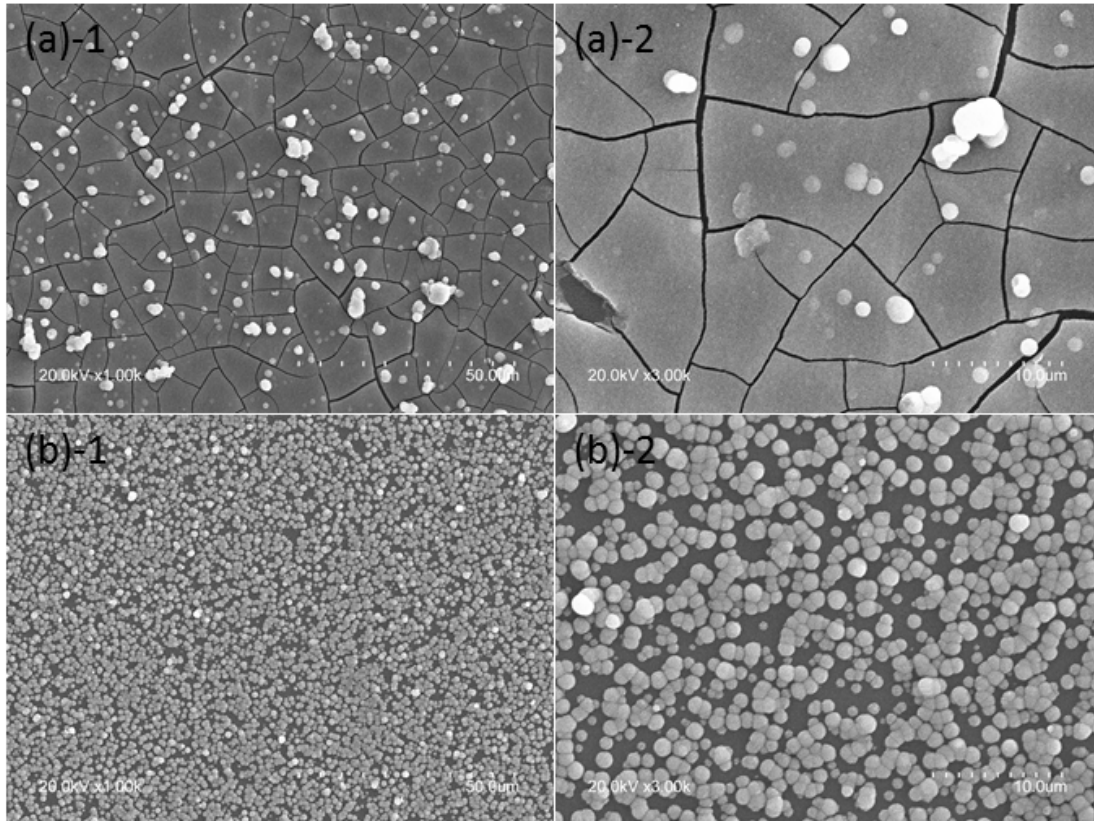


Figure 4-7: SEM micrographs of the silicon wafer surface immersed in 0.05 M $(\text{NH}_4)_2\text{TiF}_6$ and 0.15 M H_3BO_3 solution at 50 °C for 12 h with (a) PEI modified seed at $2 \mu\text{g mL}^{-1}$ (b) PAA modified seed at $2 \mu\text{g mL}^{-1}$.

4.3.6 Customized the LPD-derived TiO_2 coating in the presence of seed

Fig.4-8 shows the typical morphology of the sphere-like TiO_2 crystallites on the substrates at high magnification. Clearly, sphere-like TiO_2 crystallites were formed by small crystallites around 50 nm. We also studied the morphology of the TiO_2 precipitates by collecting the sediment in the deposition solution after reaction through centrifugation for 20 min at 4000 rpm. Fig.4-9 showed the typical SEM micrographs of the TiO_2 crystallites formed cluster in sedimentation. Microscale TiO_2 particles were formed by nanoscale TiO_2 crystallites which possess a nano-scale secondary structure at high

magnification. And the microscale TiO_2 particles further formed cluster structures, forming hierarchical structure.

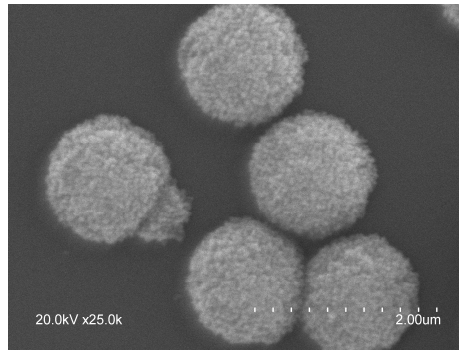


Figure 4-8: Typical SEM micrographs of sphere-like TiO_2 crystallites on the silicon wafer surface.

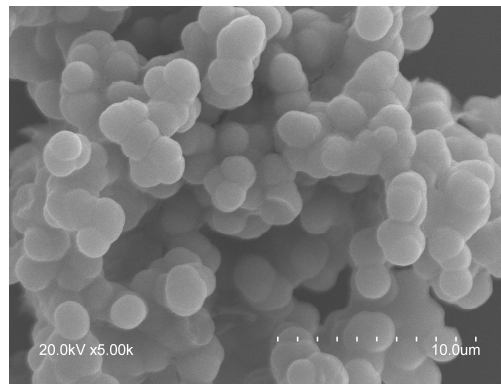


Figure 4-9: Typical SEM micrograph of TiO_2 crystallites formed clusters in sedimentation.

In order to introduce the hierarchical structure on the top of the substrate surface, the piranha solution treated silicon wafer immersed in the deposition solution was tilted certain degree from vertical line with the deposit side faced up. Fig.4-9 shows the surface morphology after the deposition reaction for 6 h. Similar cluster structure has been reported by Zhang et al [36] with different precursor solution composition. However, in our system, the presence of seed was used only to facilitate the nucleation growth in the liquid phase in stead of being embeded at the interface of substrate. The formation of

cluster by TiO_2 crystallite was driven by gravity. No evidence was found that seed crystals involved in the formation of clusters either by adding 1-D TiO_2 nanopartilces or 2-D SiO_2 rods.

4.3.7 Surface wettability

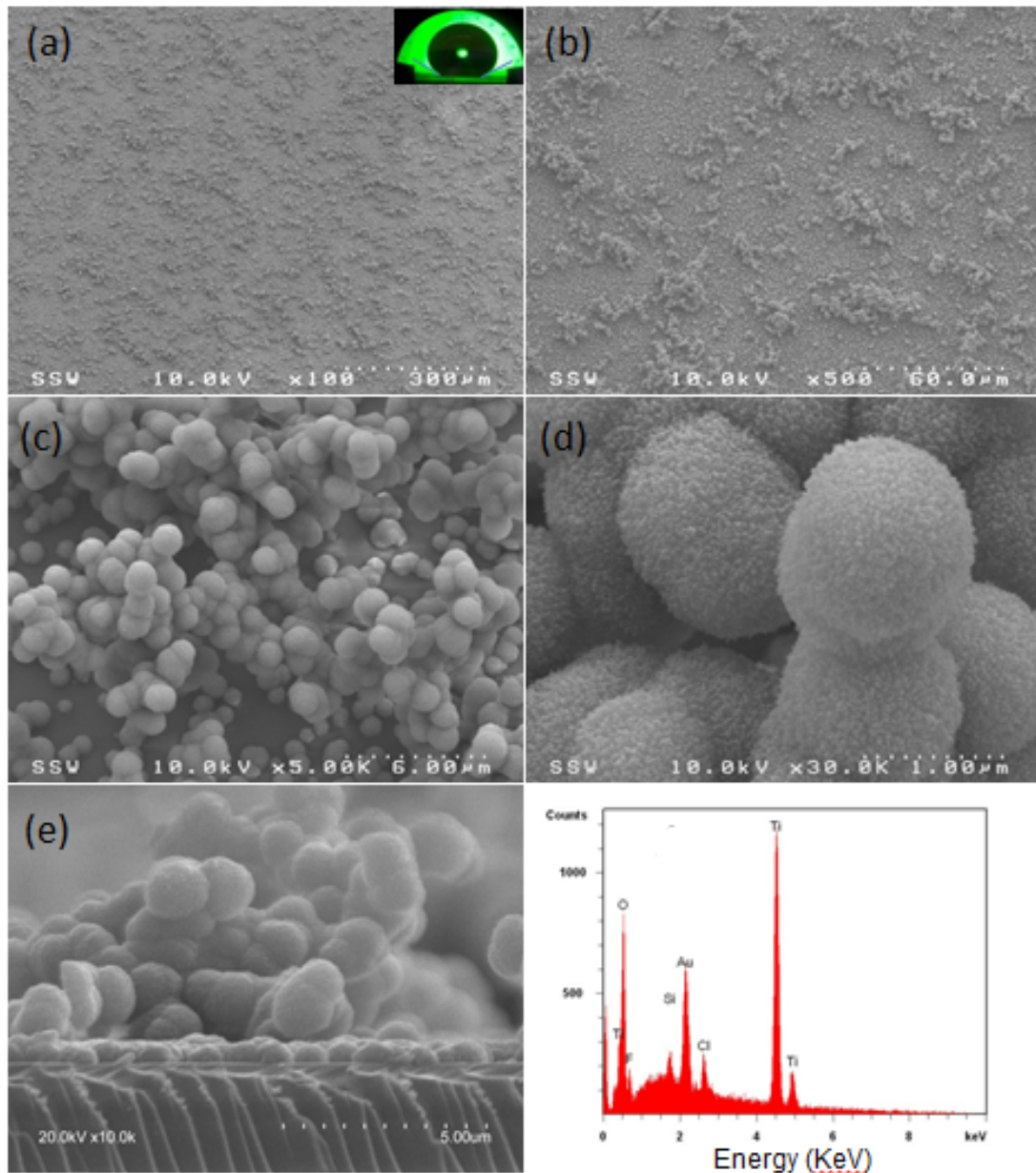


Figure 4-10: SEM micrographs of the fluorinated silicon wafer surface with coating which immersed in 0.05 M $(\text{NH}_4)_2\text{TiF}_6$ and 0.15 M H_3BO_3 solution at 50 °C for 6 h

with seed at $1\mu\text{g mL}^{-1}$. Optical image of the hexadecane contact angle is inserted in the top-right corner of the SEM images. (a)-(d) The top view of the surface coating with different magnification. (e) The cross-section view of the TiO_2 particles formed cluster structure. EDX result showed the chemical composition of the cluster.

The surface wettability of the prepared TiO_2 coating with and without hierarchical structure on silicon wafer surface has been studied by contact angle (CA) and sliding angle (SA) measurements. Fig. 4-10 shows the contact angle for hexadecane of the sample fluorinated with PFTS, the contact angle value of hexadecane increased up to 157° , which demonstrated a superoleophobic surface. Water droplets hardly stick to the surface and would roll off quite easily even without incline the surface. In comparison, the coating surface without hierarchical structure after the same fluorination treatment showed complete wet state by hexadecane droplet, although the contact angle for water droplet was around 130° . The pristine LPD-derived TiO_2 coating surface is hydrophilic, which attributed to the hydrophilic property of the TiO_2 crystallites. The droplet of water immediately wet the surface when contact to the bare surface. As illustrated above, hierarchical TiO_2 cluster consisting of microscale particles with nanoscale texture formed surface. The cluster also showed microscale pores among several particles instead of dense packed structure. The superoleophobic properties of the samples after surface decoration with low surface energy group indicated that the hierarchical structure containing micro-pores play important role in the enhancement of contact angle of droplet with low surface tension.

There exist two main configurations on wetting states when a liquid droplet deposited on a solid surface modified with hydrophobic texture, Wenzel state, which describes a complete wetting of the surface including partial nanostructure and Cassie-Baxter state, defines partial wetting due to air trapped in the rough area. In our present study, the fluorinated LPD-derived TiO_2 coating with hierarchical structure exhibited non-wetting property and excellent repellence towards hexadecane droplet, indicating Cassie-Baxter state exist in the system.

4.3.8 Bacterial adhesion activity of the LPD-derived TiO₂ coating

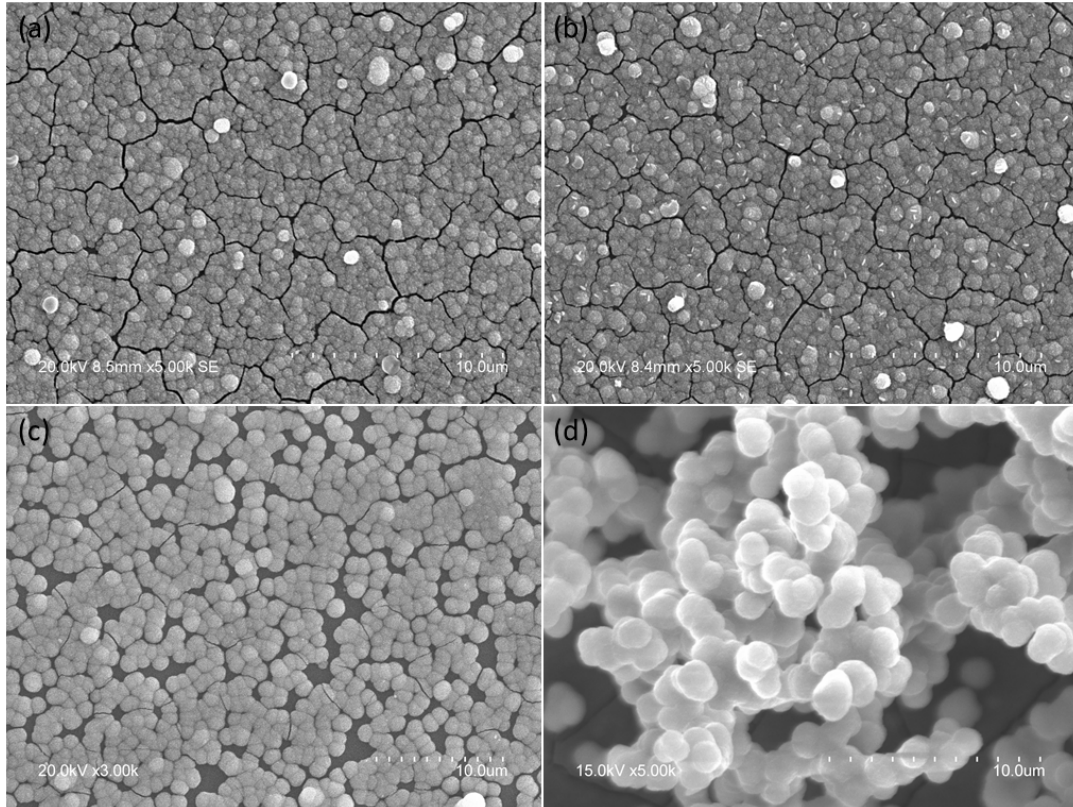


Figure 4-11: Representative SEM micrographs of the silicon wafer substrates with LPD-derived TiO₂ coating after 6 h incubation in *E. coli* suspensions: (a) pristine LPD-derived TiO₂ coating deposited for 6 h without seed, (b) fluorinated pristine LPD-derived TiO₂ coating deposited for 6 h without seed, (c) LPD-derived TiO₂ coating deposited for 12 h with seed, (d) fluorinated LPD-derived TiO₂ coating with hierarchical structure.

E. coli, which is a Gram-negative bacterium, was used as a model bacterium to evaluate the surface bacterial adhesion property of the prepared samples. Since extensive research has been established on the strong photoredox-based bacteria-killing ability of titanium dioxide, only bacterial adhesion on the prepared surface has been investigated in this

chapter. Fig.4-11 shows the preliminary bacterial adhesion results. All samples were immersed in an E.coli suspension (10^8 CFU mL⁻¹) for 6 h. It is obvious that E. coli bacteria appeared on fluorinated LPD-derived TiO₂ coating surfaces. In contrast, for pristine LPD-derived TiO₂ coating surfaces and fluorinated LPD-derived TiO₂ coating surfaces with hierarchical structures, E. coli bacteria were seldom observed. It is reported that substratum surface roughness, hydrophilic/hydrophobic property of the substrate and electrostatic interactions are key factors to govern the extent of bacterial adhesion [37-39]. Pristine LPD-derived TiO₂ coatings have hydrophilic surface wettabilities, and have negative surface charges in PBS solution, which discourage the adhesion of bacteria carrying a net negative surface charge [40]. For the fluorination modified surface, fluorine moiety on the particle surface shielded negative surface charge. Plus the fluorinated TiO₂ coating without hierarchical structure demonstrated hydrophobic properties, which promoted the bacteria adhesion. While for the fluorinated LPD-derived TiO₂ coating with hierarchical structure, the entrapped air among the dual-scale surface texture and micro-scale pores limited the effective contact area for bacteria adhesion. Other bacterial strains demonstrating adhesion and subsequent growth behavior on the resulting superoleophobic surface will be investigated in future studies.

4.4 Conclusions

Crystalline TiO₂ films have been successfully deposited on butyl rubber, cotton sheets and silicon wafer substrates through LPD method in mild environments. Fabrication of LPD-derived TiO₂ coatings on various substrate surfaces with seed dispersed in deposition solution allowed resultant surface structure to be tailored. After surface fluorination, the LPD-derived TiO₂ coating surface with hierarchical structure showed superoleophobicity due to the dual-scale surface roughness and entrapped air among the structure and low surface energy decoration. Both pristine and superoleophobic TiO₂ coating displayed antibacterial adhesion property. More antifouling tests will be investigated in future work. The LPD-derived TiO₂ coatings are highly customized which have the potential application biomedical engineering fields such as biosensors.

4.5 References

- [1] Park KD, Kim YS, Han DK, Kim YH, Lee EHB, Suh H, et al. Bacterial adhesion on PEG modified polyurethane surfaces. *Biomaterials*. 1998;19:851-9.
- [2] Chapman RG, Ostuni E, Liang MN, Meluleni G, Kim E, Yan L, et al. Polymeric thin films that resist the adsorption of proteins and the adhesion of bacteria. *Langmuir : the ACS journal of surfaces and colloids*. 2001;17:1225-33.
- [3] Kingshott P, Wei J, Bagge-Ravn D, Gadegaard N, Gram L. Covalent attachment of poly(ethylene glycol) to surfaces, critical for reducing bacterial adhesion. *Langmuir : the ACS journal of surfaces and colloids*. 2003;19:6912-21.
- [4] Makhluif S, Dror R, Nitzan Y, Abramovich Y, Jelinek R, Gedanken A. Microwave-assisted synthesis of nanocrystalline MgO and its use as a bactericide. *Advanced Functional Materials*. 2005;15:1708-15.
- [5] Applerot G, Perkas N, Amirian G, Girshevitz O, Gedanken A. Coating of glass with ZnO via ultrasonic irradiation and a study of its antibacterial properties. *Appl Surf Sci*. 2009;256:S3-S8.
- [6] Fujishima A, Zhang XT, Tryk DA. TiO₂ photocatalysis and related surface phenomena. *Surf Sci Rep*. 2008;63:515-82.
- [7] Sunada K, Watanabe T, Hashimoto K. Studies on photokilling of bacteria on TiO₂ thin film. *J Photochem Photobiol A-Chem*. 2003;156:227-33.
- [8] Sunada K, Kikuchi Y, Hashimoto K, Fujishima A. Bactericidal and detoxification effects of TiO₂ thin film photocatalysts. *Environmental science & technology*. 1998;32:726-8.
- [9] Maness PC, Smolinski S, Blake DM, Huang Z, Wolfrum EJ, Jacoby WA. Bactericidal activity of photocatalytic TiO₂ reaction: Toward an understanding of its killing mechanism. *Applied and environmental microbiology*. 1999;65:4094-8.

- [10] Seifried S, Winterer M, Hahn H. Nanocrystalline titania films and particles by chemical vapor synthesis. *Chem Vapor Depos.* 2000;6:239-44.
- [11] Stathatos E, Lianos P, DelMonte F, Levy D, Tsiourvas D. Formation of TiO₂ nanoparticles in reverse micelles and their deposition as thin films on glass substrates. *Langmuir : the ACS journal of surfaces and colloids.* 1997;13:4295-300.
- [12] Lakshmi BB, Dorhout PK, Martin CR. Sol-gel template synthesis of semiconductor nanostructures. *Chem Mat.* 1997;9:857-62.
- [13] Carp O, Huisman CL, Reller A. Photoinduced reactivity of titanium dioxide. *Progress in Solid State Chemistry.* 2004;32:33-177.
- [14] Nagayama H, Honda H, Kawahara H. A new process for silica coating. *J Electrochem Soc.* 1988;135:2013-6.
- [15] Hishinuma A, Goda T, Kitaoka M, Hayashi S, Kawahara H. Formation of silicon dioxide films in acidic solutions. *Appl Surf Sci.* 1991;48-9:405-8.
- [16] Deki S, Aoi Y, Hiroi O, Kajinami A. Titanium(IV) oxide thin films prepared from aqueous solution. *Chem Lett.* 1996:433-4.
- [17] Niesen TP, De Guire MR. Review: Deposition of ceramic thin films at low temperatures from aqueous solutions. *J Electroceram.* 2001;6:169-207.
- [18] Tsukuma K, Akiyama T, Imai H. Liquid phase deposition film of tin oxide. *J Non-Cryst Solids.* 1997;210:48-54.
- [19] Deki S, Aoi Y, Okibe J, Yanagimoto H, Kajinami A, Mizuhata M. Preparation and characterization of iron oxyhydroxide and iron oxide thin films by liquid-phase deposition. *J Mater Chem.* 1997;7:1769-72.
- [20] Yu JG, Xiong JF, Cheng B, Liu SW. Fabrication and characterization of Ag-TiO₂ multiphase nanocomposite thin films with enhanced photocatalytic activity. *Appl Catal B-Environ.* 2005;60:211-21.

- [21] Gao YF, Masuda Y, Peng ZF, Yonezawa T, Koumoto K. Room temperature deposition of a TiO_2 thin film from aqueous peroxotitanate solution. *J Mater Chem.* 2003;13:608-13.
- [22] Masuda Y, Sugiyama T, Seo WS, Koumoto K. Deposition mechanism of anatase TiO_2 on self-assembled monolayers from an aqueous solution. *Chem Mat.* 2003;15:2469-76.
- [23] Pizem H, Sukenik CN. Effects of substrate surface functionality on solution-deposited titania films. *Chem Mat.* 2002;14:2476-85.
- [24] Wamser CA. Equilibria in the system boron trifluoride-water at 25-degrees. *Journal of the American Chemical Society.* 1951;73:409-16.
- [25] Gao YF, Masuda Y, Yonezawa T, Koumoto K. Site-selective deposition and micropatterning of SrTiO_3 thin film on self-assembled monolayers by the liquid phase deposition method. *Chem Mat.* 2002;14:5006-14.
- [26] Gao YF, Masuda Y, Koumoto K. Microstructure-controlled deposition of SrTiO_3 thin film on self-assembled monolayers in an aqueous solution of $(\text{NH}_4)_2\text{TiF}_6\text{-Sr}(\text{NO}_3)_2\text{-H}_3\text{BO}_3$. *Chem Mat.* 2003;15:2399-410.
- [27] Dutschke A, Diegelmann C, Lobmann P. Nucleation and growth of TiO_2 thin films on modified polystyrene surfaces. *Chem Mat.* 2003;15:3501-6.
- [28] Ozawa N, Kumazawa Y, Yao T. Effect of seed crystal and composition of solution on the formation of TiO_2 thin film from aqueous solution. *Thin Solid Films.* 2002;418:102-11.
- [29] Jin M, Zhang X, Emeline AV, Numata T, Murakami T, Fujishima A. Surface modification of natural rubber by TiO_2 film. *Surf Coat Technol.* 2008;202:1364-70.
- [30] Pizem H, Gershevitz O, Goffer Y, Frimer AA, Sukenik CN, Sampathkumaran U, et al. Titania deposition on PMR-15. *Chem Mat.* 2005;17:3205-13.

- [31] Ma B, Goh GKL, Ma J, White TJ. Growth kinetics and cracking of liquid-phase-deposited anatase films. *J Electrochem Soc.* 2007;154:D557-D61.
- [32] Li D, Haneda H, Labhsetwar NK, Hishita S, Ohashi N. Visible-light-driven photocatalysis on fluorine-doped TiO₂ powders by the creation of surface oxygen vacancies. *Chem Phys Lett.* 2005;401:579-84.
- [33] Xu JJ, Ao YH, Fu DG, Yuan CW. Low-temperature preparation of F-doped TiO₂ film and its photocatalytic activity under solar light. *Appl Surf Sci.* 2008;254:3033-8.
- [34] Toki S, Sics I, Hsiao BS, Murakami S, Tosaka M, Poompradub S, et al. Structural developments in synthetic rubbers during uniaxial deformation by in situ synchrotron X-ray diffraction. *J Polym Sci Pt B-Polym Phys.* 2004;42:956-64.
- [35] Yu B, Leung KM, Guo Q, Lau WM, Yang J. Synthesis of Ag-TiO₂ composite nano thin film for antimicrobial application. *Nanotechnology.* 2011;22:115603.
- [36] Zhang M, Zhang T, Cui TH. Wettability Conversion from Superoleophobic to Superhydrophilic on Titania/Single-Walled Carbon Nanotube Composite Coatings. *Langmuir : the ACS journal of surfaces and colloids.* 2011;27:9295-301.
- [37] Ostuni E, Chapman RG, Holmlin RE, Takayama S, Whitesides GM. A survey of structure-property relationships of surfaces that resist the adsorption of protein. *Langmuir : the ACS journal of surfaces and colloids.* 2001;17:5605-20.
- [38] Li BK, Logan BE. Bacterial adhesion to glass and metal-oxide surfaces. *Colloid Surf B-Biointerfaces.* 2004;36:81-90.
- [39] Crawford RJ, Webb HK, Truong VK, Hasan J, Ivanova EP. Surface topographical factors influencing bacterial attachment. *Adv Colloid Interface Sci.* 2012;179:142-9.
- [40] Jucker BA, Harms H, Hug SJ, Zehnder AJB. Adsorption of bacterial surface polysaccharides on mineral oxides is mediated by hydrogen bonds. *Colloid Surf B-Biointerfaces.* 1997;9:331-43.

Chapter 5

5 A novel method for engineering superoleophobic and conductive dual-functional coatings on flexible and stretchable substrates

5.1 Introduction

In the past few decades, the control of surface wetting has been studied extensively due to its scientific significance and the potential applications in a variety of areas, including self-cleaning [1] and anticorrosion [2] coatings. A surface is defined as “*superhydrophobic*”, if both the *advancing and receding* contact angles for an aqueous droplet exceed a value of about 140° [3]. Consequently, such a surface is also characterized by a low ($< 5^\circ$ - 20°) contact angle hysteresis (CAH). This definition is not rigorous, but it encompasses a common qualitative feature that aqueous droplets do not stick to *superhydrophobic* surface and easily roll off when the surface is tilted. The surface wetting properties are determined by both the chemical compositions and roughness of the surface. There are a large number of existed *superhydrophobic* surfaces in nature, such as the lotus leaf [4] and water strider’s legs [5], and artificial structures [6]. However, the “*superoleophobic*” surfaces that repel the hydrophobic liquids are still extremely rare [7].

A multitude of experimental strategies have been developed to produce superhydrophobic and/or superoleophobic surfaces. All of these strategies involved modifications of both the surface chemical compositions and roughness. An effective way to lower the surface energy is the introduction of fluorinated moieties to the surface by chemical or physical methods. However, simply fluorinating a surface will produce neither superhydrophobic nor superoleophobic coatings. Thus, most of research effort has been focused on creating intricate surface morphologies that have re-entrant or overhanging features [7-10], and multi-scale hierarchical structures [11-13]. For example, superoleophobic surfaces, which exhibit a contact angle greater than 150° , have been prepared by various techniques including electrochemical process [10, 14, 15], lithography [7, 9] and sol-gel [12].

However, most of these techniques are expensive and complex processes involving many fabrication steps, and therefore are difficult to scale up to coat large surface area.

Alternatively, spray coating technique, as a low-cost and convenient technique, has been widely used in industry. Considering applicability of the coating process in practice, we have developed our methods based on the spray coating technique. Recently, Steele et al. [16] described a method to fabricate superoleophobic surfaces by spray casting ZnO nanoparticles along with a waterborne perfluoroacrylic polymer. However, the stability of the resulting surface was not mentioned. Srinivasan et al. [17] prepared superoleophobic surfaces by a single step spraying poly(methyl methacrylate) (PMMA) and fluorodecyl POSS blends using the hydrochlorofluorocarbon solvent. According to the ASTM-3359 standard for adhesion testing, the coating showed poor adhesion. There is a need to prepare more robust coatings having superoleophobic characteristic alone or in combination with other functionality and good adhesion to the substrates.

Carbon black (CB) [18] is a form of amorphous carbon that has a high surface-area-to-volume ratio, only slightly lower than that of activated carbon which is commonly used in plastics, as reinforcement in tires, electronic packaging, printing inks and ultraviolet (UV) stabilization. CB is widely available and has advantages in cost and ease of mass production. The structure of CB makes it ideal for superoleophobicity because of its ability to agglomerate nanometers-sized primary carbon particles (nodules) into larger multiscale, grape-like structures up to 1 millimeter in size [19]. The multiscale aggregates are held together by van-der-Waals forces [20]. This tendency is especially pronounced for the most-fine-grained, so called “high structure” varieties of CB such as the one used in the present work.

Another important feature of CB is the presence of 6%–8% OH functionality on the surface of the agglomerates [21, 22]. These OH groups are important for bonding the perfluorosilane to the composite CB surfaces in order to lower the surface energy and produce superoleophobicity. Since primary CB particles are made from the small graphitic crystallites [19], all forms show some conductivity. Conductivity can also be enhanced by additional graphitization of CB.

It is the current technical trend of surface engineering to develop coatings with multi-function. To best of our knowledge, the invention reported here is the first simple, scalable and industry-applicable coating technology for making multifunctional surfaces that are both conductive and superoleophobic. To date there are only couples of studies that have developed coatings which potentially result in increases to both conductivity and superoleophobicity. Darmanin et al. [23, 24] used electropolymerization to deposit conductive polymer aggregates on flat surfaces and on patterned pillar structures. Wang et al. [25] used vapour-phase polymerization of polypyrrole in the presence of a fluorinated alkyl silane to deposit conductive coatings directly on fibrous substrates, thus also making them superoleophobic. There remains a need for less expensive materials and easier methods for preparing functional coatings having superoleophobic and conductive characteristics. Our spray method is indeed much simpler and more industrially applicable.

Thus, in this study, we provide an effective, simple and low-cost spray technique to fabricate CB-based coatings that are superoleophobic and conductive. The wettability and conductivity of the resultant composites may be easily tuned by varying the component loading. This superoleophobic coating has a multi-scale roughness ranging from nanometers up to micrometers. The crucial ingredient used to produce the multi-scale roughness is conductive CB, which consists of nanometer sized particles that are fused together to produce large aggregated particles. The coatings were deposited on flexible substrates and have the ability to preserve superoleophobicity even when strained to ~100%.

5.2 Experimental Section

5.2.1 Materials

Polyisoprene pellets (PIP, trans), hexane, tetrahydrofuran, hexadecane and 2,2-azobis(isobutyronitrile) (AIBN) were obtained from Sigma-Aldrich. 1H,1H,2H,2H-Perfluorodecyltrichlorosilane (PFTS) was obtained from Alfa Aesar. Conductive carbon black (CB, Vulcan XC 72) was purchased commercially from Cabot Corporation. All of

the chemicals were used in the as-received condition without further modification. Cured butyl rubber substrates were kindly provided by LANXESS Inc.

5.2.2 Preparation of Ultraviolet (UV) cross-linked coatings on butyl rubber surface

In a typical experiment to prepare sample P40C60, PIP was dissolved in hexane and ultrasonicated at room temperature for 1 hour to obtain a ~2 wt% solution. In a separate vial, the conductive CB was dispersed in hexane and ultrasonicated for 1 h to yield a ~2 wt% suspension. The PIP solution and the CB suspension were blended together and further sonicated for at least 4 hours. No surfactants or dispersant were used currently. Note that the final concentration of the blended mixture (CB + PIP) was approximately 2 wt%, though the proportion between CP and PIP varied. The UV initiator AIBN was dissolved in 200 μ l tetrahydrofuran and added to the suspension before spraying at a concentration of 2% of molar ratio of polymer. The blends were sprayed on butyl rubber substrates using an airbrush (Badger, Model 350-1H) connected to a compressed nitrogen tank (pressure 60 psi) (Fig. 5-1). Most of the coatings investigated in this study were produced by spraying 25 mL of the CB and PIP mixture on a 6 \times 6 cm² butyl rubber substrate. The coated substrates were then left in a chemical fume hood overnight at room temperature to remove any residual solvent. The air dried coatings were then exposed to ultraviolet light (365 nm) for 20 minutes to initiate the cross-linking. The cross-linked samples were then placed in a glass bottle in order to deposit the PFTS on them via chemical vapour deposition (CVD). A total of 20 μ l of PFTS was dropped in the glass bottle, sealed and then placed for 30 minutes in an oven at 75 °C.

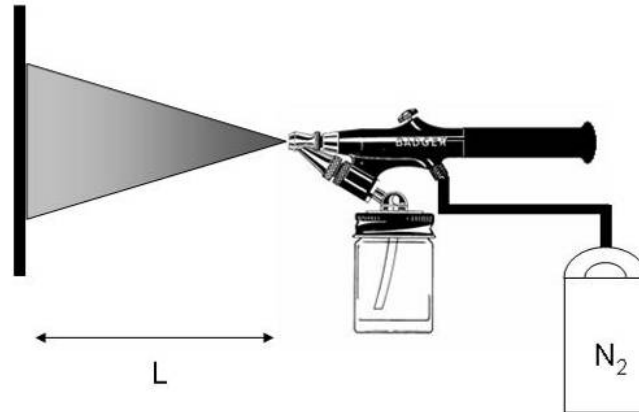


Figure 5-1: Schematic illustration of the spray apparatus. The spray distance (L) is 15 cm and the pressure P is 60 psi under room temperature ($T=25\text{ }^{\circ}\text{C}$) and a range of relative humidity (RH: 40-50%).

5.2.3 Wettability Test

Sessile droplet contact angles were measured in ambient air at room temperature using a contact angle goniometer (Model 100-00). Two low surface energy liquids were used for contact angle measurements (1) hexadecane and (2) methanol.

5.2.4 Tensile Testing

For uniaxial stretching, the coatings were sprayed on flexible butyl rubber substrates, followed by the cross link and fluorination process. The substrates were then mounted between two linear clamps and stretched to a maximum of 100% strain. This is the limit of our manual stretch testing device.

5.2.5 Surface Characterization

The surface morphology of the coatings was assessed using a Hitachi S-4500 Scanning Electron Microscope (SEM). The samples were sputter-coated with a thin layer of platinum prior to examination in order to minimize sample charging. Cross-sections of

the samples were also prepared by freeze fracturing. The samples were immersed in liquid nitrogen for 5 min and then fractured by bending. The fractured surfaces were then examined by SEM.

The outer surface was characterized using x-ray photoelectron spectroscopy (XPS) before and after tape testing. The XPS spectra were collected using a Kratos NOVA XPS from an area approximately $700 \times 300 \mu\text{m}^2$ in size, using a monochromatised Al- K_{α} x-ray beam. XPS is a very surface sensitive analytical technique, and it can provide compositional data from the outer 5-10 nm of a surface.

5.2.6 Conductivity Measurements

The electric characterization of the resulting coatings before and after fluorination via perfluorosilane was measured by the two-probe method [26] using a FLUKE 87 True RMS Multimeter. The electrical resistivity was calculated using the following equation:

$$\rho = R_s \times t \ (\Omega \text{ m}) \quad (1)$$

where ρ is the bulk resistivity and t is the thickness of coating. Sheet resistance (R_s , Ω) was measured at room temperature under ambient conditions. All experimental measurements were repeated >10 times on each coating sample to obtain average values.

5.3 Results and Discussion

5.3.1 Superoleophobic results for UV cross-linked coatings

The concentration of the PIP and CB solution is critical in controlling the morphology of the final surface produced by spraying. To investigate the effect of concentration on the surface morphology, we used four different solutions with various ratios of PIP to CB (50:50 wt%, 45:55 wt%, 40:60 wt% and 34:66 wt%) at a fixed total solute concentration of 12.5 mg mL^{-1} . The concentrations of PIP, CB, AIBN and hexane are presented in Table 1. Samples are labeled according to the weight ratio of PIP and CB (wt%). For example, P45C55 denotes 45 wt% of PIP and 55 wt% of CB.

Table 5-1: Concentration of solutions/dispersions for UV cured spray coatings.

Sample	Composition (wt%)			
	PIP	CB	AIBN	Hexane
P50C50	0.93	0.93	0.04	98.1
P45C55	0.84	1.02	0.04	98.1
P40C60	0.75	1.11	0.04	98.1
P34C66	0.63	1.24	0.03	98.1

The SEM images presented in Fig. 5-2 showed the morphology of the composite coatings sprayed on the butyl rubber substrates. At low magnification, the four different coatings have a similar morphology and consist of flat regions covered with micron sized agglomerates. However, at higher magnification the coatings containing higher CB concentrations show a more porous and finer structure when compared to the coatings with a lower CB concentration. Thus, by controlling the CB filler content we can control the morphology of the coating. At lower filler concentrations the CB agglomerates tended to be completely encased by the PIP matrix and the multiscale structure of the CB was masked. However, at higher CB concentrations, the CB particles formed microscale clusters, while the polyisoprene filled the interspaces and provided adhesion. These clusters provided the necessary micrometer-scale roughness, while the individual CB nanoparticles provide the nanoscale roughness. Such a hierarchical micro-to-nanoscale roughness is critical to produce superoleophobicity on natural and artificial surfaces. [5,6]

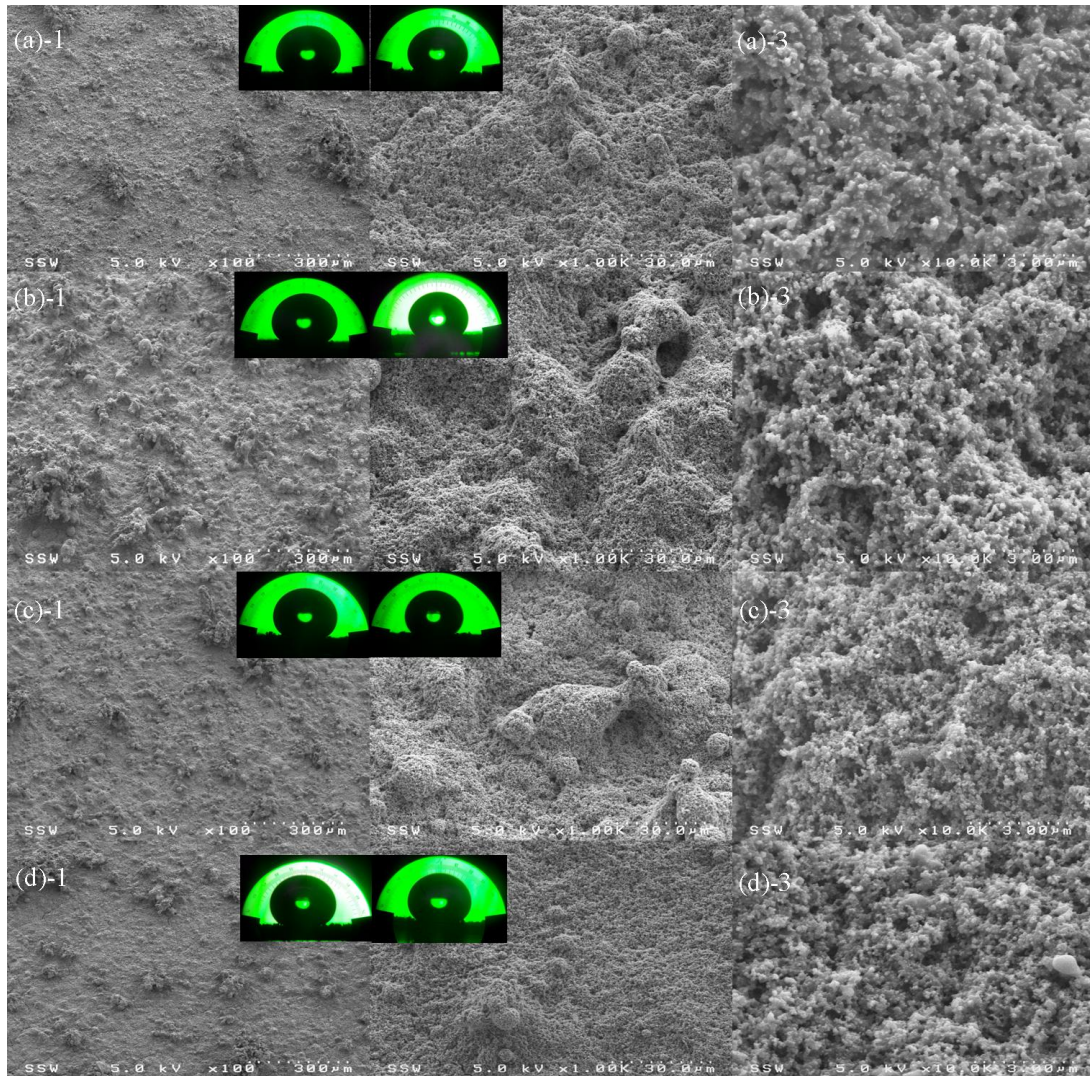


Figure 5-2: Representative SEM images at various magnifications showing the surface morphology of the UV cross-linked coatings with a solute concentration of 12.5 mg mL^{-1} . The solute concentrations are: (a) 50/50 wt% PIP/CB, (b) 45/55 wt% PIP/CB, (c) 40/60 wt% PIP/CB, and (d) 34/66 wt% PIP/CB. The insets are contact angle images of hexadecane (left) and methanol (right).

To illustrate the multiscale structures of the superoleophobic coatings, P45C55 was cross-sectioned (Fig. 5-3). A series of four SEM images show that the roughness ranged from several nanometers to hundreds of microns. Large aggregates dominated the landscape (several $100 \mu\text{m}$); however, due to the multiscale, hierarchical nature of CB, one can

observe the same hierarchical structure on nanometer scale (~ 100 nm). We presumed that the nanostructure was not a pure CB nodule, but an aggregate of several primary particles, since the CB used in our experiments has an average diameter of approximately 20 nm. Furthermore, the CB aggregates produced the “re-entrant or overhanging” feature (Fig. 5-3d) that is crucial for achieving superoleophobicity.

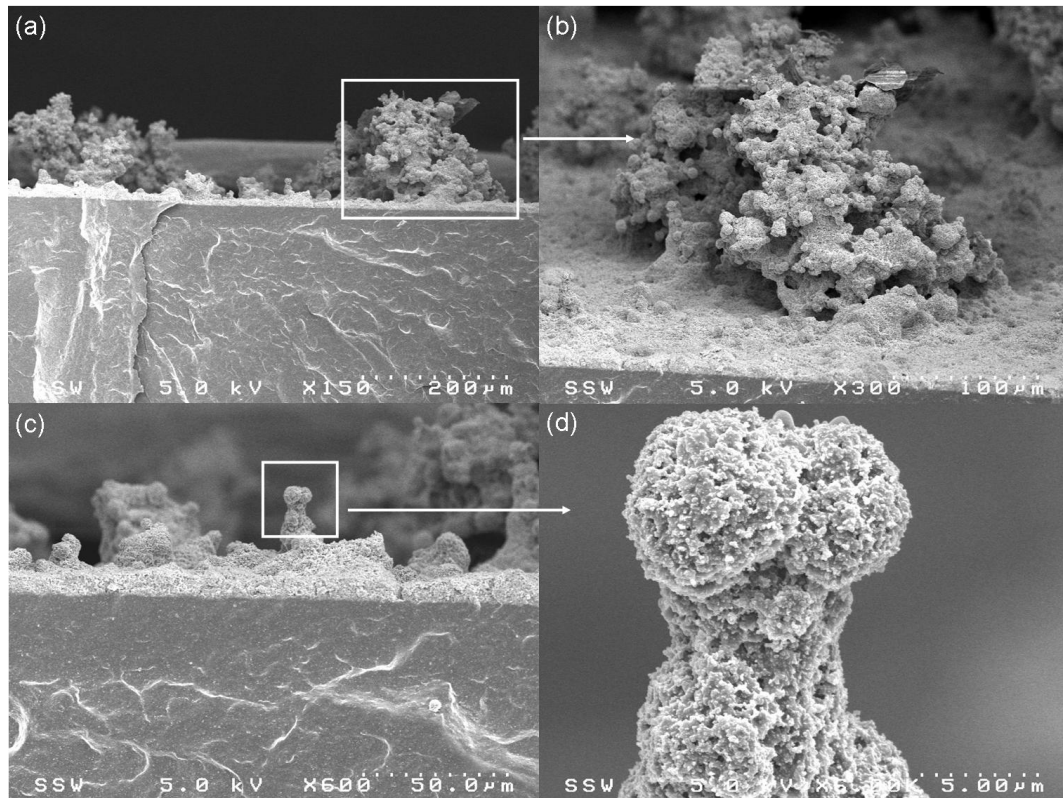


Figure 5-3: SEM images of the UV cross-linked superoleophobic coating (P45C55) in cross-section at different magnification increasing from left to right. The cross-section was produced by freeze-fracturing.

The addition of CB to the coating can affect surface wettability in two mechanisms. On one hand, the CB would influence the surface roughness of the resulting composite coatings; on the other hand, the CB provides abundant OH groups to bond the perfluorosilanes on the fluorinated coatings. The XPS high resolution C(1s) spectrum presented in Fig. 5-4 shows a peak at a binding energy of 286.5 eV that is attributed to C-

O-C and C-OH functionality. We cannot estimate the total OH contribution since we cannot distinguish between the two functional groups. However, we are confident that there are OH groups on the surface to help provide adhesion for fluorination.

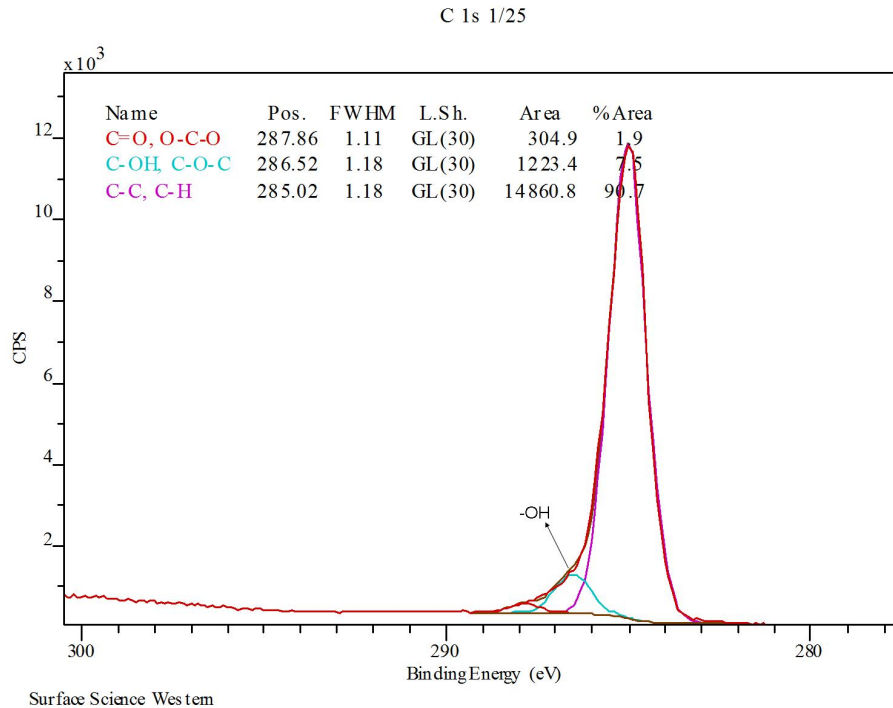


Figure 5-4: High resolution C (1s) spectrum of a spray coating containing 66% CB. Note the evidence of the –OH functionality on the surface.

Table 5-2 shows the static contact angle measurements of the composite coatings sprayed on butyl rubber as a function of CB concentration. It should be noted that for all the fluorinated samples, the water droplets roll off the samples immediately contact with the surface. It is clear that increasing the concentration of CB in the dispersion results in a corresponding increase in CA for both hexadecane and methanol. Sample P50C50 with the lowest CB concentration, has the lowest observed contact angle for hexadecane ($142 \pm 8^\circ$) and methanol ($122 \pm 6^\circ$), while sample P34C66 with the highest CB concentration has a hexadecane contact angle of $158 \pm 5^\circ$ and a methanol contact angle of $134 \pm 4^\circ$. Surface roughness and chemical composition have influence on the CA of the

corresponding surface. Thus, the samples with the lower CB concentration have the lower CA which is attributed to the lower surface roughness at the submicrometer scale and a higher overall surface energy due to fewer fluorination moieties. However, there is no significant difference in the contact angles for hexadecane and methanol between samples P40C60 and P34C66. For our coating system, the contact angle reaches a maximum value with a CB concentration of 60 % or higher. There is no advantage of increasing the CB concentration beyond this value therefore it is essential to maximize the amount of PIP in the final composite coating to ensure mechanical stability and stretch ability.

Table 4-2: Apparent contact angle of UV cross-linked spray coatings.

Sample	Contact Angle 10 μ L	
	Hexadecane	Methanol
P50C50	142 \pm 8	122 \pm 6
P45C55	153 \pm 2	134 \pm 2
P40C60	158 \pm 5	133 \pm 4
P34C66	158 \pm 5	134 \pm 4

As aforementioned, the volume of the suspension used for spraying plays an important role in the final surface morphology. To gain more insight on this issue, we sprayed 5, 15, 25 and 50 mL suspensions (12.5 mg mL⁻¹, P40C60) on a 6 \times 6 cm² butyl rubber substrate. After the same vapor fluorination process described above, the CA for hexadecane was measured. The samples prepared using a 5 mL of suspension showed a CA of 139 \pm 5 $^\circ$, while the samples prepared using a 15 mL of suspension showed a CA of 149 \pm 8 $^\circ$. Although samples made using the 15 mL suspension showed a high CA, the residue from the hexadecane droplet remained on the surface. Hexadecane droplet residue also remained on the samples made using the 5mL suspension. The residue indicates that the

hexadecane droplet cannot freely roll off on the surface. The samples prepared using a 25 and 50 mL of suspension both showed CA greater than 150° . At these volumes, we noted that the hexadecane droplets freely rolled off the surfaces without leaving any residual trail. The surface morphologies prepared from different suspension volumes were analyzed using SEM (Fig. 5-5). In general, the increase of the suspension volume could produce larger clusters as shown in the low magnification images. The two coatings using 25 and 50 mL suspension appeared to have a similar porous morphology ranged in micro-scale at higher magnifications. While the coatings made from 15 mL suspension showed relative flat morphology and less air was trapped which made the surface non-superoleophobic after fluorination.

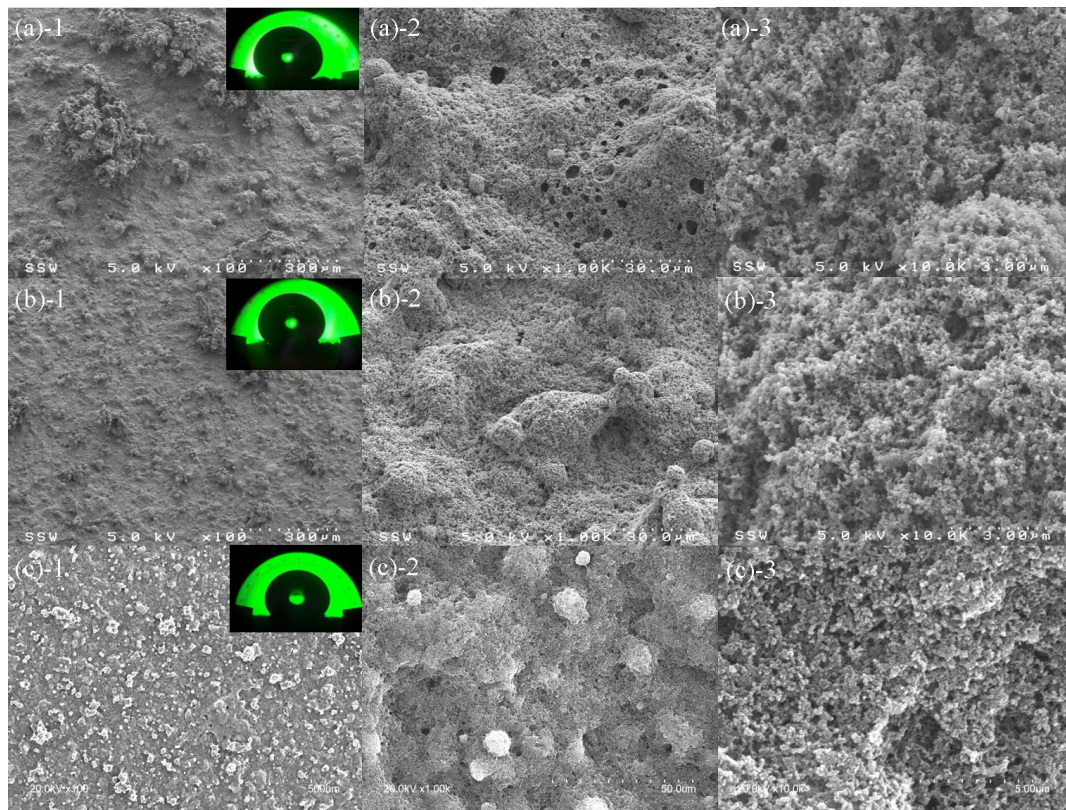


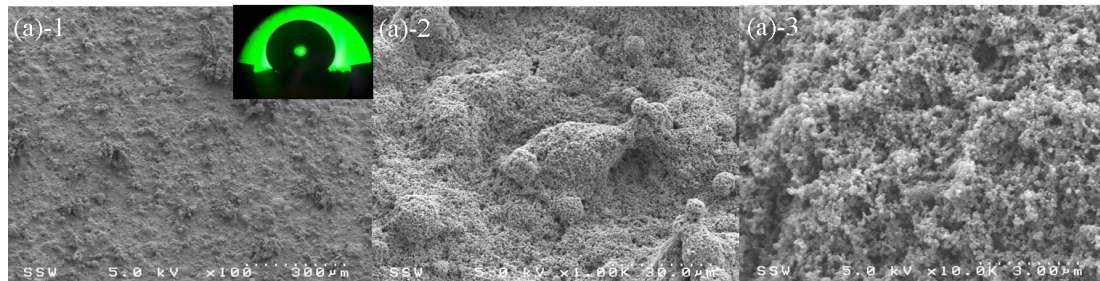
Figure 5-5: SEM images of UV cured coatings sprayed on $6 \times 6 \text{ cm}^2$ butyl rubber substrate (P40C60, 40/60 wt% PIP/CB blends, 12.5 mg mL^{-1}) using different suspension volumes: (a) 50 mL, (b) 25 mL and (c) 15 mL. Optical images of the

hexadecane contact angles are given as inserts in the top-right corner of the corresponding surface.

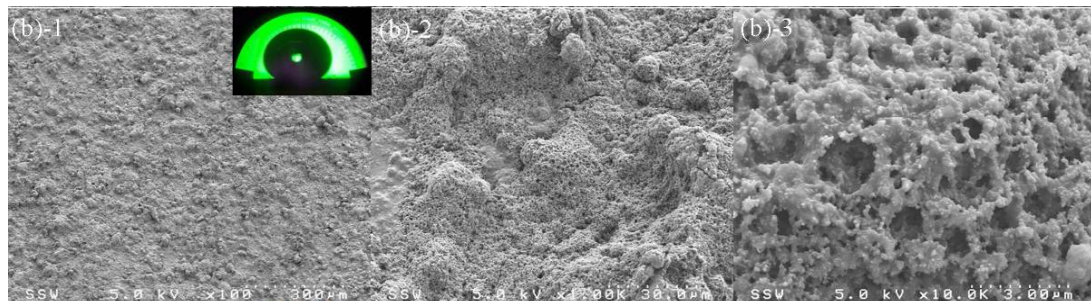
5.3.2 Adhesion of the UV Cross-linked Coatings

The adhesion of the fluorinated PIP-CB coatings was investigated using a simple tape test. Nichiban tape, typically used for automotive adhesion testing, was pressed onto the surface of the coating and then rapidly pulled away. The SEM images presented in Fig. 5-6 showing the surface morphology of two samples before and after tape test, (1) P40C60 UV cross-linked and (2) P40C60 un-cross-linked. The cross-linked (Fig 5-6 a-1) and un-cross-linked (Fig 5-7 c-1) samples have a similar surface morphology before the tape test.

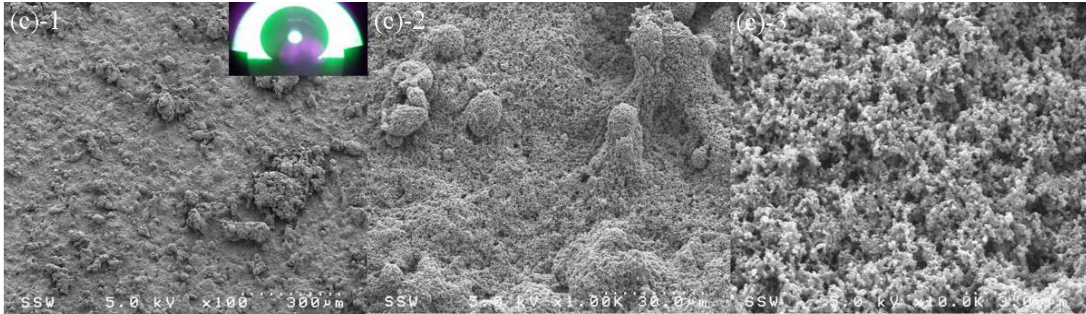
UV cured, before tape test



UV cured, after tape test



No UV curing, before tape test



No UV curing, after tape test



Figure 5-6: Different magnification SEM images showing the coating morphology before and after tape test. Sample P40 C60 (40/60 wt% PIP/CB blends, 12.5 mg mL⁻¹) was sprayed on 6×6cm² butyl rubber substrate using 25 mL of suspensions. (a) UV cured and before tape test; (b) UV cured and after tape test; (c) not UV cured and before tape test and (d) not UV cured and after tape test. Optical image of the hexadecane contact angles are inserted in the top-right corner of the SEM images.

After the tape test, most of the large clusters were removed from both samples leaving a relatively smooth surface, as seen at low magnification. At higher magnification, both samples show a loss of small nanoparticles. The physical removal of the large clusters and small nanoparticles affected the contact angle for both samples. Before the tape test, the UV cross-linked sample showed a hexadecane contact angle of $158 \pm 5^\circ$. After the tape test, the same sample remained superoleophobic with a lower contact angle of $150 \pm 5^\circ$. In addition, the droplet easily rolled off the surface without leaving any residual trail. The uncross-linked sample showed a significant change in the surface wettability. Before the

tape test the contact angle was $152\pm 2^\circ$, while after the tape test the contact angle decreased to $140\pm 2^\circ$ and the droplet was pinned on the surface. These results show that the coatings are durable and can maintain superoleophobicity after tape test.

5.3.3 Effect of cross-linking method on contact angle

We also investigated how two different methods of cross-linking affected the surface morphology and contact angle. The SEM images presented in Fig. 5-7 compared a coating cross-linked using UV light for 20 min and a coating cross-linked using HHIC for 2 min. Both coatings were made from 50/50 wt% PIP/CB blends. At low magnification, the two coatings have similar morphologies. However, at higher magnification, we clearly see that the UV cross-linked coating has a more porous structure compared to the HHIC cross-linked sample. The two different surface morphologies have a noticeable effect on the contact angle. The CA of hexadecane for the sample P50C50 treated by HHIC is around $120\pm 7^\circ$, while for the sample using UV cured has the CA around $142\pm 8^\circ$.

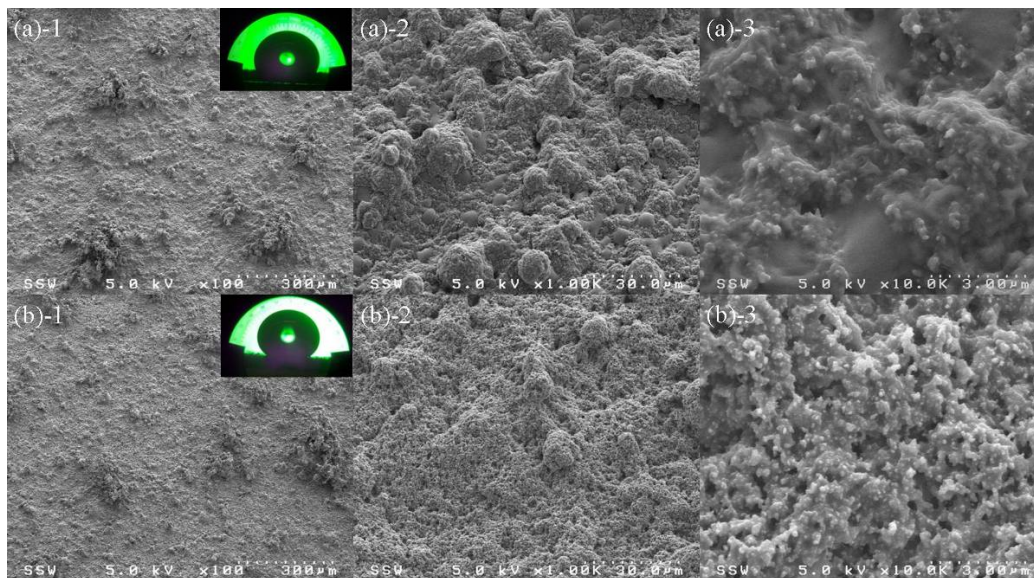


Figure 5-7: SEM morphology of coatings (P50 C50, 50/50 wt% PIP/CB blends, 12.5 mg mL^{-1}) with different crosslinking methods. (a) HHIC treatment for 2 min treatment (b) UV cured 20 min. Optical image of the hexadecane contact angles are inserted in the right corner of the corresponding SEM images.

5.3.4 Effect of Strain on Contact Angle

As mentioned earlier, the superoleophobic coating can be easily deposited onto a variety of different substrates. To understand the robustness of the coating on flexible substrates, we sprayed the coating on butyl rubber and measured the contact angle as a function of elongation. Fig. 5-8 demonstrated that the hexadecane contact angle for both coatings was consistent and remained superoleophobic up to 90 % strain. Sample P40C60 was elongated 100 % and still maintained superoleophobicity. The average contact angle remained above 150° for both samples; however, the data suggests that the contact angle begins to decrease at 90 % strain. The surface wettability of the prepared samples is highly dependent on surface hierarchical structures, which were created by the mixture of polymer matrix and CB as shown in previous SEM images. In the present study, Cassie-Baxter model was applied to study the wettability of the prepared coating surfaces on butyl rubber. When applied strains were varied, the roughness of the coating changed with stretching. The polymer matrix maintained the matrix structures in micro-scale owing to intrinsic elastomer property, whereas nanoparticles aggregates embed in the polymer matrix still maintained the nano-scale roughness. The oil droplets do not penetrate into the micro-scale “valleys” (the PIP-CB aggregates as shown in Fig. 5-3), but suspend on the surface. Further studies will be carried out by using the modified manual stretcher to accommodate greater elongations.

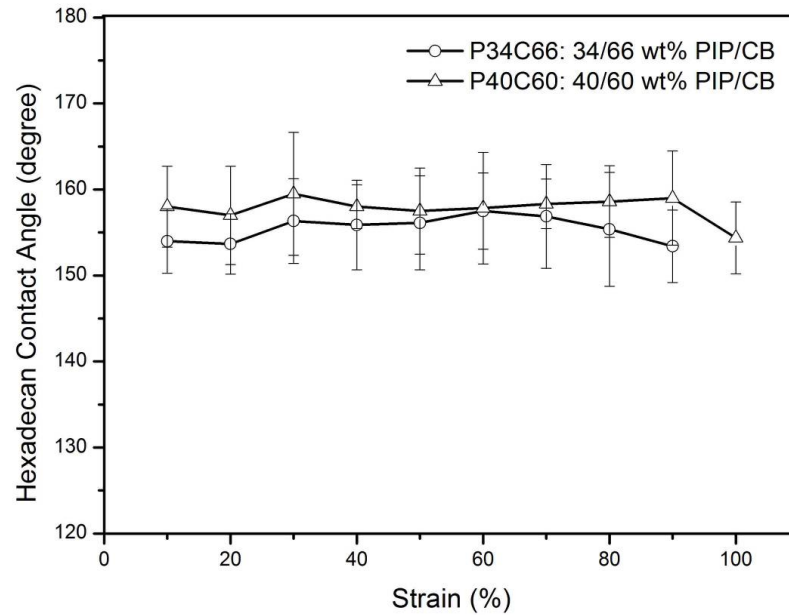


Figure 5-8: Contact angles of Hexadecane as a function of strain for coatings deposited on butyl rubber substrate. The contact angle measurements were averaged for each data point.

5.3.5 Electrical Conductivity of the UV cured coatings

The presence of conductive CB not only produces superoleophobic coatings, but also provides a conductive network. Fig. 5-9 shows room-temperature resistivity of PIP/CB composites coatings on butyl rubber substrates as a function of filler concentration. It is not surprising that the resistivity decreased as the CB content increased. The effect of resistivity before and after fluorination was also investigated. After chemical treatments with perfluorosilane, the resistivity slightly increased. The fluorination of carbon based nanomaterials can change the electronic properties from metals to semiconductors and even to insulators, depending on the type of C-F bonding and the location of the F-atoms within the carbon network [27]. In our case, it is important to note that the fluorination process occurred only on the CB surface through the OH groups using perfluorosilane. The bulk of the CB agglomerates remained untreated and maintained its conductive properties.

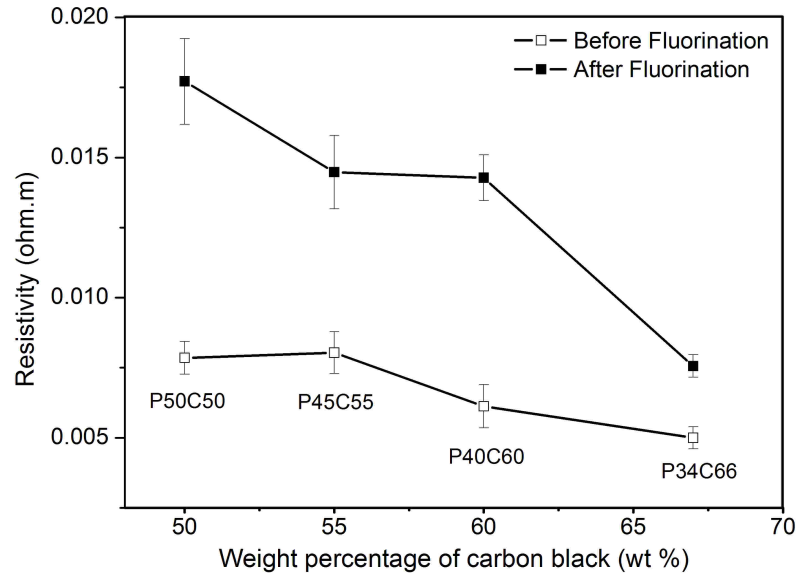


Figure 5-9: Resistivity of composite coatings on butyl rubber substrate with different CB percentage (12.5 mg mL^{-1}).

5.4 Conclusions

In summary, we have successfully developed a method to produce multifunctional surfaces that are both superoleophobic and conductive. These multi-functional coatings are easily produced by spraying a suspension of CB and polyisoprene on any substrate (polymer, metal and butyl rubber) followed by vapour fluorination. We also demonstrated that these coatings can be cross-linked using two different methods, ultraviolet light and HHIC. The superoleophobic properties were achieved by creating multiscale, re-entrant and convex structures using CB and reducing the surface energy by fluorination. The coatings were completely non-wettable by both water and hexadecane, which showed contact angles above 150 degrees with low roll-off angles. Moreover, the surface remained superoleophobic on rubber substrates when strained up to 100%. These superoleophobic surfaces also showed good conductivity due to the presence of conductive CB. The resistivity is on the order of $0.01 \Omega \cdot \text{m}$. It is anticipated that the demonstrated approach and principle could be applied to expand more multi-functional materials.

5.5 References

- [1] Gao XF, Jiang L. Water-repellent legs of water striders. *Nature*. 2004;432:36-.
- [2] Zhu Y, Zhang JC, Zheng YM, Huang ZB, Feng L, Jiang L. Stable, superhydrophobic, and conductive polyaniline/polystyrene films for corrosive environments. *Advanced Functional Materials*. 2006;16:568-74.
- [3] Quere D. Non-sticking drops. *Rep Prog Phys*. 2005;68:2495-532.
- [4] Barthlott W, Neinhuis C. Purity of the sacred lotus, or escape from contamination in biological surfaces. *Planta*. 1997;202:1-8.
- [5] Cheng L. Marine and Freshwater Skaters - Differences in Surface Fine-Structure. *Nature*. 1973;242:132-3.
- [6] Feng XJ, Jiang L. Design and creation of superwetting/antiwetting surfaces. *Adv Mater*. 2006;18:3063-78.
- [7] Tuteja A, Choi W, Ma ML, Mabry JM, Mazzella SA, Rutledge GC, et al. Designing superoleophobic surfaces. *Science*. 2007;318:1618-22.
- [8] Tuteja A, Choi W, Mabry JM, McKinley GH, Cohen RE. Robust omniphobic surfaces. *Proceedings of the National Academy of Sciences of the United States of America*. 2008;105:18200-5.
- [9] Ahuja A, Taylor JA, Lifton V, Sidorenko AA, Salamon TR, Lobaton EJ, et al. Nanonails: A simple geometrical approach to electrically tunable superlyophobic surfaces. *Langmuir : the ACS journal of surfaces and colloids*. 2008;24:9-14.
- [10] Cao LL, Price TP, Weiss M, Gao D. Super water- and oil-repellent surfaces on intrinsically hydrophilic and oleophilic porous silicon films. *Langmuir : the ACS journal of surfaces and colloids*. 2008;24:1640-3.
- [11] Marmur A. From hydrophilic to superhydrophobic: Theoretical conditions for making high-contact-angle surfaces from low-contact-angle materials. *Langmuir : the ACS journal of surfaces and colloids*. 2008;24:7573-9.
- [12] Leng BX, Shao ZZ, de With G, Ming WH. Superoleophobic Cotton Textiles. *Langmuir : the ACS journal of surfaces and colloids*. 2009;25:2456-60.
- [13] Wu WC, Wang XL, Wang DA, Chen M, Zhou F, Liu WM, et al. Alumina nanowire forests via unconventional anodization and super-repellency plus low adhesion to diverse liquids. *Chemical Communications*. 2009:1043-5.
- [14] Tsujii K, Yamamoto T, Onda T, Shibuichi S. Super oil-repellent surfaces. *Angew Chem Int Edit*. 1997;36:1011-2.

- [15] Xi JM, Feng L, Jiang L. A general approach for fabrication of superhydrophobic and superamphiphobic surfaces. *Appl Phys Lett*. 2008;92.
- [16] Steele A, Bayer I, Loth E. Inherently Superoleophobic Nanocomposite Coatings by Spray Atomization. *Nano letters*. 2009;9:501-5.
- [17] Srinivasan S, Chhatre SS, Mabry JM, Cohen RE, McKinley GH. Solution spraying of poly(methyl methacrylate) blends to fabricate microtextured, superoleophobic surfaces. *Polymer*. 2011;52:3209-18.
- [18] Carbon black User's Guide. http://carbon-black.org/user_guide.html: International carbon black association.
- [19] Britt JK, James RC. *Kirk-Othmer Encyclopedia of Chemical Technology*. Kirk-Othmer Encyclopedia of Chemical Technology: John Wiley & Sons, Inc.; 2000.
- [20] Hartley PA, Parfitt GD, Pollack LB. The role of the van der Waals force in the agglomeration of powders containing submicron particles. *Powder Technology*. 1985;42:35-46.
- [21] Boehm HP. Some Aspects of the Surface-Chemistry of Carbon-Blacks and Other Carbons. *Carbon*. 1994;32:759-69.
- [22] Given PH, Hill LW. Analysis of Surface Groups on Carbon Blacks. *Carbon*. 1969;7:649-&.
- [23] Darmanin T, Guittard F. Super oil-repellent surfaces from conductive polymers. *J Mater Chem*. 2009;19:7130-6.
- [24] Darmanin T, Guittard F, Amigoni S, de Givenchy ET, Noblin X, Kofman R, et al. Superoleophobic behavior of fluorinated conductive polymer films combining electropolymerization and lithography. *Soft Matter*. 2011;7:1053-7.
- [25] Wang HX, Xue YH, Lin T. One-step vapour-phase formation of patternable, electrically conductive, superamphiphobic coatings on fibrous materials. *Soft Matter*. 2011;7:8158-61.
- [26] Sze SM, Ng KK. *Physics and Properties of Semiconductors—A Review*. *Physics of Semiconductor Devices*: John Wiley & Sons, Inc.; 2006. p. 5-75.
- [27] Lee YS. Syntheses and properties of fluorinated carbon materials. *J Fluorine Chem*. 2007;128:392-403.

Chapter 6

6 Superoleophobic surfaces and the resistance to protein adsorption and bacterial adhesion

6.1 Introduction

Protein adsorption and microbial invasion associated infections are two major problems in the biomedical field. Biofouling is formed through microbial adhesion, growth and biofilm formation, which occurs worldwide in various industries, ranging from marine hull to biotechnological fields such as biomedical implants and biosensors. It is usually caused by adherence and colonization of microorganisms on the surfaces. Once microorganisms attach to substratum surface, subsequent formation of biofilm develops quickly. Biofouling limits the performance of devices in numerous applications, can result in device failure and serious infection. There has been increasing research interest in the development of novel anti-fouling surface. In general, surface physical and chemical properties of the substratum are both important factors in the adhesion and release of a fouling organism [1]. In order to prevent the initial nonspecific adhesion of the microorganisms, surface materials designed to resist protein adsorption and bacterial adhesion typically contain ethylene glycol (EG) [2-4], which exhibit resistance to protein adsorption and biofouling due to hydrophilic, steric repulsion and electrically neutral properties [5-7]. Other antifouling surface modified by polysaccharide [8-10], or zwitterionic [11-13] surface groups also displayed excellent reducing bio-adhesion (protein adsorption and bacterial adhesion). Extensive studies have been carried out on antifouling properties of these materials.

Inspired by nature self-cleaning creatures including lotus leaves [14] and water strider legs [15], artificial superhydrophobic surfaces with a water contact angle larger than 150° fabricated by various methods can be used as self-cleaning and anti-adhesion coatings. Such superhydrophobic non-fouling coatings not only resist adhesion of fouling agents but also allow for easy removal of contaminants. Most superhydrophobic surfaces

possess self-cleaning ability, contain over-hang or hierarchical structures which may minimize the contact area of the surface with bacteria, leading to reducing bacteria adhesion in a short contact period [16]. However, those superhydrophobic surfaces were inadequate to resist the fouling of microorganisms and proteins when exposed to medical environment containing highly oleophilic biofluids and complex macromolecules. In contrast, high performance superoleophobic surfaces showed extremely low wettability for various liquids including water and oil, which have the potential application to such an environment with oilphilic macromolecules.

The superoleophobic surfaces are hard to fabricate due to critical requirements for micro/nano structures. Although a number of superoleophobic surfaces have been developed based on chemical decoration with low surface energy moiety to dedicate micro/nano structures by using nanofabrication technology, electrochemical process or involving nanoparticles, rare robust surfaces to resist anti-scratch or anti-adhesive are achieved. Most of these researches focused on propose fabrication process and few papers have demonstrated the antifouling applications such as removal of biological and organic contaminants.

Recently, we developed a simple method to prepare stretchable superoleophobic composite surfaces by fluorination of the coatings prepared via spraying a mixture of polyisoprene and carbon black on butyl rubber surface. Carbon black has the advantage of being less costly for industrial scale production compared to the use of other nanoscale material such as nanotubes. The resultant surface coatings showed high contact angle for both water and oil droplets. Furthermore, the superoleophobic property of the composite coatings could be maintained even during the application of over 100% strain, which is attributed to the elastomeric polymer matrix of polyisoprene. With the addition of functional nanofiller-conductive carbon black, the resultant surface coatings also showed conductivity. The incorporation of functional nanofillers in composite coatings not only influences the surface morphology but also imparts unique functionalities to the resultant composite coating. It is reasonable that by incorporating various functional nanofillers to form polymer-nanoparticle composite coatings, customized coatings with the required properties can be achieved for intended applications.

In this chapter, we extend this technique to polyisoprene-carbon black-titanium dioxide system through directly adding titanium dioxide nanoparticles to the mixture solution. The elastomeric networks reinforced by the mixed filler which have very good mechanical properties. Compare with networks containing carbon black alone, the networks containing titanium dioxide-carbon black mixture had somewhat better combination of high modulus and good extensibility. The distribution of the nanofillers and surface roughness of the resultant composite coating were investigated. The prepared superoleophobic surfaces are evaluated regarding their non-fouling performance by resisting protein adsorption as well as bacterial adhesion.

6.2 Materials and methods

6.2.1 Materials

Polyisoprene pellets (PIP, trans), hexane, tetrahydrofuran, hexadecane, sulfuric acid (H_2SO_4), 2, 2-azobis(isobutyronitrile) (AIBN), hydrogen peroxide (H_2O_2) and phosphate-buffered saline (PBS, pH 7.4) were obtained from Sigma-Aldrich. 1H,1H,2H,2H-Perfluorodecyltrichlorosilane (PFTS) was obtained from Alfa Aesar. Conductive carbon black (CB, Vulcan XC 72) was purchased commercially from Cabot Corporation. Titanium dioxide (TiO_2 , Degussa P25) used in all experiments was from Degussa. 2-[methoxy(polyethyleneoxy)propyl]trimethoxysilane (MW 450-600) was purchased from Gelest and used as received. Alexa Fluor 555-dye conjugate of bovine serum albumin (BSA, AF-555 BSA; MW=66 kDa; lyophilized powder) and Alexa Fluor 546-dye conjugate of human fibrinogen (Fbg, AF-546 HF; MW=340 kDa; lyophilized powder) were purchased from Invitrogen (Life Technologies Inc. Canada) and used as received according to manufacture protocol. Silicon wafers were obtained from Aurel Corp. DI water used in the experiments was purified using a Millipore water purification system. All of the chemicals were used in the as-received condition without further modification.

6.2.2 General procedure for silane-coated glass/silicon wafer surface

6.2.2.1 Fabrication of silane-fluorinated substrates

Prior to silanization, the silicon wafer substrates were washed with pure ethanol, acetone and pure water. Followed by immersing the slides into freshly prepared piranha solution ($\text{H}_2\text{SO}_4:\text{H}_2\text{O}_2=3:1$ (volume) for 30 min at 90 °C to introduce -OH groups on surfaces. Afterwards, the surfaces were successively washed with an excess of MilliQ water and finally dried under a stream of N_2 . Immediately after activation, the slides were used for silanization by a one-step vapor deposition procedure using the trichlorosilane bearing compound. Typically, the slides were placed into a Petri dish with 20 μL silane solution and baked on a hotplate surface at 80 °C for 30 min.

6.2.2.2 Fabrication of silane-PEG substrates

Piranha-cleaned silicon substrates were incubated in 5 mM toluene solution of 2-[methoxy(polyethyleneoxy)propyl]trimethoxysilane for 18 h. The substrates were rinsed several times in toluene, ethanol, and pure water.

6.2.3 Preparation of PIP-CB-TiO₂ coatings on PET

In a typical experiment, P40C30T30(40 wt% of PIP, 30 wt% of CB and 30 wt% of TiO₂) samples were prepared by dissolving 250 mg of polyisoprene pellets, 187.5 mg of CB and 187.5 mg of TiO₂ in 20 mL of hexane, respectively, and ultrasonicated at room temperature for 2 h, followed by mixing the two dispersions and further ultrasonication for 2 h. The UV initiator AIBN was dissolved in 200 μl tetrahydrofuran and added to the suspension before spraying. The blends were sprayed on PET substrates using an airbrush (Badger, Model 350-1H) connected to a compressed nitrogen tank (pressure 60 psi). The procedures for spraying, air drying of the wet coatings overnight, UV cross-linking and fluorination with FPTS are all similar to the procedure outlined in our previous report (Chapter 5).

It is important to point out that the present coatings are not substrate-dependent; we also prepared the coatings on different engineering material surfaces, such as filter paper, stainless steel and glass slides.

6.3 Surface contact angle measurement and surface characterization

6.3.1 Contact angle measurements

Sessile droplet contact angles were measured in ambient air at room temperature using a contact angle goniometer (Rame-Hart's Model 100-00). Distilled water and hexadecane were used for the contact angle measurements. The reported static angles were calculated by averaging the angles from both the left and right sides of the droplet. At least 10 measurements on each surface were obtained for each experimental condition.

6.3.2 XPS, SEM and EDX measurements

The elemental surface composition of the superoleophobic surfaces and reference samples was determined by XPS analysis, using a Kratos Axis Ultra spectrometer. The morphology of the samples was examined on a field emission scanning electron microscope (SEM) equipped with an EDAX detector.

6.3.3 Atomic force microscope (AFM) characterization

The surface roughness parameters R_{rms} , i.e. the root mean square average of the values of all points of the profiles were determined by atomic force microscopy (AFM). AFM experiments were performed on a Dimension V AFM equipped with Nanoscope controller V (Veeco, Inc.). Rectangular silicon nitride cantilever with a nominal spring constant of 3 N m^{-1} and tip radius of less than 10 nm was used. The cantilever tip was moved to a position of interest using the Nanoscope controller software (Nanoscope 7.30, Veeco). Tapping mode with scan rate of 0.6 Hz was used in the scanning processes. The

Topography images were obtained. And the images were processed by SPM softwares (Nanoscope 7.30).

6.4 Protein solution preparation and single protein adsorption studies

Fibrinogen Conjugates (Fbg, AF-546 HF) and BSA Conjugates (BSA, AF-555): A 1 mg mL⁻¹ stock solution was prepared by reconstituting the conjugate in 5mL of 0.1M sodium bicarbonate (pH 8.3) at room temperature. Complete solubilization may take an hour or more with occasional gentle mixing. Then the solution is divided into aliquots and stored at -20 °C for future use.

Protein solutions with desired concentration (0.1mg mL⁻¹ in PBS) were freshly prepared and filtered through 0.2 µm syringe filters prior to use. The superoleophobic coatings on PET substrates and reference samples were exposed to the respective protein solution (300 µL) by using a silicone isolator (Ø 13 mm, height 2.5 mm, Grace Bio-Labs, USA), which was fixed on the glass slides with metal clamps in order to prevent leakage of protein solution. Exposure of substrates with various coatings to fluorescent protein solution was performed for 3 h. All operations were performed in the dark. After removal of the protein solutions, 0.1 M PBS (300 µL) was repeatedly added and removed after incubation for 5 min from the individual vials for three times to wash non-adsorbed proteins from the surface. Subsequently the substrates with functional coatings were dried in a stream of N₂.

Quantification of the amount of adsorbed proteins on the coating surfaces was evaluated via LSM 510 multichannel point scanning confocal microscope (excitation filter of 546 nm [band pass] and emission filter 575-640nm [band pass]) applying a 20 × or 63× objective throughout all experiments. The fluorescence images were obtained by averaging at least 6 randomly chosen areas of a sample.

The fluorescent light source was pre-warmed up for 30 min prior to image capture. Constant operation of the camera (gain value, Z-stack sets) and constant exposure time was ensured during the image collection to permit quantitative analyses of the observed

fluorescent signals. The software AxioVision is used to extract fluorescent images from the experiment data. The fluorescence microscopy images were analyzed using the software Image Pro Plus, which yielded the mean and standard of the fluorescence intensity of the interested image. The fluorescence intensity of the sample surfaces without exposure to target protein was measured to ensure quantifies the background fluorescence of the material itself. The background corrected fluorescence intensities for each coating surface was then used to compare target protein adsorption behavior.

6.5 Antifouling experiment

6.5.1 Static growth

Substrates with various coatings were immersed into a bacterial solution with 10^8 CFU mL^{-1} at 37°C in static growth conditions. Samples were replaced with fresh growth medium (TSB+ 0.25% glucose) every 24 h. After that, the substrates were taken out and washed three times with sterile PBS. Then the substrates were characterized by a scanning electron microscope (Hitachi 3400s SEM, Biotron). The sample fixation and preparation for SEM are as follows: the substrates were first immersed into 2.5 vol% glutaraldehyde in PBS at 4°C ; after 4 h, the glutaraldehyde solution was removed and the substrates were washed with PBS, followed by step dehydration with 25%, 50%, 70%, 95% and 100% ethanol for 10 min each. The substrates were then dried and sputter-coated with a thin film of platinum for imaging purposes.

6.5.2 Dynamic growth

Bacterial adhesion and growth on samples with various coatings under laminar flow were investigated in a custom-build parallel plate flow chamber (30mm length \times 10mm width \times 0.8 mm depth). The flow chamber was sterilized by irradiation of 254 nm UV light for 0.5 h. Before each experiment, the entire system was filled with sterile PBS to remove all air bubbles from the tubes and flow chamber. Flow rates were adjusted to 0.2 mL min^{-1} (corresponding with a wall shear rate of 3.6 S^{-1}). The flow rate was kept constant during the whole experiment. After 0.5 h, PBS flow was switched to a bacterial suspension

(ca. 10^8 CFU mL⁻¹). For a 24 h adhesion study, the bacteria suspension was pumped through the flow cell at 0.2 mL min⁻¹ for 3 h and then flow was terminated and bacteria solution were allowed to adhere to the surfaces under static conditions for 0.5 h. After 0.5 h, the appropriate sterile growth medium was pumped into the chamber to introduce growth for 24 h. Then the flow was switched to sterile PBS to wash the cell at the same flow rate (0.2 mL min⁻¹).

Bacterial adhesion and subsequent growth were studied by SEM after fixation using 2.5 vol% glutaraldehyde in PBS at 4°C for 4 h (the protocol is similar to that described in experiment 6.5.1). The bacterial adhesion morphology and viability on the different surfaces were also observed by confocal laser scanning microscopy (CLSM, Zeiss LSM 510 Duo Vario). Following incubation with bacteria solution and PBS wash process, 200 µl of Syto/PI dye mixture was added onto the surfaces then incubated in the dark at room temperature for 20 min. Finally, the substrates with various coatings were rinsed twice and the fluorescence was imaged using an LSM 510 multichannel point scanning confocal microscope (laser 488 nm for the SYTO 9 with a pass filter of 505–530 nm and a laser at 543 nm for the propidium iodide with a pass filter of 615 nm, magnification 63 ×, and 20 ×, respectively). All the images were obtained and analysed with the ZEN software.

6.6 Results and Discussion

6.6.1 X-ray photoelectron spectroscopy

XPS of the fluorinated composite PIP-nanoparticle surfaces (FPCT), reference PEO modified silicon wafer and PFTS modified silicon wafer were applied to confirm the key information of the resultant surfaces as reported in Table 6-1. The data in the table demonstrated that functional groups (PEO side chain and perfluorinated alkyl chain) successfully presented on the surface respectively. The survey spectra of XPS taken on PEO modified reference surface is presented in Fig.6-1. This spectrum indicates the main elements on the PEO modified silicon wafer surface. The peaks corresponding to O 1s, C

1s, Si 2p and O KLL (Auger) are observed. Fig.6-2 shows the high resolution C 1s core level XPS spectra performed on PEO modified silicon wafer surface. The observed C 1s peak was fitted with two Gaussian peaks at binding energies: (i) 284-286 eV corresponding to C-H/C-C in the PEO, (ii) 286.5-287 eV corresponding to the C-O in PEO. While the survey spectra (Fig.6-3) of PFTS monolayers shows four grouped binding energy (BE) corresponding to F 1s 685-692 eV, O 1s 530-536 eV, C 1s 282-298 eV and 97-107 eV. Based on the chemical composition, with the help of the standard spectrum data base, and through line Gaussian analysis, the fitted C 1s spectra at a binding energy of about 285.0 eV is attributed to C-C/C-H groups which arise from the CH₂ groups present in the PFTS molecule. The binding energy of 286.5 eV can be assigned to the oxidized carbon species C-O which arise from the CB surface and from adsorbed contamination [17]. The peak centered at 288.0 eV is assigned to CF_x. The remaining intense peak around 290.29 eV is assigned to the CF₂ groups of the PFTS chain. Last, the peak around 292.76 eV is assigned to carbon in CF₃ [18].

Table 5-1: XPS elemental analysis. Atomic percent concentration (at.%) of the elements taken on fluorinated polymer-nanoparticle composite surface and reference PEO and PFTS modified silicon wafer surface.

Surface	Element	Component	Position (eV)	at%
PEO_wafer	O 1s		531.10	36.9
	C 1s			22.1
		C-OH/C-O- C	286.78	63.0
		C-C/C-H	284.99	57.0
	Si 2p		98.50	41.0

Surface	Element	Component	Position (eV)	at%
PFTS_wafer	F 1s		685.45	47.1
	O 1s		531.45	12.2
	Si		98.15	17.9
	C 1s			22.9
		C-C/C-H	285.00	30.8
		C-OH/C-O-C	286.50	1.4
		CF _x	288.0	7.9
		CF ₂	290.29	51.4
		CF ₃	292.76	8.6
FPCT	F 1s		686.85	56.1
	O 1s		531.45	4.9
	C 1s		289.95	36.3
	Si 2p		101.65	2.7

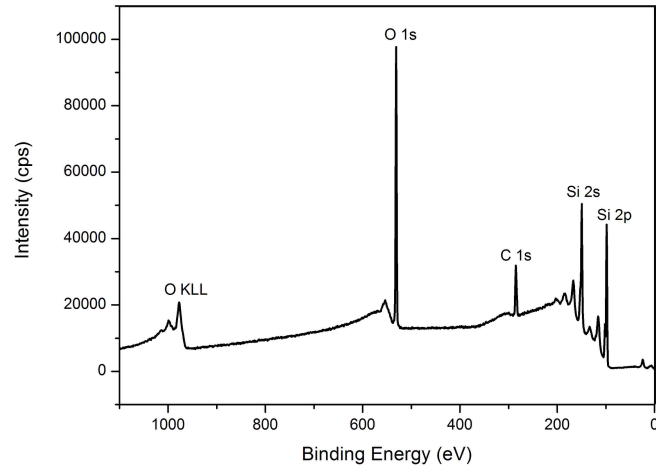


Figure 6-1: XPS survey spectra performed on PEO modified silicon wafer surface in the binding energy range of 0-1100 eV with a pass energy of 80 eV.

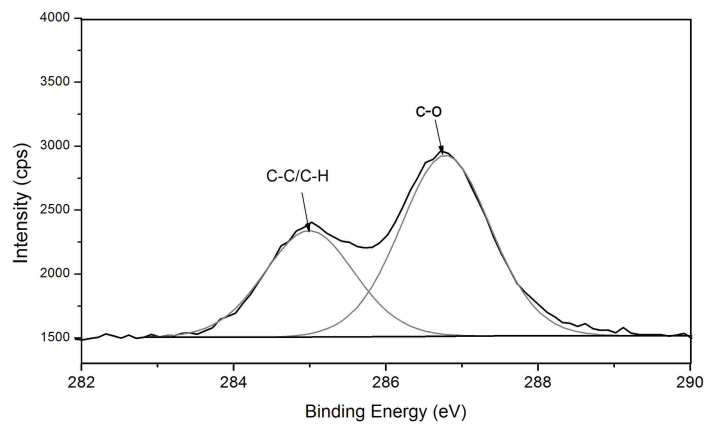


Figure 6-2: XPS high-resolution C 1s spectrum of PEO control ($(\text{EtO})_3\text{Si}-(\text{CH}_2)_3-(\text{OCH}_2\text{CH}_2)_{6-9}-\text{OCH}_3$ grafted silicon wafer). The observed C 1s peak was fitted with two Gaussian peaks at binding energies of 284.99 eV (C-C/C-H), 286.78 eV (C-O).

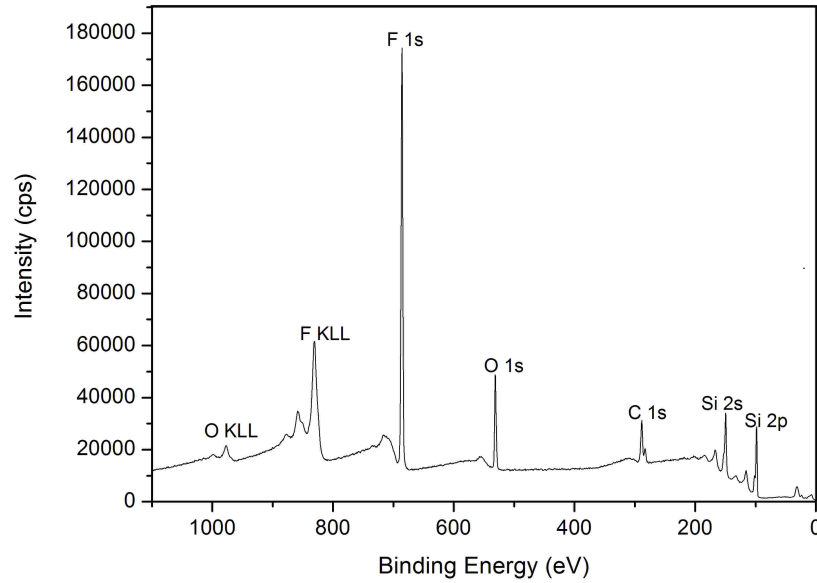


Figure 6-3: XPS survey spectra performed on PFTS modified silicon wafer surface in the binding energy range of 0-1100 eV with a pass energy of 80 eV.

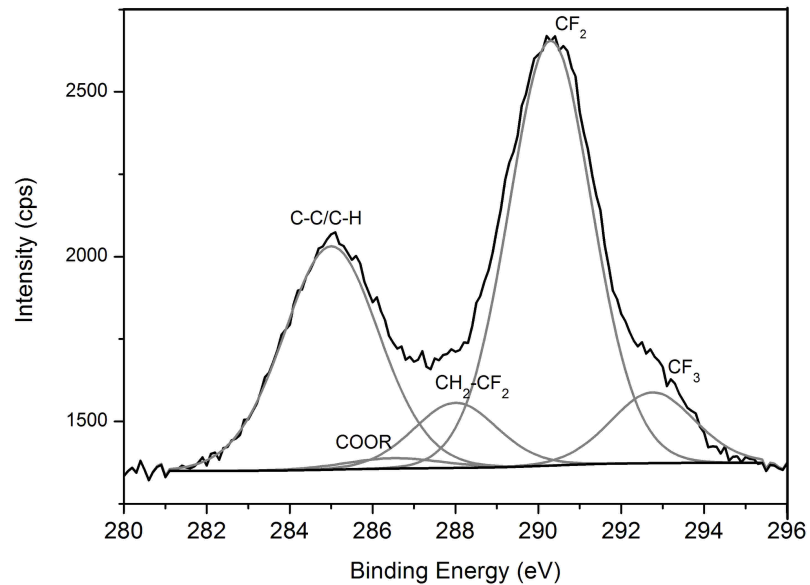
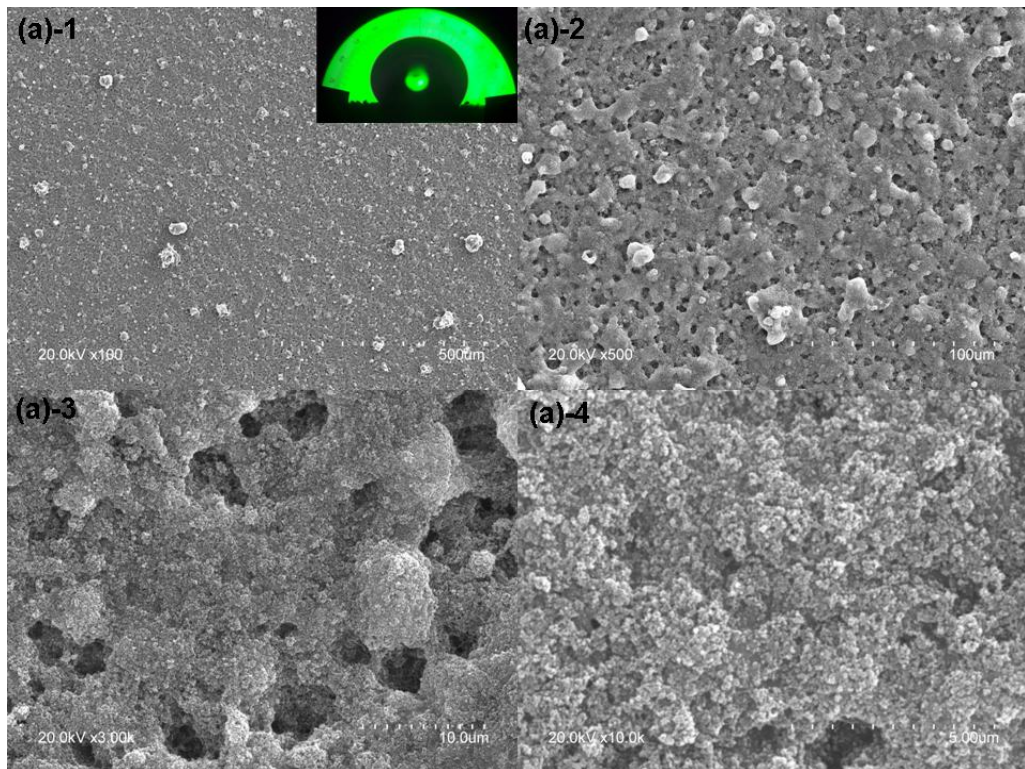


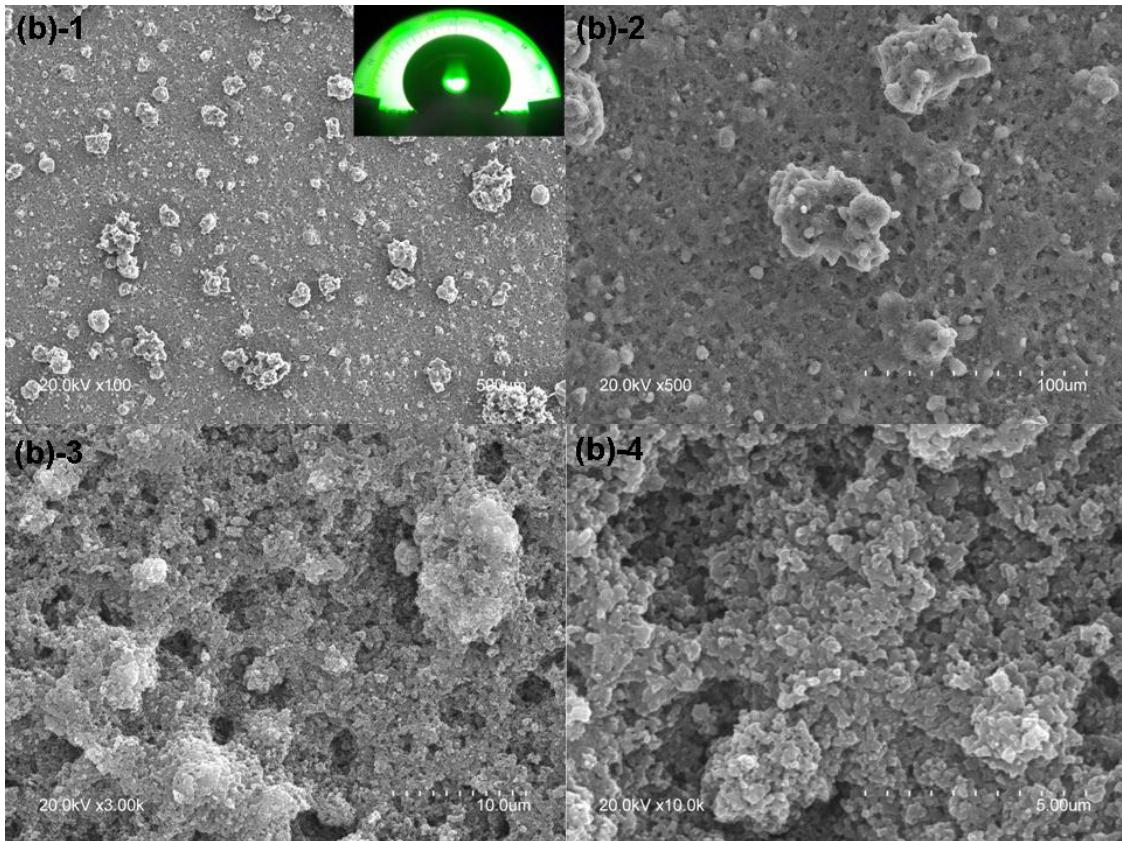
Figure 6-4: XPS high-resolution C 1s spectrum of PFTS grafted silicon wafer (PFTS control). The observed C 1s peak was fitted with five Gaussian peaks at binding energies of 285.00 eV (C-C/C-H), 286.50 eV (C-O/C-O-C), 288.0 eV (CF_x), 290.29 eV (CF₂) and 292.76 (CF₃).

6.6.2 Surface morphology of various coatings

The resultant coatings, even without any surface modification, showed superhydrophobic property with a contact angle of water more than 150° . The contact angle is far beyond typical contact angle of a bare polyisoprene surface, which is around 105° . In general, the wettability of solid surfaces by liquid depends on chemical composition and surface structure. The surface roughness has effect on the surface wettability as explained by Wenzel equation and Cassie-Baxter equation [19] and different scale of surface roughness can be used to texture the intrinsic hydrophobicity of the surface with the same material. As already disclosed, the structure and surface morphology of polymer-nanofiller composite is determined by the concentration and location of each component. It is thus important to study the relationship between the composite surface morphology and the corresponding component concentration. In our systematic study, the total solid concentration of 12.5 mg mL^{-1} was maintained. The surface morphology of the coatings sprayed on PET surface based on the constant content of polyisoprene and varying composition of CB and titanium dioxide nanofillers loadings were illustrated in Fig. 6-5. A composite coating containing continuous polymer matrix and nanofiller domain with microphase separation morphology has been achieved for all composite samples, which consisted of three immiscible components with different concentration. The coatings with various composition exhibited differences in the surface morphology even in low magnification. Fig. 6-5 (b)-1 and (c)-1 both demonstrated that large number of aggregates randomly distributed on the surface which produced large protrusion from bottom, the quantity of the protrusions increased as the increase of the CB loadings. In contrast, as shown in Fig. 6-5 (a)-1, the surface with less CB showed quite smooth morphology. The increase of CB loadings produced more aggregates in micro-scale. Surfaces with less CB loadings showed more smooth morphology in micro-scale. An air brush has been used in our experiment to fabricate the composite surface. The component concentration, viscosity, spray parameter all have influence on the morphology of the final coating surface. In our experiment, spray parameter were fixed throughout the whole experiment procedure, while the viscosity of the mixture was dominated by the concentration of polymer matrix, which was constant at 33.3 wt%. Thus the differences in the surface

morphology of composite coatings were attributed to the addition of CB. The interaction between CB to the polymer phase and the interaction between CB to the TiO_2 governed the surface morphology of the composite coating. Significant changes also have been observed in high magnification, re-entrant structure formed by higher loading of CB in the mixture.





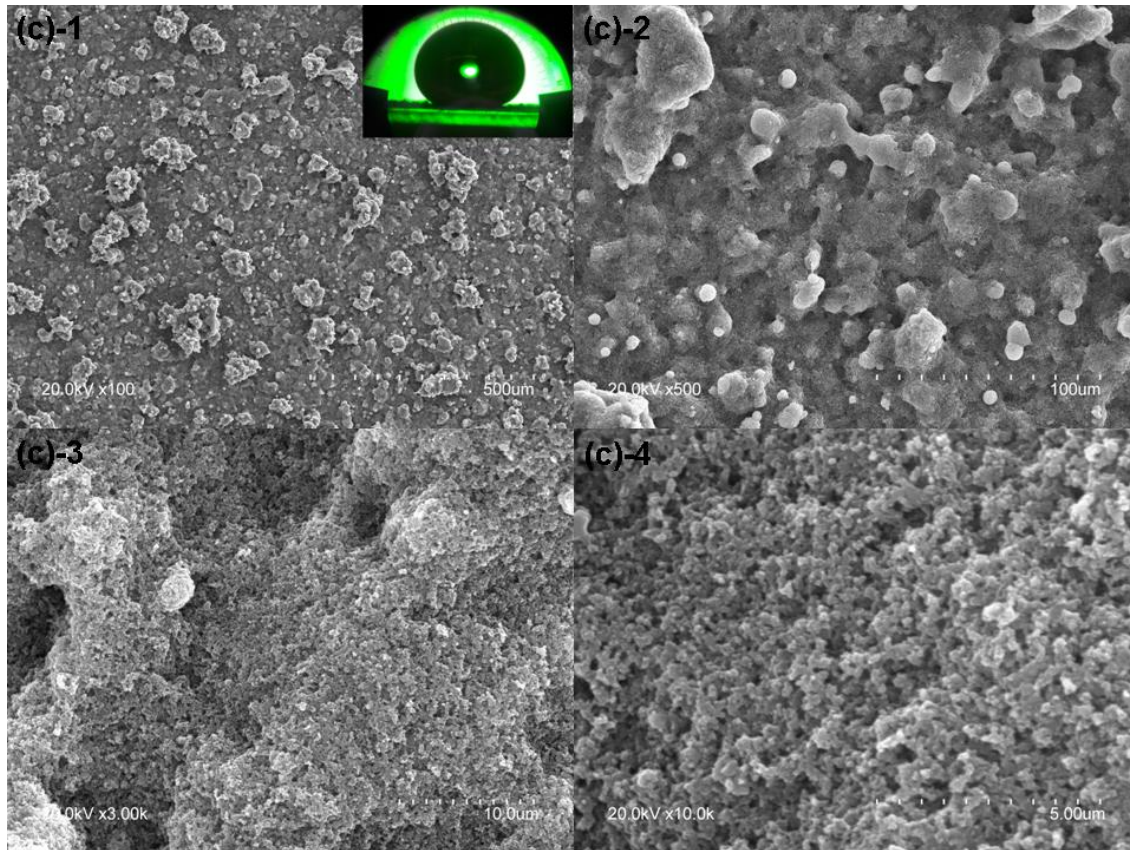


Figure 6-5: Plan view for polyisoprene-nanofiller composite coating on PET surface of 33.3 wt% of polyisoprene with different nanofiller loading: (a) CB 6.7 wt%, titanium dioxide 60.3 wt%; (b) CB 13.4 wt%, titanium dioxide 53.6 wt%; (c) CB 33.4 wt%, titanium dioxide 33.3 wt%. Optical image of the hexadecane contact angles are inserted in the top-right corner of the corresponding surface.

In order to maintain good elasticity of the resultant composite coatings, a possibly higher content of polymer matrix is favoured. We further increased the content of polyisoprene, and decreased the content of nanofillers and the same spray parameter has been used to prepare the composite coatings. Fig. 6-6 showed the surface morphology of the composite coatings with higher content of polymer matrix. It is clearly observed that more micro-aggregate protrusion structures formed on the surface with less polymer content, compared to that of the surfaces with higher polymer content. The enlarged view of protrusion revealed that macrophase of polymer and nanofiller immiscible component

formed nano-scale structure. This porous re-entrant structure is self-organized during spray process. The superoleophobicity is attributed to local nanoscale with porous structure together with microscale protrusions. The system composition, spray process both have influence on the final morphology, which also indicates that resultant surface structures can be easily customized as requested by controlling the component concentration. The spray process is easily automatized, which has the potential for large-scale production.

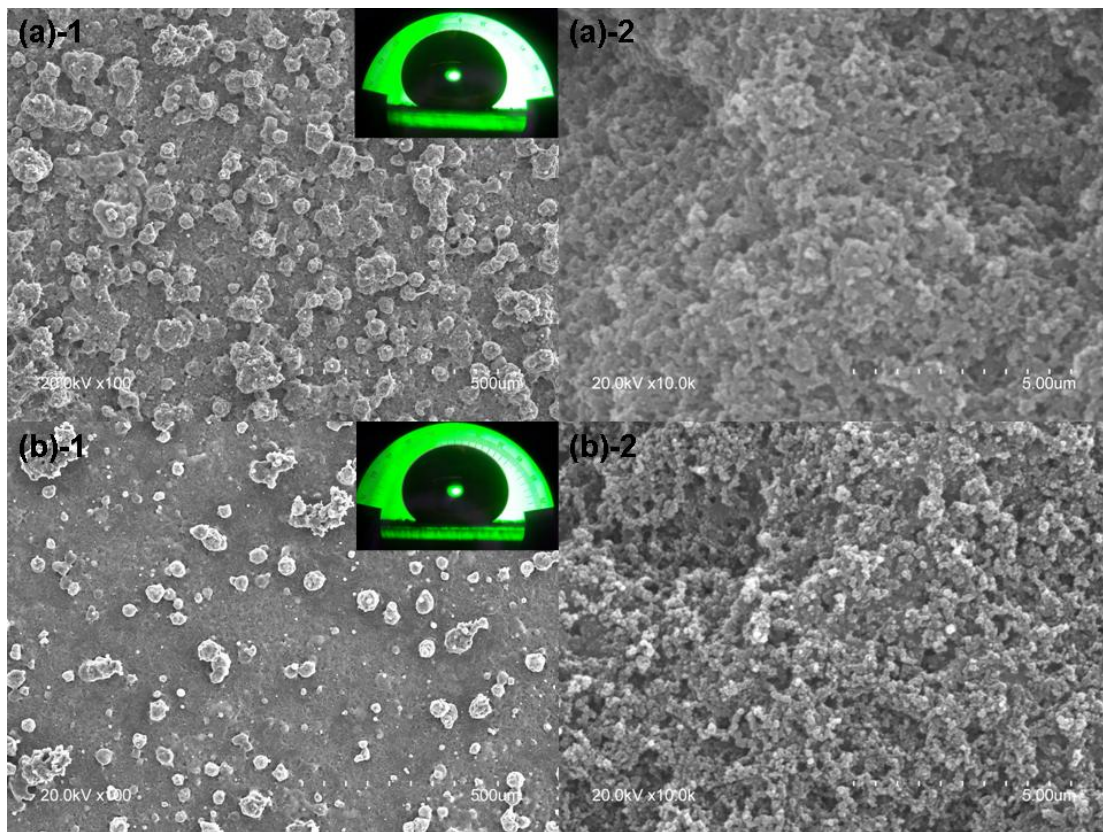


Figure 6-6: Plan view for polyisoprene-nanofiller composite coating on PET surface (a) polyisoprene 40 wt%, CB 30 wt%, titanium dioxide 30 wt%; (b) polyisoprene 50 wt%, CB 25 wt%, titanium dioxide 25 wt%. Optical image of the hexadecane contact angles are inserted in the top-right corner of the corresponding surface.

To stress the importance of adding the component of CB, the composite surfaces with polyisoprene as polymer matrix and titanium dioxide as nanofiller have been prepared. As shown in Fig. 6-7, instead of porous structure similar to the samples containing CB, the PIP-TiO₂ samples showed wrinkle-like morphology. No appearance of nanostructure of TiO₂ observed on the top surface. It is well known that TiO₂ nanoparticles flocculate spontaneously in low polarity solvent owing to its high polarity and surface area. In contrast, polyisoprene is well dissolved in nonpolar solvent hexane in our experiment. Macrophase separation immediately occurred when the mixture was sprayed on the PET surface. The resultant composite coating showed polymer matrix on top and embedded the nanoparticles at the bottom.

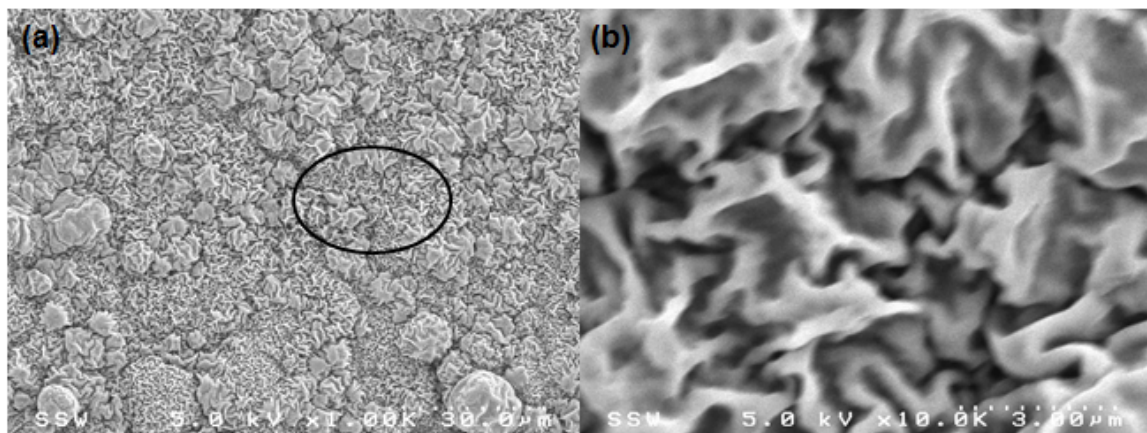


Figure 6-7: (a) Plan view for Polyisoprene-TiO₂ composite coating (polyisoprene 33 wt%, titanium dioxide 67 wt%) on PET surface. (b) the zoom-in image of the area as highlighted by the black circle in (a).

In our previous report, CB showed good interaction with polyisoprene due to apolar-interaction. At higher CB concentrations, the CB particles formed microscale clusters, whereas the polyisoprene filled the interspaces and provided adhesion. However, at lower CB loading, the agglomerates were completely encased by the PIP matrix resulting in a smooth structure. When adding CB to polymer-titanium dioxide mixture, which contains

opposite surface charge of TiO_2 , the electrostatic interaction produced large agglomerates providing micrometer-scale roughness, while the individual CB and titanium dioxide nanoparticles created nanoscale roughness. Fig.6-8 shows surface morphology of a typical superoleophobic sample. The composite surfaces consisted of randomly assembled CB and titanium dioxide in polymer matrix, which demonstrated hierarchical roughness. The polymer matrix formed continuous film while maintaining certain porosity owing to immiscible nanoparticles phase. The EDX mapping confirmed the composition based on CB, titanium dioxide with polymer matrix enriched in the particle aggregates adjacent.

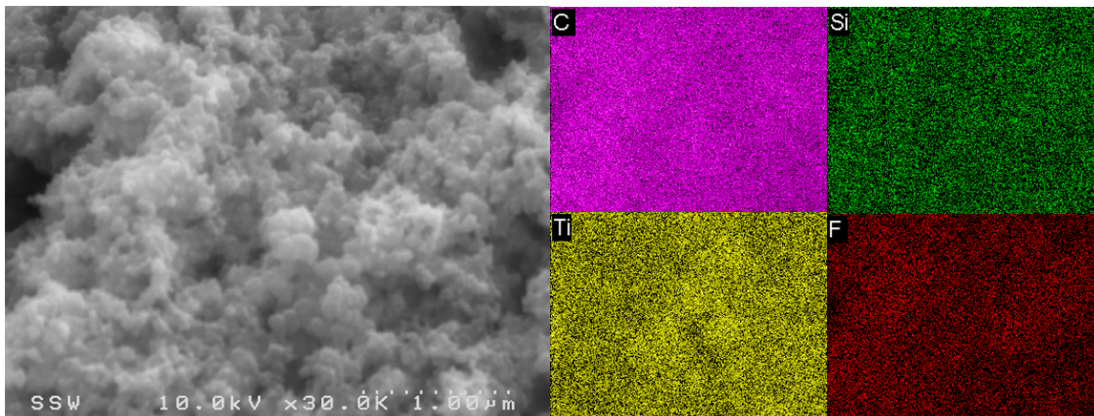


Figure 6-8: Details of a superoleophobic surface coating on PET surface with composition of polyisoprene 40 wt%, CB 30 wt% and titanium dioxide 30 wt% and EDX element mapping.

To evaluate the surface properties of the resultant surface coatings, contact angle measurements were carried out by using water and hexadecane as test liquids. Table 6-2 illustrates the hexadecane contact angle of the resultant surface coatings with various compositions. The results clearly showed that the oleophobicity of the coating surface increases with the increase of CB nanofiller loadings. At low CB loading content, the contact angle of hexadecane droplet is around 130° , which is typical of fluorinated rough

surface. With further increases of CB loading, the contact angle of hexadecane increased to over 150° , and the hexadecane droplet could free rolling on the surface without leaving any trace.

Table 6-2: Apparent contact angle for hexadecane of various coatings.

Sample	Contact Angle (hexadecane 10 μ L)
PIP33% TiO ₂ 67%	85 \pm 4 $^\circ$
PIP 33.3% CB 6.7% TiO ₂ 60.3%	130 \pm 5 $^\circ$ trace leaving
PIP 33.3% CB 13.4% TiO ₂ 53.6%	140 \pm 5 $^\circ$ trace leaving
PIP 33.3% CB 33.4% TiO ₂ 33.3%	153 \pm 3 $^\circ$ freely roll off
PIP 40% CB 30% TiO ₂ 30%	154 \pm 2 $^\circ$ freely roll off
PIP 50% CB 25% TiO ₂ 25%	150 \pm 2 $^\circ$ freely roll off

The composite surfaces with certain CB loadings created a rough surface with hierarchical structure on both micrometer and nanometer scales. The behaviour of the hexadecane droplet is related to the coating morphology and low surface energy after chemical fluorination. While for all the fluorinated samples containing CB component, the water droplets rolled away immediately as they were placed on the surfaces, even without tilting the substrate due to the low surface energy of fluorine silane.

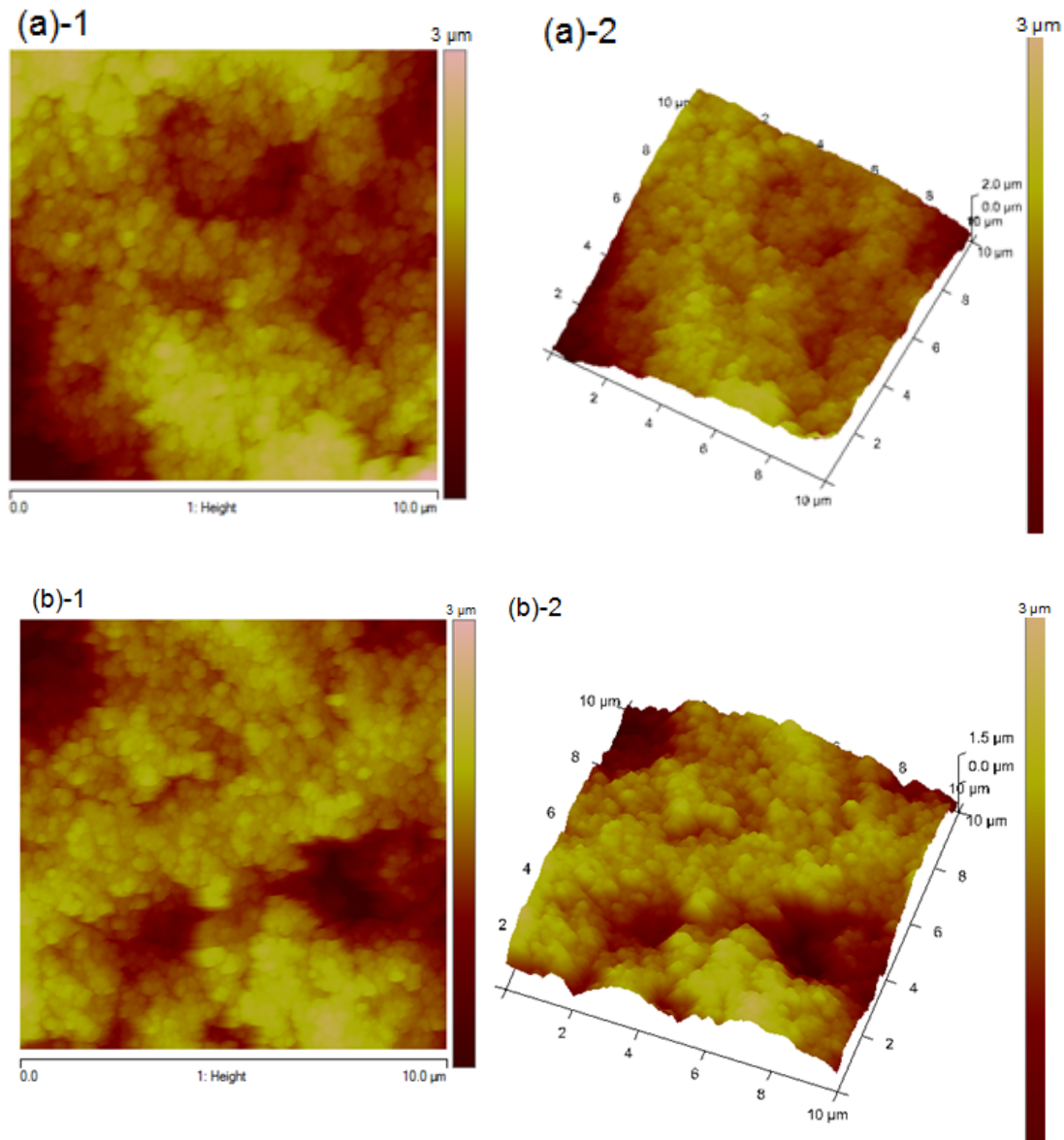


Figure 6-9: 2D and 3D AFM topographical images of (a) composite film with the composition of PIP 40 wt%, CB 30 wt%, titanium dioxide 30 wt%, $R_q=500\pm 46$ nm. (b) composite film with the composition of PIP 50 wt%, CB 25 wt%, titanium dioxide 25 wt%, $R_q=375\pm 47$ nm. RMS roughness (R_q) of the composite coating surface, defined as the standard deviation of the elevation, z values. The average RMS roughness value was determined for responding surface from three different locations.

In order to better reveal the effect of surface texturing on oil droplet repellency, quantitative characterization of the re-entrant structure of the superoleophobic coatings has been done using AFM measurements. Fig.6-9 shows the 2D and 3D AFM images of superoleophobic composite coatings, both surfaces exhibited similar surface topography with hierarchical structure. These two coatings were prepared using different composition, and the one containing higher nanofiller loading has the RMS roughness of 500 nm and exhibited higher contact angle of 154° compare to the other one with less nanofiller loading which had less contact angle.

6.6.3 Single protein adsorption on various surfaces

Albumin (66 kDa, pI 4.8) was chosen as one of the interest proteins since it is the most abundant plasma protein in serum and be well known to adhere well to surfaces and widely used as a surface blocking agent. Fibrinogen (340 kDa pI 5.5) is also a prevalent protein from plasma, which promotes platelet adhesion onto the surface and plays an important role in the process of surface-induced thrombosis [20]. The plasma proteins adsorbed onto fresh prepared superoleophobic coatings and bare surface references. In addition, silicon wafer surfaces chemically grafted with PFTS and PEO silane and composite polyisoprene-titanium dioxide coating with and without fluorination were used for comparative purpose. Single protein adsorption was quantified with fluorescent labeled BSA and Fbg after 3 h immersion of the surfaces with the respective protein in PBS by means of confocal fluorescence microscopy. The adsorption amount was analyzed to determine protein resistance ability of the sample surfaces.

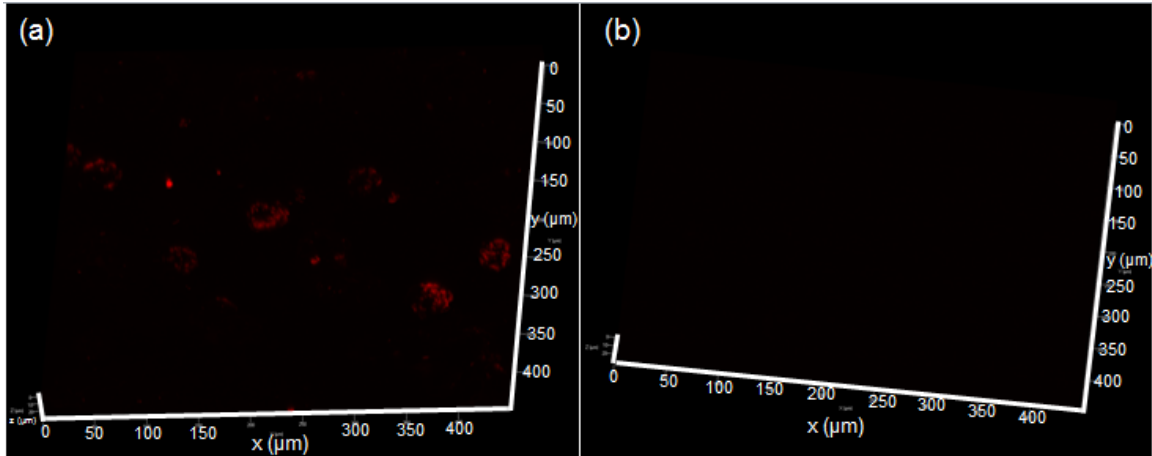


Figure 6-10: Representative fluorescence microscopy graphs of samples immersed in 0.1 mol L^{-1} BSA PBS solution surface for 3 h. (a) PCT (PIP 40 wt%, CB 30 wt%, titanium dioxide 30 wt%), (b) FPCT (superoleophobic coatings with the composition of PIP 40 wt%, CB 30 wt%, titanium dioxide 30 wt%).

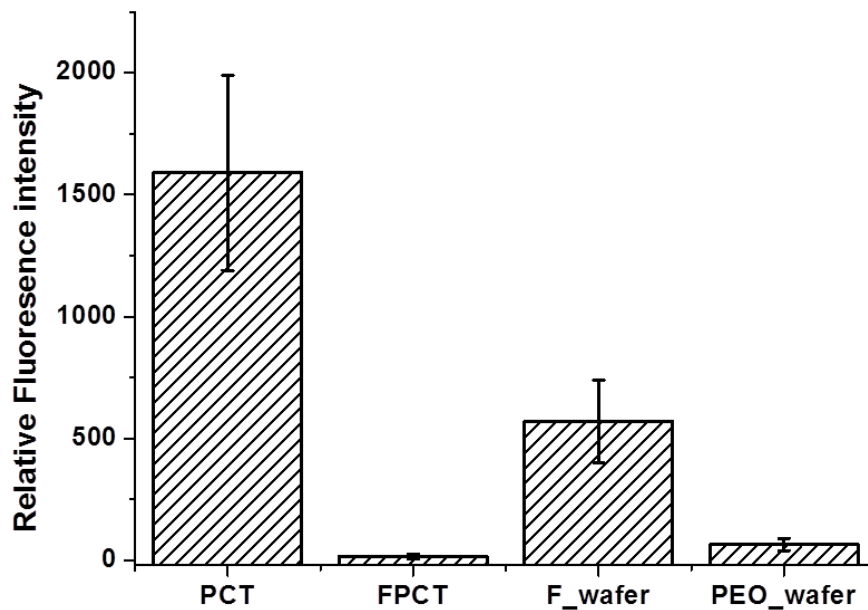


Figure 6-11: Relative BSA (0.1 mg mL^{-1}) adsorption on various surfaces for 3 h. FPCT stands for superoleophobic coatings with the composition of PIP 40 wt%, CB 30 wt%, titanium dioxide 30wt%. Fluorinated silicon wafer and PEO silane modified silicon wafer was used as reference.

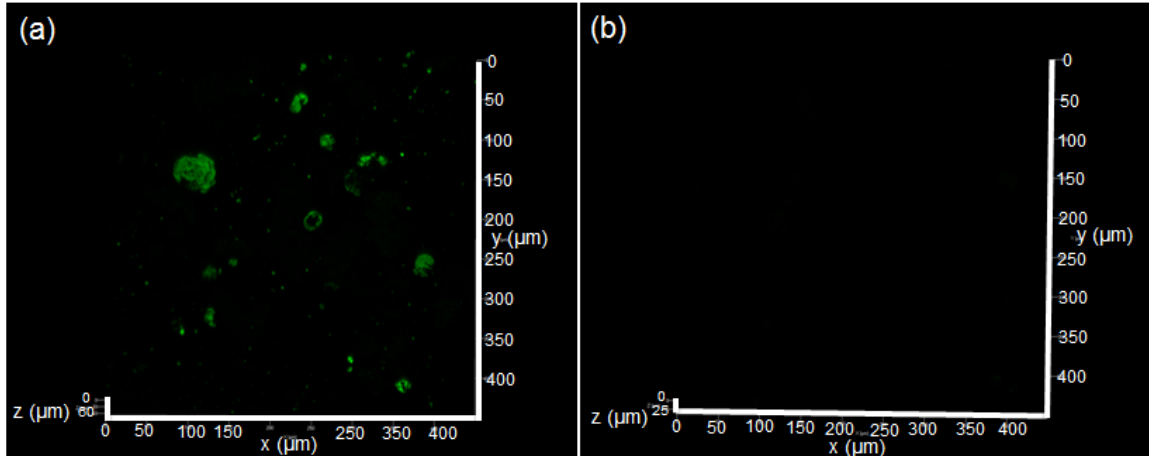


Figure 6-12: Representative fluorescence microscopy graphs of samples immersed in 1 mg L^{-1} BSA PBS solution surface for 3 h. (a) PCT (PIP 40 wt%, CB 30 wt%, titanium dioxide 30 wt%), (b) FPCT (superoleophobic coatings with the composition of PIP 40 wt%, CB 30 wt%, titanium dioxide 30 wt%).

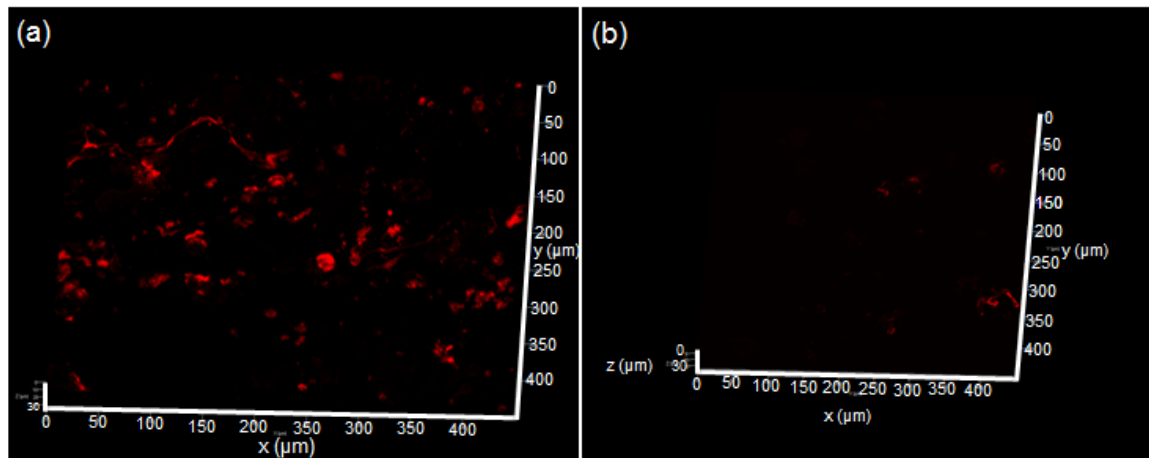


Figure 6-13: Representative fluorescence microscopy graphs of samples immersed in 0.1 mg L^{-1} fibrinogen PBS solution surface for 3 h. (a) PCT (PIP 40 wt%, CB 30 wt%, titanium dioxide 30 wt%), (b) FPCT (superoleophobic coatings with the composition of PIP 40 wt%, CB 30 wt%, titanium dioxide 30 wt%).

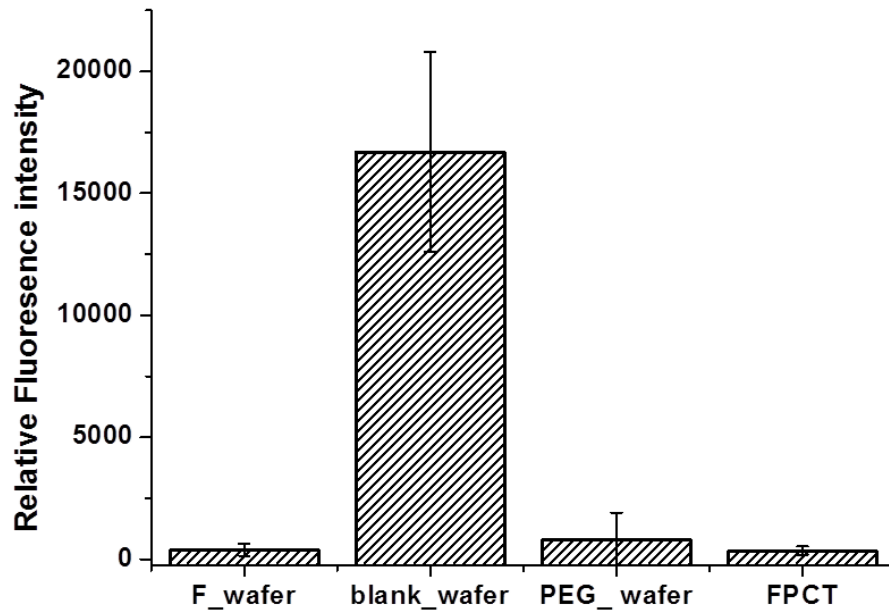


Figure 6-14: Relative fibrinogen (0.1mg mL^{-1}) adsorption on various surfaces for 3 h. FPCT stands for superoleophobic coatings with the composition of PIP 40 wt%, CB 30 wt%, titanium dioxide 30 wt%. Fluorinated silicon wafer and PEO silane modified silicon wafer was used as reference.

Fig. 6-11 shows representative qualitative value of BSA adsorption on pristine PIP-CB-TiO₂ (PCT) composite, fluorinated PIP-CB-TiO₂ composite (FPCT), PEG modified silicon wafer (PEG_wafer) and fluorinated silicon wafer (F_wafer). In these BSA adsorption experiments, less BSA adsorption was observed qualitatively on FPCT and PEG_wafer surfaces after 3 h interaction. The fluorescence level on FPCT surface was three-fold smaller than that of PEG_wafer. The hydrophobic F_wafer presented 30-fold higher fluorescence level compare to that of FPCT. While the superhydrophobic PCT surface exhibited the highest BSA adsorption, which is almost 100-fold fluoresce level of FPCT. BSA has a greater affinity toward hydrophobic surfaces compared to hydrophilic surfaces. Higher adsorption observed on pristine PIP-CB-TiO₂ composite and fluorinated flat silicon wafer compared to the PEG modified surface due to the strong hydrophobic interactions between BSA and the surface. Compared to flat F_silicon wafer, pristine PCT composite displayed high surface roughness, resulting in a significant higher BSA

adsorption. PCT composite coating has the same hierarchical surface structure as FPCT, which entrapped air leading to superhydrophobicity. However, the hierarchical structure in absence of low surface energy cannot prevent the adsorption of lyophilic molecular. Transport of a protein molecule depends on its diffusion through the liquid to the solid-liquid interface. Given the superoleophobic surface, with porous hierarchical structure and low surface energy on the top, the entrapped air limited the contact surface area and protein solution could not penetrate into the bulk in a short period of time.

We further applied protein concentration 10 times up to 1 mg mL^{-1} . After 3 h incubation, the superoleophobic surface still showed excellent non-specific adsorption resistance towards BSA PBS solution. The confocal image in Fig. 6-12 clearly shows that bare PCT composites adsorb a large number of BSA after 3 h interaction using the same protein concentration. It is noted that the isolated intense areas of fluorescence in the confocal image correspond to the protrusion area in previous SEM images. This result also indicated that material showing superhydrophobicity may not sufficient to resistant to protein-fouling. As we know, the protein adsorption strongly depends on the protein concentration, protein solution with higher concentration will be applied in further studies together with the cell adhesion behaviour.

Representative confocal images of Fbg adsorption on PCT composite with and without fluorination are illustrated in Fig. 6-13. Fluorinated composite surfaces exhibited remarkable less Fbg adsorption owing to entrapped air and lower surface energy. Further quantitative protein adsorption results has been shown in Fig. 6-14. The comparable fibrinogen adsorption values on ethylene oxide modified wafer and fluorinated silicon wafer was not unexpected, owing to the existence of trifluoromethyl group introduced by fluorination process. In early work by Han et al. [21], the hydrophobic self-assembled monolayer formed by reacting with the same PFTS alkyltrichlorosilane on PDMS surface and exhibited lower platelet and fibrinogen deposition than the surfaces composed with hydrophilic groups with short ethylene oxide chain length.

We consider that other factors such as the surface charge of the composite coating may play an important role in the protein adsorption. Further study is needed to elucidate the

surface charge effect on the protein adsorption. The protein conformational difference when exposure to the superoleophobic material will be investigated to study the biocompatibility.

6.6.4 Bacterial adhesion on various surfaces

Previously, we have demonstrated that superoleophobic surfaces based on fluorinated CB and titanium dioxide and polyisoprene coating (FPCT) exhibited highly resistance to nonspecific protein adsorption. The bacterial adhesion experiments on FPCT surface, pristine PCT composite coating and pristine PET reference with bacterial strain E.coli were further tested.

Fig. 6-14 illustrates the SEM images of substrates with various coatings after immersion in E.coli suspension at a concentration of approximately 2×10^8 CFU mL⁻¹ for 24 h. It is clearly observed that E.coli bacteria adhered on the pristine PCT composite coating surface and pristine PET substrate. Seldom bacteria were observed on superoleophobic FPCT coating surface. Physiochemical properties of substrate surfaces are the dominate factors to control the bacterial adhesion.[1] Several *in vitro* and *in vivo* studies have shown that rough surface promote bacteria binding to substrates [22-24]. Although the pristine PCT composite coatings showed superhydrophobic property in the initial incubation, lyophilic extracellular matrix materials excreted by bacteria touch to surface during the initial adhesion step followed by bacteria binding. The intrinsic high surface roughness of the composite coatings promoted the accumulation of bacteria, resulting in higher bacteria adhesion comparing to the pristine PET substrate.

The superoleophobic substrates were immersed into the bacterial PBS solution to carry out the antifouling experiment. Unlike the reference samples, the bacterial solution touched the substrate normally. There was a silver shine covered the whole superoleophobic surface because of the total reflection of light, where trapped air in the rough surface prevented the solution actually touching the substrate.

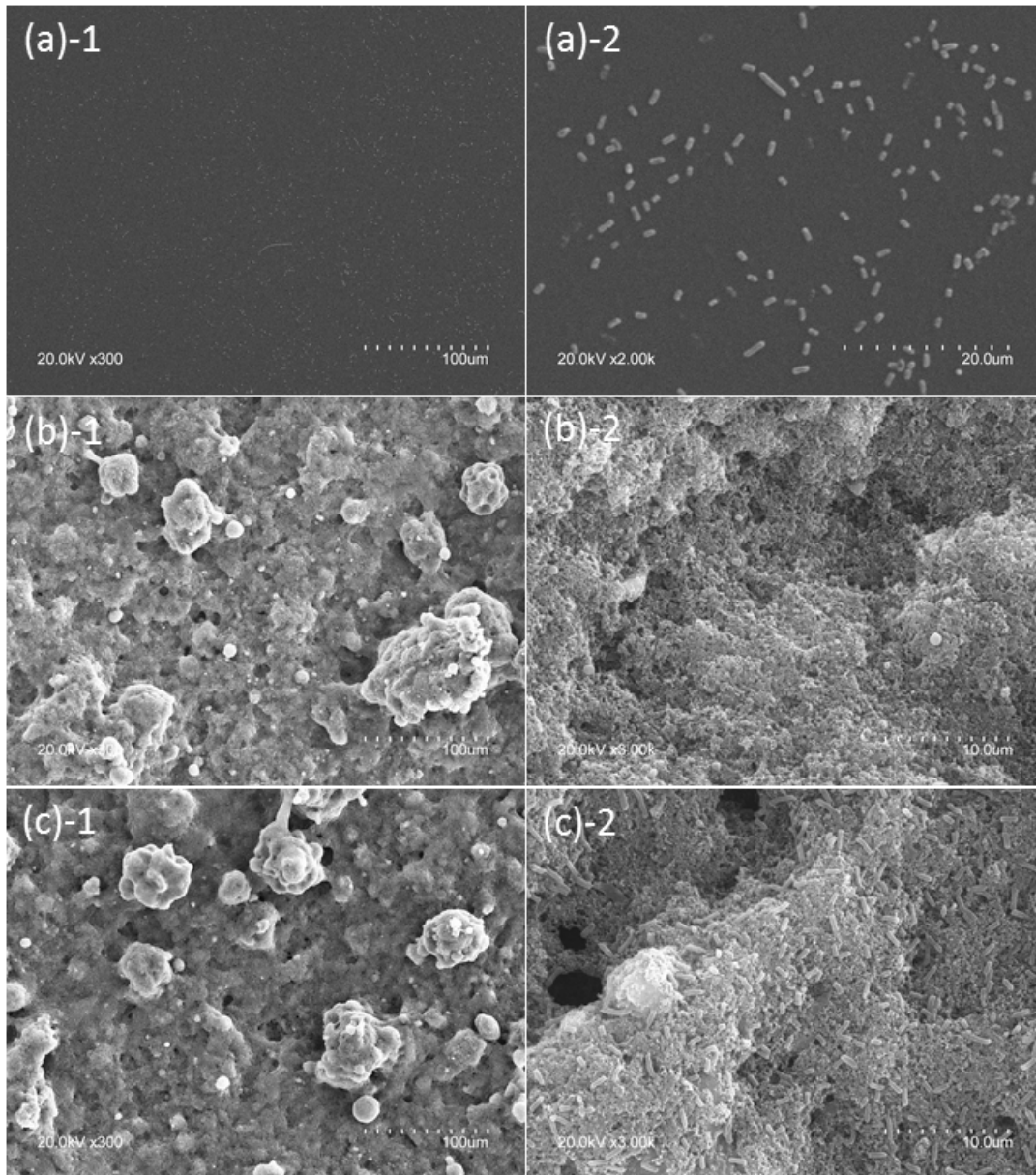


Figure 9: SEM images after various coatings immersed in E.coli suspensions (10^8 CFU mL⁻¹) for 24 h at different magnification: (a) pristine PET substrate, (b) FPCT composite coating on PET substrate, (c) pristine PCT composite coating on PET substrate.

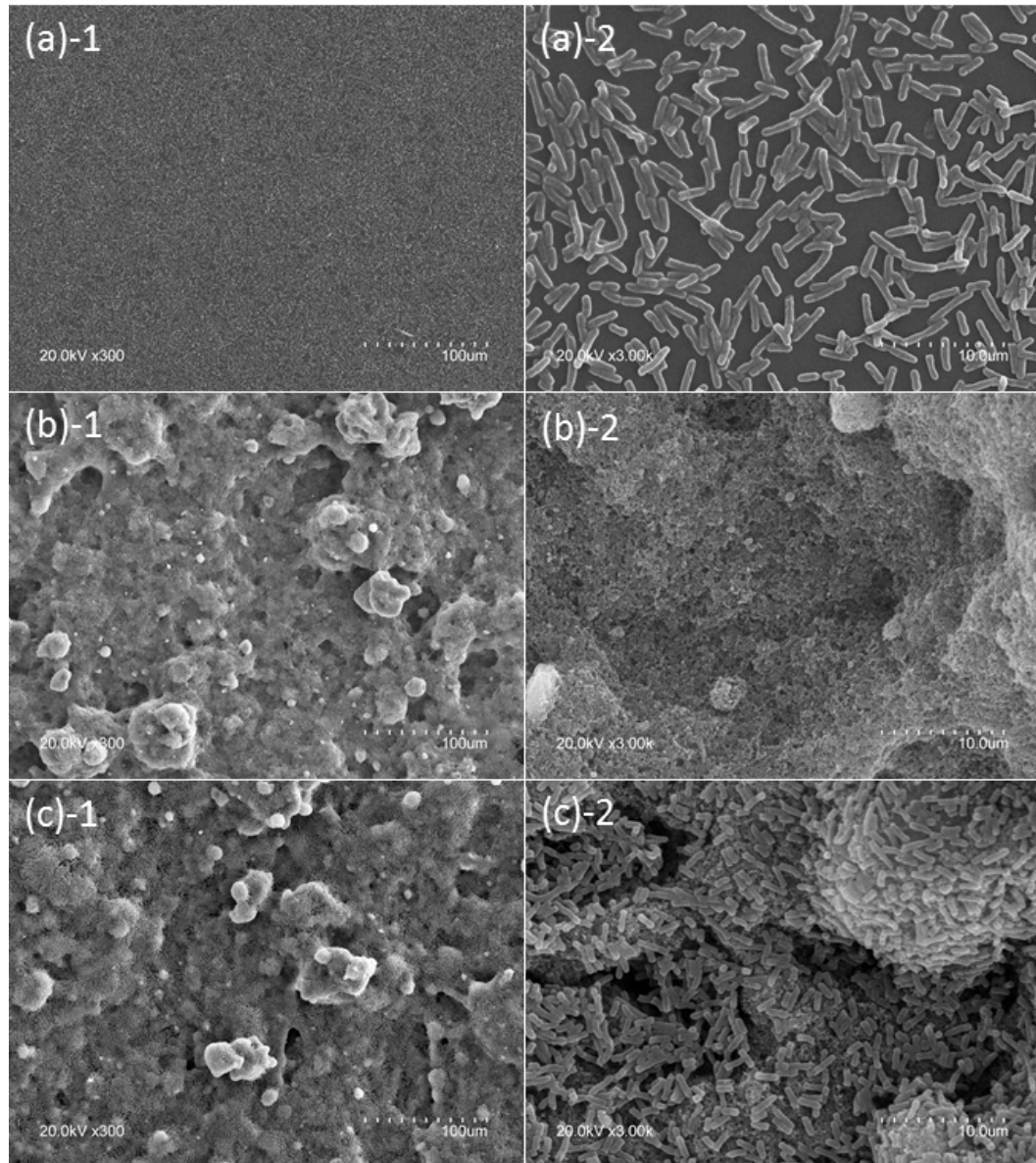


Figure 10: SEM images of various coatings after dynamic growth using a parallel-plate flow chamber with E coli 10^8 CFU mL $^{-1}$ for 24 h (shear rate 3.6 s $^{-1}$). (a) pristine PET substrate, (b) FPCT composite coating on PET substrate, (c) pristine PCT composite coatings on PET substrate.

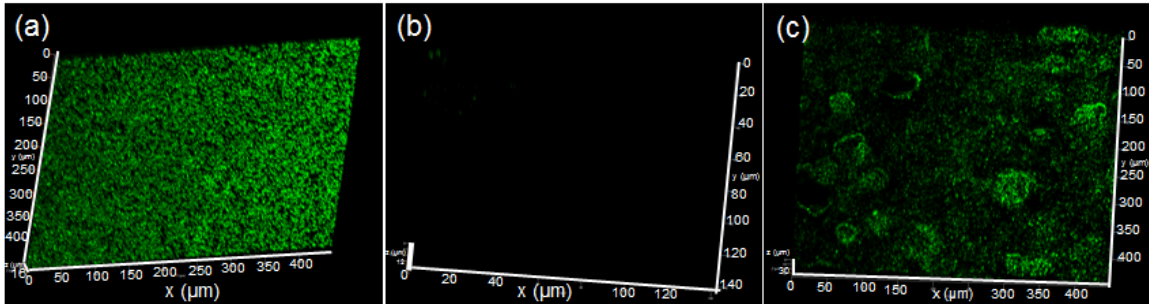


Figure 11: Representative fluorescence microscopy images of attached E.coli cells from a suspension with 10^8 CFU mL⁻¹ for 24 h dynamic growth. Bacterial cells were stained with LIVE/DEAD BacLight. Live cells fluoresce green. (a) Pristine PET substrate imaged at 20× (b) FPCT superoleophobic coating imaged at 63×, (c) Pristine PCT composite coating imaged at 20×.

Parallel plate chambers were introduced to study the bacteria adhesion several decades ago, with the advantage of controlling the operating shear forces and mass transport as well as real-time observation microorganism adhering behavior [25]. Fig 6-16 shows representative qualitative images of accumulated E.coli on PET, FPCT and PCT. The similar bacteria adhesion trend was observed on these three samples under dynamic flow growth condition correspond to nonspecific protein adsorption and consequent bacteria adhesion. The hydrophobic and rough pristine PCT surface displayed the highest bacteria accumulation. Compare to static growth assay results, larger number of bacteria adhered on pristine PET substrate and pristine PCT composite coatings due to higher mass of bacteria transport in the presence of appropriate shear force. Higher fluoresce signal was captured on the protrusion area in contrast to groove parts of the pristine PCT composite surfaces as shown in Fig. 6-17, which indicated more bacteria accumulation in these area.

Superoleophobic coatings exhibited remarkable resistance to E.coli suspension in both static growth and dynamic growth condition in 24 h incubation. It has been reported that the presence of fluoroalkoxysilane prevented the adhesion of bacteria to the modified substrate and hindered the consequent growth and the formation of biofilm [26, 27]. In our case, this remarkable resistance of the superoleophobic surface coating to high E.coli

concentration suspension is attributed to excellent oil repelling ability owing to the synergetic effect of surface fluorosilane and hierarchical roughness. The bacteria adhesion is the initial step in the formation of a biofilm. Once bacteria attach to the defect spot of the coating, they start to replicate and gradually change the surface property. Long-term bacterial adhesion and possible biofilm formation time-lapse profile will be further tested to investigate the robust and efficiency of the superoleophobic surface.

6.7 Conclusions

Superoleophobic surfaces with immiscible polymer and nanofillers have been prepared. An appropriate morphology by controlling of the composition and nanofiller-polymer interaction is critical to achieve the superoleophobic surface. This general strategy is obviously not limited to the loading of inorganic titanium dioxide particles. Other nanoparticles with intrinsically property might be used as well. It was clearly demonstrated that the prepared superoleophobic composite coating based on polymer and nanofillers exhibited excellent resistance to protein adsorption and extraordinarily reduced bacterial adhesion in a 24 h incubation period. This biofouling resistance is due to the synergetic effect of low surface energy and entrapped air, which render superoleophobicity to the material. On-going work is being carried out to investigate a wide range of pathogen as models on the bacteria adhesion to superoleophobic surfaces. Long time bacteria and protein adhesion behavior and protein conformation difference when exposure to the suproleophobic surfaces should be considered in future work.

6.8 References

- [1] Magin CM, Cooper SP, Brennan AB. Non-toxic antifouling strategies. *Mater Today*. 2010;13:36-44.
- [2] Harris JM, Zalipsky S, American Chemical Society. Division of Polymer Chemistry., American Chemical Society. Meeting. Poly(ethylene glycol) : chemistry and biological applications. Washington, DC: American Chemical Society; 1997.

- [3] Kingshott P, Thissen H, Griesser HJ. Effects of cloud-point grafting, chain length, and density of PEG layers on competitive adsorption of ocular proteins. *Biomaterials*. 2002;23:2043-56.
- [4] Ma HW, Li DJ, Sheng X, Zhao B, Chilkoti A. Protein-resistant polymer coatings on silicon oxide by surface-initiated atom transfer radical polymerization. *Langmuir : the ACS journal of surfaces and colloids*. 2006;22:3751-6.
- [5] Jeon SI, Andrade JD. Protein Surface Interactions in the Presence of Polyethylene Oxide .2. Effect of Protein Size. *Journal of colloid and interface science*. 1991;142:159-66.
- [6] Jeon SI, Lee JH, Andrade JD, Degennes PG. Protein Surface Interactions in the Presence of Polyethylene Oxide .1. Simplified Theory. *Journal of colloid and interface science*. 1991;142:149-58.
- [7] Bjorling M. Interaction between Surfaces with Attached Poly(Ethylene Oxide) Chains. *Macromolecules*. 1992;25:3956-70.
- [8] Rabea EI, Badawy MET, Stevens CV, Smagghe G, Steurbaut W. Chitosan as antimicrobial agent: Applications and mode of action. *Biomacromolecules*. 2003;4:1457-65.
- [9] Devlieghere F, Vermeulen A, Debevere J. Chitosan: antimicrobial activity, interactions with food components and applicability as a coating on fruit and vegetables. *Food Microbiol*. 2004;21:703-14.
- [10] Cui D, Szarpak A, Pignot-Paintrand I, Varrot A, Boudou T, Detrembleur C, et al. Contact-Killing Polyelectrolyte Microcapsules Based on Chitosan Derivatives. *Advanced Functional Materials*. 2010;20:3303-12.
- [11] Chen SF, Zheng J, Li LY, Jiang SY. Strong resistance of phosphorylcholine self-assembled monolayers to protein adsorption: Insights into nonfouling properties of zwitterionic materials. *Journal of the American Chemical Society*. 2005;127:14473-8.

- [12] Cheng G, Zhang Z, Chen SF, Bryers JD, Jiang SY. Inhibition of bacterial adhesion and biofilm formation on zwitterionic surfaces. *Biomaterials*. 2007;28:4192-9.
- [13] Jiang SY, Cao ZQ. Ultralow-Fouling, Functionalizable, and Hydrolyzable Zwitterionic Materials and Their Derivatives for Biological Applications. *Adv Mater*. 2010;22:920-32.
- [14] Feng L, Li SH, Li YS, Li HJ, Zhang LJ, Zhai J, et al. Super-hydrophobic surfaces: From natural to artificial. *Adv Mater*. 2002;14:1857-60.
- [15] Gao XF, Jiang L. Water-repellent legs of water striders. *Nature*. 2004;432:36-.
- [16] Ma JW, Sun YK, Gleichauf K, Lou J, Li QL. Nanostructure on Taro Leaves Resists Fouling by Colloids and Bacteria under Submerged Conditions. *Langmuir : the ACS journal of surfaces and colloids*. 2011;27:10035-40.
- [17] Hoque E, DeRose JA, Hoffmann P, Mathieu HJ. Robust perfluorosilanized copper surfaces. *Surf Interface Anal*. 2006;38:62-8.
- [18] C.D. Wagner WMR, L.E. Davis, J.F. Moulder, G.E. Muilenberg *Handbook of X-ray Photoelectron Spectroscopy*. Minnesota: PerkinElmer Co.; 1979.
- [19] Marmur A. Wetting on hydrophobic rough surfaces: To be heterogeneous or not to be? *Langmuir : the ACS journal of surfaces and colloids*. 2003;19:8343-8.
- [20] Horbett TA. Principles underlying the role of adsorbed plasma-proteins in blood interactions with foreign materials. *Cardiovasc Pathol*. 1993;2:S137-S48.
- [21] Han DK, Jeong SY, Kim YH, Min BG. Surface characteristics and blood compatibility of polyurethanes grafted by perfluoroalkyl chains. *J Biomater Sci-Polym Ed*. 1992;3:229-41.
- [22] Quirynen M, Vandermei HC, Bollen CML, Schotte A, Marechal M, Doornbusch GI, et al. An in-vivo study of the influence of the surface-roughness of implants on the microbiology of supragingival and subgivaival plaque. *J Dent Res*. 1993;72:1304-9.

[23] Wu Y, Zitelli JP, TenHuisen KS, Yu XJ, Libera MR. Differential response of Staphylococci and osteoblasts to varying titanium surface roughness. *Biomaterials*. 2011;32:951-60.

[24] Bollen CML, Papaioanno W, VanEldere J, Schepers E, Quirynen M, vanSteenberghe D. The influence of abutment surface roughness on plaque accumulation and peri-implant mucositis. *Clin Oral Implant Res*. 1996;7:201-11.

[25] Busscher HJ, Vandermei HC. Use of flow chamber devices and image-analysis methods to study microbial adhesion. *Methods Enzymol*. 1995;253:455-77.

[26] Vilcnik A, Jerman I, Vuk AS, Kozelj M, Orel B, Tomsic B, et al. Structural Properties and Antibacterial Effects of Hydrophobic and Oleophobic Sol-Gel Coatings for Cotton Fabrics. *Langmuir : the ACS journal of surfaces and colloids*. 2009;25:5869-80.

[27] Tang HY, Cao T, Liang XM, Wang AF, Salley SO, McAllister J, et al. Influence of silicone surface roughness and hydrophobicity on adhesion and colonization of *Staphylococcus epidermidis*. *J Biomed Mater Res Part A*. 2009;88A:454-63.

Chapter 7

7 Summary and Outlook

This dissertation presents the results from the majority of my Ph.D. research program, which focused on surfaces with antifouling properties including active bactericide agent TiO_2 and passive superoleophobic coating surfaces. The thesis consists of two major sections: the first section focuses on the design and fabrication of TiO_2 nanomaterials and the consequent application for antibacterial adhesion, and the second section focuses on the design and fabrication of superoleophobic surfaces and consequent application for antibacterial and anti-protein adhesion.

In the first section, mesoporous TiO_2 thin films of polycrystalline anatase containing silver nanoparticles were prepared by the template sol-gel method on silicon substrates; customer tailored resultant silver nanoparticles containing TiO_2 film can be achieved by tuning the precursor solution composition. No toxic chemicals are required to reduce silver ions. Silver nanoparticles were uniformly distributed and strongly attached to the mesoporous TiO_2 matrix, which displayed excellent antibacterial activity for a long period. To extend the TiO_2 nanomaterial application to visible light range, nitrogen doped TiO_2 nanoparticles and nanothin films were prepared using sol-gel technique. Extensive characterization results showed the resultant powder in nanometer scale size range with mesoporous structure. The presence of nitrogen and the interstitial doping states of nitrogen was confirmed by UV-visible spectra and XPS characterization. The enhanced photoactivity to degrade methyl blue and achieve *E. coli* inactivation was observed.

In Chapter 4 we developed a modified method to deposit TiO_2 coatings on desired substrates in mild environmental conditions. The resultant surface structure is controllable in the presence of various seeds, as required. After surface modification with low surface energy fluoroalkyl containing silane, superoleophobic surface have been achieved owing to the dual-scale surface structure and low surface energy decoration. Both pristine and superoleophobic coatings displayed antibacterial adhesion, which have potential applications as biosensors.

In the second section, on the basis of a review of general principles and experimental methods for fabrication superoleophobic surfaces, we explored a novel type of surface coating containing a polymer matrix and functional nanomaterials. This is not only practical and low-cost in the fabrication process, but can easily be tuned to express the required functionalities. Besides developing and characterizing the fabrication process, the resultant superoleophobic coatings were evaluated in terms of surface structure and chemical composition, robust mechanical properties, wettability and conductivity. By applying a spray technique, the mixture of polymer and nanomaterials can self-assemble forming hierarchical structures. We found that the superoleophobic surface containing polyisoprene and conductive CB were completely nonwetable by both water and hexadecane, which showed contact angles above 150° with low roll-off angles. The surface remained superoleophobic on rubber substrates when strained up to 100%. The resistivity is on the order of 0.01 ohm.m.

We found the superoleophobic surfaces with immiscible polymer and nanofillers can be obtained by appropriate control of the composition ratio. The general strategy is not limited to the loading of polyisoprene and CB. Other polymers such as PDMS, butyl rubber, triblock polymer including polystyrene-polyisoprene-polystyrene can be serve as the polymer matrix and inorganic nanomaterials such as TiO_2 , carbon nanotubes and Fe_3O_4 can serve as the functional compositions. The resultant composite surface coatings with the combined properties of intrinsic properties of inorganic particle and polymer can be tailored.

Surfaces with extreme wetting properties are currently receiving considerable attention in regards to their potential for application as protein resistant coatings. It was clearly demonstrated that the prepared superoleophobic composite coatings based on polyisoprene, CB and TiO_2 exhibited excellent resistance to protein adsorption and extraordinarily reduced bacterial adhesion in a 24 h incubation period. This excellent biofouling resistance is attributed to the synergetic effect of low surface energy and entrapped air, which render superoleophobicity to the material. It is anticipated that the demonstrated approach and principle could be applied to expand more multi-functional materials.

For future work, theoretical mechanism of wetting of the rough polymer-nanomaterial surfaces will be investigated to fulfill the design concept and experimental method. In particular, wettability varies with the external strain on the substrate, which in principle can change the surface morphology will be extensively studied. An appropriate model to describe corresponding wettability will be built, which provides a fundamental understanding to the design of more controllable functional surfaces. The mechanism of forming self-assembled hierarchical structures by spray method will be studied.

As for the antifouling studies with current used strategy, long-term antifouling experiments will be carried out to study the durability of the functional surface coating and to extend the potential applications. More types of bacterial strains will be studied to fully understand the adhesion on the surfaces with hierarchical structures. Antifouling ability influenced by the external stimuli such as applied strain will be studied.

The development of superoleophobic and self-cleaning surfaces is important for basic research as well as biomedical applications. More active bactericidal agents will be applied to the superoleophobic system, such as the introduction of nitrogen-TiO₂ nanopowders and silver doped TiO₂ nanopowders with visible or dark bactericidal ability to the polymer-nanomaterial composite system will be investigated. The combination of active agents with passive strategy will enhance the antifouling ability of surface coating. By using multifunctional compositions, the resultant composite coatings inherit the intrinsic property of each ingredient can be achieved. Moreover, the controllable surface can respond to the external stimuli and can be used to design smart antifouling surfaces. Such surfaces with designed patterns with areas of contrasting bacterial adhesion properties will have potential in biosensor applications.

Curriculum Vitae

Name: Binyu Yu

Post-secondary Education and Degrees: Sichuan University
Chengdu, China
2001-2008 M.Sc.

The University of Western Ontario
London, Ontario, Canada
2008-2012 Ph.D

Honours and Awards: Province of Ontario Graduate Scholarship
2009-2010

Western Graduate Research Scholarship (WGRS), UWO

Related Work Experience Research Assistant/
The University of Western Ontario
2008-2012

Teaching Assistant
The University of Western Ontario
2009-2011

Publications:

Yu BY, Leung KM, Guo QQ, Lau WM, Yang J. Nanotechnology. 2011;22.

Karamdoust S, Yu BY, Bonduelle CV, Liu Y, Davidson G, Stojcevic G, et al. J Mater Chem. 2012;22:4881-9.

He J, Yu BY, Hourwitz MJ, Liu YJ, Perez MT, Yang J, et al. Angew Chem-Int Edit. 2012;51:3628-33.

Wang T, Yin ZH, Wen X, Yu BY, Deng XP, Zhao CS. Sep Sci Technol. 2010;45:142-7.

Yang KG, Ma JJ, Zhou H, Li BQ, Yu BY, Zhao CS. Desalination. 2009;245:232-45.